

# Theoretical Investigation of Catalytic Methane Cracking and Carbon Nanotube Growth

by

Jingde Li

A thesis  
presented to the University of Waterloo  
in fulfillment of the  
thesis requirement for the degree of  
Doctor of Philosophy  
in  
Chemical Engineering

Waterloo, Ontario, Canada, 2014

© Jingde Li 2014

## **AUTHOR'S DECLARATION**

I hereby declare that I am the sole author of this thesis. This is a true copy of the thesis, including any required final revisions, as accepted by my examiners.

I understand that my thesis may be made electronically available to the public.

## Abstract

Methane cracking on transition metal surfaces is a catalytically important reaction. It is a key step to produce hydrogen and carbonaceous nanomaterials, such as carbon nanotubes (CNT) or carbon nanofibers (CNF), which display unique mechanical and electrical properties, and have been widely used as electronic components, polymer additives, gas storage, and catalyst support materials. Although the catalytic methane cracking and CNT/CNF growth have drawn lots of attentions, the understanding of the catalytic methane cracking properties and CNT/CNF growth mechanism is still limited.

To develop a better understanding of the catalytic methane cracking and the CNT/CNF growth process, the activation of the C–H bond of methane and the creation C–C bonds on transition metal catalysts, especially Ni, have been studied at atomic level using Density Functional Theory (DFT). Ni is of particular interest because, among the different metals commonly used in the methane cracking and CNT/CNF production, Ni-based catalysts show very good catalytic activity at relatively moderate temperatures. In this research, factors that affect the methane dissociation properties, e.g. effects of the catalyst structure, carbon deposition, oxide support and alloying, were analyzed using DFT calculations. The study of the Ni catalyst surface topology effect on methane dehydrogenation properties was conducted on various Ni catalyst surfaces, i.e., Ni (100), Ni (111) and Ni (553). The transition states for methane sequential dehydrogenations on the three surfaces were identified. The results show that the adsorption of  $\text{CH}_x$  ( $x=1-3$ ) and H species is favoured on less packed surfaces, e.g., Ni (100) and Ni (553). Moreover, it was found that the Ni (553) and Ni (100) promote the dissociation of  $\text{CH}_x$  species by lowering the activation barriers when compared to Ni (111). The above study was conducted on clean Ni catalyst surfaces. During the reactions, however, there will be carbon atoms deposited on the Ni surface. To provide a more realistic modeling of the reaction, the study of Ni catalytic methane cracking is then further extended by taking into account the effects of carbon atoms depositions. Methane dissociation on clean, surface-carbon, and subsurface-carbon-covered Ni (111) surfaces were investigated. The results show that the existence of surface and subsurface C atoms destabilized the adsorption of the surface hydrocarbon species when compared to the clean Ni (111) surface. Moreover, it was found that the presence of carbon atoms increase the  $\text{CH}_x$  ( $x=4-1$ ) species activation barriers especially on the surface-carbon-covered (1/4 ML) Ni (111) surface, where  $\text{CH}_x$  ( $x=4-1$ ) species encounter the highest energy barriers for dissociation due to the electronic deactivation induced by C–Ni bonding. The calculations also show that  $\text{CH}_x$  dissociation barriers are not affected by neighboring C atoms at low surface carbon coverage (1/9 ML).

The DFT study of Ni catalytic methane dissociation, so far, only focuses on Ni catalyst surface. However, in the actual process, the Ni catalyst is usually deposited on oxide support; little is known about the effect of the support, especially the metal-support interface, on the dissociation properties of methane. Therefore, the dissociations of methane and hydrogen on Ni cluster supported on  $\gamma$ -Al<sub>2</sub>O<sub>3</sub> support were investigated using DFT calculations. Two systems: Ni<sub>4</sub> cluster supported on the spinel model of  $\gamma$ -Al<sub>2</sub>O<sub>3</sub> (100) surface, S(Ni<sub>4</sub>), and on the non-spinel model of  $\gamma$ -Al<sub>2</sub>O<sub>3</sub> (100) surface, NS(Ni<sub>4</sub>), have been used to model Ni<sub>4</sub>/ $\gamma$ -Al<sub>2</sub>O<sub>3</sub>. For both models, it was found that CH<sub>4</sub> and H<sub>2</sub> dissociations are kinetically preferred at the particular Ni atoms located at the nickel-alumina interface when compared with the top of the Ni cluster. Also, the study of CH<sub>3</sub> and H adsorption on different sites of the S(Ni<sub>4</sub>) and NS(Ni<sub>4</sub>) show that CH<sub>3</sub> and H bonded with the Ni atom at Ni<sub>4</sub>/ $\gamma$ -Al<sub>2</sub>O<sub>3</sub> interface are more stable than at the top site adsorption. Hirshfeld charge analysis showed that the surface Al atom works primarily as a charge donation partner when CH<sub>3</sub> and H are bonded with the Ni atom at the interface. This also resulted in an up shift of the d-orbital around the Fermi energy, which finally stabilized the interface adsorption by this Al (donor)–Ni–adsorbates (acceptor) effect. The results obtained in the present analysis indicate that the metal-oxide interface plays an essential role in the dissociation of methane and hydrogen.

During the methane cracking process, carbon is deposited on the catalyst. Part of these carbon atoms will exist in the form of CNT, and some of them is deposited as encapsulating carbon in the form of graphene, which causes catalyst deactivation. To understand the role of metal elements in the growth of CNT or graphene, some crucial processes occur on the (111) surface of different transition metals, i.e., Fe, Co, Ni, and Cu was analyzed using DFT. These processes consist of methane cracking to produce C, C atoms surface diffusion and C nucleation reactions. This study showed that Ni-based catalyst is a suitable substrate for growing CNT: it has a moderate reactivity towards C–H bond activation; low energy barrier for C atom surface diffusion, and a relatively high nucleation barrier for the surface C atoms. Meanwhile, this study also showed that Cu may be a suitable catalyst for synthesis of graphene due to the low diffusion and nucleation barriers of C adatoms on Cu. One key limitation of Cu is the low reactivity of this metal towards methane dissociation, which dominates the growth rate and reaction conditions of the process. Since Fe and Ni were found more reactive towards C–H bond breaking reactions, the results from this study indicate that Cu based alloys, e.g. Cu<sub>8</sub>Ni, may be a suitable catalyst for the mass production of graphene.

To further extend the understanding regarding the behavior of the carbon atoms during the Ni catalyst CNT growth, the structure, nucleation energetics, and mobility of carbon intermediates up to 6 atoms on

the Ni (111) surface were investigated. This study showed that carbon clusters were more thermodynamically stable than adsorbed atomic carbon, with linear carbon structures being more stable than branched and ring structures. The results also showed that carbon chains have higher mobility than branched configurations. The transition states and energy barriers for the formation of different carbon clusters were also studied. The results suggest that the formation of the branched carbon configurations is kinetically favored as it presents lower energy barriers than those obtained for carbon chains.

Furthermore, based on the above DFT calculations results, a Ni catalytic CNT growth mechanism based on carbon species surface diffusion was developed. A multi-scale modeling approach that integrates DFT calculations and kinetic Monte Carlo (KMC) simulation was developed, in which the energetic results obtained from DFT calculations were used to set-up the kinetic database for the KMC simulation. The KMC simulations explicitly follow the elementary steps involved in the CNT growth that include CH<sub>4</sub> dissociation, C surface and bulk diffusion, C nucleation, C<sub>3</sub> trimer diffusion and C and C<sub>3</sub> incorporation into CNT wall. The KMC simulations show that CNT growth is dominated by the C surface diffusion. Moreover, it was found that the surface diffusion of the small C cluster, e.g., C<sub>3</sub> trimer, is also a critical step in the growth mechanism of the CNT. It prevents fast nucleation of the C atoms on the catalyst surface, and therefore inhibits the deactivation of the catalyst. The CNT growth rates predicted by KMC simulations fit well with the experimental data, verifying the proposed CNT growth mechanism. This study will therefore provide insight regarding the mechanism and kinetic properties of Ni catalytic methane cracking and CNT growth process.

In summary, a systematic theoretical investigation of the catalytic methane cracking and CNT growth process was performed in this study. It was found the catalyst structure, carbon deposition, and the  $\gamma$ -Al<sub>2</sub>O<sub>3</sub> support has significant effect on the CH<sub>x</sub> dissociation properties. Moreover, DFT analysis also shows that the reactivity of the catalyst towards C–H bond activation and CNT or graphene growth varies with different transition metals. Finally, based on the DFT study of the carbon cluster nucleation, a CNT growth model that accounts for carbon cluster diffusion and nucleation was proposed. Using the kinetic parameters that obtained by the DFT calculations, a KMC simulation was developed. By comparing the CNT growth rate predicted by the KMC simulations with the experimental data, the proposed CNT growth mechanism is validated.

## **Acknowledgements**

I would like to express my sincere gratitude and appreciation to my supervisors, Professor Eric Croiset and Professor Luis Ricardez-Sandoval, for their great support, motivation, guidance and helpful advices during my PhD study. I would also like extend my appreciation and thanks to my PhD exam committee members for their valuable comments:

Professor Lichang Wang (Southern Illinois University, Department of Chemistry and Biochemistry)

Professor Marcel Nooijen (University of Waterloo, Department of Chemistry)

Professor Yuning Li (University of Waterloo, Department of Chemical Engineering)

Professor Nasser Mohieddin Abukhdeir (University of Waterloo, Department of Chemical Engineering)

Thanks to all of the group members who were always ready to help in any part of the project. During my PhD study, I have received great help from them: Shabnam Rasoulia, Sami Bahakim, Hussein Sahraei, Bhushan Patil and Dave Evans. My former supervisor, Professor Minhua Zhang, Tianjin University, China; Thanks a lot for your support. Also to all my friends in China, particularly, Dr. Zhongfeng Geng, thanks a lot for your encouragement.

This work was made possible by access to the facilities of the Shared Hierarchical Academic Research Computing Network (SHARCNET: [www.sharcnet.ca](http://www.sharcnet.ca)) and Compute/Calcul Canada. I would like to thank the SHARCNET technical members especially Jemmy Hu, for his valuable technical support throughout the project. Special thanks are extended to the China Scholarship Council (CSC) for their sponsorship during my study and the Natural Sciences and Natural Science and Engineering Research Council of Canada (NSERC) for financial support.

Finally, I would like to acknowledge my parents, my brother, and all my family, thanks a lot for your support, patience and sacrifice.

## Table of Contents

AUTHOR'S DECLARATION.....	ii
Abstract.....	iii
Acknowledgements.....	vi
Table of Contents.....	vii
List of Figures.....	xi
List of Tables.....	xvii
Chapter 1 Introduction and Motivation.....	1
1.1 Research objectives.....	4
1.2 Research contribution.....	4
1.3 Outline of the thesis.....	5
Chapter 2 Background and Literature Review.....	7
2.1 Overview.....	7
2.2 Density Function Theory (DFT).....	8
2.3 Catalytic methane cracking.....	11
2.3.1 Catalysts for catalytic methane cracking.....	11
2.3.2 DFT study of catalytic methane cracking.....	12
2.4 Catalytic CNF/CNT growth.....	14
2.5 Microkinetic study of catalytic methane cracking and CNT/CNF growth.....	21
2.6 KMC approach.....	24
Chapter 3 Methane Dissociation on Flat and Stepped Ni surfaces.....	28
3.1 Introduction.....	28
3.2 Computational details.....	30
3.2.1 Calculation methods.....	30
3.2.2 Surface models.....	32
3.3 Results and discussion.....	33
3.3.1 Adsorption of CH <sub>x</sub> and H species.....	33
3.3.2 Minimum energy path for methane activation.....	42
3.3.3 Electronic structure analysis.....	52
3.4 Summary.....	57
Chapter 4 Effect of Carbon on the Ni Catalytic Methane Cracking Reaction.....	59

4.1 Introduction .....	59
4.2 Computational details.....	60
4.2.1 Calculation methods .....	60
4.2.2 Surface models .....	61
4.3 Results and discussion.....	62
4.3.1 Convergence with respect to the slab thickness and unit cell dimensions.....	62
4.3.2 CH <sub>x</sub> (x =3-0) adsorption .....	63
4.3.3 Methane dissociation .....	68
4.3.4 Free energy for CH <sub>4</sub> successive dehydrogenation .....	76
4.4 Summary .....	77
Chapter 5 Effect of Metal–Support Interface during CH <sub>4</sub> Dissociation on Ni/ $\gamma$ -Al <sub>2</sub> O <sub>3</sub> .....	78
5.1 Introduction .....	78
5.2 Computational details.....	80
5.2.1 Calculation methods .....	80
5.2.2 Surface models .....	80
5.3 Results and discussion.....	82
5.3.1 Ni <sub>4</sub> Cluster Supported on the $\gamma$ -Al <sub>2</sub> O <sub>3</sub> (100).....	82
5.3.2 CH <sub>3</sub> and H adsorption on Ni <sub>4</sub> / $\gamma$ -Al <sub>2</sub> O <sub>3</sub> (100) .....	84
5.3.3 CH <sub>3</sub> and H adsorption on Ni <sub>5</sub> / $\gamma$ -Al <sub>2</sub> O <sub>3</sub> (100) .....	96
5.3.4 Metal-support interaction .....	99
5.3.5 CH <sub>4</sub> and H <sub>2</sub> dissociation on Ni <sub>4</sub> / $\gamma$ -Al <sub>2</sub> O <sub>3</sub> (100).....	101
5.4 Summary .....	105
Chapter 6 Effects of Metal Elements in Catalytic Growth of Carbon Nanotubes/Graphene.....	107
6.1 Introduction .....	107
6.2 Computational details.....	109
6.2.1 Calculation methods .....	109
6.2.2 Surface models .....	109
6.3 Results and discussion.....	110
6.3.1 Dehydrogenation energetics .....	110
6.3.2 Mobility of C monomers .....	112
6.3.3 Stability of C species and barriers for carbon dimer and trimer nucleation .....	113
6.3.4 Effect of transition metals on CNTs/Graphene growth .....	116

6.3.5 Cu <sub>8</sub> Ni and Cu <sub>8</sub> Fe alloys for graphene production .....	117
6.4 Summary .....	118
Chapter 7 Carbon Clusters on the Ni (111) Surface .....	120
7.1 Introduction .....	120
7.2 Computational details.....	122
7.2.1 Calculation methods .....	122
7.2.2 Surface models .....	122
7.3 Results and discussion.....	123
7.3.1 Adsorption of carbon atoms and clusters (C <sub>2</sub> –C <sub>6</sub> ) on Ni (111) .....	123
7.3.2 Mobility of the carbon species on the Ni (111) surface .....	130
7.3.3 Carbon cluster nucleation on Ni (111) .....	132
7.4 Summary .....	137
Chapter 8 Carbon Nanotube Growth: Kinetic Monte Carlo Simulations .....	139
8.1 Introduction .....	139
8.2 Simulation details .....	141
8.2.1 CNT growth mechanism.....	141
8.2.2 DFT modeling and intrinsic kinetics calculations .....	142
8.2.3 Elementary steps in KMC simulation.....	145
8.2.4 Accelerated kinetic Monte Carlo (AKMC) .....	147
8.3 Results and discussion.....	150
8.3.1 Validation of the CNT growth model.....	151
8.3.2 Ni particle size effect.....	152
8.3.3 Sensitivity on the kinetic parameters.....	153
8.3.4 Role of C cluster surface diffusion.....	155
8.3.5 Carbon bulk diffusion and bamboo–like CNT .....	156
8.4 Summary .....	157
Chapter 9 Conclusions and Recommendations.....	159
9.1 Conclusions .....	159
9.2 Recommendations .....	161
Publications.....	163
Copyright Permissions.....	164
References.....	168

Appendix..... 196

## List of Figures

Figure 1.1 Schematics of tip-growth mechanism for carbon filament growth. Reprinted from [23] with permission from Elsevier. ....	2
Figure 2.1 SEM micrographs of a Ni/SiO <sub>2</sub> catalyst after exposure to methane. Reprinted from [23] with permission from Elsevier. ....	15
Figure 2.2 Schematic picture of the formation of a full fibre (left) and a hollow tube (right). In the case of the fibre, the nucleation has taken place over the entire back of the metal particle; in the case of the tube, the nucleation has been restricted to the vicinity of the gas-metal interface. Reprinted from [9] with permission from Elsevier. ....	16
Figure 2.3 (a-d) ETEM image sequence showing a growing CNF in 3:1 NH <sub>3</sub> :C <sub>2</sub> H <sub>2</sub> at 1.3 mbar and 480 °C. The video was recorded at 30 frames/s, and the time of the respective pictures is indicated. Reprinted from [11] with permission from the the American Chemical Society. ....	17
Figure 2.4 A sequence of TEM images showing the formation of an incomplete knot in less than 6s. Reprinted from [12] with permission from the American Chemical Society. ....	18
Figure 2.5 (a) Schematic of the growth process. (b) Bright field image and electron energy loss spectroscopy Ni and carbon edge elemental maps of a PECVD CNF at 500°C. Reprinted from [13] with permission from the American Physical Society. ....	19
Figure 2.6 Initial, transition, and final states in the front growth mechanism (a) base growth mechanism (b) and atom-exchange growth mechanism (c) modeled using DFT calculations. Reprinted from [15] with permission from the American Physical Society. ....	20
Figure 2.7 Snapshots of growth process trajectory of a seed nanotube on a Fe <sub>38</sub> cluster. Reprinted from [85] with permission from the American Chemical Society. ....	21
Figure 2.8 Mechanism of the formation of filamentous carbon by the methane cracking. Reprinted from [88] with permission from Elsevier. ....	23
Figure 2.9 KMC algorithm flow chart. ....	26
Figure 3.1 Top views of a) Ni (100), b) Ni (111) and c) Ni (553) surfaces. The upper step Ni atoms on Ni (553) are represented by green balls. ....	33
Figure 3.2 The adsorption sites considered on a 2×1 unit cell of Ni (553) surface are: (a) upper-step fcc site, (b) upper-step hcp site, (c) step top site, (d) step bridge site, (e) lower-step hcp site, and (f) lower-step fcc site. The upper step Ni atoms are represented by green balls. ....	34
Figure 3.3 Top views of CH <sub>x</sub> (x=0-3) and H adsorbed on Ni (100). Blue: Ni, white: H, black: C. ....	37

Figure 3.4 Top views of $\text{CH}_x$ ( $x=0-3$ ) and H adsorbed on Ni (111). Blue: Ni, white: H, black: C.....	38
Figure 3.5 Top views of $\text{CH}_x$ ( $x=0-3$ ) and H adsorbed on Ni (553). Blue: Ni, white: H, black: C.....	38
Figure 3.6 Geometric structures of the initial state (I.S), transition state (T.S), and final state (F.S) of the four steps of $\text{CH}_4$ dehydrogenation on Ni (100) surface. Blue: Ni, gray: C, and white: H.....	46
Figure 3.7 Geometric structures of the initial state (I.S), transition state (T.S), and final state (F.S) of the four steps of $\text{CH}_4$ dehydrogenation on Ni (111) surface. Blue: Ni, gray: C, and white: H.....	48
Figure 3.8 Geometric structures of the initial state (I.S), transition state (T.S), and final state (F.S) of the four steps of $\text{CH}_4$ dehydrogenation on Ni (553) surface. Green: Ni at upper step, blue: Ni at down the step gray: C, and white: H.....	51
Figure 3.9 Projected density of states (PDOS) for isolated C atom and surface Ni atoms involved in C adsorption for the three respective surfaces: the Ni (111), Ni (100) and Ni (553). The vertical green lines donate the Fermi level.....	54
Figure 3.10 Reaction energy diagram of reaction paths of the $\text{CH}_x$ ( $x=1-4$ ) dissociation reaction on Ni (100), Ni (111) and Ni (553) surfaces.....	56
Figure 3.11 Projected density of states (PDOS) plots of the d-orbitals of the surface Ni atom for the three respective surfaces: Ni (111), Ni (100), and Ni (553). The vertical dashed lines represent the location of the corresponding d-band center. The vertical green lines indicate the Fermi level.....	57
Figure 4.1 Top views of the $2 \times 2$ unit cell for different Ni surfaces. C atoms are colored gray, H atoms white, first-layer Ni atoms green, second-layer Ni atoms cyan, third-layer Ni atoms blue.....	62
Figure 4.2 $\text{CH}_x$ ( $x = 3-0$ ) adsorption configurations on the different Ni (111) surfaces: (a–d), (e–h), and (i–l) correspond to the geometries on Ni (111)–clean, Ni (111)– $4\text{C}_{\text{sub}}$ and Ni (111)– $\text{C}_{\text{on}}$ , respectively. C atoms are colored gray, H atoms white, first-layer Ni atoms green, second-layer Ni atoms cyan, third-layer Ni atoms blue.....	64
Figure 4.3 Projected density of states (PDOS) for Ni atoms on the three respective surfaces: Ni (111)–clean, Ni (111)– $4\text{C}_{\text{sub}}$ and Ni (111)– $\text{C}_{\text{on}}$ . Note that Ni 3d* represents the Ni atom that are not bonded the C atom on Ni (111)– $\text{C}_{\text{on}}$ .....	67
Figure 4.4 Geometric structures of transition state (TS) of the four steps of $\text{CH}_4$ dehydrogenation on different Ni (111) surfaces: (a–d), (e–h), and (i–l) correspond to the TS geometries on Ni (111)–clean, Ni (111)– $4\text{C}_{\text{sub}}$ and Ni (111)– $\text{C}_{\text{on}}$ , respectively. C atoms are colored gray, H atoms white, first-layer Ni atoms green, second-layer Ni atoms cyan, third-layer Ni atoms blue.....	68
Figure 4.5 Geometric structures of transition state (TS) of the $\text{CH}_4$ and CH dissociation on C deposited (2/9 ML) Ni (111) surface modeled by $3 \times 3$ unite cell: $A_1$ and $A_2$ are the TS geometries on Ni (111)– $\text{C}_{\text{on}}$	

(2/9 ML)–A; B <sub>1</sub> and B <sub>2</sub> are the TS geometries on Ni (111)–C <sub>on</sub> (2/9 ML)–B. C atoms are colored gray, H atoms white, first-layer Ni atoms green, second-layer Ni atoms cyan, third-layer Ni atoms blue. ....	75
Figure 4.6 Gibbs free energy diagrams for the CH <sub>4</sub> dehydrogenation on different Ni (111) surfaces: Ni (111)–clean, Ni (111)–4C <sub>sub</sub> and Ni (111)–C <sub>on</sub> . ....	77
Figure 5.1 The optimized spinel type model of $\gamma$ -Al <sub>2</sub> O <sub>3</sub> (100)–1×1 surface. (a) top view; (b) side view. Oxygen atoms are shown in red and aluminum atoms in magenta. ....	82
Figure 5.2 The optimized non–spinel type model of $\gamma$ -Al <sub>2</sub> O <sub>3</sub> (100)–2×1 surface. (a) top view; (b) side view. ....	82
Figure 5.3 The optimized structure of Ni <sub>4</sub> cluster supported on the spinel type $\gamma$ -Al <sub>2</sub> O <sub>3</sub> (100) surface, S(Ni <sub>4</sub> ). (a) top view; (b) side view. Bond lengths are in Å. Dark blue balls stand for Ni atoms, and others are the same as in Figure 5.1. ....	83
Figure 5.4 The optimized structure of Ni <sub>4</sub> cluster supported on the non-spinel type $\gamma$ -Al <sub>2</sub> O <sub>3</sub> (100) surface. (a) top view; (b) side view. Bond lengths are in Å. ....	83
Figure 5.5 Side view of the stable configurations of CH <sub>3</sub> adsorbed on spinel type model of Ni <sub>4</sub> / $\gamma$ -Al <sub>2</sub> O <sub>3</sub> (100) surface, S(Ni <sub>4</sub> ). Bond lengths are in Å. Dark blue: Ni, white: H, Grey: C. ....	86
Figure 5.6 Projected density of states (PDOS) for C atom and the individual Ni atom involved in CH <sub>3</sub> adsorption on spinel type model of Ni <sub>4</sub> / $\gamma$ -Al <sub>2</sub> O <sub>3</sub> (100) surface, S(Ni <sub>4</sub> ): (a) top site adsorption (b) interface-1 (int1) adsorption. The pink line represents the d orbital of the individual Ni atom before CH <sub>3</sub> adsorption. ....	89
Figure 5.7 Side view for the stable configurations of CH <sub>3</sub> adsorbed on non–spinel type model of Ni <sub>4</sub> / $\gamma$ -Al <sub>2</sub> O <sub>3</sub> (100) surface, NS(Ni <sub>4</sub> ). Bond lengths are in Å. Dark blue: Ni, white: H, Grey: C. ....	90
Figure 5.8 Projected density of states (PDOS) for C atom and the individual Ni atom involved in CH <sub>3</sub> adsorption on non-spinel type model of Ni <sub>4</sub> / $\gamma$ -Al <sub>2</sub> O <sub>3</sub> (100) surface, NS(Ni <sub>4</sub> ): (a) top site adsorption (b) interface 1 (int1) adsorption. The pink line represents the d orbital of the individual Ni atom before CH <sub>3</sub> adsorption. ....	91
Figure 5.9 Side view for the stable configurations of H adsorbed on spinel type model of Ni <sub>4</sub> / $\gamma$ -Al <sub>2</sub> O <sub>3</sub> (100) surface, S(Ni <sub>4</sub> ). Bond lengths are in Å. Bond lengths are in Å. Dark blue: Ni, White: H. ....	92
Figure 5.10 Projected density of states (PDOS) for H atom and the individual Ni atom involved in H adsorption on spinel type model of Ni <sub>4</sub> / $\gamma$ -Al <sub>2</sub> O <sub>3</sub> (100) surface, S(Ni <sub>4</sub> ): (a) top site adsorption (b) interface1 (int1) adsorption. Note that the Pink line represents the d orbital of the individual Ni atom before H adsorption. ....	93

Figure 5.11 Side view for the stable configurations of H adsorbed on non-spinel type model of Ni <sub>4</sub> /γ-Al <sub>2</sub> O <sub>3</sub> (100) surface, NS(Ni <sub>4</sub> ). Bond lengths are in Å. Dark blue: Ni, White: H. ....	94
Figure 5.12 Projected density of states (PDOS) for H atom and the individual Ni atom involved in H adsorption on non-spinel type model of Ni <sub>4</sub> /γ-Al <sub>2</sub> O <sub>3</sub> (100) surface, NS(Ni <sub>4</sub> ): (a) top site adsorption (b) interface 1 (int1) adsorption. The pink line represents the d orbital of the individual Ni atom before H adsorption.....	95
Figure 5.13 The optimized structure of Ni <sub>5</sub> cluster supported on the spinel (left) and non-spinel (right) type γ-Al <sub>2</sub> O <sub>3</sub> (100) surface. Bond lengths are in Å. Oxygen atoms are shown in red and aluminum atoms in magenta. Dark blue balls stand for Ni atoms. ....	97
Figure 5.14 Side view for the stable configurations of CH <sub>3</sub> adsorbed on spinel type model of Ni <sub>5</sub> /γ-Al <sub>2</sub> O <sub>3</sub> (100) surface, S(Ni <sub>5</sub> ). Bond lengths are in Å. Dark blue: Ni, white: H, Grey: C.....	98
Figure 5.15 Side view for the stable configurations of CH <sub>3</sub> adsorbed on non-spinel type model of Ni <sub>5</sub> /γ-Al <sub>2</sub> O <sub>3</sub> (100) surface, NS(Ni <sub>5</sub> ). Bond lengths are in Å. Dark blue: Ni, white: H, Grey: C.....	98
Figure 5.16 Side view for the stable configurations of H adsorbed on spinel type model of Ni <sub>5</sub> /γ-Al <sub>2</sub> O <sub>3</sub> (100) surface, S(Ni <sub>5</sub> ). Bond lengths are in Å. Dark blue: Ni, white: H. ....	98
Figure 5.17 Side view for the stable configurations of H adsorbed on non-spinel type model of Ni <sub>5</sub> /γ-Al <sub>2</sub> O <sub>3</sub> (100) surface, NS(Ni <sub>5</sub> ). Bond lengths are in Å. Dark blue: Ni, white: H. ....	99
Figure 5.18 The potential energy profile and geometric structures of the initial state (I.S), transition state (T.S), and final state (F.S) for CH <sub>4</sub> dissociation on spinel type model of Ni <sub>4</sub> /γ-Al <sub>2</sub> O <sub>3</sub> (100) surface, S(Ni <sub>4</sub> ), at the top site and interface. Dark blue (Ni), gray (C), white (H). ....	102
Figure 5.19 The potential energy profile and geometric structures of the initial state (I.S), transition state (T.S), and final state (F.S) for CH <sub>4</sub> dissociation on non-spinel type model of Ni <sub>4</sub> /γ-Al <sub>2</sub> O <sub>3</sub> (100) surface, NS(Ni <sub>4</sub> ), at the top site and interface. Dark blue (Ni), gray (C), white (H). ....	103
Figure 5.20 The potential energy profile and geometric structures of the initial state (I.S), transition state (T.S), and final state (F.S) for H <sub>2</sub> dissociation on spinel type model of Ni <sub>4</sub> /γ-Al <sub>2</sub> O <sub>3</sub> (100) surface, S(Ni <sub>4</sub> ), at the top site and interface. Dark blue (Ni), white (H).....	104
Figure 5.21 Geometric structures of the initial state (I.S), transition state (T.S), and final state (F.S) for H <sub>2</sub> dissociation on the top and interface site of the Ni <sub>4</sub> / γ-Al <sub>2</sub> O <sub>3</sub> (100). Dark blue (Ni), gray (C), white (H). ....	105
Figure 6.1 Top views of the (111) surfaces of the a) Ni metal; (b) Fe metal. Note that the first layer atoms are in darker color. ....	110
Figure 6.2 Sketches of the TS for CH <sub>4</sub> dissociation on the (111) surfaces of the a) Fe; b) Ni. ....	110

Figure 6.3 Sketches of the TS for CH dissociation on the (111) surfaces of the a) Fe; b) Ni; c) Cu. ....	111
Figure 6.4 Sketches of the most stable adsorption configuration of carbon monomer, dimer and trimer on the (111) surfaces of the a) Fe; b) Ni. ....	114
Figure 6.5 Sketches of the TS for C <sub>2</sub> and C <sub>3</sub> nucleation on the (111) surfaces of the a) Fe; b) Ni. ....	115
Figure 7.1 Optimized geometries for selected carbon species on Ni (111): a) atomic carbon C@hcp; b) dimer C <sub>2</sub> @hcp-fcc; c) trimer C <sub>3</sub> @fcc-hcp-fcc; d) trimer C <sub>3</sub> @hcp-fcc-hcp; e) three single carbon 3C@hcp-hcp-hcp; f) three single carbon 3C@fcc-fcc-fcc. ....	126
Figure 7.2 Optimized geometries for tetramer (C <sub>4</sub> -chain; C <sub>4</sub> -branch) and pentamer (C <sub>5</sub> -chain; C <sub>5</sub> -branch; C <sub>5</sub> -ring) on Ni (111). ....	127
Figure 7.3 Optimized geometry for C <sub>6</sub> (C <sub>6</sub> -chain; C <sub>6</sub> -branch; C <sub>6</sub> -ring) on Ni (111). ....	128
Figure 7.4 Projected density of states (PDOS) in atomic C, C <sub>2</sub> dimer and C <sub>3</sub> trimer adsorption systems. The vertical green-dash line donates the Fermi level. Ni (a) and Ni (b) represent two different Ni atoms on the metal surface. Ni (a) has only one C–Ni bonding, whereas Ni (b) has two C neighbors (two C–Ni bonding). C(a) and C(b) in the C <sub>2</sub> @Ni(111) system are the two carbon atom in the dimer. In C <sub>3</sub> @Ni(111), C(a) is the one of the two siding C atom in the trimer with one C–C bonding, whereas C(b) is the middle C with two C–C bonding. ....	130
Figure 7.5 Pictorial views of the diffusion mechanisms of selected carbon clusters on Ni (111). ....	131
Figure 7.6 Reaction energy diagram of reaction paths for the C cluster (C <sub>2</sub> ~C <sub>4</sub> ) formation on Ni (111) surface. All energies are relative to the energy of the coadsorbed [C+C]*. ....	133
Figure 7.7 Reaction energy diagram of reaction paths for the C <sub>5</sub> cluster formation on Ni (111) surface. All energies are relative to the energy of the coadsorbed [C <sub>4</sub> (L)+C]*. ....	135
Figure 7.8 Geometric structures of the transition state (T.S.) for the formation of C <sub>5</sub> (L) and C <sub>5</sub> (B) clusters on Ni (111) surface: a) C <sub>5</sub> (L) formation by adding a C atom to a C <sub>4</sub> chain; b) C <sub>5</sub> (L) formation by adding a C <sub>3</sub> trimer to a C <sub>2</sub> dimer; c) C <sub>5</sub> (B) formation by adding a C atom to a branched C <sub>4</sub> ; d) C <sub>5</sub> (B) formation by adding a C <sub>3</sub> trimer to a C <sub>2</sub> dimer. ....	135
Figure 7.9 Reaction energy diagram of reaction paths for the C <sub>6</sub> cluster formation on Ni (111) surface. All energies are relative to the energy of the coadsorbed [C <sub>5</sub> (B)+C]*. ....	136
Figure 7.10 Geometric structures of the transition state (T.S.) for the formation of C <sub>6</sub> (L) and C <sub>6</sub> (B) clusters on Ni (111) surface: a) C <sub>6</sub> (L) formation by adding a C atom to a C <sub>5</sub> chain; b) C <sub>6</sub> (L) formation by adding a C <sub>3</sub> trimer to a C <sub>3</sub> trimer; c) C <sub>6</sub> (B) formation by adding a C atom to a branched C <sub>5</sub> ; d) C <sub>6</sub> (B) formation by adding a C <sub>3</sub> trimer to a C <sub>3</sub> trimer. e) C <sub>6</sub> (R) formation by adding a C atom to a bended C <sub>5</sub> chain; f) C <sub>6</sub> (R) formation by adding a C <sub>3</sub> trimer to a C <sub>3</sub> trimer. ....	137

Figure 8.1 The proposed CNT growth mechanism: a) reaction or processes that occur on the Ni catalyst surface; b) reactions that occur on the Ni/CNT growth edge. Some of the important processes were labeled, and they correspond to the elementary steps in Table 1. Orange: Ni, white: H, black: C, light blue: movable H, dark blue: movable C. .... 142

Figure 8.2 CNT growth rate predicted by a ConKMC and AKMC simulation by using the same kinetic parameters under different temperature on a 150×150 lattice ( $d=30\text{nm}$ ). .... 151

Figure 8.3 CNT growth rates obtained at different temperatures predicted by AKMC simulations. The experimental data is taken from reference [48]..... 153

Figure 8.4 Sensitivity of the CNT growth rates on the  $\text{CH}_4$  dissociation energetics. The simulations were performed on different particle size at different temperatures:  $d=40\text{nm}$  at  $T=500^\circ\text{C}$  and  $550^\circ\text{C}$ ,  $d=60\text{nm}$  at  $T=600^\circ\text{C}$  and  $d=60\text{nm}$  at  $T=650^\circ\text{C}$ . .... 155

Figure 8.5 The ratio  $S$  between number of C atoms that go through bulk diffusion and surface diffusion at different temperatures and size of Ni particles. .... 157

## List of Tables

Table 3.1 Adsorption energy (eV) of CH <sub>x</sub> fragments on the three-layer and the four-layer slabs model of Ni (111) and Ni (100) .....	35
Table 3.2 Adsorption energies (eV) of the CH <sub>x</sub> (x=0-3) and H on various surface models. The energetics in bold are the adsorption energies at the most stable adsorption sites.....	36
Table 3.3 Relative energies (eV) of the initial state (I.S), transition State (T.S), and final state (F.S). Distances between detached H <sub>a</sub> and the nearest C ( $dC - H_a$ ) and Ni ( $dNi - H_a$ ) for each elementary step of CH <sub>4</sub> dissociation on a Ni (100) surface.....	43
Table 3.4 Relative energies (E) of the initial state (I.S), transition state (T.S), and final state (F.S). Distances between detached H <sub>a</sub> and the nearest C ( $dC - H_a$ ) and Ni ( $dNi - H_a$ ) for each elementary step of CH <sub>4</sub> dissociation on a Ni (111) surface.....	44
Table 3.5 Comparison of CH <sub>x</sub> Dissociation barriers (in bold) on Ni flat surfaces with previous studies...	45
Table 3.6 Relative energies (E) of the initial state (I.S), transition state (T.S), and final State (F.S). Distances between detached H <sub>a</sub> and the nearest C ( $dC - H_a$ ) and Ni ( $dNi - H_a$ ) for each elementary step of CH <sub>4</sub> dissociation on a Ni (553) surface.....	45
Table 3.7 Average energy ( $\epsilon d$ ) and width ( $Wd$ ) of the d-Band of the surface Ni atoms. ....	54
Table 4.1 Adsorption energies (eV) of CH <sub>x</sub> fragments (x =3-0) fragments on the 2×2 three-layer, 2×2 four-layer and 3×3 three-layer slab model of Ni (111) surface. ....	63
Table 4.2 Adsorption energies, $E_{ads}$ (eV), of CH <sub>x</sub> (x =3-0) fragments on various Ni surface models. The adsorption energies in the bracket were calculated by using dispersion corrected RPBE-D3 functional...	65
Table 4.3 Relative energies (eV) to the initial state (I.S.) of the transition state (T.S.) and final state (F.S.) for each elementary step of CH <sub>4</sub> dissociation on Ni (111)–clean surface. Distances between detached H <sub>a</sub> and the nearest C ( $dC - H_a$ ) and Ni ( $dNi - H_a$ ) atoms, as well as the two closest bonding distances between the C atom in the CH <sub>x</sub> adsorbates and the surface Ni atoms ( $dC - Ni$ ) are also shown. ....	69
Table 4.4 Relative energies (eV) to the initial state (I.S.) of the transition state (T.S.) and final state (F.S.) for each elementary step of CH <sub>4</sub> dissociation on Ni (111)–4C <sub>sub</sub> surface. Distances between detached H <sub>a</sub> and the nearest C ( $dC - H_a$ ) and Ni ( $dNi - H_a$ ) atoms, as well as the two closest bonding distances between the C atom in the CH <sub>x</sub> adsorbates and the surface Ni atoms ( $dC - Ni$ ) are also shown. ....	71
Table 4.5 Relative energies (eV) to the initial state (I.S.) of the transition state (T.S.) and final state (F.S.) for each elementary step of CH <sub>4</sub> dissociation on Ni (111)–C <sub>on</sub> surface. Distances between detached H <sub>a</sub> and	

the nearest C ( $dC - Ha$ ) and Ni ( $dNi - Ha$ ) atoms, as well as the two closest bonding distances between the C atom in the $CH_x$ adsorbates and the surface Ni atoms ( $dC - Ni$ ) are also shown. ....	73
Table 4.6 Activation energies of $CH_4$ and CH dissociation on various Ni surfaces modeled by $3 \times 3$ unit cell.....	75
Table 5.1 Hirshfeld charges of the supported $Ni_4/\gamma-Al_2O_3$ (100) complexes.....	84
Table 5.2 The adsorption energies for $CH_3$ and H on the supported $Ni_4/\gamma-Al_2O_3$ (100) complexes. ....	86
Table 5.3 Hirshfeld charges for $CH_3$ adsorbed on supported $Ni_4/\gamma-Al_2O_3$ (100) complexes. ....	87
Table 5.4 The d-band energy (eV) of the Ni atoms involved in $CH_3$ and H adsorption at the top and int1 sites on the supported $Ni_4$ cluster.....	89
Table 5.5 Hirshfeld charges for H adsorbed on supported $Ni_4/\gamma-Al_2O_3$ (100) complexes. ....	92
Table 5.6 Hirshfeld charges of the supported $Ni_5/\gamma-Al_2O_3$ (100) complexes.....	97
Table 5.7 The adsorption energies for $CH_3$ and H on the supported $Ni_5/\gamma-Al_2O_3$ (100) complexes.....	99
Table 5.8 The metal support interaction ( $E_{MSI}$ , eV) upon $CH_3$ and H adsorption on $S(Ni_4)$ and $NS(Ni_4)$ . ....	100
Table 6.1 Activation energy, $E_a$ (eV), for the dissociation of $CH_4$ and CH on the (111) surfaces of Fe, Co, Ni and Cu. Distances between detached $H_a$ and C ( $dC - Ha$ ) and the nearest Metal ( $dM - Ha$ ) in the TS of each elementary reaction step are also shown. ....	111
Table 6.2 Carbon monomer (C) diffusion barriers and activation energy, $E_a$ (eV), for carbon dimer ( $C_2$ ) and trimer ( $C_3$ ) nucleation on the (111) surfaces of Fe, Co, Ni and Cu. Distances between activated C-C bond ( $d_{C-C}$ , Å) in the TS are also shown.....	112
Table 6.3 The adsorption energy, $E_{ads}$ (eV), of carbon monomer (C), dimer ( $C_2$ ) and trimer ( $C_3$ ) on the (111) surfaces of Fe, Co, Ni and Cu. ....	114
Table 6.4 Activation energy, $E_a$ (eV), for the dissociation of $CH_4$ and CH on the (111) surfaces of $Cu_8Fe$ and $Cu_8Ni$ alloy. Distances between detached H and C ( $d_{C-H}$ ) and the nearest Metal ( $d_{M-H}$ ) in the TS of each elementary reaction step are also shown. Note that the carbon monomer (C) diffusion barrier is the energy for C atom to diffuse away from sitting beside the Fe or Ni atom.....	117
Table 7.1 Adsorption energies, $E_{ads}$ , (eV), of a single C atom at different surface sites of Ni (111) as obtained with different surface unit cells and carbon coverages, $\theta_C$ : on top of a surface Ni atom (top), bridging two surface Ni atoms (bri), at an fcc or hcp three-fold hollow site.....	124
Table 7.2 Adsorption energy per atom for the adsorption of two carbon atoms (named $C^1$ and $C^2$ ) on a $2 \times 2$ slab model ( $\theta_C = 1/2$ ) (Site Occupation and the shortest distance between C atoms, $d(C1 - C2)$ , are also shown).....	125

Table 7.3 Adsorption energies per carbon atom for a C <sub>2</sub> dimer formed at neighboring fcc and hcp sites and two single C Atoms (at the nearby hcp sites) for different $\theta_C$ [ $d(C1 - C2)$ , is the C-C distance] ..	125
Table 7.4 Adsorption and cluster-metal interaction energies per carbon atom for C <sub>3</sub> trimers formed around a Ni atom on the (111) surface at a coverage of 1/3 ML, [ $d_{(C-C)}$ is the shortest C <sub>v</sub> C distance between two C atoms] ..	127
Table 7.5 Adsorption and cluster-metal interaction energies per carbon atom for selected small carbon clusters on the (111) surface. ....	128
Table 7.6 Diffusion barriers of selected carbon species. ....	132
Table 8.1 Vibrational frequencies ( $>200\text{ cm}^{-1}$ ) of the transition states, forward ( $E_{a,f}$ ) and backward ( $E_{b,f}$ ) activation energy barriers of elementary steps for CNT growth on Ni (111).....	144
Table 8.2 Vibrational frequencies ( $>200\text{ cm}^{-1}$ ) of gas phase and surface species on Ni (111) used in the kinetic model of CNT growth. ....	145

# Chapter 1

## Introduction and Motivation

Methane catalytic activation is an important reaction step in many chemical processes, particularly in methane cracking, and Chemical Vapor Deposition (CVD), in which hydrogen and carbon nanotubes (CNT) or nanofibers (CNF) are formed. Methane is also the main component of natural gas and used to synthesize CO and hydrogen, via reforming processes (steam reforming, partial oxidation, dry reforming, or combination thereof). The hydrogen produced by such reforming processes is mixed with large amounts of CO, which may limit its applicability as a potential power source. For example, in proton exchange membrane (PEM) fuel cells technology, even a small trace of CO (typically above 10 ppm) will poison the electro-catalysts in the fuel cell [1,2]; thus, expensive H<sub>2</sub> purification process is needed, making methane cracking an attractive alternative for the production of CO-free hydrogen. Methane cracking consists in breaking methane into molecular hydrogen and carbon. Experimental observations have shown that methane cracking is unlikely to happen (within reasonable time) at temperatures below 1000°C without the presence of a catalyst. However, catalytic cracking of methane can occur at temperatures between 500 and 800°C [3]. Among the different transition metals commonly used in catalytic methane cracking, Ni-based supported catalysts show very good catalytic activity at relatively moderate temperatures [4-8]. The most frequently used supports are SiO<sub>2</sub>, Al<sub>2</sub>O<sub>3</sub>, and MgO [6,8].

Typically, the catalytic activity of supported Ni catalysts decreases with time due to the deposition of large amounts of carbon on the catalyst. In fact, the deposited carbon, as a co-production in the catalytic methane decomposition, can form CNT or CNF. In the past years, these materials have received considerable attention due to their extraordinary physical and chemical properties and their potential applications in the industry. For example, CNT/CNF with diameters ranging from 2 to 500nm are used as catalyst supports, electrodes for fuel cells and lithium ion batteries, adsorbents for hydrogen, polymer additives, and as gas storage materials [9-12].

Although there is an extensive literature on experimental studies for methane dissociation on transition metals, little is known about microscale picture of the catalytic methane cracking. For example, experimental investigations on the mechanism of catalytic reaction is quite challenging because of the difficulty in extracting information at the microscopic scale, e.g., identification of active surface sites, or in accurately describing the barrier heights for the elementary reactions. In the past years, theoretical studies using e.g. Density Functional Theory (DFT) have been conducted for methane dissociation on

various transition metal surfaces [13-22]. These studies, however, have mainly focused on the estimation of the  $\text{CH}_x$  chemisorption properties and methane dehydrogenations on low-index (111) Ni, Co or Rh surfaces.

For the study of CNT/CNF production by methane cracking, although significant advances have been made through experimentation and simulations, the catalytic CNT/CNF growth mechanism still under debate. A mechanism generally accepted for the CNF growth over metallic particles is as follows [23] (see Figure 1.1) : *i*) methane first cracks on the metal surface forming hydrogen and carbon; *ii*) carbon atoms, which can form subsurface carbides, dissolve and diffuse through the bulk of the solid or through quasi-liquid metal particles; *iii*) due to the cooling down of the particles that lower the carbon solubility or due to oversaturation, carbon is then expelled and precipitates as more or less perfect polyaromatic layers; then the catalyst is lifted up which represent the CNF growth process. This continuous process is always used to explain why the metal particles are most often located at the tip of the CNFs.

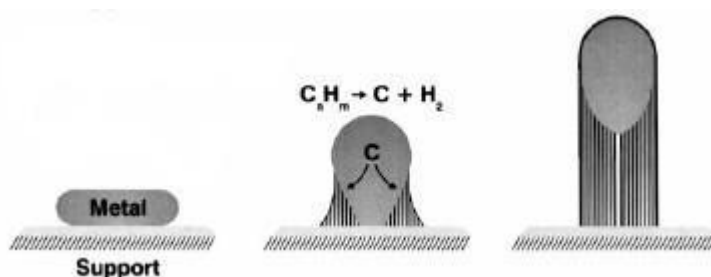


Figure 1.1 Schematics of tip-growth mechanism for carbon filament growth. Reprinted from [23] with permission from Elsevier.

Recently, DFT have been applied to investigate the mechanism of catalytic CNT/CNF growth at the atomic-scale [24-27]. It has been found that the energy barriers for carbon atoms diffusion on Ni (111) surface are around 0.4~0.5eV, while the bulk diffusion barrier through Ni particle is 1.72 eV [26]. This shows that the surface diffusion of carbon atoms on a Ni particle surface is more favorable than the diffusion of carbons through the subsurface and bulk Ni. Hence, that study concluded that the most probable diffusion process is carbon atoms surface diffusion, which is the dominant process that contributes to the growth of CNT/CNF [25-27]. Note that both carbon nanotubes (CNT) and carbon nanofibers (CNF) have a hollow structure. The primary differences between the materials are their morphology. CNF, also known as Stacked-Cup Carbon Nanotubes (SCCNT), have a unique morphology in that graphene planes are canted from the fiber axis, resulting in exposed edge planes on the interior and

exterior surfaces of the fiber. CNTs, on the other hand, typically resemble an assembly of concentric cylinders of graphene. Although they are different materials, they are produced in a similar manner, and mostly depend on the reaction conditions and the size of the catalyst. The study of how the C atoms could result in CNT or CNF is beyond the scope of this research. Thus, in this study, when discussing their growth process in terms of carbon diffusion and nucleation, it is assumed that the CNT and CNF growth follows the same mechanism.

In summary, most of the previous theoretical studies on methane cracking reaction have focused on describing chemisorption properties and dehydrogenation pathways on low-index (111) metal surfaces. A systematic investigation of catalytic methane cracking by considering factors that may affect the methane dissociation properties, e.g., effects of the catalyst structure, carbon deposition, oxide support and alloying, is still lacking in the literature. Concerning the CNT/CNF growth mechanism, the debate is now concentrated on the bulk or surface diffusion mechanisms. However, all the studies on this debate have focused on the behavior and property of single carbon atoms [24-27]. The property and role of the carbon clusters, formed by the nucleation of carbon atoms, on the Ni surfaces during the catalytic growth of CNT/CNF have been rarely reported.

Therefore, in this study, the above mentioned issues will be addressed by theoretical DFT calculations. First, methane cracking on clean Ni surfaces with different surface topology was studied through DFT calculations. In order to evaluate the effect of carbon deposition and oxide support, the DFT study is then extended to methane dissociation on Ni surface covered by C atoms and  $\gamma$ -Al<sub>2</sub>O<sub>3</sub> supported Ni clusters. Also, the nucleation of carbon atoms and the diffusion of the formed carbon clusters were also studied. Moreover, based on the DFT calculation results for methane cracking, carbon diffusion and nucleation, a Ni catalytic CNTs growth mechanism based on carbon species surface diffusion and nucleation was proposed. A multi-scale modeling approach that integrates DFT calculations and kinetic Monte Carlo (KMC) simulation was developed for a better understanding of the mechanism of methane cracking and CNT/CNF growth on Ni catalyst. In this approach, the DFT energetic results for the methane cracking, together with the carbon diffusion and nucleation energetics were used to construct the kinetic database for the KMC simulation. The simulations explicitly follow the elementary steps involved in the CNT growth that include CH<sub>4</sub> dissociation, carbon surface and bulk diffusion, carbon atoms nucleation, C<sub>3</sub> trimer diffusion and C and C<sub>3</sub> incorporation into CNT wall. By comparing the KMC simulation results with experimental data, it provides validation of the proposed CNT/CNF growth

mechanism. It predicts the relative reaction rates of elementary reactions on the catalyst surface at industrially relevant temperatures and pressures.

## 1.1 Research objectives

Based on the above, the goal of this research is to provide a better understanding of the nature of Ni catalytic methane cracking and CNT/CNF growth mechanism. To achieve this goal, a few aspects that may reveal the catalyst's effects on methane dissociation properties and the critical steps that govern CNT/CNF growth were explored using DFT calculations. The specific objectives of this study are:

*i)* to understand the influence of the Ni catalyst surface topologies by studying methane dissociation on different Ni surfaces, e.g. flat and step surface;

*ii)* evaluate more realistic kinetic parameters for methane dissociation by studying C–H bond activation on various carbon deposited Ni surfaces;

*iii)* understand the role of  $\gamma$ -Al<sub>2</sub>O<sub>3</sub> support, especially the metal-support interface, on the dissociation properties of methane using a  $\gamma$ -Al<sub>2</sub>O<sub>3</sub> supported Ni cluster models;

*iv)* provide insights regarding the CNT/CNF growth mechanism by studying the carbon cluster diffusion and nucleation properties from DFT calculations;

*v)* develop a first-principle-based kinetic Monte Carlo (KMC) model for Ni catalytic methane cracking and CNT/CNF growth process.

The DFT calculations conducted in this study were performed on SHARCNET ([www.sharcnet.ca](http://www.sharcnet.ca)) under the umbrella of Compute/Calcul Canada using the program BAND.

## 1.2 Research contribution

To the best of the author's knowledge, the theoretical study of catalytic methane cracking reported in the open literature mainly focus on CH<sub>x</sub> (x=1-4) dissociation properties on various transition metal surfaces. For the study of CNT growth mechanism, the debate is now concentrated on the surface and bulk diffusion of the surface C atom. Knowledge about the factors that may affect the stability of these CH<sub>x</sub> species and the activation of the C–H bond, e.g. the effect of catalyst structure, carbon deposition, oxide support and the property and role of the carbon clusters in CNT growth mechanism is still limited.

Theoretical studies on these topics, however, are essential for a better understanding of heterogeneous catalytic methane cracking and CNT growth mechanism.

This study represents a first systematic investigation of catalytic methane cracking reaction. The effect of catalyst structure, carbon deposition and catalyst support, which are critical factors in the practical catalytic reaction system, are evaluated by DFT calculations. Moreover, it is the first time that a detailed investigation on carbon clusters diffusion and nucleation kinetics was performed. Based on the DFT investigation on the properties of the carbon cluster, a CNT growth mechanism that involves the critical steps during CNT growth, e.g. methane cracking, carbon surface and bulk diffusion and nucleation, has been developed. For the first time, the proposed CNT growth mechanism is validated by comparing the CNT growth rate obtained by first-principle-based KMC simulation with experimental results. KMC simulation proposed here is arguably the most advanced proposed published simulation on the CNT growth.

### **1.3 Outline of the thesis**

This thesis consists of nine chapters as follows:

Chapter 1 gives the overview of the thesis, including introduction and fundamentals of the catalytic methane cracking and CNT growth. The main objectives and contributions of the research are also presented in this chapter.

Chapter 2 reviews and summarizes the literature about catalytic methane cracking and CNT/CNF growth. It also gives an introduction to Density Functional Theory (DFT).

Begin with Chapter 3, factors that may affect the methane dissociation properties in the practical catalytic reaction system, e.g. the catalyst structure, carbon deposition, oxide support and alloying, were analyzed using DFT calculations. For example, Chapter 3 presents a DFT study on the effect of Ni catalyst surface topology on methane dehydrogenation by using three different Ni catalyst surfaces, e.g. Ni (100), Ni (111), and Ni (553); effect of carbon atoms depositions was studied in Chapter 4 by modeling methane dissociation on clean, surface-carbon, and subsurface-carbon covered Ni (111) surface; the role of the  $\gamma$ -Al<sub>2</sub>O<sub>3</sub> support, especially the metal-support interface, on the dissociation properties of methane is reported in Chapter 5.

The above Chapters focus on only methane cracking reactions, In Chapter 6,  $\text{CH}_x$  dissociation, carbon diffusion together with C–C bond coupling are studied together to evaluate the reactivity of different metal catalyst, i.e., Fe, Co, Ni, and Cu towards CNTs/graphene growth.

Following the DFT calculation results reported in Chapter 6, a detailed investigation on the behavior of the carbon atoms during the Ni catalyst CNT growth, the structure, nucleation energetics, and mobility of carbon intermediates on the Ni (111) surface was presented in Chapter 7.

In Chapter 8, a comprehensive Ni catalytic CNT growth model was developed. The model includes the critical elementary steps that involved in the CNT growth, e.g.  $\text{CH}_x$  dissociation, C surface and bulk diffusion, C cluster nucleation and diffusion, etc. Based on this model, a first-principle-based KMC simulation was conducted to study the Ni catalytic methane cracking and CNT growth process. In this study, the kinetic parameters for methane dissociation on clean Ni (111) surface reported in Chapter 4 and carbon nucleation kinetics obtained in Chapter 7 are used to construct the kinetic data base for the KMC simulation.

Chapter 9 concludes the results obtained from this study and provides recommendations for further studies.

## Chapter 2

### Background and Literature Review

This chapter provides the background to catalytic methane cracking and carbon nanotubes (CNTs) or carbon nanofibers (CNFs) synthesis. The first section presents an overview of the topic. Since the study will be performed using Density Functional Theory (DFT), a brief introduction of the fundamental theory of the quantum mechanical calculations is given in section 2.2. Literature reviews on the studies of catalytic methane cracking and CNT/CNF growth are provided in section 2.3 and 2.4, respectively. Micro-kinetic study of catalytic methane cracking and CNT/CNF growth are discussed in Section 2.5.

#### 2.1 Overview

The stability and reactivity of hydrocarbon molecules and fragments on metal surfaces is of great importance for the understanding of several catalytic elementary steps. Among the hydrocarbon molecules, methane is of most importance. This molecule is of low value as such but could provide a low-cost energy production source by hydrogen extraction. The reforming of  $\text{CH}_4$  is a major catalytic reaction that has been used to synthesize CO and hydrogen. For several applications where hydrogen is used as a power source, the production of highly purified hydrogen is essential. Thus, recently, methane cracking has become a topic of increasing importance because it produces CO-free hydrogen and also is important for carbon nanotubes (CNTs) or carbon nanofibers (CNFs) synthesis by standard techniques such as Chemical Vapour Deposition (CVD) [1,2]. The overall reaction describing methane cracking is as follows:



In this reaction, methane is dissociated on the surface of a catalyst where molecular hydrogen is formed whereas the remaining carbon is nucleated to form CNTs or CNFs. These carbonaceous nano-structured materials display unique mechanical and electrical properties, and have drawn attention in various research fields. For instance, CNTs have been suggested for gas storage purposes [3] and as catalysts for chemical reactions [4] thanks to their advantageous surface/volume ratio and to the great number of possible active sites on the nanotubes walls. CNTs have been used as electronic components, polymer additive [5-7]. Therefore, in the past decades, the catalytic growth of CNT/CNF has been

extensively studied both theoretically and experimentally [8-15]. The CNT/CNF growth mechanism, however, still remains unclear.

## 2.2 Density Function Theory (DFT)

The study of the chemical bond between a surface and a molecule is the fundamental basis for understanding surface chemical reactivity and catalysis. Experimental investigations on the nature of the catalytic surface reactions are challenging because of the difficulty in extracting information at the microscopic scale. Quantum chemistry calculations, however, can provide useful and important perspectives on chemical reactions that are not accessible through experimental observations. It has been used to study the fundamental aspects of the catalytic reactions such as reaction pathway due to the theoretical developments, especially accuracy improvement of Density Functional Theory (DFT).

DFT is one of the most popular and versatile methods available in condensed-matter physics, computational physics, and computational chemistry to find an approximated solution for the Schrödinger equation, the fundamental equation that describes the quantum behavior of atoms or molecules [16]. Within this theory, the properties of a many-electrons system can be determined by using functionals, representing spatially dependent electron densities. Hence, the name DFT comes from the use of functionals of the electron density.

The Schrödinger equation is the key equation in quantum mechanics that describes the behavior of a particle in a force field. One simple form of the Schrödinger equation is as follows:

$$H\Psi = E\Psi \quad (2.2)$$

where,  $H$  is the Hamiltonian operator;  $\Psi$  is the wavefunctions, or eigenstates of the Hamiltonian and  $E$  is the energy of the state  $\Psi$ . The Schrödinger equation for multiple electrons systems with defined quantities of the Hamiltonian operator,  $H$ , is generally expressed as follows:

$$\begin{aligned} H &= \sum_{I=1}^N \frac{P_I^2}{2M_I} + \sum_{i=1}^{N_e} \frac{P_i^2}{2m} + \sum_{i>j} \frac{e^2}{|r_i-r_j|} + \sum_{I>J} \frac{Z_I Z_J e^2}{|R_I-R_J|} - \sum_{i,I} \frac{z_I e^2}{|R_I-r_i|} \\ &= T_n + T_e + V_{ee} + V_{nn} + V_{ne} \end{aligned} \quad (2.3)$$

where,  $N$  and  $N_e$  are the number of nuclei and electrons respectively,  $M_I$  and  $m$  are the nuclei and electron mass,  $P_i$  are the momentum,  $R$  and  $r$  are the coordinates of nuclei and electrons respectively,  $Z_I$  is the charge on the  $I_{th}$  nucleus. The first and second terms ( $T_n$  and  $T_e$ ) on the right hand side of the Equation

(2.3) are the kinetic energy of nucleus and electrons, respectively. The following three terms ( $V_{ee}$ ,  $V_{nn}$ ,  $V_{ne}$ ) represent the electron-electron, nucleus-nucleus and electron-nucleus interaction potentials, respectively. In principle, all the physical properties of atoms and molecules are included in the solution of equation (2.2). However, for only a few systems, it can be solved analytically, e.g.,  $H_2$ . There are no analytic solutions to the Schrödinger equation for systems with multiple electrons. To solve the Schrödinger equation for these systems, approximations have to be introduced. One major approximation is the Born-Oppenheimer (BO) approximation. A key observation in quantum mechanics is that the atomic nuclei are much heavier than the electrons, and the mass of each proton or neutron is 1,800 times heavier than the mass of an electron. That is, the nucleus motion is much slower than the motion of electrons. Thus, one can assume that the electrons are moving in a field of fixed nuclei. Accordingly, the Born-Oppenheimer approximation states where the electron motion and the nucleus motion can be separated. This approximation enables the partition of the Schrödinger equation into two parts, one for the nuclei and the other for all the electrons. In the first step, the nucleus kinetic energy is neglected, that is, subtracted from the total molecular Hamiltonian. In the remaining electronic Hamiltonian,  $H_e$ , the nucleus positions are entered as parameters. The electron-nucleus interactions are not removed and the electrons still "feel" the Coulomb potential of the nuclei clamped at certain positions in space. The electronic Schrödinger equation that describes the motion of electrons in a field of fixed nuclei is as follows:

$$H_e(\mathbf{r}, \mathbf{R})\Psi(\mathbf{r}, \mathbf{R}) = E_e\Psi(\mathbf{r}, \mathbf{R}) \quad (2.4)$$

The quantity  $\mathbf{r}$  stands for all electronic coordinates and  $\mathbf{R}$  for all nucleus coordinates. The electronic energy  $E_e$  depends on the chosen positions  $\mathbf{R}$  of the nuclei. In other words,  $E_e$  is a function of the positions of these nuclei,  $E_e(R_1, \dots, R_M)$ . This is also known as the Potential Energy Surface (PES),  $E_e(\mathbf{R})$ . In the second step of the BO approximation, the nucleus kinetic energy is reintroduced and the Schrödinger equation for the nucleus motion (equation 2.5) is solved.

$$[T_n + E_e(\mathbf{R})]\Psi(\mathbf{R}) = E\Psi(\mathbf{R}) \quad (2.5)$$

The eigenvalue  $E$  is the total energy of the molecule.

DFT states that the ground-state energy from the Schrödinger equation is a unique functional of the electron density  $n(\mathbf{r})$ , which uniquely determines all properties, including the energy and wave function of the ground state [17]. The latter means that the Schrödinger equation can be solved by finding a function of the three spatial variables and the electron density, rather than a function of  $3N$  variables as in the wave function. An important property of the functional is defined in the second Hohenberg-Kohn

theorem: the electron density that minimizes the energy of the overall functional is the true electron density corresponding to the full solution of the Schrödinger equation. The energy functional in DFT is formulated as follows [16]:

$$E[\{\Psi_i\}] = \frac{\hbar^2}{2m} \sum_i \int \Psi_i^* \nabla^2 \Psi_i d^3r + \int V(\mathbf{r}) n(\mathbf{r}) d^3r + \frac{e^2}{2} \int \int \frac{n(\mathbf{r})n(\mathbf{r}')}{|\mathbf{r} - \mathbf{r}'|} d^3r d^3r' + E_{ion} + E_{XC}[\{\Psi_i\}] \quad (2.6)$$

The terms on the right-hand side in (2.6) are, in order, the electron kinetic energies, the coulomb interactions between the electrons and the nuclei, the coulomb interactions between pairs of electrons, and the coulomb interactions between pairs of nuclei, and the last term,  $E_{XC}[\{\Psi_i\}]$ , is the exchange-correlation functional. The latter is defined to include all the quantum mechanical effects that are not considered in the other energy terms. The calculation of the right electron density is performed by solving a set of equations in which each equation only involves a single electron. This set of equations, also known as the Kohn – Sham equation, is as follows [18]:

$$\left[ \frac{\hbar^2}{2m} \nabla^2 + V(\mathbf{r}) + V_H(\mathbf{r}) + V_{XC}(\mathbf{r}) \right] \Psi_i(\mathbf{r}) = \epsilon_i \Psi_i(\mathbf{r}) \quad (2.7)$$

The left-hand side of the Kohn-Sham equation considers three potentials, i.e.  $V$ ,  $V_H$ , and  $V_{XC}$ . The first potential defines the interaction between an electron and the collection of atomic nuclei. The second potential, the Hartree potential, describes the coulomb repulsion between the electrons being considered in one of the Kohn-Sham equations and the total electron. Finally,  $V_{XC}$ , the exchange-correlation potential, includes all the many-particle interactions.

Solving the Kohn-Sham equation is an iterative procedure that can be summarized as follows:

- i)* Define an initial guess for electron density,  $n(\mathbf{r})$ .
- ii)* Solves the Kohn-Sham equations for the single-particle wave functions,  $\Psi_i(\mathbf{r})$ .
- iii)* Calculate a new electron density from the single particle wave functions by using  $n_{KS}(\mathbf{r}) = 2 \sum_i \Psi_i^* \Psi_i(\mathbf{r})$ .
- iv)* Compare the new calculated electron density,  $n_{KS}(\mathbf{r})$ , with the electron density used in solving the Kohn-Sham equation,  $n(\mathbf{r})$ . If the two densities are the same, then this is the ground-state electron density, and it can be used to compute the total energy. If the two densities are different, then the trial electron density must be re-estimated and go back to step *ii)* again, until a self-consistent solution of the Kohn-Sham equations is found.

It is worth noticing that solving the Kohn-Sham equations require the specification of the exchange-correlation function,  $E_{XC}[\{\Psi_i\}]$ . One of the approximations to the exchange-correlation energy functional is the Local Density Approximation (LDA) [19], which states that the electron density is constant at all points in space, so the exchange-correlation energy functional depends solely upon the value of the electronic density at each point in space. The other well established approach to approximate the exchange-correlation function is the generalized gradient approximation (GGA) [20]. Although it is also a local approximation, it takes into account the gradient of the electron density at the same coordinate. For systems where the charge density is slowly varying, the GGA has proved to be an improvement over LDA [20].

## 2.3 Catalytic methane cracking

The reactivity of methane on metal surfaces is a catalytically important reaction. By catalytic cracking reaction, methane goes through different carbonaceous species as intermediates, which are the basic chemicals used hydrocarbon synthesis industry. The sequential dehydrogenation of methane is also essential for the production of CO-free hydrogen and CNT/CNF.

### 2.3.1 Catalysts for catalytic methane cracking

Non-catalytic methane cracking is a very slow process for practical application at temperatures below 1000°C, whereas catalytic cracking of methane can occur at temperatures as low as 500°C [21]. The experimental studies of methane cracking mainly focus on the development of an effective catalyst and the investigation of different factors affecting catalyst activity. Muradov et al. [22] used iron oxide as a catalyst for the cracking of methane and reported that equilibrium conversions were achieved at temperatures above 800 °C. Zhang et al. [23] reported that methane cracking takes place at low temperatures (550°C) over a 16.4wt% Ni/SiO<sub>2</sub> catalyst. Takenaka et al. [24] claimed that Ni (40-wt%)/SiO<sub>2</sub> is one of the most effective catalysts for methane cracking. Rahman et al. [25] reported that the catalytic decomposition of methane may be carried out at an even lower temperature between 500 and 550°C on a 5-wt% Ni/ $\gamma$ -Al<sub>2</sub>O<sub>3</sub> catalyst. In most of the studies, nickel has been described as the most active catalyst for methane cracking. Cobalt is also a good catalyst for methane cracking, but it has higher cost compared to nickel.

The performance of the metal catalyst is also a function of the electronic state and dispersion. For example, Echevoyen et al. [26] and Figueiredo et al. [27] observed improved performance of the Ni-based

catalyst with copper addition. Figueiredo et al. [27] attributed the improved stability to an electronic promotion effect. The enhanced methane conversion was explained by the influence of copper on the dispersion of the nickel by inhibiting the formation of nickel aluminate, which increased the metallic nickel phase available for reaction and the nickel surface area subject to reaction. Chesnokov et al. [28] developed a nickel-based catalyst with addition of other metals, such as copper and iron (e.g. 70%Ni-10%Cu-10%Fe/Al<sub>2</sub>O<sub>3</sub>) for methane cracking. In that study, they reported that the addition of iron increased the optimal operating temperature range from 600–675°C for Ni/Cu/Al<sub>2</sub>O<sub>3</sub> to 700–750°C while maintaining good catalyst stability.

Previous studies on this subject have also found that the support material can affect the metal surface area and the metal's electronic state [26], and therefore affect the performance of the catalyst [29-30,31]. Ermakova et al. [21] studied the effect of magnesia and silica as supports for Ni catalytic methane cracking and reported a lower methane conversion using magnesia as compared with that using silica. In that study, the authors stated that the low methane conversion using magnesia is due to the formation of a solid solution between Ni and magnesium, which reduced the surface area of the Ni catalyst. In another study, using X-ray diffraction to characterize nickel on different supports (SiO<sub>2</sub>, TiO<sub>2</sub>, graphite, Al<sub>2</sub>O<sub>3</sub>, MgO and SiO<sub>2</sub>·MgO), Takenaka et al. [31] found that, for equivalent surface area, the lower the interaction between nickel and the support, the higher the methane conversion.

### **2.3.2 DFT study of catalytic methane cracking**

Due to their industrial and commercial importance, the adsorption and decomposition of methane on transition metal catalysts have been extensively studied [32-45]. Lee et al. [42, 43] studied the activated dissociative adsorption of CH<sub>4</sub> on Ni (111) by molecular beam techniques coupled with High-Resolution Electron Energy Loss Spectroscopy (HREELS). That study reported that the adsorbed CH<sub>3</sub> radical and H atom were identified as the products of the dissociative reaction. The existence of the chemisorbed CH<sub>3</sub>, CH<sub>2</sub> and CH on Ni (111) has also been reported by Secondary Ion Mass Spectroscopy (SIMS) and X-ray Photoelectron Spectroscopy (XPS) [44, 45]. Nevertheless, experimental investigations on the nature of the decomposition of methane on transition metal surfaces are challenging because of the difficulty in extracting information at the microscopic scale, e.g., identification of active surface sites, or in accurately describing the barrier heights for the elementary reactions.

Advances in computational sciences have enabled the application of DFT to study the fundamental aspects of the catalytic methane cracking reaction. For example, Au et al. [46] conducted extensive cluster-based DFT calculations for methane activation, which includes Ru, Rh, Ir, Pd, Pt, Cu. Kua et al.

[47] performed a complete study of  $\text{CH}_x$  ( $x=0-3$ ) adsorption on Pt, Ir, Pd, Rh, and Ru clusters. These metal clusters models suffer from edge effects, which limit the accuracy of these results. Also, Henkelman et al. [48] demonstrated that the surface relaxations with specific cluster size can greatly influence the DFT calculation results. Thus, with the increase of computational power, more and more periodic-slab based DFT calculations have been applied to study methane activation on metals. Michaelides [49] reported energies for  $\text{CH}_x$  hydrogenation reactions on Pt (111). Michaelides et al. [50] also studied the dehydrogenation of  $\text{CH}_3$  on Ni (111) by DFT. Zuo et al. [51] studied the dehydrogenation of  $\text{CH}_4$  on Co (111) surface by DFT. They calculated the adsorption energies of the adsorbed  $\text{CH}_x$  ( $x=0-4$ ) species and located the transition states in  $\text{CH}_4 \rightarrow \text{CH}_3 \rightarrow \text{CH}_2 \rightarrow \text{CH} \rightarrow \text{C}$  reaction pathways. Watwe et al. [37] studied the stability of  $\text{CH}_x$  species on Ni (111) and reported that the threefold site is preferred by the  $\text{CH}_x$  intermediates. Lai et al. [52] reported an activation barrier of 0.73 eV for the reaction:  $\text{CH}_4(\text{gas}) \rightarrow \text{CH}_3(\text{ads}) + \text{H}(\text{ads})$  on Ni (100). Nave et al. [53] analyzed 24 transition states (TSS) for the first C–H bond breaking of methane on five metal surfaces: Ni (111), Ni (100), Pt (111), Pt (100), and Pt (110). Wang et al. [54] presented a comparative study of  $\text{CH}_x$  chemisorption on Ni (111), Ni (100) and Ni (110) surfaces using plane wave DFT calculations. In that study, the reaction energies along the methane successive dehydrogenation pathway were also calculated. By comparing these thermodynamic schemes of  $\text{CH}_4$  dissociation, they reported that Ni (100) is the preferred surface for  $\text{CH}_4$  dissociation, when compared to Ni (110) and Ni (111). However, that study did not include a study on the kinetic properties for methane dissociation.

Recently, DFT calculations and experiments have shown that the step edges in general are more reactive towards the adsorption and dissociation of a number of simple molecules such as CO, NO,  $\text{O}_2$  and  $\text{N}_2$  [55-60]. For the study on methane dissociation, Bengaard et al. [61] used a Ni (211) surface to study the effects of surface steps on the activation of the first C–H bond breaking in methane. That study showed that the activation energy on Ni (211) is 0.20 eV lower than that reported for the Ni (111) surface. The higher activity of the step surface over the terraces has been confirmed by Frank Abild-Pedersen et al. [62], who investigated  $\text{CH}_4(\text{gas}) \rightarrow \text{CH}_3(\text{ads}) + \text{H}(\text{ads})$  reaction on the terraces and steps of a Ni (111) surface by DFT calculations combined with Ultra High Vacuum (UHV) experiments.

Based on the above, Ni-based catalysts have shown very good activity for catalytic methane cracking reaction. Experimental studies also showed that the performance of the catalyst is affected by the nature of the support and by doping with other metal elements such as Cu or Fe. For the theoretical investigation of catalytic methane cracking reaction, the published study mainly focus on the estimation of the  $\text{CH}_x$

( $x=1-4$ ) adsorption and dissociation properties on various metal surfaces, especially the (111) surface. Comparative studies of methane dissociative adsorption reactions on low-coordinated Ni (100) and Ni (211) step surface were also reported [61]. Nevertheless, there are no systematic DFT studies on the complete dehydrogenation energetics for the transformation of  $\text{CH}_4$  to C and H on Ni as a function of catalyst site morphology (flat and step). Moreover, for a comprehensive understanding of the nature of this reaction, theoretical studies of the effects of the support and carbon deposited on methane dissociation is also necessary. These types of studies, however, are still missing in the open literature.

## **2.4 Catalytic CNF/CNT growth**

A generally accepted micro-scale process for catalytic methane cracking on catalyst surface is: first, methane dissociates into  $\text{CH}_3$  and H atom on the catalyst surface; adsorbed  $\text{CH}_3$  further dehydrogenate into  $\text{CH}_2$  and H. The surface dehydrogenation reaction continues until C is produced. Depending on the catalyst, catalyst particle size and reaction conditions, the carbon atoms form either CNF or CNT (Figure 2.1). Due to the extraordinary property of these carbon materials, research in this field has undergone an explosive growth. Niu et al. [63] prepared free-standing mats of entangled nanotubes electrodes with an open porous structure from carbon nanotubes of high purity and narrow diameter distribution, which is highly desirable for high power and long cycle life of electrochemical capacitors. Xie et al. [64] added multiwalled carbon nanotubes (MWCNT) into polar liquids, e.g., distilled water, to prepare a nanofuild that has higher thermal conductivities than the base fluids. Carbon nanotubes or nanofibres have also been applied for gas storage. Gadd et al. [65] used carbon nanotubes to store Argon using a hot isostatically pressing (HIPing) technique. Research conducted by Dillon et al. [66] showed that single wall nanotubes are good adsorbent for hydrogen storage at ambient temperatures.

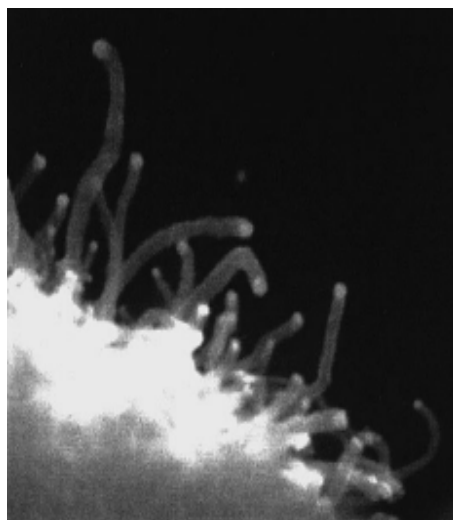


Figure 2.1 SEM micrographs of a Ni/SiO<sub>2</sub> catalyst after exposure to methane. Reprinted from [23] with permission from Elsevier.

Since these carbon materials are suitable for different applications, the production of CNF/CNT is of great interest. Thus far, there have been a tremendous number of studies on the growth of carbon nanotubes. The catalytic Chemical Vapour Deposition (CVD) method [67] is the most widely used method to produce carbon nanotubes. In CVD, the carbon atoms are sourced from the decomposition of a hydrocarbon gas (methane, ethylene, etc.) at the surface of supported catalytic particles (Fe, Co, or Ni). Depending on the temperature, different products are obtained. Although there are no general rules, the tendency is to obtain multi-walled nanotubes at medium temperatures (between 500 and 900°C) and SWNTs at higher temperatures (750–1200°C) [68]. A very important aspect of these studies is on the CVD synthesis of high yield CNTs at low growth temperatures. Kong et al. extensively studied the growth of high-quality SWCNTs from the CVD of methane [69]. Low growth temperatures were reported by Mo et al. [70] who synthesized a mixture of SWCNTs and MWCNTs at 600°C using acetylene as carbon source and a mechanically mixed Al<sub>2</sub>O<sub>3</sub>/Ni as catalyst. Similarly, other studies have focused on the parameters and reaction conditions that affect the growth of CNTs. Mora et al. [71] studied the effect of catalyst (Fe-based) composition, hydrocarbon flow rate, and synthesis temperature on the single-walled carbon nanotubes (SWCNTs) growth. That study showed that the catalyst composition has a significant effect on the catalyst lifetime. Proper modification of its composition with Mo can prolong the catalyst lifetime and therefore improve the yield of grown SWCNTs. That study also showed that an increase in flow rate or temperature results in an increase of the nanotubes growth rate. Lu et al. [72] found that the

diameter of carbon nanotubes in the CVD method can be controlled by the hydrocarbon feeding rate. Anna et al. [73] performed a review on the role of metal nanoparticles in the catalytic production of single-walled carbon nanotubes, and the effect of various parameters on SWCNT formation, in which it is reported that the form of the precipitated carbon is dictated by the catalyst particle size, carbon feed rate and reactor conditions. Also, the feed rate of carbon to the metal particles must be controlled in order to selectively produce SWCNTs and to avoid accumulation of amorphous carbon.

Based on the above, many efforts have been made toward unveiling the mechanism of SWNT growth in the CVD process to produce SWNTs with high productivity and desired atomic structures [74-78]. Despite all these efforts, the growth mechanisms of CNTs still remain somewhat controversial. A general four step process has often been proposed (Figure 2.2): *i*) Gas precursor (ethylene, acetylene, methane) first adsorbed on the catalyst surface; *ii*) the surface reactions, such as methane cracking, produce adsorbed carbon and hydrogen atoms; *iii*)  $H_2$  molecules desorb and carbon atoms diffuse through the bulk of the catalyst particles; *iv*) the carbons then nucleate and are incorporated into graphene overlayers for the growth of the CNT. The key step in this mechanism is believed to be the diffusion of carbon species through the particle from the surface on which the dehydrogenation of hydrocarbons occurs near the rear faces [8]; *v*) during CNT/CNF growth, the deposited carbon on the metal/gas interface can also form a layer called encapsulating carbon, which blocks reactant access, and causes catalyst deactivation [79]. As a result of carbon deposition on nickel, the catalyst activity changes as the reaction proceeds.

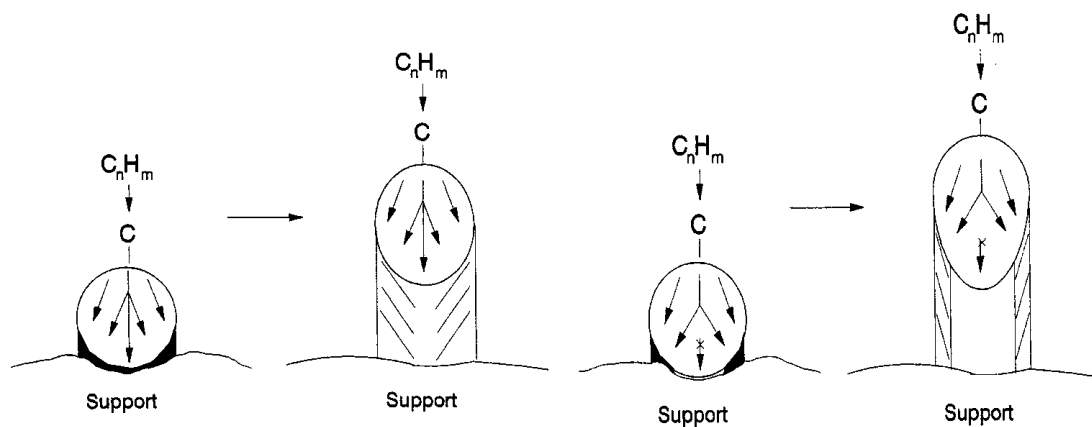


Figure 2.2 Schematic picture of the formation of a full fibre (left) and a hollow tube (right). In the case of the fibre, the nucleation has taken place over the entire back of the metal particle; in the case of the tube, the nucleation has been restricted to the vicinity of the gas-metal interface. Reprinted from [9] with permission from Elsevier.

In this mechanism, some studies have suggested that the driving force for carbon bulk diffusion is the temperature gradient [80,81], created in the metal catalyst particle by the exothermic decomposition of the hydrocarbon at the exposed front faces and endothermic deposition of carbon at the rear faces, which are initially in contact with the support surface. Note that for endothermic hydrocarbon decomposition, it is argued that the heat is supplied by the radiation from the surroundings to the gas/metal interface [80]. There are also other studies that suggest that the carbon diffusion driving force is the carbon concentration gradient between the surface and bulk [82-84]. The steady state growth results from a delicate balance between dissociation of the carbon-containing gases and carbon diffusion through the catalyst particle, and a balance between carbon diffusion through the catalyst particle and rate of nucleation and formation of graphitic layers [83].

In recent years, atomic-scale environmental transmission electron microscope (ETEM) and *in situ* time resolved X-ray photoelectron spectroscopy (XPS) techniques are used to monitor carbon nanofibre growth, which enables the study of these processes at higher resolution. Hofmann et al. [11] studied the carbon nanotube growth using  $C_2H_2$  decomposition over a nickel catalyst, and they suggested that the nucleation and growth of graphene layers are associated with the dynamic formation and restructuring of monoatomic step-edges at the nickel surface (Figure 2.3).

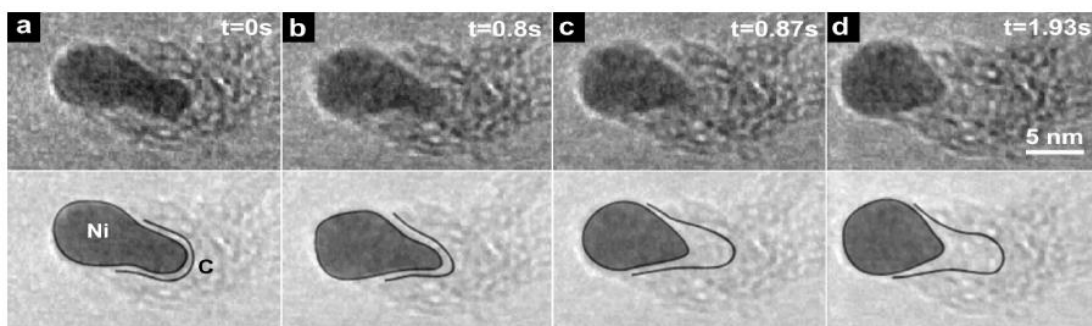


Figure 2.3 (a-d) ETEM image sequence showing a growing CNF in 3:1  $NH_3:C_2H_2$  at 1.3 mbar and 480 °C. The video was recorded at 30 frames/s, and the time of the respective pictures is indicated. Reprinted from [11] with permission from the the American Chemical Society.

Lin et al. [12] reported the formation of bamboo-like multiwalled carbon nanotubes, by *in situ* high-resolution transmission electron microscope (HRTEM), via catalytic decomposition of  $C_2H_2$  on Ni catalyst at  $650^\circ C$ . In those experiments, a tip-based growth mode was observed (Figure 2.4) and the catalyst particle remained as crystalline metallic Ni at  $650^\circ C$  during the growth process. That study showed that the mechanism of CNT growth is not through C precipitation from  $Ni_3C$  but rather through the diffusion of C adatoms followed by nucleation and growth. Two possible diffusion pathways were proposed: bulk diffusion and surface diffusion to the boundary of the Ni-graphene growth interface, with the latter being the dominant process due to a lower activation energy barrier and lower coordination number. Hofmann et al. [13] also reported that the surface diffusion is a low activation energy path for nanotube growth (Figure 2.5).

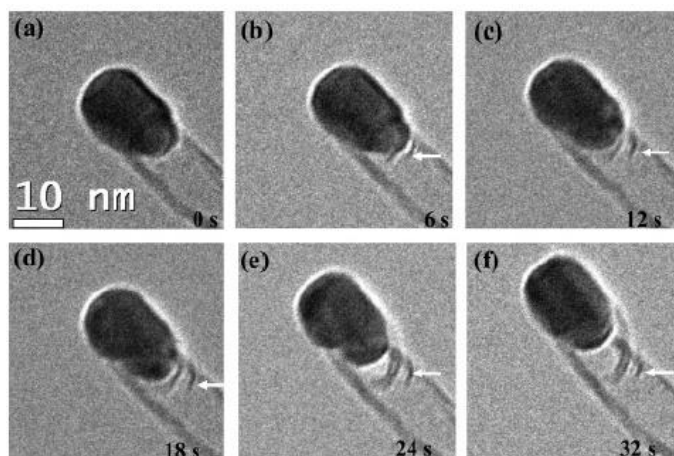


Figure 2.4 A sequence of TEM images showing the formation of an incomplete knot in less than 6s.  
Reprinted from [12] with permission from the American Chemical Society.

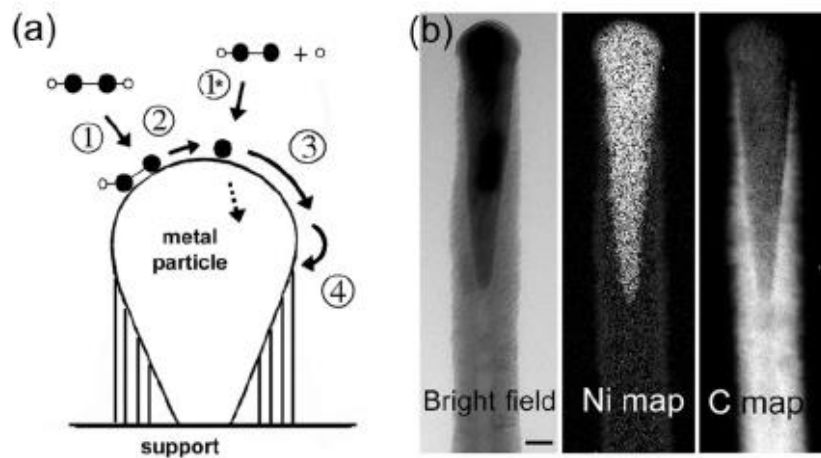


Figure 2.5 (a) Schematic of the growth process. (b) Bright field image and electron energy loss spectroscopy Ni and carbon edge elemental maps of a PECVD CNF at 500°C. Reprinted from [13] with permission from the American Physical Society.

In addition to these experimental works, theoretical methods, such as DFT, have also been applied to investigate the carbon nanotube growth mechanism. Cinquini et al. [14] studied carbon adsorption and diffusion on the surface and subsurface of Ni and Ni<sub>3</sub>Pd alloy. The DFT calculations showed that, on the Ni surface, the diffusion of carbon is fast and the surface diffusion barriers (0.45 eV) are smaller than that for penetration through the bulk (1.72 eV). Abild-Pedersen et al. [15] studied the growth mechanisms for catalytic carbon nanofibre by *ab initio* DFT calculations (Figure 2.6). This study showed that nickel step-edge sites act as the preferential growth centers for graphene layers on the nickel surface. Based on different transport pathways of carbon atoms by surface or subsurface diffusion, they proposed three mechanisms for graphene growth: *i*) front growth, *ii*) base growth by C incorporation and *iii*) atom-exchange at the Ni step edge with energy barriers of 1.43, 1.42 and 1.40 eV, respectively.

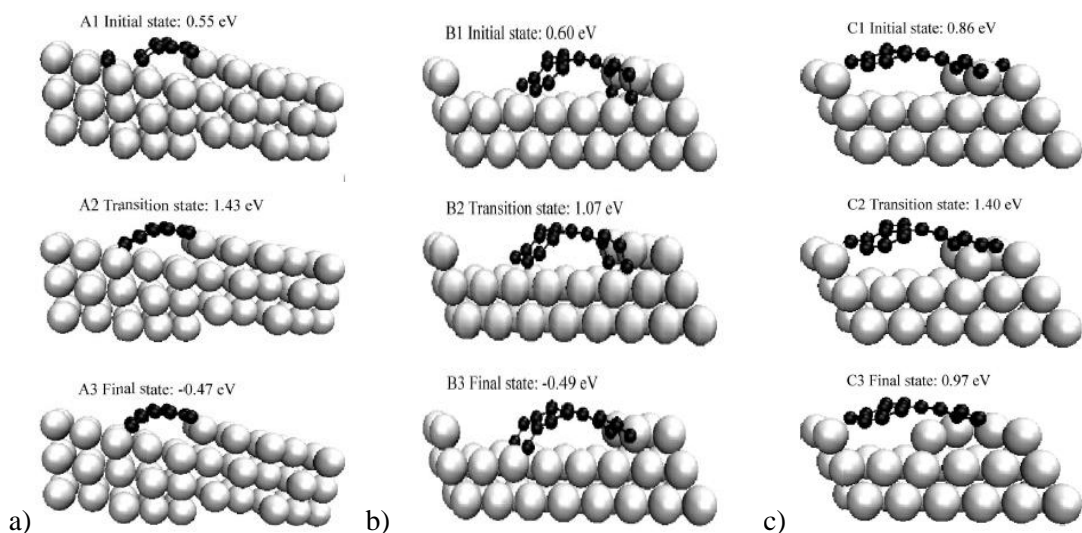


Figure 2.6 Initial, transition, and final states in the front growth mechanism (a) base growth mechanism (b) and atom-exchange growth mechanism (c) modeled using DFT calculations. Reprinted from [15] with permission from the American Physical Society.

Recently, Ohta et al. [85,86] reported a rapid growth of a single-walled carbon nanotube on an iron cluster by performing Density-Functional Tight-Binding molecular dynamics simulations. That study showed that the continuous growth of the SWCNs is due to the repetitive insertion and subsequent bridging of the carbon fragment ( $C_1, C_2$ ) formation resulting in the rapid formation of five-, six-, seven-, and sometimes even eight-membered rings, at the C-Fe interface (Figure 2.7).

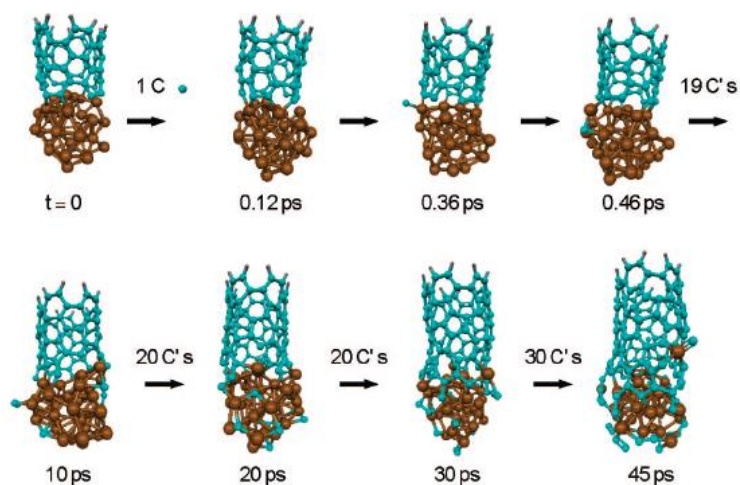


Figure 2.7 Snapshots of growth process trajectory of a seed nanotube on a  $\text{Fe}_{38}$  cluster. Reprinted from [85] with permission from the American Chemical Society.

## 2.5 Microkinetic study of catalytic methane cracking and CNT/CNF growth

A primary goal of research and development in heterogeneous catalysis is the identification of catalytic materials and reaction conditions that lead to efficient catalytic processes, which can be implemented in industrial practice through appropriate reaction engineering [87]. A micro-kinetic model is one of the most powerful tools that can be used to evaluate the performance of these systems. These models can be used to predict the reaction rates for each elementary reaction under different reaction conditions, determine the rate-limiting steps, and calculate the conversions of reactants or yields of productions. Based on this information, the evaluation of the catalyst and the optimization of the reaction process or operating conditions can be performed more effectively.

The kinetics of methane cracking and CNT/CNF growth has been studied extensively over the past four decades [88-92]. The derivation of these microkinetic models are based on the bulk diffusion mechanism of CNT/CNF growth. The model usually consists of two aspects: the surface reactions with a gradual dehydrogenation of methane and the CNT/CNF growth by C bulk diffusion. For example, Snoeck et al. [88] developed a kinetic model for the formation of filamentous carbon on a nickel catalyst by methane cracking based on the mechanism show in Figure 2.8. The model includes the following steps:

Surface reactions:





Dissolution/segregation:



Diffusion of carbon through nickel:



Precipitation/Dissolution of carbon:



where  $C^*$  is the adsorbed carbon on the Ni surface;  $C_{Ni,f}$  and  $C_{Ni,r}$  are the carbon dissolved in nickel at the gas side of the particle and at the support side of the particle, respectively;  $C_{Ni,w}$  is the carbon at the carbon filament.

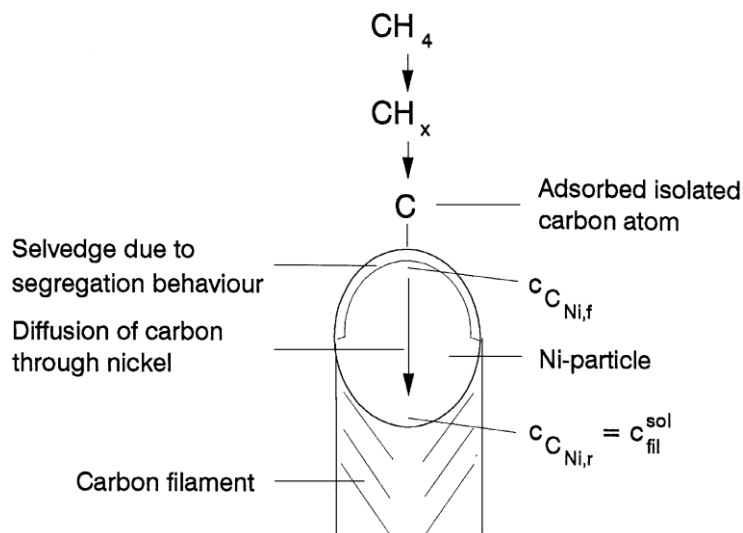


Figure 2.8 Mechanism of the formation of filamentous carbon by the methane cracking. Reprinted from [88] with permission from Elsevier.

In this model, Snoeck et al. assumed that a segregation/ dissolution equilibrium exists at the gas side of the nickel particle between adsorbed carbon ( $C^*$ ) and carbon dissolved in nickel ( $C_{Ni,f}$ ). It is also assumed that there is a carbon precipitation/dissolution equilibrium between  $C_{Ni,r}$  and  $C_{Ni,w}$ . In that study, the dehydrogenation of the first C–H bond is assumed as the rate-determining step, whereas in some other studies, adsorption of methane on the surface of catalyst is treated as the rate-determining step [89,90].

Different from the above mentioned studies, in which the methane dissociation reaction starts with methane surface adsorption, there are studies arguing that methane cracking proceeds with a stepwise dehydrogenation of the surface species after a direct dissociative adsorption of methane [91,92]:



It was then postulated that both the dissociative chemisorption step and the dehydrogenation of the adsorbed methyl group would be rate-determining.

## 2.6 KMC approach

It can be observed that, to perform microkinetic modelling, one has to make an assumption of the reaction mechanism and treat the reaction steps as either being in thermodynamical equilibrium or as kinetically hindered one-way reactions. In many studies, only one of the reaction steps is treated in non-thermodynamical equilibrium making it the rate-limiting step. This will limit the accuracy of the microkinetic modelling study in the absence of a good of knowledge about the reaction mechanism as well as the physical properties that determine the equilibrium and rate constants of the reactions. Moreover, it is known that microkinetic modeling treats adsorbate species using the mean-field approximation, expressing reaction rates in terms of species coverages. It neglects the dynamic effects such as surface restructuring and possible interactions between adsorbate-adsorbate, which may be important parameters in certain systems [93-95]. Kinetic Monte Carlo (KMC) simulation, however, models the catalytic surface as a lattice of reaction sites, explicitly performing each reaction on the lattice as function of time and processing conditions [96,97]. This approach can explicitly track the diffusion, adsorption/desorption and reaction of the reactants/intermediates [98, 99]. In addition, KMC simulations also show the rate-determining step and the most abundant reaction intermediate. Moreover, KMC simulation is a suitable strategy to bridge the gap between the results obtained by DFT at the molecular scale and the macroscopic behavior of catalytic reaction observed in the experiments.

In the variable time step KMC model, the catalyst surface is simulated using an  $N \times N$  2D lattice. Each position on the lattice represents active site of the catalyst. The intrinsic kinetic database calculated with the DFT analysis, the size of the lattice, and the reaction conditions are the key inputs needed to develop the KMC simulation for this process. The simulated system is allowed to evolve according to algorithm described in Figure 2.9 and is summarized as follows:

- i)* Generate an initial configuration and set the initial time  $t_0$ . In most of the cases, an empty lattice, which represents a clean catalyst surface, is taken as the initial configuration.
- ii)* List all possible events that could occur on the current lattice configuration and time  $t$ , and then determine the rate of each event. Since the kinetic parameters (activation energy, pre-exponential factor) for a specific event have been obtained by DFT calculations, the rate for the possible event is calculated under the framework of transition state theory, which has been discussed in section 2.2.
- iii)* Calculate the total rates  $R$  of all these events by summing all possible surface reaction rates,  $r_i$ , and generate two random uniformly distributed numbers  $\rho_1$  and  $\rho_2$  that are in the range of (0,1]. The total rate

is subsequently used along with random number the variable time-step equation given below to determine the time step at which some possible event on the surface will occur,

*iv)* The total rate  $R$  is used along with the random number  $\rho_1$  to pick up an event from the event list obtained at step *ii*). The event is chosen by comparing the cumulative reaction probability distribution given below against  $\rho_1$ :

$$P_i = \sum_1^i r_i/R \quad (2.18)$$

If the random number  $\rho_1$  is between  $P_{i-1}$  and  $P_i$ , then event  $i$  is chosen as the executed event.

*v)* Update the configuration of the system (species on the lattice). Remove the executed event and add new enabled processes.

*vi)* A time interval is generate by the variable time-step equation given below to determine the time step at which the chosen event on the surface will occur:

$$\Delta t = -\frac{1}{R} \ln \rho_2 \quad (2.19)$$

The total time is then updated by adding the calculated variable time step  $\Delta t$  to the current time  $t$ :

$$t = t + \Delta t \quad (2.20)$$

*vii)* If the maximum simulated time,  $t_{max}$ , are fulfilled then stop; Otherwise, go back to step *ii*).

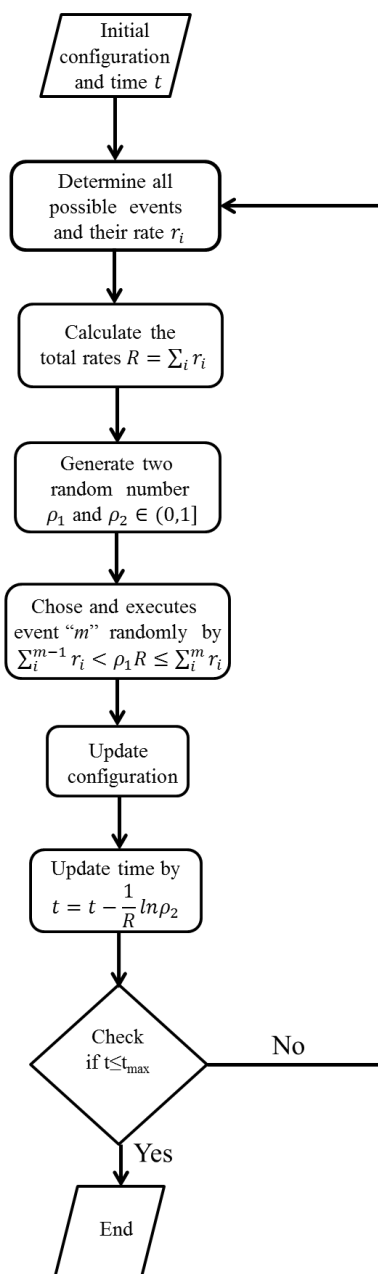


Figure 2.9 KMC algorithm flow chart.

As mentioned above, DFT study of the catalytic reaction mechanism allows one to predict the events that occur on the catalyst surface at the molecular level, which is quite difficult to be obtained through experimental measurements or observations. It can therefore be used to generate a first-principles-based kinetic database, e.g. activation energies and pre-exponential factors of the chemical reactions, for the

KMC simulations. This combined DFT/KMC approach maintains important atomic features of a catalytic metal surface and can therefore offer an efficient strategy to bridge the gap between the results obtained by DFT at the microscopic scale and the dynamic behaviors of the working catalyst surface under given operating conditions. Previously, this approach was successfully used to study the mechanism of catalytic surface reactions, for instance, to examine the decomposition of acetic acid on Pd (111) [100]. Aleksandrov et al. [101], studied the ethylene conversion to ethylidyne on Pd (111) and Pt (111) surfaces using KMC simulations, on the basis of reaction enthalpies and barriers obtained from DFT calculation. The simulations predicted the most plausible pathway and estimate apparent activation energy for the formation of ethylidyne that agree well with experimental results. Using KMC simulations, Stamatakis et al. [102] provided evidence that the active site for water-gas shift reaction on platinum surfaces may be condition specific and may entail multiple individual sites under certain conditions.

In summary, DFT is a powerful tool that enables the study of the catalytic surface reactions in great detail. The DFT calculated kinetic parameters for the proposed reaction steps can be used to construct the kinetic data base in KMC modeling, which is usually referred as KMC simulations. Such simulations provide accurate prediction of the dynamics of the catalytic reactions under various reaction conditions. Reliable statistical estimates of macroscopic reaction rates obtained by KMC simulation can thus be compared with experimental data, and therefore provide a validation of the proposed reaction mechanism. The resulting KMC model can also be used as a tool for catalyst design and optimization.

## Chapter 3

### Methane Dissociation on Flat and Stepped Ni surfaces

In this chapter, effect of catalyst surface structure on methane cracking reactions was studied by DFT calculations. Ni catalyst was modeled by Ni (100), Ni (111), and Ni (553) surface with either flat or stepped surface structures. The stability of  $\text{CH}_x$  species on the three surfaces was evaluated and transition states for methane sequential dissociations were identified. The simulation results show that low-coordinated Ni surface e.g. Ni (553) step surface, is more reactive than the highly-packed Ni (111) surface. This chapter is organized as follows: section 3.1 presents a background and motivation of this study. Details about the DFT calculation method and models are described in section 3.2; DFT calculation results are presented in section 3.3. A summary of the DFT simulation is provided at the end of this chapter.

#### 3.1 Introduction

In the past decade, the use of hydrogen as a source of alternative clean energy has attracted much attention. Conventionally, hydrogen is produced from steam reforming of natural gas [1-5]. In this process, methane reacts with water on a catalyst surface, typically Ni based [6-8], to form hydrogen and carbon monoxide (CO). In some applications the presence of CO may be detrimental. For example, CO above 10 ppm may completely poison the catalyst in a proton-exchange-membrane (PEM) fuel cell [9, 10]. The direct cracking of methane as an alternative route for CO-free hydrogen production is a promising technology [11-14]. The sequence of  $\text{CH}_4$  dehydrogenation reactions that transform  $\text{CH}_4$  to C and H on catalyst surfaces are also often regarded as crucial steps for the production of carbon nanotubes (CNTs) and carbon nanofibers (CNFs) by Chemical Vapor Deposition (CVD) [15-17]. Accordingly, catalytic methane dissociation for hydrogen and CNTs/CNFs production has recently gained increasing attention [19-22].

Recently, the adsorption and decomposition of methane on Ni-based catalysts have been extensively studied [23-36]. Lee et al. [33, 34] studied the activated dissociative adsorption of  $\text{CH}_4$  on Ni (111) by molecular beam techniques coupled with High-Resolution Electron Energy Loss Spectroscopy (HREELS). This study reported that the adsorbed  $\text{CH}_3$  radical and H atom were identified as the products of the dissociative reaction. The existence of the chemisorbed  $\text{CH}_3$ ,  $\text{CH}_2$  and CH on Ni (111) has also

been reported by Secondary Ion Mass Spectroscopy (SIMS) and X-ray Photoelectron Spectroscopy (XPS) [35, 36]. Nevertheless, experimental investigations on the nature of the decomposition of methane on transition metal surfaces are challenging because of the difficulty in extracting information at the microscopic scale, e.g., identification of active surface sites, or in accurately describing the barrier heights for the elementary reactions.

Advances in computational sciences have enabled the application of Density Functional Theory (DFT) to study the fundamental aspects of the catalytic methane cracking reaction. Watwe et al. [28] studied the stability of  $\text{CH}_x$  species on Ni (111) and reported that the threefold site is preferred by the  $\text{CH}_x$  intermediates. Michaelides et al. [37] studied the dehydrogenation of  $\text{CH}_3$  on Ni (111) using DFT analysis. This study showed that the reaction,  $\text{CH}_3(\text{ads}) \rightarrow \text{CH}_2(\text{ads}) + \text{H}(\text{ads})$ , is about 0.5 eV endothermic with an activation energy in excess of 1 eV. Haroun et al. [38] conducted DFT calculations on the dissociative adsorption of methane on a Ni (111) surface with and without adatom. This study reported that the presence of a Ni adatom facilitates  $\text{CH}_4$  dissociation with a lower activation energy when compared to the flat surface. Wenzhen et al. [39] reported an activation barrier of 0.73 eV for the reaction:  $\text{CH}_4(\text{gas}) \rightarrow \text{CH}_3(\text{ads}) + \text{H}(\text{ads})$  on Ni (100). Nave et al. [40] analyzed 24 transition states (TSs) for the first C–H bond breaking of methane on five metal surfaces: Ni (111), Ni (100), Pt (111), Pt (100), and Pt (110). Wang et al. [41] presented a comparative study of  $\text{CH}_x$  chemisorption on Ni (111), Ni (100) and Ni (110) surfaces using plane wave DFT calculations. In this study, the reaction energies along the methane successive dehydrogenation pathway were also calculated. By comparing these thermodynamic schemes of  $\text{CH}_4$  dissociation, they reported that Ni (100) is the preferred surface for  $\text{CH}_4$  dissociation, when compared to Ni (110) and Ni (111). However, this study did not include a study on the kinetic properties for methane dissociation. Recently, DFT calculations and experiments have shown that the step edges in general are more reactive towards the adsorption and dissociation of a number of simple molecules such as CO, NO,  $\text{O}_2$  and  $\text{N}_2$  [42-47]. For the study of methane dissociation, Bengaard et al. [48] used a Ni (211) surface to study the effects of surface steps on the activation of the first C–H bond breaking in methane. This study showed that the activation energy on Ni (211) is 0.20 eV lower than that reported for the Ni (111) surface. The higher activity of the step surface over the terraces has been confirmed by Frank Abild-Pedersen et al. [49], who investigated  $\text{CH}_4(\text{gas}) \rightarrow \text{CH}_3(\text{ads}) + \text{H}(\text{ads})$  reaction on the terraces and steps of a Ni (111) surface by DFT calculations combined with Ultra High Vacuum (UHV) experiments.

Based on the above, most of the previous theoretical studies on methane cracking reaction have focused on the estimation of the  $\text{CH}_x$  chemisorption properties and methane successive dehydrogenations

on Ni (111) surface. Methane dissociative adsorption reactions,  $\text{CH}_4(\text{gas}) \rightarrow \text{CH}_3(\text{ads}) + \text{H}(\text{ads})$ , on low-coordinated Ni (100), and Ni (211) step surface were also reported. Nevertheless, few theoretical studies have systematically analyzed the complete dehydrogenation pathways and the energetics for the transformation of  $\text{CH}_4$  to C and H on these low-coordinated flat and step Ni surfaces. To the authors' knowledge, the investigation of the  $\text{CH}_4$  successive dehydrogenation that leads to C and H on Ni (100) and high-index Ni step surfaces has not been reported in the open literature. That is, a systematic comparative study of  $\text{CH}_x$  adsorption and methane dehydrogenation reactions on different flat and step Ni surfaces is not currently available. Such a study is fundamental to gain a comprehensive understanding of the methane cracking reaction on Ni based catalysts and expected to play an important role in practical cases involving polycrystalline Ni systems.

In the present work, a systematic theoretical study of the activation of methane and its corresponding fragments on Ni (100), Ni (111) and Ni (553) surfaces have been performed. The Ni (553) surface is chosen because it is a high Miller indices index step surface, which has never studied before. It consists of (111) terraces and (111) orientated monoatomic steps. Thus, it provides a different surface topology from that of Ni (211) surface considered in previous works which contains (111)-like terraces and (100) steps [48]. DFT calculations on the adsorption and diffusion of the  $\text{CH}_x$  and H species on these three Ni surfaces have been conducted. Moreover, the TSs and energetics for the  $\text{CH}_4$  sequential dissociation reactions on these surfaces have been identified. Furthermore, comparisons between the adsorption properties of the  $\text{CH}_x$  species on Ni (100), Ni (111) and Ni (553) and between the energy profiles of the dissociation reactions are presented in this work.

## **3.2 Computational details**

### **3.2.1 Calculation methods**

The DFT calculations performed in this study were performed using the program BAND [50, 51] on SHARCNET ([www.sharcnet.ca](http://www.sharcnet.ca)) under the umbrella of Compute/Calcul Canada. In BAND, the surfaces are modeled by a slab with translational symmetry in two directions. Also, the electron wave functions were developed on a basis set of numerical atomic orbitals (NAOs) and of Slater type orbitals (STOs). For the core of the atoms (in this case Ni and C), a frozen core approximation was used to reduce the size of the basis set. The calculations performed on this study were spin-unrestricted and the Revised Perdew-Burke-Ernzerhof (RPBE) generalized gradient approximation (GGA) for the exchange and correlation

energy terms were employed. It is the revision suggested by Hammer et al. [52] to improve adsorption energetics compared to the PBE functional originally developed by Perdew, Burke, and Ernzerhof [53]. This functional is applied for the present study because it has been widely used for catalysis applications and provides reliable adsorption energetics of the transition metal system (e.g. Pt, Ni) [54-57]. The ground-state atomic geometries were obtained by minimizing the forces on each atom to below 0.05 eV/Å. A characteristic of the BAND program is to perform numerical integrations for all the matrix elements [58]. The accuracy of the integration in real space and the sampling of the Brillouin zone for the integration accuracy in k-space are the two major numerical parameters in the calculation [59]. The general precision parameter for numerical integration in real space in BAND (named: Accuracy) was set to 4, which is a reasonable value for this parameter [60,61]. The k-space parameter was set to 3, which represents that the quadratic tetrahedron method [62] was used in the present analysis for k-space numerical integration. Scalar relativistic corrections were included through the zeroth-order regular approximation (ZORA) [63]. The search and verification of the transition states (TS) were conducted using the following procedure [64-66]:

*i)* A geometry of the transition state is proposed based on the geometries of the reactant and product in a particular elementary step.

*ii)* Frequency calculations are conducted at the proposed geometric point. The lowest vibrational mode in the direction of the transition state (TS) is sought from the frequency calculations. The search for the transition state is performed starting from this point (lowest vibrational mode) using the hessian of this frequency run.

*iii)* Frequency calculations are performed on the transition state obtained from the previous step. The TS is confirmed if there is only one imaginary frequency corresponding to a single negative vibrational mode. Otherwise, a new geometry is needed, i.e., go back to step *i*). This procedure continues up until the TS with only one negative vibrational mode is identified.

*iv)* The TS is further verified by slightly perturbing the TS along the reaction coordinate, corresponding to the normal mode with imaginary frequency, in the direction of the product or reactant.

*v)* The perturbed transition state geometry obtained in step *iv*) is then optimized, yielding the corresponding geometry of the product or the reactant in a particular elementary step.

In order to describe the interactions between CH<sub>x</sub> (x=0-3), H and the Ni surfaces, the adsorption energies ( $E_{ads}$ ) of the adsorbates were defined by the following equation:

$$E_{ads} = E_{A/sl\bar{a}b} - E_{sl\bar{a}b} - E_{A, gas}, \quad (3.1)$$

where  $E_{A/sl\bar{a}b}$  represents the energy for the slab with the adsorbate A on the surface,  $E_{sl\bar{a}b}$  is the energy of a clean relaxed Ni slab and  $E_{A, gas}$  is the energy of the free adsorbate A in the gas phase. A negative  $E_{ads}$  corresponds to a stable adsorbate/slab system. Please note that unless otherwise specifically stated, the same DFT calculation methods, e.g. functional, basis set and parameters, is used in the DFT calculations conducted in other chapters.

### 3.2.2 Surface models

The models for the Ni (100), Ni (111), and Ni (553) surfaces are shown in Figure 3.1. Ni (111) has the most compact surface with a coordination number of 9 for each surface atom. Ni (100) is a more open surface with a coordination number of 8 for the surface atoms. The Ni (553) surface is stepped, consisting of (111) terraces and (111) orientated monoatomic steps. The coordination number of the surface atoms is 9 on the upper terraces, 7 at the step edge, and 11 for atoms at the bottom of the step. The Ni (100) and Ni (111) surfaces were modeled using a three layers slab with a  $2 \times 2$  unit cell. For the relaxation of the Ni surfaces, experimental work of Lu et al. [67] found that the relaxation of Ni (111) is less than 2% (with respect to the bulk). A previous DFT study by Sautet et al. [29] has also shown that the top layer of Ni (111) undergoes only very small inward relaxation (0.6%). For the (100) surface, experimental studies [68-70] have shown that the (100) surfaces of different metals (including Ni) do not reconstruct, with a probable relaxation of the outer layers of the metal crystals. Therefore, to reduce computational effort, in all calculations performed on the Ni (100) and the Ni (111) surfaces, the Ni atoms of the uppermost layer and the adsorbed species were allowed to relax whereas the Ni atoms in the remaining layers were constrained in their bulk positions with the experimental lattice parameter  $3.52 \text{ \AA}$  [71]. Tests concerning the accuracy and convergence with slab thickness were also performed on Ni (111) and Ni (100). That is, the adsorption energies of the optimal geometries obtained with three layer slab were recalculated with a four-layer slab. The results listed in Table 3.1 show that on Ni (111), the largest deviation was for H adsorption, which increased by 0.07 eV when using the four layer model. However, this relative deviation is less than 3%. On the Ni (100), the largest deviation (5%) was obtained for  $\text{CH}_2$  adsorption (see Table 3.1). This shows that a reasonable convergence of the binding energies is already obtained with a 3-layer thick slab. The Ni (553) step surface was represented by a thirteen layers slab of a  $2 \times 1$  unit cell. The top five layers were allowed to relax whereas the bottom layers of metal atoms were constrained in their bulk positions also with the experimental lattice parameter  $3.52 \text{ \AA}$ .

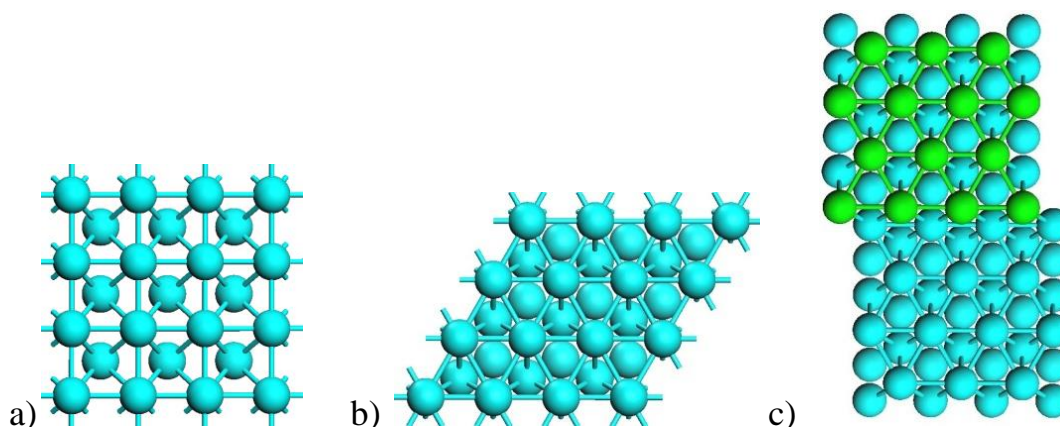


Figure 3.1 Top views of a) Ni (100), b) Ni (111) and c) Ni (553) surfaces. The upper step Ni atoms on Ni (553) are represented by green balls.

### 3.3 Results and discussion

#### 3.3.1 Adsorption of $\text{CH}_x$ and H species

The three surfaces considered in this study exhibit metal surface atoms with a range of local atomic environments. As illustrated in Figure 3.1, the Ni (100) surface has a square arrangement of atoms, whereas the Ni (111) surface has a hexagonal structure. The Ni (553) surface can be considered as a stepped surface with (111) terraces and (111) step. According to the surface morphology, there are four adsorption sites on Ni (111) surface. Atop adsorption is directly above a surface atom whereas a bridge is bridging between two surface atoms. The hexagonal close packed (hcp) and face-centered cubic (fcc) sites are two different threefold hollow sites, with a surface atom in the second and third layer, respectively. The Ni (100) surface exhibits three high-symmetry sites: a fourfold hollow site, a bridge site between two Ni atoms, and atop site above a single Ni atom. The adsorption sites on the Ni (553) surface are labeled in Figure 3.2. This work will focus on the adsorption sites in the step regions in Ni (553) since they exhibit different coordination numbers as compared to the sites on the (111) terrace surface. Thus, six adsorption sites near the step Ni atoms on Ni (553) surface were considered in the present analysis. Table 3.2 reports the adsorption energies of  $\text{CH}_x$  ( $x=0-3$ ) and H species on Ni (100), Ni (111), and Ni (553) surfaces. The adsorption energies at the most stable adsorption sites are shown in bold; and their corresponding adsorption configurations are shown in Figure 3.3-3.5.

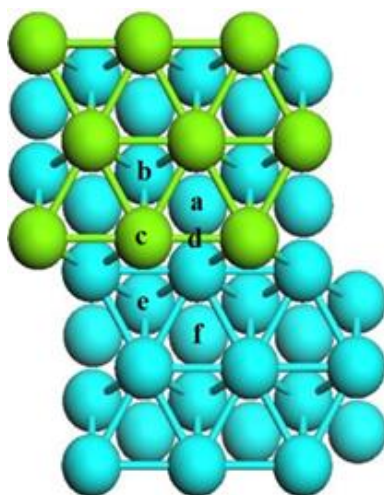


Figure 3.2 The adsorption sites considered on a  $2\times 1$  unit cell of Ni (553) surface are: (a) upper-step fcc site, (b) upper-step hcp site, (c) step top site, (d) step bridge site, (e) lower-step hcp site, and (f) lower-step fcc site. The upper step Ni atoms are represented by green balls.

Table 3.1 Adsorption energy (eV) of CH<sub>x</sub> fragments on the three-layer and the four-layer slabs model of Ni (111) and Ni (100)

	Three-Layer	Four-layer	Ref.
Ni (111)			
CH <sub>3</sub>	-1.33	-1.28	-1.30 <sup>[6]</sup> , -1.46 <sup>[37]</sup> , -1.81 <sup>[41]</sup>
CH <sub>2</sub>	-3.21	-3.25	-3.30 <sup>[6]</sup> , -3.26 <sup>[37]</sup> , -3.85 <sup>[41]</sup>
CH	-5.70	-5.69	-5.90 <sup>[6]</sup> -6.35 <sup>[41]</sup>
C	-6.22	-6.20	-6.00 <sup>[6]</sup> -6.61 <sup>[41]</sup>
H	-2.65	-2.72	-2.80 <sup>[6]</sup> , -2.60 <sup>[37]</sup> , -2.77 <sup>[41]</sup>
Ni (100)			
CH <sub>3</sub>	-1.44	-1.37	-1.84 <sup>[41]</sup>
CH <sub>2</sub>	-3.76	-3.58	-4.18 <sup>[41]</sup>
CH	-6.43	-6.35	-7.05 <sup>[41]</sup>
C	-7.27	-7.23	-8.08 <sup>[41]</sup>
H	-2.67	-2.68	-2.81 <sup>[41]</sup>

[6] A three layer model with top-most layer relaxation (RPBE functional)

[37] A three layer model with no surface relaxation (PW functional)

[41] A three layer model with top two surfaces relaxation (PBE functional)

Table 3.2 Adsorption energies (eV) of the CH<sub>x</sub> (x=0-3) and H on various surface models. The energetics in bold are the adsorption energies at the most stable adsorption sites.

adsorbate	Ni (100)			Ni (111)				Ni (553)					
	top	bri	hollow	top	bri	hcp	fcc	top <sup>Step</sup>	bri <sup>Step</sup>	fcc <sup>U</sup>	hcp <sup>U</sup>	fcc <sup>L</sup>	hcp <sup>L</sup>
CH <sub>3</sub>	-1.33	<b>-1.44</b>		-1.12	-1.10	<b>-1.33</b>	-1.31	-1.22	<b>-1.53</b>	-1.38			
CH <sub>2</sub>	-2.75	-3.35	<b>-3.76</b>	-2.48	-2.82	<b>-3.21</b>	-3.19		<b>-3.33</b>	-3.30	-3.30	-3.19	
CH	-4.24	-5.39	<b>-6.43</b>	-3.80	-5.53	<b>-5.70</b>	-5.64		-5.10	-5.40	-5.42	-5.55	<b>-5.65</b>
C	-4.36	-5.65	<b>-7.27</b>	-4.21	-5.74	<b>-6.22</b>	-6.12	-5.70	-6.24	-6.36	-6.27	<b>-6.69</b>	
H	-1.99	<b>-2.67</b>	-2.36	-1.92	-2.37	<b>-2.65</b>	-2.64	-1.69	-2.69	<b>-2.78</b>	-2.73	-2.70	-2.44

The data that are not reported on some specific adsorption sites indicate that no stable adsorption configurations were found at this site. That is, the adsorbed species moved to other adsorption site after geometry optimization.

### 3.3.1.1 Carbon and hydrogen adsorption

The most stable adsorption configurations for C on the various Ni surfaces are shown in Figures 3.3b, 3.4b, and 3.5b. For C on Ni (100), C adsorption at the hollow site (see Figure 3b) has the maximum bonding energy ( $-7.27$  eV). Frequency analysis showed that the bridge site adsorption is a first-order saddlepoint (transition state) on the potential energy surface for C. Thus, the bridge site can be considered as the transition state (TS) for C diffusion on the Ni (100) surface. The estimated diffusion barrier is approximately 1.62 eV. Hence, this relatively high energy barrier indicates that the diffusion of C on the Ni (100) surface is a highly activated process and may rarely occur. The situation for C adsorption on Ni (111) surface is quite similar to that observed on the Ni (100) surface. That is, the most stable configuration for the adsorption of C on the Ni (111) surface is a three hollow site with C adsorbed at an hcp site (see Figure 4b). The corresponding adsorption energy is  $-6.22$  eV. This is in reasonable agreement with that ( $-6.00$  eV) reported by Blaylock et al. [6], as show in Table 3.1. Note that the functional (PRBE) and model used in that study are the same as those used in the present study. However, Blaylock et al. employed plane wave basis set and ultrasoft pseudopotentials for the description of electrons which is expected to cause this small deviation (3.5%). In the present study, C adsorption energy on Ni (111) is 1.05 eV lower than the fourfold hollow site C adsorption on Ni (100). The strong stabilization of C in the fourfold hollow sites compared to the threefold hollow sites reflects the need of the C atom to satisfy its valence. As in the Ni (100) configuration, the C bridge site adsorption on Ni

(111) was found to be a diffusion TS. The corresponding diffusion barrier obtained for this process was 0.48 eV, which is in agreement with the value reported by Cinquini et al. (0.45 eV) [72]. It should be noted that Wang et al. [41] reported a higher adsorption energy for C adsorption on Ni (111) (−6.61 eV) and Ni (100) (−8.08 eV) using a three-layer model with top-two layer relaxation, as shown in Table 3.1. However, Wang et al. [41] used a plane-wave DFT method and a functional (PBE) that are different from those used in the present model (STO-DFT, functional: PRBE). Thus, the numerical results obtained by Wang and co-workers are expected to be different to the results obtained in the present study since different modeling methods were used. Although adsorption energies obtained by the present analysis were different than those reported in [41], they were consistent with the present study in terms of the strong C bonding energy on Ni (100) as compared with Ni (111). For C adsorption on Ni (553) step surface, C is preferentially adsorbed on the threefold hcp site below the step edge with an adsorption energy of −6.69 eV (see Figure 3.5b). The DFT calculations showed that carbon diffusion via the step to the lower terrace on Ni (553) proceeds with a barrier of 0.66 eV, whereas a barrier of 0.99 eV was obtained in the reverse direction. The results obtained for the C adsorption and diffusion among the three surfaces show that C on Ni (100) and Ni (553) has higher diffusion barriers due to the strong bonding energies on these two surfaces when compared to Ni (111). Moreover, this result may restrict the (100) surface from being favored by nucleation for carbon nanofiber or nanotube growth, due to the low mobility of these carbon atoms.

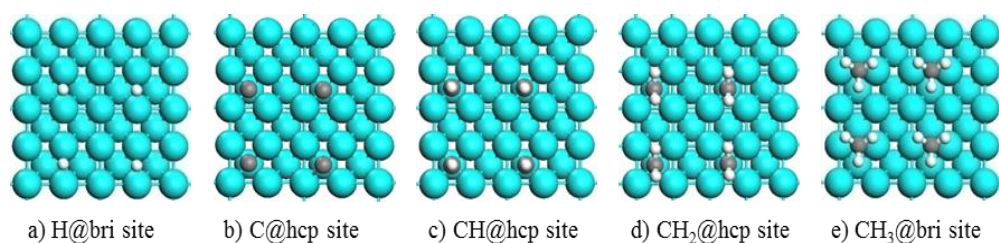


Figure 3.3 Top views of CH<sub>x</sub>(x=0-3) and H adsorbed on Ni (100). Blue: Ni, white: H, black: C.

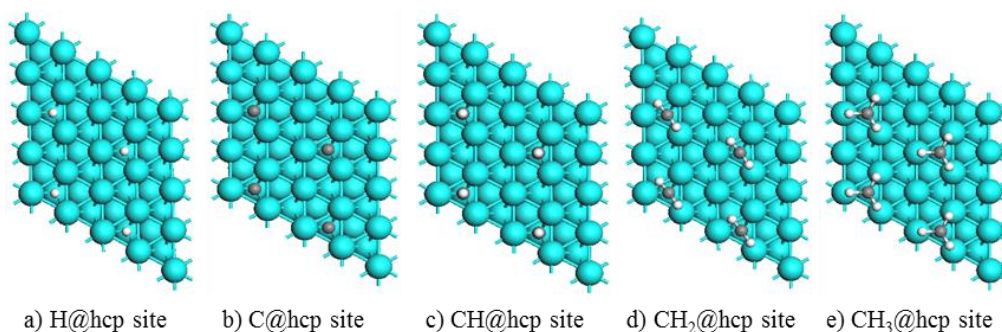


Figure 3.4 Top views of CH<sub>x</sub> (x=0-3) and H adsorbed on Ni (111). Blue: Ni, white: H, black: C.

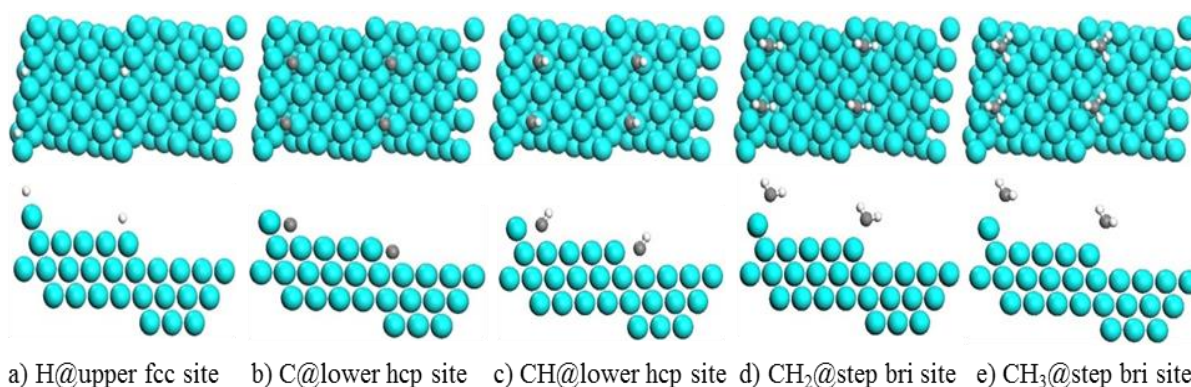


Figure 3.5 Top views of CH<sub>x</sub> (x=0-3) and H adsorbed on Ni (553). Blue: Ni, white: H, black: C.

For H on Ni (100) surface, it was found that binding is slightly more favored at the bridge site (see Figure 3.3a) than on the hollow site. On the other hand, H adsorption at the bridge site on Ni (111) is a less stable configuration than the hcp site adsorption (see Figure 3.4a). As shown in Table 3.2, the hcp site H adsorption energy on Ni (111) is  $-2.65$  eV, which is slightly more stable than the fcc site adsorption ( $-2.64$  eV). This result is slightly different than the results from the study conducted by Michaelides [37], in which the GGA Perdew-Wang functional and a three-layer unrelaxed Ni slab were employed. In that study, the H hcp and fcc adsorption energy were reported to be  $-2.54$  and  $-2.60$  eV, respectively. However, a good agreement can still be gained if comparison is made in term of H adsorption energy on Ni (111). As mentioned above, the H adsorption energy on Ni (111) reported in the present study is consistent with the study of Blaylock et al. [6] who reported an adsorption energy of  $-2.80$  eV (see Table 3.1). Further frequency analysis shows that H adsorbed at the bridge site on Ni (111) surface is a transition state whereas the H adsorbed at the bridge site on the Ni (100) surface is a local minimum. The diffusion barrier for H on Ni (111) and Ni (100) is 0.28 and 0.31 eV, respectively. The

diffusion barrier was calculated by taking the energy difference between the hollow and bridge H adsorption sites. From Table 3.2, it can be observed that the upper fcc site (see Figure 3.5a) on Ni (553) surface is more energetically favorable than the two flat surfaces to adsorb H. The diffusion of H from the upper to the lower terrace via the bridge site along the step edge needs to overcome a barrier of 0.09 eV. These results show that there is no apparent difference for the mobility of H on the Ni (100) and the Ni (111) flat surfaces. However, the diffusion of H over the step edge on Ni (553) is a faster process since it needs to overcome a relatively low energy barrier.

### 3.3.1.2 CH adsorption

The most stable adsorption configurations of CH on the three different Ni surfaces are shown in Figures 3.3c, 3.4c, and 3.5c. CH binding on Ni (100) shows apparent site preference when compared to the Ni (111) and the Ni (553) surfaces. As shown in Table 3.2, the adsorption energy of CH at the fourfold hollow site is much higher than that observed at the bridge and at the top sites on the Ni (100) surface. The diffusion of CH occurs via bridge site adsorption, which has been confirmed as a diffusion TS by frequency analysis. The corresponding diffusion barrier is 1.04 eV, which indicates that the CH diffusion on Ni (100) is a highly activated process. For CH on Ni (111), the most stable adsorption site is the hcp hollow site followed by the fcc adsorption site. This result agrees with a previous HREELS experimental study which showed that CH binds most favorably to threefold site in a symmetric structure on Ni (111) [36]. Moreover, the calculated CH hcp site adsorption energy (-5.70 eV) is in agreement with the one reported by Blaylock et al. [6], i.e., -5.90 eV (see Table 3.1). As on the Ni (100) surface, the CH adsorbed at the bridge site on Ni (111) was found to be a TS. The results show that CH diffusion on Ni (111) surface needs to overcome a barrier of 0.17 eV, which is a much lower energy barrier than that obtained for the CH diffusion on Ni (100). Thus, a higher mobility is expected for CH on Ni (111) surface. With regards to the Ni (553) surface, CH tends to chemisorb at the threefold fcc site behind the step at the lower terrace. The CH surface diffusion barrier over the edge to the lower terrace is calculated to be 0.33 eV. As in the case of the C adsorption atom, these results show that CH is strongly bonded at the hollow site on Ni (100) and it has the highest mobility on the Ni (111) surface.

### 3.3.1.3 CH<sub>2</sub> adsorption

The most stable adsorption configurations of CH<sub>2</sub> on Ni (100), Ni (111) and Ni (553) are shown in Figures 3.3d, 3.4d, and 3.5d, respectively. As shown in Table 3.2, the most stable CH<sub>2</sub> adsorption

configuration on Ni (111) is located at the hcp site followed by the fcc site with adsorption energy of  $-3.21$  and  $-3.19$  eV, respectively. Michaelides [37] reported a most stable adsorption energy of  $-3.26$  eV at the fcc site, followed by  $-3.22$  eV at the hcp site. This shows an agreement with the value obtained in this work with respect to  $\text{CH}_2$  adsorption energy at the threefold site on Ni (111) surface. This result is also consistent with the study of Blaylock et al. [6], who reported an adsorption energy of  $-3.30$  eV (see Table 3.1). For the configuration of  $\text{CH}_2$  on the two flat surfaces, one of the two H atoms is bonded to a surface metal atom to form the so-called C–H–Ni three-center bond, which is a low energy configuration state [73,74], while the other C–H bond is tilted away from the surfaces. As stated by Michaelides et al. [75], the decrease in the vibrational frequency (‘soft’ vibrational mode) in hydrocarbons species can be attributed to the formation of the three-center bond. As expected, the ‘soft’ C–H vibrational frequencies of  $\text{CH}_2$  were observed upon  $\text{CH}_2$  adsorption on Ni (100) and Ni (111) surfaces. The ‘soft’ C–H stretching frequency occurs at  $-2579\text{ cm}^{-1}$  on Ni (111) and at  $-2035\text{ cm}^{-1}$  on Ni (100), which corresponds to redshift of approximate  $274\text{ cm}^{-1}$  and  $818\text{ cm}^{-1}$ , respectively, compared to the usual gas-phase C–H stretching frequency of  $-2853\text{ cm}^{-1}$ . These ‘soft’ vibrational frequencies indicate a weak C–H bond that may consequently affect the dehydrogenation of the fragment. The C–H stretching frequency of  $\text{CH}_2$  on Ni (100) shows a significant shift when compared to that observed on Ni (111). Therefore, the stretching C–H bond scission on Ni (100) might be much easier than on the Ni (111) surface. However, the C–H bond activation energies on these surfaces cannot be compared fairly because of the different initial adsorption geometries of  $\text{CH}_2$  on Ni (100) (fourfold) as compared to Ni (111) (threefold) and their possible different dissociation pathways. Frequency analysis also showed that  $\text{CH}_2$  adsorbed at the bridge sites on Ni (100) and Ni (111) is the TS for  $\text{CH}_2$  diffusion. The energy barriers for the diffusion process were found to be  $0.41$  eV and  $0.39$  eV on Ni (100) and Ni (111), respectively. The calculation for  $\text{CH}_2$  adsorption on the Ni (553) surface shows that the step-bridge site is the most stable adsorption site. The ‘soft’ C–H vibrational frequency was not observed for Ni (553) indicating that the C–H–Ni three center bond is not formed. This can be confirmed by the observed long bond distance ( $2.59\text{ \AA}$ ) between the H and surface Ni atom (see Figure 3.5d), on the Ni (553) surface.

#### 3.3.1.4 $\text{CH}_3$ adsorption

The most stable adsorption configurations of  $\text{CH}_3$  on the three different Ni surfaces are shown in Figures 3.3e, 3.4e, and 3.5e. On Ni (100), no stable configurations were found for  $\text{CH}_3$  hollow site adsorption, and the C atom always points toward the top site of the adjacent Ni atoms after geometry

optimization. CH<sub>3</sub> bridge site adsorption with one of the H atoms in the CH<sub>3</sub> species pointing toward a fourfold vacancy was found to be the most stable configuration. This result is consistent with a previous DFT-GGA study [39]. A slight redshift of ~130 cm<sup>-1</sup> for the C–H stretching frequency was observed indicating the formation of a weak C–H–Ni three-center bond. The diffusion barrier for CH<sub>3</sub> on Ni (100) is estimated to be 0.11 eV. CH<sub>3</sub> is found to be most stable when it is adsorbed on the Ni (111) surface through its carbon atom on the hcp site with the three H atoms pointing to the surface atoms to form three C–H–Ni three-center bonds. The corresponding adsorption energy is –1.33 eV, which is consistent with the results reported by Blaylock et al. (1.30 eV) [6] and Michaelides et al. (–1.48 eV) [37]. Similarly, a redshift of ~346 cm<sup>-1</sup> for the C–H stretching frequencies was observed on Ni (111), which is in good agreement with that the value reported in a previous study (~300 cm<sup>-1</sup>) [75]. These results indicate that the stretching of C–H bond in CH<sub>3</sub> is weakened by the formation of the relatively strong C–H–Ni three-center bonds on Ni (111) when compared to that on Ni (100). However, the small deviation in the redshift suggests that there is no significant difference between the C–H bond strength for CH<sub>3</sub> adsorption on the two flat surfaces. Frequency analysis showed that the bridge site adsorption is a diffusion TS since diffusion of CH<sub>3</sub> often occurs via bridge site on Ni (111). The corresponding diffusion barrier was calculated to be 0.15 eV. This result indicates that the diffusion of CH<sub>3</sub> is favored on Ni (111) and Ni (100) surfaces. For the adsorptions of CH<sub>3</sub> on Ni (553) step surface, the step–bridge site adsorption was found to be the most stable configuration (–1.53 eV). As in the case of the CH<sub>2</sub> adsorption, the formation of the C–H–Ni three-center bond on Ni (553) was not observed. This can be supported by the long H–Ni atom distance 2.69 Å (Table 3.6), indicating no H–Ni bond formation.

The results presented in Table 3.2 enable a comparison of the adsorption behavior on the (100), (111), and (553) surfaces. This study showed that the strongest binding energy for C, CH and CH<sub>2</sub> was on Ni (100). The stepped Ni (553) surface also exhibits higher binding energies for C when compared to Ni (111). The highest binding energy for CH<sub>3</sub> and H was observed on Ni (553). These calculations show that the binding energies of C are stronger on the open Ni (100) and Ni (553) stepped surfaces than on the close packed Ni (111) surfaces, while the binding energies for CH<sub>3</sub> and H are not very sensitive to the surface structure.

In order to assess the quantitative effect of surface relaxation on the results presented in this study, DFT calculations were conducted on a model with the top-two layers of the Ni atoms were relaxed. In those calculations, the adsorption energies for C and CH<sub>3</sub> on Ni (111) and Ni (100) at their most stable adsorption sites were estimated assuming that the top two layers of the Ni atoms were relaxed. The results

of these DFT calculations are as follows: *i*) on the Ni (111) surface, the corresponding adsorption energies obtained for C and CH<sub>3</sub> were -6.18 and -1.33 eV, respectively. As shown in Table 3.1 the corresponding adsorption energies for C and CH<sub>3</sub> when only the top most-layer was relaxed on the Ni (111) surface were -6.22 and -1.33 eV, respectively. These results show that the relaxation of the top-two layers in the model did not change the CH<sub>3</sub> adsorption energy and it only resulted in a deviation of 0.6% (0.04 eV) for C adsorption with respect to the results obtained when only the top-most layer was relaxed. *ii*) On the Ni (100) surface, the adsorption energies for C and CH<sub>3</sub> were (top-two layers relaxed) -7.29 and -1.46 eV, respectively. These results are also close to those obtained when only the top-most layer was relaxed, i.e., C: -7.27 eV and CH<sub>3</sub>: -1.44 eV (see Table 3.1). These small deviations introduced by the relaxation of the top-two layers of Ni atoms shows the reliability of the results obtained by relaxing only the top most layer of the Ni surface.

The previous results were obtained with slabs using experimental lattice constants in the fixed layers. The bulk lattice constant using the same method and parameters described in Section 3.2 were calculated. The value obtained from the DFT calculations was 3.51885 Å, which is in very good agreement with the experimental lattice constant (3.52 Å). To study the errors introduced by using the experimental and calculated bulk lattice constants, CH<sub>x</sub> and H adsorption on Ni (111), modeled by a three-layer slab with the calculated bulk lattice constants, were estimated. The adsorption energies were found to be -1.34, -3.29, -5.69, -6.18, and -2.66 eV for CH<sub>3</sub>, CH<sub>2</sub>, CH, C, and H, respectively. As shown in Table 3.1, the corresponding adsorption energies obtained on Ni (111) using the experimental lattice constants were -1.33, -3.26, -5.70, -6.22, and -2.65 eV, respectively. Thus, there is a good agreement between the adsorption energies obtained from experimental and calculated bulk lattice constants.

### 3.3.2 Minimum energy path for methane activation

The reaction pathways and reaction energetic for the transformations of CH<sub>4</sub> to C and H on the Ni (100), Ni (111), and Ni (553) surfaces have been systematically studied using DFT analysis. The transition states along the reaction coordinates for each elementary reaction were located and presented in Figures 3.6–3.8. Estimates for the activation barriers, the reaction energies corresponding to each elementary dehydrogenation steps on different surfaces (and the key geometric parameters) are listed in Tables 3.3–3.6. A comparison between the reaction profiles on the different surfaces is shown in Figure 3.10.

Table 3.3 Relative energies (eV) of the initial state (I.S), transition State (T.S), and final state (F.S). Distances between detached  $H_a$  and the nearest C ( $d_{C-H_a}$ ) and Ni ( $d_{Ni-H_a}$ ) for each elementary step of  $CH_4$  dissociation on a Ni (100) surface.

	States	$E$ (ev)	$d_{C-H_a}$ (Å)	$d_{Ni-H_a}$ (Å)
$CH_4$	I.S	0.00	1.13	
	T.S	1.23	1.64	1.56
	F.S	0.67	3.23	1.87
$CH_3$	I.S	0.00	1.10	2.17
	T.S	0.62	1.74	1.56
	F.S	0.09	3.61	1.80
$CH_2$	I.S	0.00	1.11	1.81
	T.S	0.22	1.44	1.69
	F.S	-0.33	2.49	1.79
$CH$	I.S	0.00	1.11	2.62
	T.S	0.64	1.55	1.69
	F.S	-0.03	2.49	1.79

Table 3.4 Relative energies ( $E$ ) of the initial state (I.S), transition state (T.S), and final state (F.S). Distances between detached  $H_a$  and the nearest C ( $d_{C-H_a}$ ) and Ni ( $d_{Ni-H_a}$ ) for each elementary step of  $CH_4$  dissociation on a Ni (111) surface.

	States	$E$ (eV)	$d_{C-H_a}$ (Å)	$d_{Ni-H_a}$ (Å)
CH <sub>4</sub>	I.S	0.00	1.11	
	T.S	1.31	1.63	1.59
	F.S	0.91	3.09	1.69
CH <sub>3</sub>	I.S	0.00	1.13	2.17
	T.S	0.89	1.75	1.49
	F.S	0.16	3.09	1.72
CH <sub>2</sub>	I.S	0.00	1.11	2.23
	T.S	0.41	1.68	1.50
	F.S	-0.38	2.88	1.74
CH	I.S	0.00	1.11	2.69
	T.S	1.38	1.75	1.49
	F.S	0.42	2.88	1.72

Table 3.5 Comparison of CH<sub>x</sub> Dissociation barriers (in bold) on Ni flat surfaces with previous studies.

Reaction	Ni (111)					Ni(100)		
CH <sub>4</sub> →CH <sub>3</sub> +H	<b>1.31</b>	1.34 <sup>[6]</sup>	1.32 <sup>[77]</sup>	1.17 <sup>[78]</sup>	1.06~1.10 <sup>(40)</sup>	<b>1.23</b>	1.19 <sup>[77]</sup>	0.91~0.96 <sup>[40]</sup>
CH <sub>3</sub> → CH <sub>2</sub> +H	<b>0.89</b>	0.68 <sup>[6]</sup>	0.82 <sup>[78]</sup>	0.79 <sup>[79]</sup>				
CH <sub>2</sub> → CH+H	<b>0.41</b>	0.30 <sup>[6]</sup>	0.37 <sup>[78]</sup>	0.36 <sup>[79]</sup>				
CH→ C+H	<b>1.38</b>	1.40 <sup>[6]</sup>	1.37 <sup>[78]</sup>	1.40 <sup>[79]</sup>				

Table 3.6 Relative energies (E) of the initial state (I.S), transition state (T.S), and final State (F.S). Distances between detached H<sub>a</sub> and the nearest C ( $d_{C-H_a}$ ) and Ni ( $d_{Ni-H_a}$ ) for each elementary step of CH<sub>4</sub> dissociation on a Ni (553) surface.

	States	E (eV)	$d_{C-H_a}$ (Å)	$d_{Ni-H_a}$ (Å)
CH <sub>4</sub>	I.S	0.00	1.11	
	T.S	1.08	1.60	1.54
	F.S	0.08	3.02	1.70
CH <sub>3</sub>	I.S	0.00	1.11	2.69
	T.S	0.71	1.79	1.52
	F.S	-0.08	2.52	1.62
CH <sub>2</sub>	I.S	0.00	1.11	2.59
	T.S	0.15	1.54	1.68
	F.S	-0.51	3.12	1.74
CH	I.S	0.00	1.11	2.36
	T.S	0.47	1.59	1.59
	F.S	-0.29	3.19	1.71

### 3.3.2.1 Methane dissociation on Ni (100)

Dissociation of methane on Ni (100) occurs at the top of a surface Ni atom. The geometry of the transition state is shown in Figure 3.6. In the transition state, the methyl fragment is slightly tilted and the H atom moves over the top of the Ni atom. In the TS, the activated C–H bond (denoted as C–H<sub>a</sub> hereafter) is stretched from 1.11 Å in the gas phase to 1.64 Å in the TS. The C and H<sub>a</sub> atoms are bonded with the top Ni atom with bond distances of 2.12 and 1.56 Å, respectively. The shorter Ni–H<sub>a</sub> distance indicates that the hydrogen atom is bonded with the top Ni atom. The final configuration was methyl adsorbed in the bridge site and the H<sub>a</sub> atom adsorbed in a neighbored hollow site. As shown in Table 3.5, the calculated energy barrier is 1.23 eV, which is in very good agreement with the one reported by Bengaard et al. [76] (1.19 eV). In that study, DFT calculations were conducted to study the energy barrier of CH<sub>4</sub> dissociation on Ni (100) with the slab kept rigid to reduce the computational effort. As shown in Table 3.3, the reaction energy for this process is 0.67 eV, which suggests that the CH<sub>4</sub> dissociation reaction on Ni (100) is a highly endothermic process.

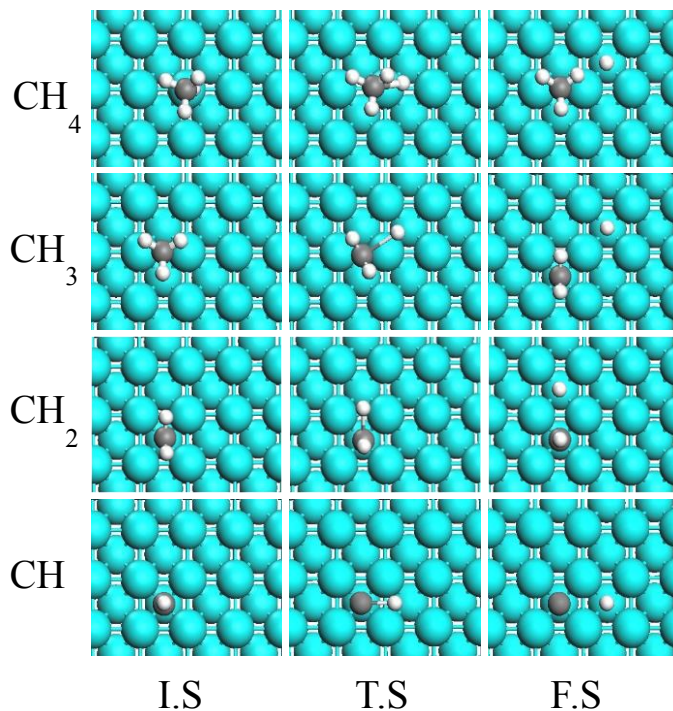


Figure 3.6 Geometric structures of the initial state (I.S), transition state (T.S), and final state (F.S) of the four steps of CH<sub>4</sub> dehydrogenation on Ni (100) surface. Blue: Ni, gray: C, and white: H.

In the TS obtained for the dissociation of CH<sub>3</sub> on the Ni (100) surface, the activated C–H<sub>a</sub> bond is stretched from 1.10 to 1.74 Å. The H<sub>a</sub> atom is located near an atop site, forming a bond with the surface Ni atom with a bond distance of 1.56 Å. The TS has an energy of 0.62 eV above the ground state of the reactant. This reaction leads to the production of CH<sub>2</sub> and H, which is sited at adjacent hollow sites sharing a single common Ni surface atom. The reaction energy for methyl dissociation is 0.09 eV, which indicates that the dehydrogenation of CH<sub>3</sub> on Ni (100) is nearly thermal neutral.

The reaction energy and the corresponding activation energy for the dissociation of CH<sub>2</sub> on Ni (100) are –0.33 and 0.22 eV, respectively. Dissociation occurs over the bridge between the surface Ni atoms and results in the CH and H sited on the nearby hollow sites. At the TS, the activated C–H<sub>a</sub> stretched from 1.11 to 1.44 Å. This result shows that the energy for CH<sub>2</sub> dissociation is exothermic on the Ni (100) surface; the low activation energy indicates that the dehydrogenation of CH<sub>2</sub> is kinetically favored on Ni (100).

The dehydrogenation process CH→C+H has an energy barrier of 0.64 eV. The reaction energy is calculated to be –0.03 eV. Thus, CH dehydrogenation on Ni (100), as in the case of CH<sub>3</sub>, is almost a thermal neutral process. At the TS, the C H bond is stretched from 1.11 to 1.55 Å, which leads to the product C and H, located on two hollow sites.

### 3.3.2.2 Methane dissociation on Ni (111)

As shown in Figure 3.7, the activation of the first C–H bond in methane also occurs over the top of a Ni atom on the Ni (111) surface. In the TS, the activated H<sub>a</sub> atom points toward the adjacent fcc hollow site whereas the CH<sub>3</sub> fragment is slightly off the top site. The calculations show that the C–H<sub>a</sub> bond distance stretched from 1.11 Å in the gas phase to 1.63 Å in the TS. The C and H<sub>a</sub> atoms are bonded with the top Ni atom with bond distances of 2.18 and 1.59 Å, respectively. As shown in Table 3.4, the calculated activation barrier for this reaction is 1.31 eV, which is in good agreement with the study of Bengaard et al. [76] and Blaylock et al. [6], who reported a barrier of 1.32 and 1.34 eV for methane dehydrogenation on Ni (111), respectively. As mentioned in Section 3.1.1, Wang et al. [41] used a model with the top two layers relaxed and reported higher CH<sub>x</sub> adsorption energies than those obtained with the present DFT model. However, the qualitative results from that study are the same to those obtained with the present DFT model: *i*) the adsorption strength of the CH<sub>x</sub> species are in the same order, i.e., C > CH > CH<sub>2</sub> > H > CH<sub>3</sub> on Ni (111) and Ni (100); *ii*) the CH<sub>x</sub> bonding energy on Ni (100) is stronger than on Ni

(111), and *iii*) the dehydrogenation barriers [77] for the  $\text{CH}_x$  species are in good agreement with those obtained in the present analysis (see Table 3.5). Furthermore, Nave and coworkers [40] showed that the  $\text{CH}_4$  dissociation on Ni (111) and Ni (100) has a barrier in the range of 1.06–1.10 and 0.91–0.96 eV, respectively (see Table 3.5). That study used a plane-wave basis DFT method with a four-layer slab and top two layers relaxed, which is different to the present model. Although the numerical results are different than those obtained with the present modeling method, both studies reached the same qualitative results regarding the reactivity between Ni (100) and Ni (111), i.e., the energy barrier is lower by 0.1–0.2 eV on Ni (100) when compared to Ni (111). The reaction energy obtained from the present DFT calculation is 0.91 eV on Ni (111), which is 0.24 eV higher than that obtained on the Ni (100) surface. From a thermodynamic and reaction kinetics point of view, the high reaction and activation energies indicate that  $\text{CH}_4$  decomposition on Ni (111) is not as favorable as on the Ni (100) surface.

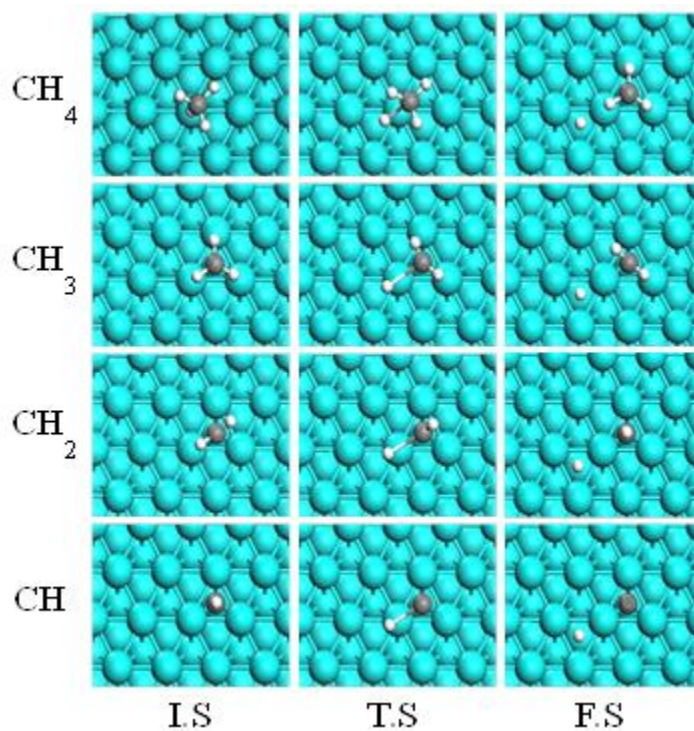


Figure 3.7 Geometric structures of the initial state (I.S.), transition state (T.S.), and final state (F.S.) of the four steps of  $\text{CH}_4$  dehydrogenation on Ni (111) surface. Blue: Ni, gray: C, and white: H.

For the dehydrogenation of CH<sub>3</sub> on Ni (111), hydrogen abstraction takes place over the top of a Ni surface atom. The CH<sub>2</sub> fragment bends and rotates toward the stretched direction but remains adsorbed at the hcp site. At the TS, the methyl species is highly distorted and the C–H<sub>a</sub> bond stretched from 1.13 to 1.75 Å. The H<sub>a</sub> atom forms a strong bond with the surface Ni atom (bond distance: 1.49 Å). The energy barrier for the CH<sub>3</sub> dehydrogenation on Ni (111) is approximately 0.89 eV. This is higher than the one (0.68 eV) reported by Blaylock et al. [6], but agrees with a previous theoretical GGA-DFT study presented by Mueller et al. (0.79 eV) [78], as shown in Table 3.5. This barrier is 0.27 eV higher than that for CH<sub>3</sub> dissociation on Ni (100) which can be related to the difference of CH<sub>3</sub> adsorption configuration and its dissociation pathway between the two surfaces. On Ni (111), the CH<sub>3</sub> is initially adsorbed on the threefold hcp hollow site; the C–H<sub>a</sub> bond scission takes place over the top of a Ni surface atom. In the case of Ni (100), CH<sub>3</sub> dehydrogenation starts from the bridge site adsorption configuration whereas C–H<sub>a</sub> bond scission occurs slightly off the atop site, which results in a TS with the H<sub>a</sub> atom sitting closer to a bridge site. The adsorption energy calculations showed that H adsorption at the bridge site (–2.67 eV) on Ni (100) is more stable than its top site adsorption (–1.92 eV) on Ni (111). Therefore, the TS is stabilized on Ni (100) with a much lower energy than the TS on Ni (111). The reaction energy obtained for CH<sub>3</sub> dissociation on Ni (111) is 0.16 eV (endothermic reaction).

In the case of the CH<sub>2</sub> dehydrogenation reaction on Ni (111), the H<sub>a</sub> atom that points to the top of the Ni atom is stretched and the CH fragment rotates upwards with the C atom strongly bonded to the three Ni atoms at hcp site. At the TS, the C–H<sub>a</sub> bond is stretched from 1.11 to 1.68 Å. DFT calculations showed that the dehydrogenation of CH<sub>2</sub> to CH needs to overcome an energy barrier of 0.41 eV, which is slightly higher than that reported by Blaylock et al. [6] (0.30 eV). However, the energy barrier obtained in the present analysis (0.41 eV) agrees well with the study presented by Mueller et al. [78] (0.36 eV), as shown in Table 3.5. In the present study, it was found that the barrier is 0.19 eV higher than that observed for the Ni (100) surface. As in the CH<sub>4</sub> dissociation on the Ni (100) surface, the H<sub>a</sub> atom is located slightly off the ontop site on the Ni (111) surface which leads to the destabilization of the TS and therefore to a higher activation energy. The value for the reaction energy is –0.38 eV on Ni (111). The results obtained in this work agree with the theoretical study by Mueller et al. [78] who reported a reaction energy of –0.44 eV.

The subsequent dissociation of CH to C and H is shown in Figure 3.7. During the dissociation process, C remains at the hcp hollow site while the H<sub>a</sub> moves over the adjacent Ni atom with the C–H bond stretched to 1.75 Å in the TS. The results showed that the CH dehydrogenation proceeds with an energy barrier of 1.38 eV, which is in good agreement with the study of Blaylock et al. [6] (1.40 eV) and

Mueller et al. [78] (1.40 eV) (see Table 3.5). This barrier is much higher than that obtained for the CH dissociation (0.64 eV) on Ni (100) surface. This is because the C–H<sub>a</sub> bond scission occurs over the top of Ni atom on Ni (111). The results also show that the CH dehydrogenation is a strongly structure-sensitive process, i.e., the difference in surface atom topology of the catalyst has a strong effect on the reaction barriers. The high barriers indicate that CH dehydrogenation on Ni (111) surface is kinetically unfavorable, making it the rate-determining step for CH<sub>4</sub> dissociation on the Ni (111) surface. Furthermore, the reaction CH→C+H on Ni (111) is calculated to be endothermic by 0.42 eV, which agrees with a recent theoretical study performed by Mueller et al. (0.50 eV) [78].

### 3.3.2.3 Methane dissociation on Ni (553)

The dissociation of methane on a Ni (553) surface occurs over the Ni atom on the step edge. This process has an activation barrier of 1.08 eV. The barrier is lower by 0.23 eV when compared to that obtained for the Ni (111) flat surface. As expected, the presence of step sites has a strong influence on the activation energy [79-82]. This must be attributed to the strong bonding of CH<sub>3</sub> at the step edge. Indeed, the results of the adsorption energies show that CH<sub>3</sub> is 0.20 eV more stable at the step edge bridge site when compared to the flat Ni (111) surface. Moreover, the reaction energy for CH<sub>4</sub> dehydrogenation on Ni (553) is 0.08 eV. That is, this dehydrogenation process is a nearly thermal neutral process whereas it is highly endothermic on the Ni (100) and Ni (111) flat surfaces.

For the dissociation of CH<sub>3</sub>, the initial state adopts the favorable bridge site adsorption configuration along the step Ni atoms. The final geometry of CH<sub>2</sub> is in the bridge position, which is similar to the initial CH<sub>3</sub> adsorption geometry with the H<sub>a</sub> atom adsorbed on an adjacent bridge site (see Figure 3.8). The TS for the dehydrogenation process is also depicted in Figure 3.8. As shown in Table 3.6, the energy barrier obtained for CH<sub>3</sub> dissociation is 0.71 eV. This result is comparable to those for CH<sub>3</sub> dehydrogenation on the flat surfaces because the C–H<sub>a</sub> bond break occurs over the atop site of the surface Ni atom on Ni (100), Ni (111), and Ni (553).

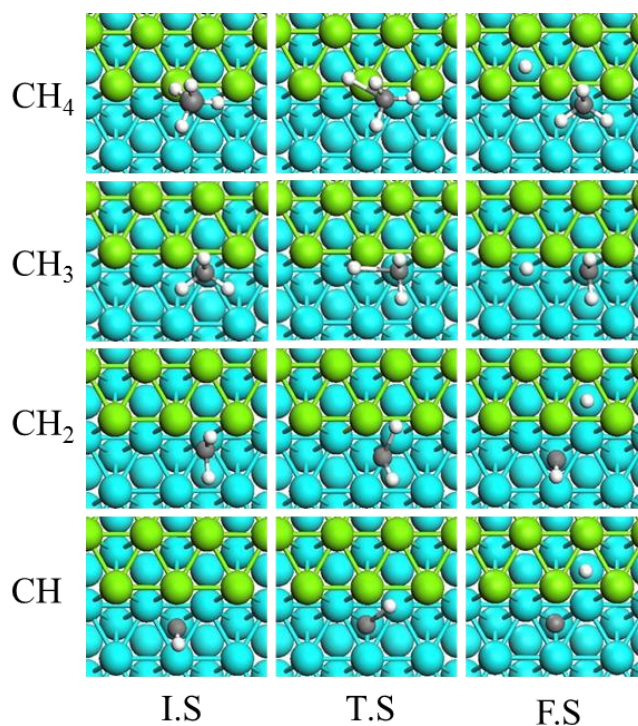


Figure 3.8 Geometric structures of the initial state (I.S.), transition state (T.S.), and final state (F.S.) of the four steps of  $\text{CH}_4$  dehydrogenation on Ni (553) surface. Green: Ni at upper step, blue: Ni at down the step gray: C, and white: H.

As a result of the  $\text{CH}_2$  dissociation, the CH fragment becomes adsorbed on the threefold hcp site on the lower terrace behind the bridge site to which  $\text{CH}_2$  was initially adsorbed. As shown in Table 3.6, the dissociation of  $\text{CH}_2$  to CH and H proceeds with a barrier of 0.15 eV on the Ni (553) surface. This energy barrier is comparable with that obtained for Ni (100) but much lower than that obtained for Ni (111). This can also be explained by the difference in the  $\text{CH}_2$  dissociation pathways on these surfaces. On Ni (111), the C–H bond scission occurs over the top of a surface Ni atom whereas the same scission occurs over the bridge site between the step-edge Ni atoms on Ni (553) and Ni (100), respectively. As mentioned above, the  $\text{H}_a$  adsorbed at the bridge site in the TS is often more stable than at the top site, which results in a lower energy TS along the reaction coordinates when compared to the TS where the  $\text{H}_a$  is located over the top site.

In the TS for CH dehydrogenation on Ni (553), the C–H bond bends over toward the upper edge Ni atoms and the breaks over the bridge site between these Ni atoms along the edge. This reaction eventually leads to a product with the H atom adsorbed at the fcc site on the upper terrace surface, while the C

remains adsorbed on the hcp site on the lower terrace to which CH was adsorbed. The activation barrier for this process is 0.47 eV. This value is significantly lower than those obtained for the flat surfaces, especially for the Ni (111) surface (1.38 eV). The reaction energy for the Ni (553) surface is 0.29 eV exothermic whereas the same reaction is thermal neutral on Ni (100) and endothermic on Ni (111), respectively. These phenomena can be explained by the analysis of the CH, C and H adsorption energy on these three surfaces. The adsorption energy for CH at its initial state on Ni (553) is  $-5.65$  eV while it is  $-6.43$  and  $-5.70$  eV on Ni (100) and Ni (111), respectively. The summation of adsorption energies for C and H as the reaction products on Ni (553), Ni (100), and Ni (111) are  $-9.47$ ,  $-9.94$  and  $-8.87$  eV, respectively. Then, the difference of adsorption energy between the products (C and H) and the reactant (CH) on Ni (553), Ni (100), and Ni (111) is approximately  $-3.82$ ,  $-3.51$ , and  $-3.17$  eV, respectively. These results show the stability of the C and H adsorption relative to the CH adsorption on each surface. The results showed that CH dehydrogenation on Ni (553) lead to a relatively most stable product, followed by dehydrogenations on Ni (100) and on Ni (111).

### 3.3.3 Electronic structure analysis

Based on Section 3.3.1, determination of adsorption energies for  $\text{CH}_x$  ( $x=1-3$ ) and H species on three surfaces showed that fragment adsorption are generally favored on less packed surfaces, e.g., Ni (100) and Ni (553). This is because of the lower metal-metal coordination numbers as compared to the highly packed Ni (111). The differences in the adsorption energies between Ni (111), Ni (100) and Ni (553) become significant as the number of H atoms in  $\text{CH}_x$  decreases, particularly for the adsorption of C, which has adsorption energies on Ni (100) and Ni (553) significantly higher than on Ni (111). The projected density of states (PDOS) and d-band analysis was conducted to provide a physical explanation of this phenomenon. The d-band center is a key parameter used to measure the distribution of solid energy levels and it characterizes the ability to eject an electron to the adsorbed molecule from the d-band of the metal. The average energy of the d-band (also called the d-band center) is calculated as follows [83]:

$$\varepsilon_d = \frac{\int_{-\infty}^{E_f} E \rho_d(E) dE}{\int_{-\infty}^{E_f} \rho_d(E) dE} \quad (3.2)$$

Similarly, the width of the d-band is calculated as follows [83]:

$$W_d = \sqrt{\frac{\int_{-\infty}^{E_f} E^2 \rho_d(E) dE}{\int_{-\infty}^{E_f} \rho_d(E) dE}} \quad (3.3)$$

where  $\rho_d$  represents the density of states projected onto the Ni atom's d band and  $E_f$  is the Fermi energy. The d-band position has been widely used as one of the relevant metrics for characterizing different kinds of metals [83-87]. Previous DFT calculations have shown that the valence C atom PDOS was mainly due to 2s and 2p electrons for isolated C atom, while it was 4s and 3d electrons for the case of isolated Ni atom [88]. Thus, the PDOS plots of the C 2s and 2p orbitals and the 4s and 3d orbitals of the surface Ni atoms involved in C adsorption on various Ni surfaces were estimated (see Figure 3.9). The existence of a large overlap between the C 2p and Ni 3d orbitals was observed on the three surfaces. This observation suggests that the formation of adsorption bonding was mainly due to the mixing between the carbon 2p and nickel 3d orbitals. The analysis of the PDOS also revealed the splitting of the C 2p orbitals, indicating bonding 2p states just below the Fermi level and antibonding 2p states above the Fermi level. Following Figure 3.9, the integration of the overlapped 2p orbitals PDOS curve below (above) Fermi level gives the number of occupied (unoccupied) C 2p states. Then, the fractional band filling (the fraction of occupied states) for C 2p orbital on Ni (111), Ni (553) and Ni (100) is 0.47, 0.55 and 0.59, respectively. These results indicate the progressive filling of the C 2p bonding state of the 'surface molecule' formed upon the C adsorption on the three Ni surfaces, which result in the progressive increase of the bonding strength between C and the Ni surfaces. Moreover, the  $\varepsilon_d$  and  $W_d$  for surface Ni atoms involved in C adsorption were calculated (see Table 3.7). The  $\varepsilon_d$  for the Ni atom on Ni (100) is shifted upward when compared to the surface Ni atoms in Ni (553) and Ni (111), respectively. The bandwidth of Ni (100) surface atom is also the smallest among the three surfaces followed by Ni (553) and Ni (111). Thus, the change in the adsorption energy is mainly due to the electronic effect, where  $\varepsilon_d$  shifts down and up. Take the  $\varepsilon_d$  on Ni (553) as the reference, the upshift of  $\varepsilon_d$  of Ni (100) empties more antibonding states and makes the interaction between C and Ni stronger. A shift of  $\varepsilon_d$  of Ni (111) to lower energy leads to more antibonding states being occupied and weakens the interaction. This result also explains the higher adsorption energy of C on Ni (100) than on Ni (553) and Ni (111).

Table 3.7 Average energy ( $\epsilon_d$ ) and width ( $W_d$ ) of the d-Band of the surface Ni atoms.

Surface	Clean surface <sup>a</sup>		Surface + C* <sup>b</sup>	
	$\epsilon_d$ (eV)	$W_d$ (eV)	$\epsilon_d$ (eV)	$W_d$ (eV)
Ni (111)	-1.78	2.08	-2.11	2.47
Ni (100)	-1.64	1.95	-1.87	2.28
Ni (553)	-1.57	1.91	-2.03	2.41

<sup>a</sup>Only the edge atoms are considered for Ni (553). <sup>b</sup>All the atoms involved in C adsorption are considered.

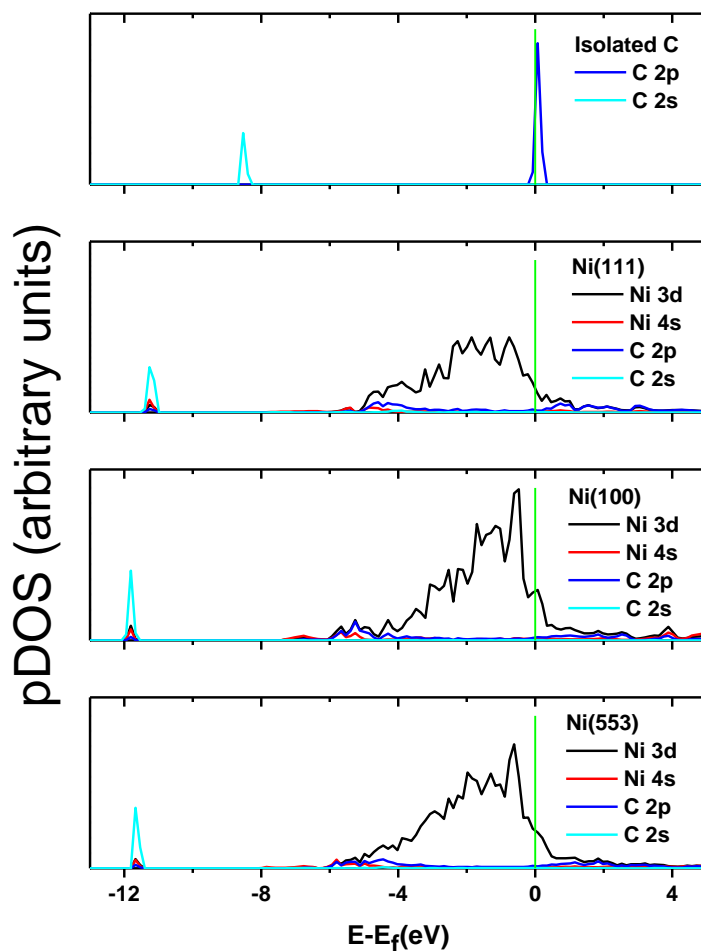


Figure 3.9 Projected density of states (PDOS) for isolated C atom and surface Ni atoms involved in C adsorption for the three respective surfaces: the Ni (111), Ni (100) and Ni (553). The vertical green lines donate the Fermi level.

The energy profile for the dehydrogenation of CH<sub>4</sub> on Ni (111), Ni (100), and Ni (553) surfaces is shown in Figure 3.10. It can be seen that the highest activation barriers in methane dehydrogenation are those for CH<sub>4</sub>, CH<sub>3</sub>, and CH dissociation. On Ni (111), CH dehydrogenation proceeds with the highest barrier (1.38 eV), which implies that CH dehydrogenation into C and H is the rate-determining step for CH<sub>4</sub> dissociation. That is to say, CH is the most abundant CH<sub>x</sub> species of CH<sub>4</sub> dehydrogenation on Ni (111). On Ni (100) and Ni (553), CH<sub>4</sub> dissociative adsorption, CH<sub>4</sub> → CH<sub>3</sub> + H, was the rate-determining step with barrier heights of 1.23 eV and 1.08 eV, respectively. C is the most abundant intermediate species on the two surfaces. These results show that CH<sub>4</sub> dehydrogenation on the surfaces that contain low-coordinated surface atoms is the most preferable reaction pathway in comparison with those on Ni (111) surfaces, which agrees with previous theoretical simulation studies [89,90]. The electronic structure analysis was conducted to gain insight into the physical origin of the difference in catalytic activity for the different Ni surfaces. The projected densities of states (PDOS) of metallic Ni d-band (see Figure 3.11) on various Ni surfaces were calculated in this study. In this analysis, only the edge atom on the Ni (553) surface was considered in the calculations. In general, the closer the d-band center to the Fermi level, the more reactive the surface. Likewise, a decrease of the bandwidth leads to a more reactive surface metal atom [83]. The reaction barrier of a specific reaction is related to its reaction pathway and the electronic structure of the catalyst surface atoms. Hence, a clear insight of the electronic structure effect on the reaction barriers can be gained if reactions with similar reaction pathway are compared. As an example, consider the methane dissociative adsorption, CH<sub>4</sub> → CH<sub>3</sub> + H. As discussed in Section 3.3.2, this reaction has similar reaction pathways on the three different Ni surfaces (the C–H<sub>a</sub> bond scission occurs over the top of a Ni atom). As shown in Tables 3.3–3.6, the corresponding reaction energy barriers on the three surfaces for this reaction follow the order: Ni (553) < Ni (100) < Ni (111). As shown in Table 3.5, the d-band center of Ni (111) surface is farther away from the Fermi level than that observed on the Ni (100) and the Ni (553) surfaces. Likewise, Table 3.7 also shows that the step Ni atoms on Ni (553) have the highest d-band energy, which is closer to the Fermi level. Accordingly, the reactivity of the Ni atoms on these three surfaces follows the order: Ni (553) > Ni (100) > Ni (111). This result is consistent with the DFT calculations obtained from the present study since the reaction barriers for CH<sub>4</sub> dissociation decrease on stepped Ni (553) and Ni (100) when compared to those obtained on Ni (111).

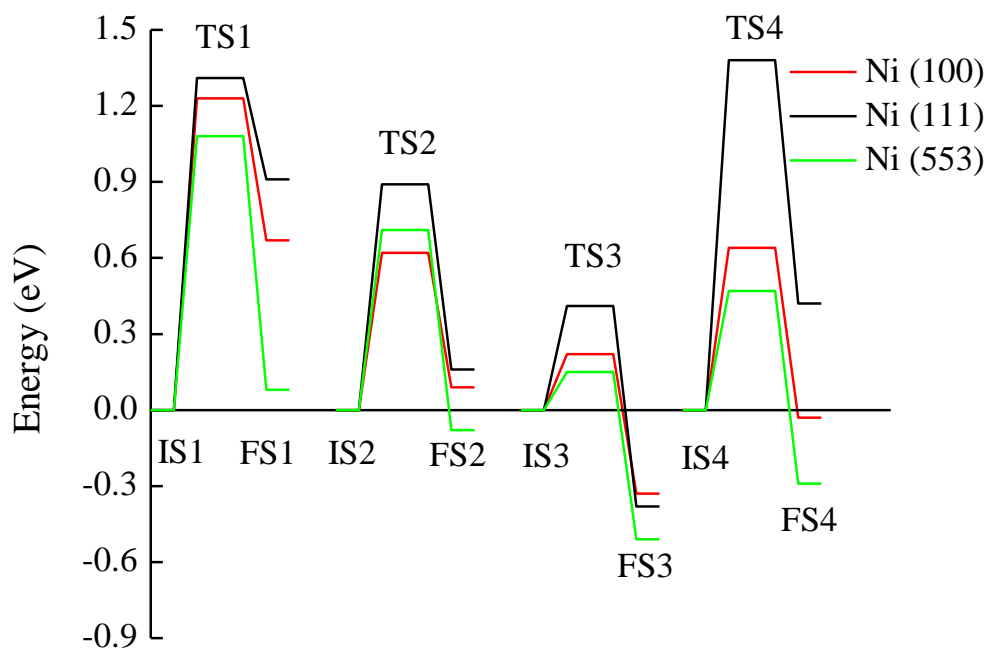


Figure 3.10 Reaction energy diagram of reaction paths of the  $\text{CH}_x$  ( $x=1-4$ ) dissociation reaction on Ni (100), Ni (111) and Ni (553) surfaces.

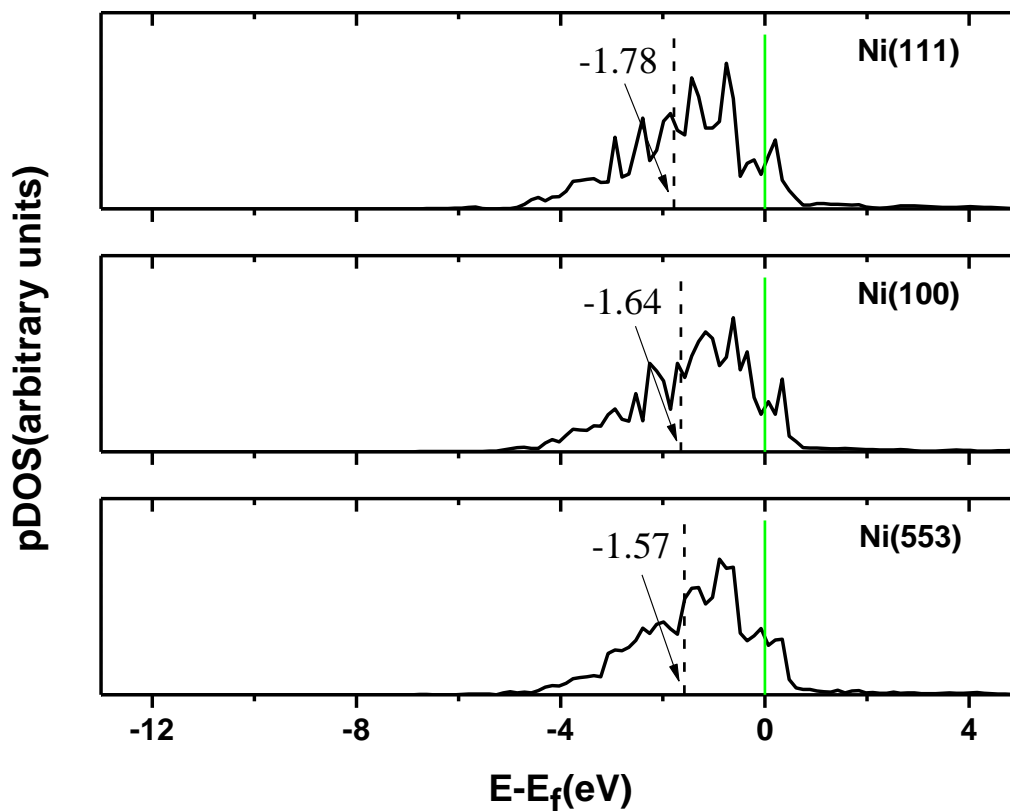


Figure 3.11 Projected density of states (PDOS) plots of the d-orbitals of the surface Ni atom for the three respective surfaces: Ni (111), Ni (100), and Ni (553). The vertical dashed lines represent the location of the corresponding d-band center. The vertical green lines indicate the Fermi level.

### 3.4 Summary

A systematic self-consistent periodic DFT study has been presented for methane decomposition on Ni (100), Ni (111) and Ni (553) surfaces. The geometry, site preference, and relative stability of adsorbed H and  $\text{CH}_x$  ( $x=0-3$ ) intermediates were investigated. Also, the decomposition mechanisms have been studied from energetic and geometrical points of view. The key results obtained by the present simulation study can be summarized as follows:

*i)* The preferred sites of the adsorbed species are located on the basis of the adsorption energies. On the Ni (100) surface, the hollow site is preferred for the hydrocarbon groups except  $\text{CH}_3$  and H, which are adsorbed at the bridge sites. On Ni (111) surface, the  $\text{CH}_x$  ( $x=0-3$ ) species and H are more likely to be adsorbed at the threefold hcp sites. The preferred sites are different on Ni (553) surface:  $\text{CH}_3$  and  $\text{CH}_2$

adsorbed on the bridge sites along the step edge are found to be the most stable whereas CH and H prefer to bond at the hcp sites on the terrace behind the step edge. Furthermore, the upper terrace on the fcc site is preferred for H adsorption. The most-significant difference in adsorption energy of the  $\text{CH}_x$  species between the three surfaces is the much-larger adsorption energy of C on both the Ni (100) and the Ni (553) surfaces. This significant deviation for C adsorption energy on various Ni surfaces was studied in terms of PDOS analysis. This analysis showed that the C–Ni interaction results in the formation of bonding and antibonding states between C 2p and Ni 3d orbitals where the bonding states are largely occupied on Ni (100) followed by Ni (553) as compared to that on Ni (111). This result explains the relatively strong C adsorption energy obtained from the DFT calculations on the Ni (100) and Ni (553) surfaces.

*ii)* Among the  $\text{CH}_x$  ( $x=1-3$ ) and H species studied, the DFT calculations showed that  $\text{CH}_3$  is the most diffusive specie on both Ni (100) and Ni (111). The mobility of the  $\text{CH}_x$  fragment and H atom between the flat surfaces showed that the C atom has the highest mobility on Ni (111) with a diffusion barrier of 0.48 eV. The C diffusion on Ni (100) proceeds with a barrier of 1.62 eV, which indicates that the surface diffusion of C atom on Ni (100) is a highly activated process and may rarely occur. Similar results were obtained for CH, i.e., diffusion barriers on Ni (100) and Ni (1 1 1) are 1.04 and 0.17 eV, respectively. No significant differences were calculated for H and  $\text{CH}_2$  diffusion on Ni (100) and Ni (111) surfaces.

*iii)* On the basis of the analysis of activation barriers, it is found that CH dehydrogenation is the rate-determining step for  $\text{CH}_4$  dissociation on Ni (111). Similarly, the first C–H bond scission of  $\text{CH}_4$  on Ni (100) and Ni (553) is the rate-determining step. Moreover, CH radical was found to be the most abundant fragment on Ni (111), which agrees with the theoretical results reported by Watwe et al. [28]. On Ni (100) and Ni (553), C was found to be the most abundant species. This result suggests that the C formation is highly likely to occur at the step and the open surfaces. The present study of  $\text{CH}_4$  dissociation on both flat and stepped Ni surfaces indicates that surfaces with low co-ordination number are strongly favored for  $\text{CH}_4$  successive dissociations. This is explained by the investigation of the d-band center of the Ni atoms on the three surfaces. The results show that the Ni atoms with low co-ordination number shift the d-band center toward the Fermi level and change the width of the d-band, which make the surfaces more reactive.

## Chapter 4

### Effect of Carbon on the Ni Catalytic Methane Cracking Reaction

This chapter presents a DFT study of the effect of carbon deposition on the Ni catalytic methane cracking reaction. Three catalyst models were used: Ni (111)–clean, Ni (111)–4C<sub>sub</sub>, and Ni (111)–C<sub>on</sub>, which represent clean, surface-covered, subsurface-covered Ni (111) surface, respectively. The stability of CH<sub>x</sub> species and the kinetic properties of methane dissociation were studied on the three models. The organization of the paper is as follows: an introduction of this study is given in the first section. In section 4.2, the computational methods and models used in this study are described. The results of the DFT calculations performed to describe the adsorption and dissociation properties of the CH<sub>x</sub> species on the three Ni surfaces are presented in section 4.3. Concluding remarks are given at the end of this chapter.

#### 4.1 Introduction

Methane activation on catalyst surfaces are crucial steps for the production of CO-free hydrogen, carbon nanotubes (CNTs) [1-4]. Because of their industrial and commercial importance, the decomposition of methane on Ni-based catalysts has been extensively studied by experimentalists [5-9] and theoreticians [10-14]. On the theoretical side, most of the studies have focused on CH<sub>x</sub> adsorption and dissociation on different Ni or Ni-based alloy surfaces. Wang et al. [15] presented a comparative study of CH<sub>x</sub> (x=3-0) chemisorption on Ni (111), Ni (100), and Ni (110) surfaces using plane wave DFT calculations. Bengaard et al. [16] reported the effects of surface steps on the activation of methane by using a Ni (211) step surface. Liu et.al [17] conducted a series of DFT calculations on methane dissociation on different pure metals (Fe, Co, Ni and Cu) and bimetals (NiFe, NiCo and NiCu). All these studies were conducted on clean surfaces which are far from the actual situation of the transition metal catalysts where the reactions take place on surfaces with deposited carbon atoms. These carbon atoms may *i*) chemisorb strongly on the Ni catalysts surface blocking access of reactants to metal surface sites; *ii*) diffuse from the surface to the octahedral sites of the first subsurface layer or dissolution in bulk nickel forming carbidic nickel [18,19]; *iii*) totally encapsulate a metal particle and thereby completely deactivate the Ni catalyst and stopping the CNTs growth process [20].

To the authors' knowledge, theoretical study of the effect of carbon deposition on the kinetic properties of catalytic methane dissociation has not been reported in the open literature. Such a study is

fundamental for a comprehensive understanding of the methane cracking reaction on Ni-based catalysts. It is also expected to play an important role in the estimation of more realistic kinetic parameters for this system, in particular  $\text{CH}_x$  dissociation barriers as a function of carbon deposition, where the effect of the deposited C atoms on the rate parameters (including coverage dependencies in activation energies) is usually not considered in the analysis [21].

In this work, a theoretical study on the activation of methane, and its corresponding fragments on carbon deposited Ni (111) surface were performed. The (111) surface was chosen because it is lowest energy facets [22], and usually dominate the surfaces of metal nanoparticles [23]. The objective of this study is to evaluate the energetics of reactive intermediates caused by the presence of carbon atoms on Ni (111). Two models were used to account for the different carbon deposition cases: Ni (111) surface with pre-covered C atom, referred to as Ni (111)- $\text{C}_{\text{on}}$ ; and a Ni (111) surface where all subsurface octahedral sites are occupied by carbon atoms, referred to as Ni (111)- $4\text{C}_{\text{sub}}$  (see Figure 3.1). Note that the formation of a carbon-rich subsurface layer has been observed by many experimental studies [24-26]. The present DFT calculations also show that C at the subsurface of the Ni (111) surface is slightly stable by 0.02 eV than the C adsorption on the Ni (111) surface, indicating the thermodynamic stability of the Ni-C subsurface alloy.

The adsorption of the  $\text{CH}_x$  species on clean Ni (111) referred to as Ni (111)-clean, Ni (111)- $4\text{C}_{\text{sub}}$ , and Ni (111)- $\text{C}_{\text{on}}$  surfaces was first studied. Then, the Transition States (TS) and energetics for the  $\text{CH}_4$  sequential dissociation reactions on these surfaces were identified. Since Ni catalytic methane cracking reaction usually occurs at temperatures above 773K [27], the corresponding Gibbs free energy barriers at this temperature were calculated. Comparisons between the adsorption and the dissociation properties of the  $\text{CH}_x$  species on the three surfaces are also presented in this study.

## 4.2 Computational details

### 4.2.1 Calculation methods

The same DFT calculation method is used as in Section 3.2.1, Chapter 3. The  $\text{CH}_x$  ( $x=3-0$ ) adsorption energies ( $E_{\text{ads}}$ ) were calculated as the difference in total energy between the optimized  $\text{CH}_x/\text{Ni}$  complex ( $E_{\text{CH}_x/\text{Ni}}$ ) and the sum of the energies of the optimized bare surface ( $E_{\text{Ni}}$ ) and gas-phase  $\text{CH}_x$  molecules ( $E_{\text{CH}_x}$ ), i.e.,

$$E_{ads}(CH_x) = E_{CH_x/Ni} - E_{Ni} - E_{CH_x} \quad (4.1)$$

Meanwhile, the interactions between adsorbates on the surface is defined by the following equation [28]

$$E_{int}(A, B) = E_{(A+B)/Ni} + E_{Ni} - E_{ads}(A) - E_{ads}(B) \quad (4.2)$$

where  $E_{(A+B)/Ni}$  is the total energy of A and B co-adsorbed on the Ni slab,  $E_{ads}(A)$  and  $E_{ads}(B)$  are the adsorption energies of A and B adsorbed on separate Ni slabs. A positive  $E_{int}(A, B)$  means a repulsive interaction.

The free energy of the reactions G was calculated as follows [29,30]: for gas-phase species  $CH_4(g)$ ,

$$\begin{aligned} G(T, P) &= E_{total} + E_{ZPE} + \Delta H^0(0 \rightarrow T) - TS(T, P) \\ &= E_{total} + E_{ZPE} + \Delta H^0(0 \rightarrow T) - TS^0(T, P) + RT \ln\left(\frac{P}{P^0}\right) \end{aligned} \quad (4.3)$$

where  $E_{total}$  is the total energy determined by DFT calculations.  $E_{ZPE}$  is the zero-point energy, which is calculated by

$$E_{ZPE} = \sum_{i=1}^{3N-6(5)} \frac{N_A h v_i}{2} \quad (4.4)$$

where  $N_A$  is Avogadro's number, h is Plank's constant,  $v_i$  is the frequency of the normal mode, and  $N$  is the number of atoms involved in the system.  $\Delta H^0(0 \rightarrow T)$  is the enthalpy change from 0 K,  $S^0(T, P)$  is the standard entropy at temperature T. Both  $\Delta H^0(0 \rightarrow T)$  and  $S^0(T, P)$  can be calculated directly from the DFT thermodynamic calculations.

For adsorbed species ( $CH_3, CH_2$ , et al.),

$$G(T, P) = E_{total} + E_{ZPE} + \Delta U^0(0 \rightarrow T) - TS^0(T) \quad (4.5)$$

$$\Delta U^0(0 \rightarrow T) = \sum_{i=1}^{3N} \frac{N_A h v_i e^{-h v_i / k_B T}}{1 - e^{-h v_i / k_B T}} \quad (4.6)$$

$$S^0(T) = \sum_{i=1}^{3N} -R \ln(1 - e^{-h v_i / k_B T}) + \frac{N_A h v_i e^{-h v_i / k_B T}}{T(1 - e^{-h v_i / k_B T})} \quad (4.7)$$

#### 4.2.2 Surface models

In the present study, the Ni (111) surface was modeled using periodic three-layer slabs with a  $2 \times 2$  unit cell. Convergence with respect to number of metal layers and unit cell dimensions was tested on  $2 \times 2$

four-layer unit cells and  $3\times 3$  three-layer unit cells, respectively. Binding energies of  $\text{CH}_x$  species ( $x=3-0$ ) on three layer  $2\times 2$  slabs were almost the same with that obtained on four-layer  $2\times 2$  slabs, whereas it is 0–0.33 eV larger compared to that on three-layer  $3\times 3$  slabs. A detailed discussion of the comparisons between these models is presented in the Section 4.3.1. The Ni (111)–clean, Ni (111)– $4\text{C}_{\text{sub}}$  and Ni (111)– $\text{C}_{\text{on}}$  surfaces used in the present study are shown in Figure 4.1. The bottom layer of the slab was fixed in its bulk positions with a calculated lattice parameter of 3.52 Å, whereas the Ni atoms of the remaining layers and the adsorbed species were set free to relax.

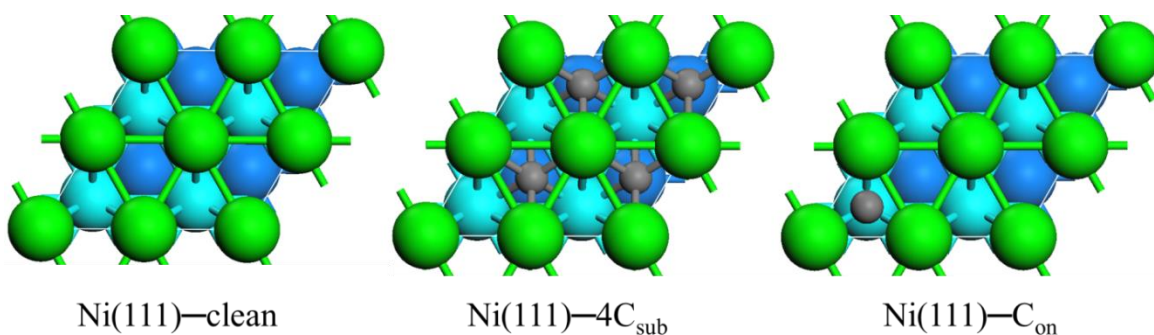


Figure 4.1 Top views of the  $2\times 2$  unit cell for different Ni surfaces. C atoms are colored gray, H atoms white, first-layer Ni atoms green, second-layer Ni atoms cyan, third-layer Ni atoms blue.

## 4.3 Results and discussion

### 4.3.1 Convergence with respect to the slab thickness and unit cell dimensions

The  $\text{CH}_x$  ( $x=3-0$ ) adsorption energies of the optimal geometries obtained with a  $2\times 2$  three-layer slab were recalculated using a  $2\times 2$  four-layer slab and  $3\times 3$  three-layer slab (see Table 4.1). The results show that on a  $2\times 2$  four-layer slab, the largest deviation in adsorption energy observed was for the  $\text{CH}_3$  adsorption (3.8%). i.e., the fourth layer model decreased the adsorption energy by 0.05 eV with respect to the  $2\times 2$  three-layer slab model, indicating that three layers are good enough to describe the system. Binding energies of  $\text{CH}_x$  species on three-layer  $3\times 3$  slabs is about 0.01–0.33 eV smaller compared to that obtained on three layer  $2\times 2$  slab. For example, the adsorption energy for  $\text{CH}_3$  is decreased from  $-1.33$  on three layer  $2\times 2$  slab to  $-1.11$  eV on three-layer  $3\times 3$  slab. And for CH adsorption, it is changed from  $-5.68$  to  $-5.69$  eV. Although there are deviations in the  $\text{CH}_x$  adsorption energies by using different size of the unit cells, the goal of the present study is to analyze the C deposition effect on the  $\text{CH}_x$  adsorption and dissociation. Hence, the study is focused on the comparisons between the clean Ni (111) surface and C

deposited models. As discussed in the revised manuscript, an analysis of  $\text{CH}_x$  dissociation on the three layer  $2\times 2$  slab and  $3\times 3$  slab found that, on the  $3\times 3$  slab with C surface coverage of  $1/9\text{ML}$ ,  $\text{CH}_x$  dissociation barriers are not affected by its neighboring C atom. However, on Ni surface with high C coverage, e.g.,  $1/4\text{ML}$  modeled with a  $2\times 2$  slab, the deposited C will have significant effect on the  $\text{CH}_x$  dissociation kinetics. Accordingly, the three layer  $2\times 2$  slab was used as a basis in present study to perform the comparisons between the different models.

Table 4.1 Adsorption energies (eV) of  $\text{CH}_x$  fragments ( $x = 3-0$ ) fragments on the  $2\times 2$  three-layer,  $2\times 2$  four-layer and  $3\times 3$  three-layer slab model of Ni (111) surface.

adsorbates	$2\times 2$ three-layer	$2\times 2$ four-layer	$3\times 3$ three-layer
$\text{CH}_3$	-1.33	-1.28	-1.11
$\text{CH}_2$	-3.23	-3.25	-3.04
$\text{CH}$	-5.68	-5.69	-5.35
C	-6.18	-6.20	-6.19

### 4.3.2 $\text{CH}_x$ ( $x = 3-0$ ) adsorption

The adsorption of  $\text{CH}_x$  ( $x = 3-0$ ) on Ni (111)-clean, Ni (111)- $4\text{C}_{\text{sub}}$  and Ni (111)- $\text{C}_{\text{on}}$  surfaces was examined first. The geometries of the most stable adsorption configurations are shown in Figure 4.2, the corresponding adsorption energies are listed in Table 4.2. Note that the present models for Ni (111)- $4\text{C}_{\text{sub}}$  and Ni (111)- $\text{C}_{\text{on}}$  corresponding a carbon with surface coverage of  $1/4$  monolayer and carbon with sublayer coverage of one monolayer, respectively. In the realistic conditions, when the C surface coverage is low, e.g.  $1/9$ ,  $\text{CH}_x$  ( $x=3-0$ ) adsorption could occurs either at the neighboring sites of the deposited C atom or at the active sites that far away from the deposited C atom. This will result in too many adsorption configurations to be considered and makes the DFT calculation very expensive. Most importantly is that, the latter case, where the adsorption occurs at the site that far away from the C atom is similar as  $\text{CH}_3$  adsorption at the clean surface. Accordingly, the adsorption of  $\text{CH}_x$  on the low C coverage surface will not significantly affected by the deposited C atom. Therefore, a relatively high carbon surface coverage, e.g.  $1/4$  monolayer, was considered in the present study. For the C sublayer model, a more realistic scenario is that C atoms will diffusion into both the sublayer and bulk of the catalyst with more C

atoms accumulated in the sublayer than in the bulk, due to the high energy barrier for bulk diffusion [31]. Moreover, the reactivity of the Ni catalyst top surface will be more likely affected by the C atoms deposited at the first subsurface layer. Thus, only C atoms deposited in the first sublayer was considered in the present study. The reason why C coverage of one monolayer is considered is that, at low sublayer C coverage ( $<1\text{ML}$ ), the sublayer C atoms will have more significant deactivation effect on the Ni atoms that it directly bonded with, as compared to the other top surface Ni atoms. This will result in a different activity of the surface Ni atoms, and therefore, introduce complexity of the DFT calculations. Therefore, to simplify the DFT calculation, the deactivation effect by the C subsurface deposition is studied using a model with the one monolayer subsurface C atoms.

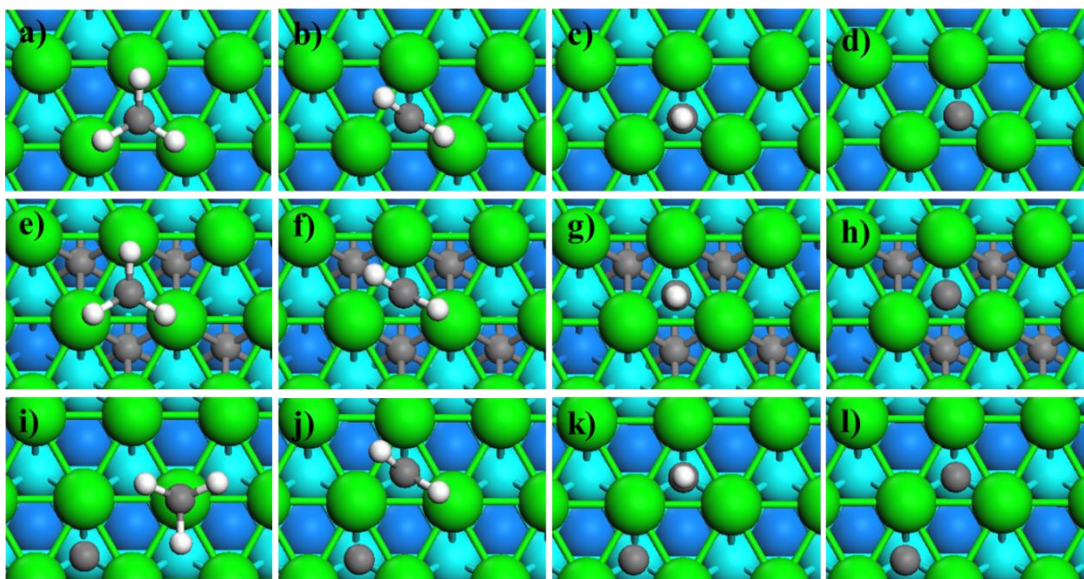


Figure 4.2  $\text{CH}_x$  ( $x = 3-0$ ) adsorption configurations on the different Ni (111) surfaces: (a–d), (e–h), and (i–l) correspond to the geometries on Ni (111)–clean, Ni (111)– $4\text{C}_{\text{sub}}$  and Ni (111)– $\text{C}_{\text{on}}$ , respectively. C atoms are colored gray, H atoms white, first-layer Ni atoms green, second-layer Ni atoms cyan, third-layer Ni atoms blue.

Table 4.2 Adsorption energies,  $E_{ads}$  (eV), of  $\text{CH}_x$  ( $x=3-0$ ) fragments on various Ni surface models. The adsorption energies in the bracket were calculated by using dispersion corrected RPBE-D3 functional.

Surface	$\text{CH}_3$	$\text{CH}_2$	CH	C
Ni(111)–clean	-1.33(-1.90)	-3.23	-5.68	-6.18(-6.49)
Ni(111)–4C <sub>sub</sub>	-1.35(-1.99)	-2.84	-4.93	-4.96(-5.23)
Ni(111)–C <sub>on</sub>	-0.97(-1.12)	-2.73	-5.03	-4.96(-5.22)

As shown in Figure 4.2, the most stable site for  $\text{CH}_3$  adsorption on both the Ni (111)–clean and Ni (111)–4C<sub>sub</sub> surfaces is the hcp site, with three H atoms pointing towards the surrounding Ni atoms. The adsorption energy of  $\text{CH}_3$  on Ni (111)–clean is -1.33 eV, which is consistent with the result reported by Blaylock et al. (1.30 eV) [44] and Michaelides et al. (-1.48 eV) [10]. On Ni (111)–4C<sub>sub</sub>, the corresponding adsorption energy obtained by the present study is -1.35 eV. This shows that the introduction of sub-surface carbon atoms has very little effects on the  $\text{CH}_3$  binding strength with respect to that on clean Ni (111). However, on Ni (111)–C<sub>on</sub> surface, the most favored site for  $\text{CH}_3$  adsorption is changed to the top site and the  $\text{CH}_3$  adsorption energy decreases to -0.97 eV due to the strong repulsive interaction (0.86 eV) between the deposited C atoms and  $\text{CH}_3$ . The less stability of  $\text{CH}_3$  adsorption on Ni (111)–C<sub>on</sub> can be also supported by the  $d_{\text{C-Ni}}$  bonding distance. On the Ni (111)–clean surface, the two closest  $d_{\text{C-Ni}}$  bonding distances were found to be 2.29 and 2.26 Å, respectively (see Table 4.3). On the Ni (111)–C<sub>on</sub> model, when  $\text{CH}_3$  is adsorbed at the hcp site, the corresponding  $d_{\text{C-Ni}}$  bonding distances are longer and changed to 2.32 and 2.38 Å, respectively.

$\text{CH}_2$  was found most stable at the hcp site on the Ni (111)–clean surface. This most favored adsorption site is not affected by the presence of carbon on the surface or on the subsurface. On Ni (111)–clean surface, the corresponding adsorption energy is calculated to be -3.23eV, which is in agreement with the adsorption energy value of -3.22 eV reported by Michaelides [10] for  $\text{CH}_2$  at the hcp site. This result is also consistent with the study of Blaylock et al. [44], who reported adsorption energies of -3.30 eV for  $\text{CH}_2$  adsorption. The adsorption energy of  $\text{CH}_2$  on Ni (111)–4C<sub>sub</sub> was found to be 0.39 eV lower than that at the Ni (111)–clean surface. This result indicates that the deposition of C atoms in the surface weakens the  $\text{CH}_2$  adsorption. Similar to the case of  $\text{CH}_3$  adsorption,  $\text{CH}_2$  on Ni (111)–C<sub>on</sub>, the corresponding adsorption energy was found to be even lower (-2.73 eV) due to the repulsive interaction (0.47 eV) between the adsorbed C and  $\text{CH}_2$ . As shown in Table 4. 2 and 4.4, on the Ni (111)–clean

surface, CH<sub>2</sub> hcp hollow site adsorption has two closest  $d_{C-Ni}$  bonding distance of 1.98 and 2.02 Å, respectively. However, on the Ni (111)-C<sub>on</sub> model, the corresponding  $d_{C-Ni}$  bonding distance was found to be of 1.95 and 2.21 Å, respectively, showing the less stability of CH<sub>2</sub> adsorption on Ni (111)-C<sub>on</sub> model.

The most favored adsorption site (hcp) for CH adsorption is the same for the three models here. On a Ni (111)-clean surface, the CH adsorption energy at the hcp sites was found to be -5.68 eV. This result is also in agreement with the study of Blaylock et al. [32], who reported an adsorption energy of -5.90 eV for CH adsorption. The CH adsorption energies are -4.93 and -5.03 eV on Ni (111)-4C<sub>sub</sub> and Ni (111)-C<sub>on</sub>, respectively, indicating that the adsorption of CH is predicted to be reduced by the deposition of C atoms.

The most stable configuration for the adsorption of C on the Ni (111)-clean surface is that where C was adsorbed at an hcp site (see Figure 4.2d). The corresponding adsorption energy is -6.18 eV. This is in reasonable agreement with that reported by Blaylock et al. [32] (-6.00 eV). C adsorption on both Ni (111)-4C<sub>sub</sub> and Ni (111)-C<sub>on</sub> also favours the hcp site, with the same reduced adsorption energies of -4.96 eV.

The conventional DFT functionals do not take into account van der Waals interactions, that is, London dispersion. These interactions might crucial for the metal surface adsorption systems [33,34]. To evaluate the effect of dispersion correction on the adsorption energy of the hydrocarbon species, CH<sub>3</sub> and C adsorption on Ni (111)-clean, Ni (111)-4C<sub>sub</sub> and Ni (111)-C<sub>on</sub> models were performed using the RPBE-D3 functional [35] as well (see Table 4.2). As shown in Table 4.2, the results of this analysis that the non-dispersion-corrected calculations underestimate the binding energies between the adsorbates and the Ni surfaces. To have a better understanding of the electronic effects between C and Ni, the projected density of states (PDOS) of surface Ni atoms over Ni (111)-clean, Ni (111)-4C<sub>sub</sub> and Ni (111)-C<sub>on</sub> was calculated. As shown in Figure 4.3, there is a significant down shift of the d-orbital for the Ni atom on Ni (111)-4C<sub>sub</sub> when compared to that on Ni (111)-clean surface. This indicates that the hybridization of d-orbitals with nearby subsurface carbon atoms stabilizes the metal's d band, shifting it down, away from the Fermi level, and therefore making Ni less reactive. The carbon pre-covered surface, Ni (111)-C<sub>on</sub>, shows a similar electronic poisoning effect: Ni d states are stabilized when C is deposited on hcp site of the surface. This behavior is also accompanied by a slight downward shift of the d states of surface Ni atoms that are bonded with the C atom, whereas the next nearest neighbor Ni atom (Ni 3d\*) are almost unaffected, as shown in Figure 4.3. This shows that the strong chemical bonding between C and Ni could

electronically modifies the Ni atoms' abilities to adsorb or dissociate the  $\text{CH}_x$  species. Meanwhile, it was also observed that the downshift of the Ni d state is larger in Ni (111)- $4\text{C}_{\text{sub}}$  than Ni (111)- $\text{C}_{\text{on}}$ . Therefore, it is expected that the Ni atoms on the Ni (111)- $\text{C}_{\text{on}}$  to have a higher reactivity than the Ni (111)- $4\text{C}_{\text{sub}}$  surface. However, the adsorption energy results have shown that  $\text{CH}_x$  adsorption on Ni (111)- $\text{C}_{\text{on}}$  is generally less stable than that on Ni (111)- $4\text{C}_{\text{sub}}$  surface, especially for the larger  $\text{CH}_3$  and  $\text{CH}_2$  molecules. This effect is due to the strong repulsive interaction between the  $\text{CH}_x$  and the pre-covered C atom under the present studied surface coverage.

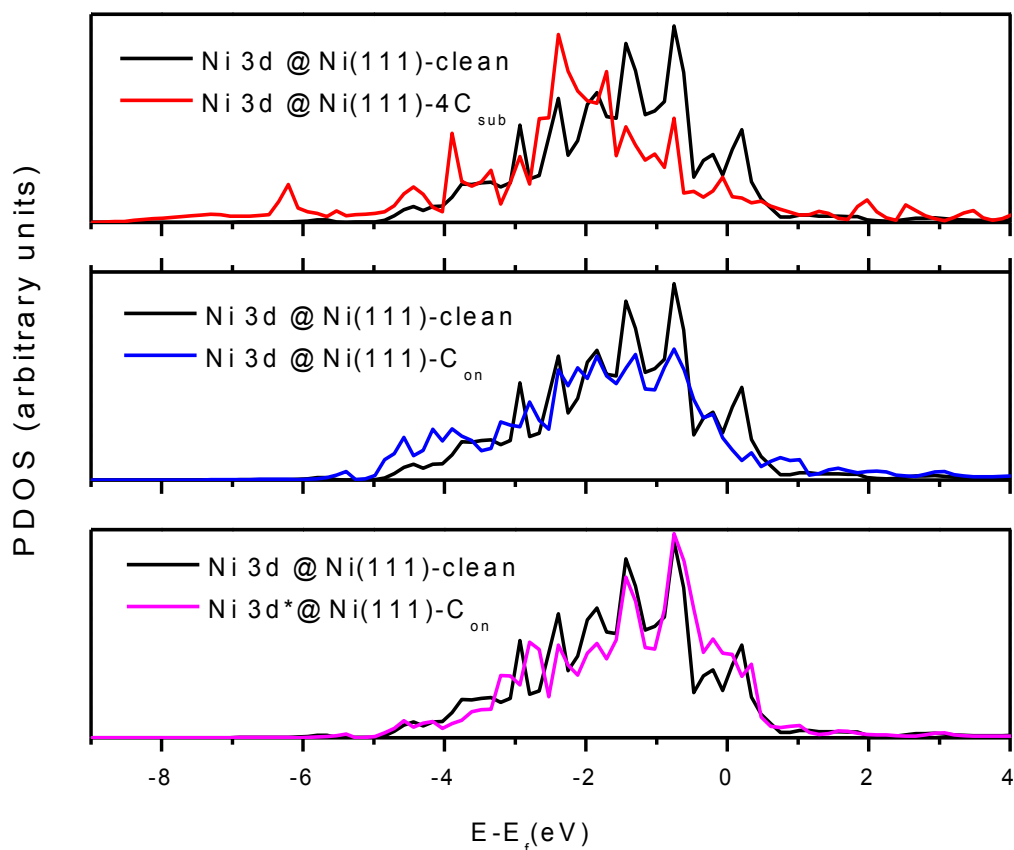


Figure 4.3 Projected density of states (PDOS) for Ni atoms on the three respective surfaces: Ni (111)-clean, Ni (111)- $4\text{C}_{\text{sub}}$  and Ni (111)- $\text{C}_{\text{on}}$ . Note that Ni 3d\* represents the Ni atom that are not bonded the C atom on Ni (111)- $\text{C}_{\text{on}}$ .

### 4.3.3 Methane dissociation

To elucidate the effect of deposited C on the kinetics of methane dissociation, the successive dissociation of  $\text{CH}_4$  to form surface C and H were investigated in detail on Ni (111)–clean, Ni (111)– $4\text{C}_{\text{sub}}$  and Ni(111)– $\text{C}_{\text{on}}$  surfaces, respectively. The geometries of the transition states (TS) for the four successive dehydrogenation steps are shown in Figure 4.4; the corresponding activation energies and reaction energies are listed in Tables 4.3 to 4.5.

#### 4.3.3.1 Methane dissociation on Ni (111)–clean surface

Dissociation of methane on Ni (111) occurs at the top of a surface Ni atom. The geometry of the transition state is shown in Figure 4.4a). In the TS, the methyl fragment is slightly tilted and the H atom moves over the top of the Ni atom. The activated C–H bond (denoted as C– $\text{H}_a$  hereafter) is stretched from 1.11 Å in the gas phase to 1.62 Å. The C and  $\text{H}_a$  atoms are bonded with the top Ni atom with bond distances of 2.10 and 1.56 Å, respectively. As shown in Table 4.3, the calculated activation barrier for this reaction is 1.23 eV, which is in good agreement with the study of Wang et al. [36], who reported a barrier of 1.17 eV for methane dehydrogenation on Ni (111). The reaction energy for this process is 0.65 eV, which suggests that the  $\text{CH}_4$  dissociation reaction on clean Ni (111) surface is a highly endothermic process.

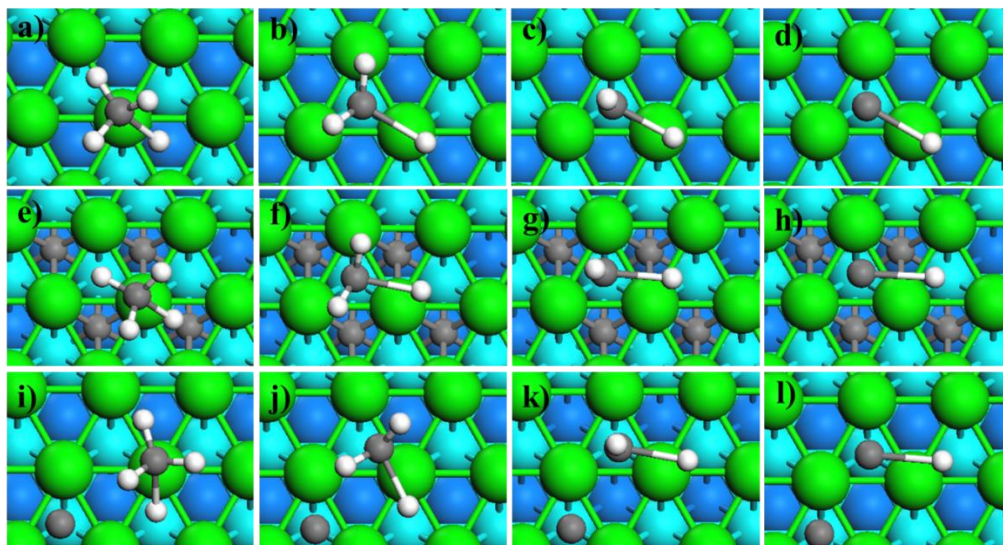


Figure 4.4 Geometric structures of transition state (TS) of the four steps of  $\text{CH}_4$  dehydrogenation on different Ni (111) surfaces: (a–d), (e–h), and (i–l) correspond to the TS geometries on Ni (111)–clean, Ni

(111)-4C<sub>sub</sub> and Ni (111)-C<sub>on</sub>, respectively. C atoms are colored gray, H atoms white, first-layer Ni atoms green, second-layer Ni atoms cyan, third-layer Ni atoms blue.

Table 4.3 Relative energies (eV) to the initial state (I.S.) of the transition state (T.S.) and final state (F.S.) for each elementary step of CH<sub>4</sub> dissociation on Ni (111)-clean surface. Distances between detached H<sub>a</sub> and the nearest C ( $d_{C-H_a}$ ) and Ni ( $d_{Ni-H_a}$ ) atoms, as well as the two closest bonding distances between the C atom in the CH<sub>x</sub> adsorbates and the surface Ni atoms ( $d_{C-Ni}$ ) are also shown.

	States	E (eV)	$d_{C-Ni}^1$ (Å)	$d_{C-Ni}^2$ (Å)	$d_{C-H_a}$ (Å)	$d_{Ni-H_a}$ (Å)
CH <sub>4</sub>	T.S.	1.23		2.10	1.62	1.56
	F.S.	0.65	2.16	2.18	3.00	1.68
CH <sub>3</sub>	I.S.	0.00	2.29	2.26	1.11	2.27
	T.S.	0.85	2.00	1.92	1.76	1.50
	F.S.	0.19	2.00	1.90	2.82	1.67
CH <sub>2</sub>	I.S.	0.00	1.98	2.02	1.13	2.14
	T.S.	0.29	1.88	1.85	1.68	1.49
	F.S.	-0.61	1.85	1.85	2.90	1.70
CH	I.S.	0.00	1.85	1.85	1.10	2.27
	T.S.	1.36	1.79	1.80	1.71	1.51
	F.S.	0.41	1.78	1.77	2.88	1.70

In the TS obtained for the dissociation of CH<sub>3</sub> on the Ni (111) surface, the activated C-H<sub>a</sub> bond is stretched from 1.11 to 1.76 Å. The H<sub>a</sub> atom forms a strong bond with the surface Ni atom (bond distance: 1.50 Å). The energy barrier for the CH<sub>3</sub> dehydrogenation on Ni (111) is 0.85 eV. This result is also in good agreement with that reported by Wang et al. [36] (0.82 eV).

In the case of the CH<sub>2</sub> dehydrogenation reaction on Ni (111), the H<sub>a</sub> atom that points to the top of the Ni atom is stretched and the CH fragment rotates upwards with the C atom strongly bonded to the three Ni atoms at hcp site. At the TS, the C-H<sub>a</sub> bond is stretched from 1.13 to 1.68 Å. DFT calculations showed

that the dehydrogenation of  $\text{CH}_2$  to  $\text{CH}$  needs to overcome an energy barrier of 0.29 eV, which is slightly lower than that reported by Wang et al. [36] (0.37 eV). However, the energy barrier obtained in the present analysis agrees well with the study presented by Blaylock et al. (0.30 eV) [32]. As seen in Table 4.3, this is the lowest energy barrier among all dissociation steps. Hence the dissociation of  $\text{CH}_2$  is the fastest of all dissociations.

The dehydrogenation process  $\text{CH} \rightarrow \text{C} + \text{H}$  has an energy barrier of 1.36 eV, which is in good agreement with the study of Blaylock et al. [35] (1.40 eV). At the TS, the  $\text{C}-\text{H}_a$  bond is stretched from 1.10 to 1.71 Å, which leads to the product C and H, located on two hollow sites. Furthermore, the reaction  $\text{CH} \rightarrow \text{C} + \text{H}$  on Ni (111) is calculated to be endothermic by 0.41 eV.

#### **4.3.3.2 Methane dissociation on Ni (111)- $4\text{C}_{\text{sub}}$ surface**

As shown in Figure 4.4e, the activation of the first  $\text{C}-\text{H}$  bond in methane also occurs over the top of a Ni atom on Ni (111)- $4\text{C}_{\text{sub}}$  surface. In the TS, the activated  $\text{C}-\text{H}_a$  bond is stretched from 1.11 Å in the gas phase to 1.64 Å. The C and  $\text{H}_a$  atoms are bonded with the top Ni atom with bond distances of 2.19 and 1.55 Å, respectively. The dissociation energy barrier is calculated to be 1.46 eV, which is higher by 0.23 eV when compared to clean Ni (111) surface. The reaction energy obtained from the present DFT calculation is 0.79 eV on Ni (111)- $4\text{C}_{\text{sub}}$ , which is 0.14 eV higher than that obtained on the Ni (111)-clean surface. The high reaction and activation energies indicate that  $\text{CH}_4$  decomposition on Ni (111)- $4\text{C}_{\text{sub}}$  is not as favorable as on the clean Ni (111) surface.

Table 4.4 Relative energies (eV) to the initial state (I.S.) of the transition state (T.S.) and final state (F.S.) for each elementary step of CH<sub>4</sub> dissociation on Ni (111)-4C<sub>sub</sub> surface. Distances between detached H<sub>a</sub> and the nearest C ( $d_{C-H_a}$ ) and Ni ( $d_{Ni-H_a}$ ) atoms, as well as the two closest bonding distances between the C atom in the CH<sub>x</sub> adsorbates and the surface Ni atoms ( $d_{C-Ni}$ ) are also shown.

	States	E (eV)	$d_{C-Ni}^1$ (Å)	$d_{C-Ni}^2$ (Å)	$d_{C-H_a}$ (Å)	$d_{Ni-H_a}$ (Å)
CH <sub>4</sub>	T.S.	1.46		2.19	1.64	1.55
	F.S.	0.79	2.29	2.28	2.69	1.68
CH <sub>3</sub>	I.S.	0.00	2.27	2.28	1.12	2.28
	T.S.	1.10	2.11	1.97	2.00	1.53
	F.S.	0.81	2.07	1.96	2.51	1.64
CH <sub>2</sub>	I.S.	0.00	2.06	2.09	1.11	2.22
	T.S.	0.35	1.95	1.86	1.80	1.55
	F.S.	-0.15	1.85	1.84	2.61	1.65
CH	I.S.	0.00	1.90	1.92	1.10	
	T.S.	1.48	1.85	1.84	1.73	1.58
	F.S.	1.12	1.85	1.83	2.49	1.68

The geometries of TS for the activation of CH<sub>3</sub> on Ni (111)-4C<sub>sub</sub> is similar to that obtained for the Ni(111)-clean surface except that the C-H bonds present different orientations. In the TS, CH<sub>2</sub> is located at the hcp site, and the detached H atom tilted towards the adjacent hcp site (Figure 4.4f). The dissociation of CH<sub>3</sub> to CH<sub>2</sub> and H proceed with a barrier of 1.10 eV on the Ni (111)-4C<sub>sub</sub> surface, as shown in Table 4.4. This energy barrier is 0.25 eV higher than that obtained for Ni (111)-clean surface.

Similar results were obtained for CH<sub>2</sub> and CH dehydrogenation. In the configuration of the TS for CH<sub>2</sub> and CH dehydrogenation, CH and C remain chemisorbed at the hcp site with the detached H atom tilted towards the adjacent hcp site. At the TS in CH<sub>2</sub> dissociation, the activated C-H<sub>a</sub> stretched from 1.11 to 1.80 Å. The reaction energy and the corresponding activation barrier for the dissociation of CH<sub>2</sub> on Ni

(111)-4C<sub>sub</sub> are -0.15 and 0.35 eV, respectively. The CH dehydrogenation on Ni (111)-4C<sub>sub</sub> has an energy barrier of 1.48 eV. The reaction energy obtained from the present analysis was 1.12 eV, which indicates that CH dehydrogenation on Ni (111)-4C<sub>sub</sub> is a highly endothermic process. At the TS, the C-H bond is stretched from 1.10 to 1.73 Å. Based on these calculations, one can clearly see that CH<sub>x</sub> dissociation on Ni (111)-4C<sub>sub</sub> have higher energy barriers as compared with that on Ni (111)-clean surface, showing the deactivation effect caused by the accumulation of C atoms in the subsurface of Ni (111) surface.

#### 4.3.3.3 Methane dissociation on Ni (111)-C<sub>on</sub> surface

For CH<sub>4</sub> dissociation on the Ni (111)-C<sub>on</sub> surface, the geometry of the TS is shown in Figure 4i). In the TS, the lengths of the C-Ni and C-H<sub>a</sub> bond on the Ni (111)-C<sub>on</sub> are 2.09 and 1.68 Å, respectively. The energy barrier for the initial activation of methane is calculated to be 1.69 eV (Table 4.5). This is about 0.46 and 0.23 eV higher than that on the Ni (111)-clean and Ni (111)-C<sub>sub</sub> surface, respectively. This result indicates that the deactivation effect caused by the on-surface C deposition is more significant as compared with that of subsurface C, because of the strong repulsion between the surface C atom and CH<sub>3</sub>. Moreover, the observed high activation energy on the Ni (111)-C<sub>on</sub> and Ni (111)-C<sub>sub</sub> surface means that if the activation energies determined for the clean surface is used in any simulation, it will result in an overestimation of the decomposition rate.

In the geometries of the TS for CH<sub>3</sub> dehydrogenation on Ni (111)-C<sub>on</sub> surface, both CH<sub>2</sub> and H were found slightly off the top site towards to adjacent hcp sites with a C-H<sub>a</sub> bond of 1.74 eV. The corresponding reaction energy and energy barrier obtained for this system were 1.07 and 1.32 eV, respectively. That is, the activation energy barrier obtained on this C pre-covered surface is quite higher than that observed on Ni (111)-clean (0.85 eV) and Ni (111)-C<sub>sub</sub> surface (1.10 eV).

Table 4.5 Relative energies (eV) to the initial state (I.S.) of the transition state (T.S.) and final state (F.S.) for each elementary step of CH<sub>4</sub> dissociation on Ni (111)-C<sub>on</sub> surface. Distances between detached H<sub>a</sub> and the nearest C ( $d_{C-H_a}$ ) and Ni ( $d_{Ni-H_a}$ ) atoms, as well as the two closest bonding distances between the C atom in the CH<sub>x</sub> adsorbates and the surface Ni atoms ( $d_{C-Ni}$ ) are also shown.

	States	E (eV)	$d_{C-Ni}^1$ (Å)	$d_{C-Ni}^2$ (Å)	$d_{C-H_a}$ (Å)	$d_{Ni-H_a}$ (Å)
CH <sub>4</sub>	T.S.	1.69		2.09	1.68	1.56
	F.S.	1.38		2.02	2.46	1.75
CH <sub>3</sub>	I.S.	0.00		2.01	1.10	2.21
	T.S.	1.32	2.96	1.90	1.74	1.56
	F.S.	1.07	2.61	1.96	2.61	1.69
CH <sub>2</sub>	I.S.	0.00	1.95	2.21	1.11	2.17
	T.S.	0.72	1.90	1.85	1.71	1.50
	F.S.	0.11	1.88	1.86	2.48	1.68
CH	I.S.	0.00	1.87	1.85	1.11	
	T.S.	1.87	1.86	1.78	1.72	1.54
	F.S.	1.39	1.84	1.76	2.46	1.69

The TS configurations for CH<sub>2</sub> and CH dissociation on Ni (111)-C<sub>on</sub> surface are similar to that obtained with the Ni (111)-4C<sub>sub</sub> surface, on which CH<sub>2</sub> (CH) is chemisorbed at the hcp site while the detached H atom is tilted towards the adjacent hcp site. The activation energy (0.72 eV) and reaction energy (0.11 eV) for CH<sub>2</sub> dehydrogenation on Ni (111)-C<sub>on</sub> is higher than in the other surfaces. The same was observed for CH dissociation, i.e., the reaction energy is found to be 1.39 eV and the dehydrogenation barrier step is calculated to be 1.87 eV, which are significantly higher than those obtained for the Ni (111)-clean and Ni (111)-4C<sub>sub</sub> surfaces, respectively. These results show that the activation energies for the dehydrogenation of CH are significantly increased when the neighboring adsorption sites are blocked by C atoms at the present studied C surface coverage.

The present Ni (111)-C<sub>on</sub> model is simulated by a 2×2 unit cell, which represent a surface C coverage of 0.25 monolayer (ML). In order to provide more insight regarding the surface C coverage effect on the methane dissociation barriers, CH<sub>4</sub> and CH dissociation on a clean and C covered (with surface coverage of 1/9ML and 2/9ML) Ni (111) surface modeled by a larger 3×3 unit cell was also considered in the present study. Only the first and last steps C-H breaking were investigated due to the fact that either CH<sub>4</sub> dissociative adsorption or CH dehydrogenation is usually reported as the rate-determining step in methane dissociation [37,38]. The energetic results are presented in Table 4.6. The result shows that both CH<sub>4</sub> and CH dissociation barriers obtained on the 1/9ML covered surface are very close to those obtained with a clean Ni (111) surface. Thus, there is a minor effect of the deposited C on the methane dissociation kinetics at low surface carbon coverage. When two C atoms are deposited on the surface (2/9ML), one can expect that CH<sub>4</sub> and CH dissociation barriers would vary according to the relative positions of the two deposited C atoms. To simplify the model, two different configurations with a long C-C distance were considered: A) both of the two C atoms sits on the hcp site, referred to as Ni (111)-C<sub>on</sub> (2/9 ML)-A; B) One of the C sits hcp site and the other occupies the fcc site, referred to as Ni (111)-C<sub>on</sub> (2/9 ML)-B. As show in Table 4.6, the CH<sub>4</sub> dissociation barrier obtained on these two 2/9 ML models is the same (1.16 eV) and is very close to that on Ni (111)-clean and Ni (111)-C<sub>on</sub> (1/9 ML). However, the results on Table 4.6 also show that, on the two Ni (111)-C<sub>on</sub> (2/9 ML) model, the reverse process for CH<sub>4</sub> dissociation (CH<sub>4</sub> production) is favored over that on Ni (111)-clean and Ni (111)-C<sub>on</sub> (1/9 ML), indicating that CH<sub>4</sub> dissociation would be hindered as the C surface coverage increases. For the case of CH dissociation, the dissociation barrier obtained with the 2/9 ML models, especially with the configuration A, are significantly higher than that on Ni (111)-clean and Ni (111)-C<sub>on</sub> (1/9 ML). These results clearly show the surface C coverage effect on the kinetics of Ni catalytic methane dissociation.

Table 4.6 Activation energies of CH<sub>4</sub> and CH dissociation on various Ni surfaces modeled by 3×3 unit cell.

Surface 3×3 unit cell	CH <sub>4</sub> → CH <sub>3</sub> + H		CH → C + H	
	$E_{a,for}(eV)$	$E_{a,back}(eV)$	$E_{a,for}(eV)$	$E_{a,back}(eV)$
Ni (111)–clean	1.14	0.65	1.17	1.21
Ni (111)–C <sub>on</sub> (1/9 ML)	1.15	0.80	1.20	0.51
Ni (111)–C <sub>on</sub> (2/9 ML)–A*	1.16	0.49	1.98	0.75
Ni (111)–C <sub>on</sub> (2/9 ML)–B*	1.16	0.57	1.44	0.32

\*A and B represent two models with different C atoms deposition configurations (see Figure 4.5). Note that forward/backward activation energy for CH<sub>3</sub> and CH<sub>2</sub> dissociation on Ni (111)–clean 3×3 unit cell are 0.73/0.95 eV and 0.34/1.05 eV, respectively.

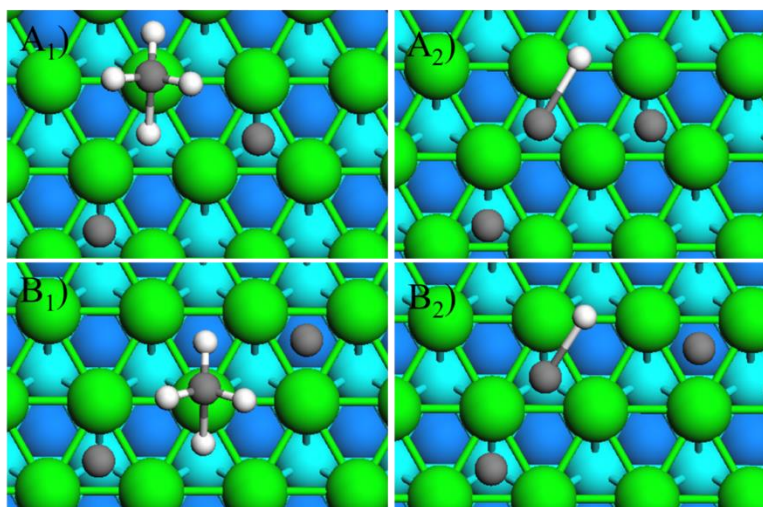


Figure 4.5 Geometric structures of transition state (TS) of the CH<sub>4</sub> and CH dissociation on C deposited (2/9 ML) Ni (111) surface modeled by 3×3 unit cell: A<sub>1</sub> and A<sub>2</sub> are the TS geometries on Ni (111)–C<sub>on</sub> (2/9 ML)–A; B<sub>1</sub> and B<sub>2</sub> are the TS geometries on Ni (111)–C<sub>on</sub> (2/9 ML)–B. C atoms are colored gray, H atoms white, first-layer Ni atoms green, second-layer Ni atoms cyan, third-layer Ni atoms blue.

#### 4.3.4 Free energy for CH<sub>4</sub> successive dehydrogenation

The Gibbs free energy barriers for CH<sub>4</sub> dehydrogenation elementary steps at 773 K are evaluated by the combined DFT calculations and thermodynamic analyses. It is calculated by including the zero-point energy correction, thermal energy correction and entropic effect. A free energy diagram along the reaction coordinate (including transition states) is presented in Figure 4.6. By comparing the free energy barriers shown in Figure 4.6, it is found that CH<sub>4</sub> dissociation on the Ni (111)-clean surface is most favorable both kinetically and thermodynamically. The free energy barriers for CH<sub>4</sub> and CH<sub>3</sub> dissociation on the Ni (111)-4C<sub>sub</sub> are comparable with that for on the Ni (111)-clean surface, showing that the deposition of C at the sublayer of the Ni catalyst has only a minor effect for the reactivity of catalyst towards CH<sub>4</sub> and CH<sub>3</sub> dehydrogenation. However, after CH<sub>3</sub> are dissociatively adsorbed on the Ni surface, the further decomposition of CH<sub>2</sub> and CH species is more difficult and the generation of C atoms is predicted to be hindered because the free energy barriers for the CH<sub>2</sub> and CH dissociation are 0.78 and 1.35 eV, much higher than those obtained on Ni (111)-clean surface (0.18 and 1.15 eV for the CH<sub>2</sub> and CH dissociation, respectively). When the C atoms are sitting on the Ni surface, CH<sub>x</sub> dissociation could be even more difficult. For example, for the CH<sub>4</sub> dehydrogenation on Ni (111)-C<sub>on</sub> surface, the free energy barrier and reaction energy is substantially increased to 1.51 and 0.82 eV, respectively. The free energy barrier for the CH dissociation to generate C is increased to 1.71 eV. Therefore, one can expect that, at the beginning of the reaction, CH<sub>4</sub> dehydrogenation occurs on the clean Ni catalyst surface. However, as the C atoms start to accumulate in the sublayer or on the surface of the Ni catalyst, it will affect the CH<sub>x</sub> dissociation properties. As observed in the experimental studies, during the Ni catalytic CH<sub>4</sub> cracking reactions, after a certain time of steady growth of the CNT/CNF, the deposited C atoms will slowly deactivate the Ni catalyst. At relatively low reaction temperature e.g. 773 K, the deactivation process could even last for more than 10h [9]. The results reported in the present study provide support of the delay of the catalyst deactivation. That is, the increase of the CH<sub>x</sub> dissociation barrier will result in a decrease of the C deposition rate, and prevents fast deactivation of the catalyst. The observations reported in the present study also allow us to consider the effect of C deposition on the CH<sub>x</sub> dissociation kinetic parameters in the microkinetic modeling of the reactions, which is usually not considered in the microkinetic analysis of CH<sub>4</sub> dehydrogenation involved processes [21,32].

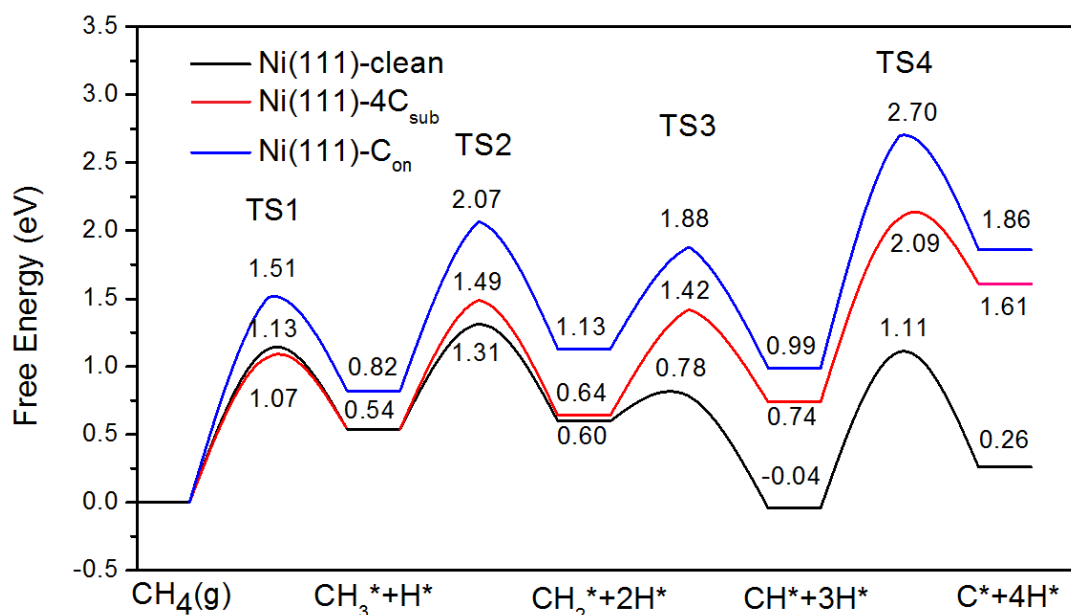


Figure 4.6 Gibbs free energy diagrams for the CH<sub>4</sub> dehydrogenation on different Ni (111) surfaces: Ni (111)-clean, Ni (111)-4C<sub>sub</sub> and Ni (111)-C<sub>on</sub>.

#### 4.4 Summary

To elucidate the role of the carbon deposition in methane dissociation reaction, a periodic DFT study has been presented for methane decomposition on Ni (111)-clean, Ni (111)-4C<sub>sub</sub> and Ni (111)-C<sub>on</sub> surfaces. The geometry, site preference, and relative stability of adsorbed CH<sub>x</sub> (x=3-0) intermediates were investigated. The results show that CH<sub>x</sub> (x=3-0) species adsorption on Ni (111)-4C<sub>sub</sub> and Ni (111)-C<sub>on</sub> is less stable as compared with that on Ni (111)-clean surface, indicating the effects of the deposited C atoms on the Ni catalyst.

The results obtained in the present analysis are in agreement with the predictions from the PDOS analysis: carbon incorporation in the surface leads to a down shift of the Ni d band, making Ni less reactive. Moreover, the study of the CH<sub>x</sub> dehydrogenation shows that the presence of carbon increases the barrier for CH<sub>x</sub> activation, especially for CH<sub>x</sub> dehydrogenation on Ni (111)-C<sub>on</sub> where the Ni surface was pre-covered with surface C atom: CH<sub>x</sub> (x=4-1) species encounter a highest energy barrier for dissociation due to the electronic deactivation induced by C-Ni bonding and the strong repulsive carbon-adsorbates interaction. This work can be used to estimate more realistic kinetic parameters for this system, where the effect of carbon deposition on the CH<sub>x</sub> dissociation barriers should be considered in the analysis.

## Chapter 5

### Effect of Metal–Support Interface during CH<sub>4</sub> Dissociation on Ni/ $\gamma$ -Al<sub>2</sub>O<sub>3</sub>

A DFT study of the effect of  $\gamma$ -Al<sub>2</sub>O<sub>3</sub> support on the methane dissociation is presented in this chapter. Two different  $\gamma$ -Al<sub>2</sub>O<sub>3</sub> models: spinel and nonspinel model of  $\gamma$ -Al<sub>2</sub>O<sub>3</sub> (100) surface have been used to model the supported Ni catalyst system, Ni<sub>4</sub>/ $\gamma$ -Al<sub>2</sub>O<sub>3</sub>. The adsorption of CH<sub>3</sub> and H, as well as the dissociation of CH<sub>4</sub> and H<sub>2</sub> are investigated. The results obtained from the DFT calculations indicate that the metal-oxide interface plays an essential role in the dissociation of CH<sub>4</sub> and H<sub>2</sub>. This study is organized as follows: an introduction of this study is given in the first section. The computational method and the models used in this study are described in section 5.2. Results and discussions are given in section 5.3. Concluding remarks are stated in section 5.4.

#### 5.1 Introduction

The dissociative adsorptions of methane and hydrogen in the presence of a catalyst has attracted interest in the past decade [1-3] since these processes are crucial in methane steam reforming and methane cracking for hydrogen and carbon nanotube production [4-8]. Due to their lower cost and good reactivity, supported Ni catalysts are the most widely used catalysts for these reactions [9-11]. Theoretical methods based on quantum chemistry can provide electronic and atomic level information that cannot be easily obtained by experimental methods. Hence, in the past years, the catalytic dissociation of CH<sub>4</sub> and H<sub>2</sub> has been extensively studied by theoreticians [12-22]. Haroun et al. [17] conducted DFT calculations on the dissociative adsorption of methane on Ni (111) surface with and without an adatom. Abild-Pedersen et al. [18] studied the effects of poisoning and step defects for methane activation on Ni (111). Studies of CH<sub>4</sub> and H<sub>2</sub> decomposition have also been conducted on single Ni atoms and Ni clusters [19-22]. Bin et al. [23] studied the influence of the nickel catalyst geometry on the dissociation barriers of H<sub>2</sub> and CH<sub>4</sub> using a Ni<sub>13</sub> cluster and Ni (111) surface. Theoretical studies focusing on CH<sub>4</sub> and H<sub>2</sub> dissociation on various Ni plane surfaces or clusters have also been reported in the literature [24-27]. However, most of the industrial heterogeneous catalysts are made of small metal nanoparticles supported on various oxide substrates, e.g., Al<sub>2</sub>O<sub>3</sub> [28,29]. Recently, DFT studies have shown that the existence of oxide support such as  $\gamma$ -Al<sub>2</sub>O<sub>3</sub> may affect the chemical reactivity of the metal catalyst for certain systems [30-34]. Briquet et al. [35] found that the aluminum oxide plays an important role in the activation of the adsorbed CO on a

Ni cluster. Valero et al. [36] showed that the metal-support interaction changes the CO and C<sub>2</sub>H<sub>4</sub> adsorption properties on  $\gamma$ -Al<sub>2</sub>O<sub>3</sub> supported Pd<sub>4</sub> cluster. Cheng et al. [37] studied the effect of  $\gamma$ -Al<sub>2</sub>O<sub>3</sub> substrate on NO<sub>2</sub> interaction with supported BaO clusters by DFT. That study reported a strong synergetic effect between the BaO clusters and the Al<sub>2</sub>O<sub>3</sub> substrate toward NO<sub>2</sub> adsorption. A DFT study performed by Kacprzak et al. [38] showed that the  $\gamma$ -Al<sub>2</sub>O<sub>3</sub> support promotes the oxidation of Pd nanoparticles at the support and nanoparticle interface. These studies have corroborated that the  $\gamma$ -Al<sub>2</sub>O<sub>3</sub> support may play an essential role on the overall behavior of certain catalytic reactions. Although Ni/ $\gamma$ -Al<sub>2</sub>O<sub>3</sub> catalysts have proven to show good activity for methane and hydrogen reactions in many experimental studies [39-43] to the authors' knowledge, no density functional theory (DFT) studies regarding the effect of the  $\gamma$ -Al<sub>2</sub>O<sub>3</sub> support on the Ni catalytic CH<sub>4</sub> and H<sub>2</sub> dissociation has been reported in the literature.

In order to understand the role of  $\gamma$ -Al<sub>2</sub>O<sub>3</sub> support at the atomic or molecular level, the CH<sub>4</sub> and H<sub>2</sub> dissociations on Ni<sub>4</sub>/ $\gamma$ -Al<sub>2</sub>O<sub>3</sub> were studied using DFT slab calculations. For the  $\gamma$ -Al<sub>2</sub>O<sub>3</sub> structure, two models, based on the defective spinel model [44,45] and nonspinel model, [46,47] have been proposed in the literature. Due to complexity of the crystallographic bulk structure of this material, a single model structure for this support has not been recognized by the scientific community. In fact, the structure of  $\gamma$ -Al<sub>2</sub>O<sub>3</sub> is still the subject of considerable debate in the open literature [48-53]. Herein, to account for the effect of the two predominant models used for  $\gamma$ -Al<sub>2</sub>O<sub>3</sub>, two systems, Ni<sub>4</sub> cluster supported on the spinel  $\gamma$ -Al<sub>2</sub>O<sub>3</sub> [noted S(Ni<sub>4</sub>)], and Ni<sub>4</sub> cluster supported on the nonspinel  $\gamma$ -Al<sub>2</sub>O<sub>3</sub> surface [noted NS(Ni<sub>4</sub>)], have been used to model Ni<sub>4</sub>/ $\gamma$ -Al<sub>2</sub>O<sub>3</sub>. The aim of the present study is to present a comprehensive understanding of the CH<sub>4</sub> and H<sub>2</sub> reaction systems, i.e., adsorption and dissociation properties at different sites of the supported Ni cluster. Moreover, previous experimental studies have shown that metal-support interaction might play a key role in the carbon nanotube growth mechanism [54-56]. Ni nanoparticles have been observed to be detached from the alumina support and were pushed upward by the carbon nanotubes. Therefore, the metal-support interaction upon adsorbate adsorption was studied here and used to understand the detachment of the Ni particle in the early stage of CNTs growth process.

In the present work, two Ni<sub>4</sub>/ $\gamma$ -Al<sub>2</sub>O<sub>3</sub> models were used to study the reactivity of  $\gamma$ -Al<sub>2</sub>O<sub>3</sub> supported Ni catalyst. That is, the pathway and energy barriers for CH<sub>4</sub> and H<sub>2</sub> dissociation at the top and interface sites on the  $\gamma$ -Al<sub>2</sub>O<sub>3</sub> supported Ni<sub>4</sub> cluster were studied using two models of  $\gamma$ -Al<sub>2</sub>O<sub>3</sub> (100) surface. Also, CH<sub>3</sub> and H adsorption, and the influence of these species on the metal support interaction, were studied and discussed in this work. The reactivity of the top and interface sites on the supported Ni<sub>4</sub> cluster was identified using the projected density of states (PDOS) method and Hirshfeld charge analysis [57].

## 5.2 Computational details

### 5.2.1 Calculation methods

The DFT calculation method used in the present study is slightly different from that in Section 3.2.1, Chapter 3. That is, the kspace parameter was set to 3 for S(Ni<sub>4</sub>) model; for the NS(Ni<sub>4</sub>) model, since a large unit cell needs to be specified which increases the computational demands. To reduce the computation costs in the calculations, the linear tetrahedron method for the kspace numerical integration (k-space parameter = 2) [58] is used for the NS(Ni<sub>4</sub>) model.

The adsorption energies ( $E_{ads}$ ) of the adsorbates were calculated as follows:

$$E_{ads}(X)=E(X-Ni_4/\gamma-Al_2O_3)-E(X)-E(Ni_4/\gamma-Al_2O_3), \quad (5.1)$$

where  $X$  represents the adsorbates. To analyze interaction between the cluster and the oxide surface, the metal–support interaction energies,  $E_{MSI}$ , were computed as follows:

$$E_{MSI}=E(X-Ni_4/\gamma-Al_2O_3)-E(X-Ni_4)'-E(\gamma-Al_2O_3)', \quad (5.2)$$

where  $E(X-Ni_4)'$  and  $E(\gamma-Al_2O_3)'$  represent the energies of the  $X-Ni_4$  fragment and the oxide surface kept in the deformed geometry of the  $X-Ni_4/\gamma-Al_2O_3$  system, respectively. Thus,  $E_{MSI}$  can be used as a measure of the change in the electronic structure at the metal–support interface induced by the adsorption of the probe molecules.

### 5.2.2 Surface models

As mentioned above, there is still controversy in the literature regarding the  $\gamma-Al_2O_3$  crystal structure: both nonspinel and spinel-like structures have been proposed. Hence, in the present study, the defective spinel and the nonspinel slab model with translational symmetry in two directions were used to model the  $\gamma-Al_2O_3$  (100) surface. The spinel-like structure of  $\gamma-Al_2O_3$  belongs to the Fd3m space group (No. 227) with lattice constants  $a=b=c=7.911 \text{ \AA}$  [59-61]. In the spinel-like structure (MgAl<sub>2</sub>O<sub>4</sub>) of  $\gamma-Al_2O_3$ , the magnesium atoms are substituted by aluminum atoms. Therefore, Al vacancies should be introduced to fully match the stoichiometry of  $\gamma-Al_2O_3$  [62]. However, there is no general agreement regarding the exact localization of the vacancies in the spinel structure [49,63]. To simplify the modeling process, the surfaces of spinel-based  $\gamma-Al_2O_3$  structures are always cleaved from ideal bulk structure, i.e., no vacancies contained in the bulk. Accordingly, the stoichiometry of the surfaces obtained for spinel-based  $\gamma-Al_2O_3$  depends on the direction of cleaving, the number of layers, and the dimension of the unit cell. The (100) surface was used in the present study to perform the DFT calculations. To speed up our calculations, the

(100) surface was modeled as a five-layer stoichiometric spinel type slab of 40 atoms, 24 oxygen and 16 aluminum atoms (Figure 5.1). For the nonspinel  $\gamma\text{-Al}_2\text{O}_3$  model proposed by Digne et al. [47,64] a periodic  $\gamma\text{-Al}_2\text{O}_3$  (100) surface slab with seven atomic layers was used to represent the model  $\gamma\text{-Al}_2\text{O}_3$  substrate in the present study (see Figure 5.2). The (100) surface was selected because it is one of the most detected and catalytically active surfaces for anchoring deposited transition metal and metal oxide particles [65,66]. Note that the  $\gamma\text{-Al}_2\text{O}_3$  (100) model used in the present study is a clean ideal surface, i.e., the surface hydroxyl groups are not considered in this model. The experimental work of Digne et al. [47,64] found that the surface coverage of hydroxyls on  $\gamma\text{-Al}_2\text{O}_3$  changes as a function of temperature. According to that work,  $\gamma\text{-Al}_2\text{O}_3$  shows two main surfaces above 600 K: the fully dehydrated (100) surface and the hydrated (110) surface. Since the reaction temperature of methane cracking is in the range of 800–1000 K, a dehydrated  $\gamma\text{-Al}_2\text{O}_3$  (100) surface is a suitable relatively simple model that can be used to study the behavior of this system. A  $\text{Ni}_4$  cluster with tetrahedral configuration was used to model Ni catalyst in this study. This cluster is the smallest unit which can provide a three-dimensional structure to probe both metal-metal and metal-support interactions as reported in many other studies [67-72]. Moreover, the study of the stability of the  $\text{Ni}_4$  clusters shows that the supported 3D  $\text{Ni}_4$  cluster is the most stable configuration, as compared with the 2D planar  $\text{Ni}_4$  structure. In the present study, the tetrahedral  $\text{Ni}_4$  cluster configuration is found to be less energetically favorable (0.03 eV) than the planar one in the gas phase. However, upon binding on the spinel model of  $\gamma\text{-Al}_2\text{O}_3$  (100) surface, the supported 2D square planar  $\text{Ni}_4$  structure is less stable than the 3D structure by 1.55 eV. The same is true for the  $\text{Ni}_4$  cluster on nonspinel model  $\gamma\text{-Al}_2\text{O}_3$  (100) surface; the 3D tetrahedron  $\text{Ni}_4$  model is more stable than the 2D  $\text{Ni}_4$  model by 1.40 eV. Therefore, this tetrahedron  $\text{Ni}_4$  cluster was chosen in the present study. For both S( $\text{Ni}_4$ ) and NS ( $\text{Ni}_4$ ), the bottom two layers of the  $\gamma\text{-Al}_2\text{O}_3$  (100) surface were kept frozen in their bulk positions whereas the remaining top layers together with the  $\text{Ni}_4$  cluster and the adsorbates were allowed to relax during the DFT calculations. It should be noted that the triple-z polarized “TZP” STO basis was used in the calculations on S( $\text{Ni}_4$ ). Due to computational limitations, a less accurate STO basis sets, namely, double-z “DZ”, was employed for the NS( $\text{Ni}_4$ ). In order to probe the reliability of the DZ basis set on the results obtained on NS( $\text{Ni}_4$ ), test calculations were performed on the  $\text{CH}_3$  adsorption properties by using TZP basis set. The adsorption energies for  $\text{CH}_3$  top and interface adsorption using the TZP basis set were  $-1.83$  and  $-2.12$  eV, respectively, compared to  $-1.87$  and  $-2.04$  eV obtained with the DZ basis set. This result suggests that the increase of the basis set size does not lead to substantial alterations in terms of adsorption energy ( $\sim 2\text{--}4\%$  error). Also, the geometrical parameters remained practically unchanged upon increase of the basis set from DZ to TZP.

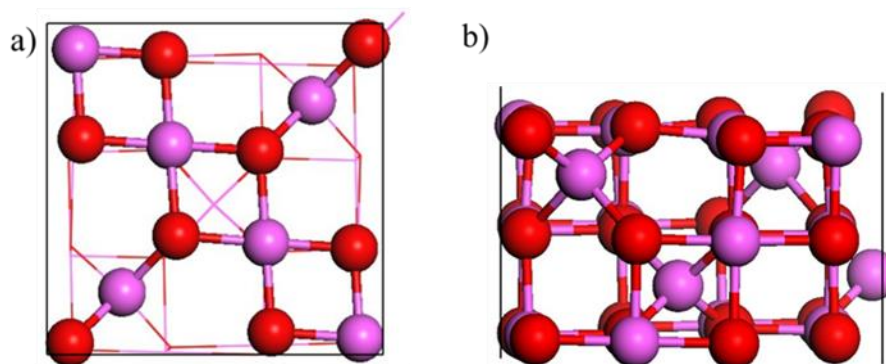


Figure 5.1 The optimized spinel type model of  $\gamma$ -Al<sub>2</sub>O<sub>3</sub> (100)-1×1 surface. (a) top view; (b) side view. Oxygen atoms are shown in red and aluminum atoms in magenta.

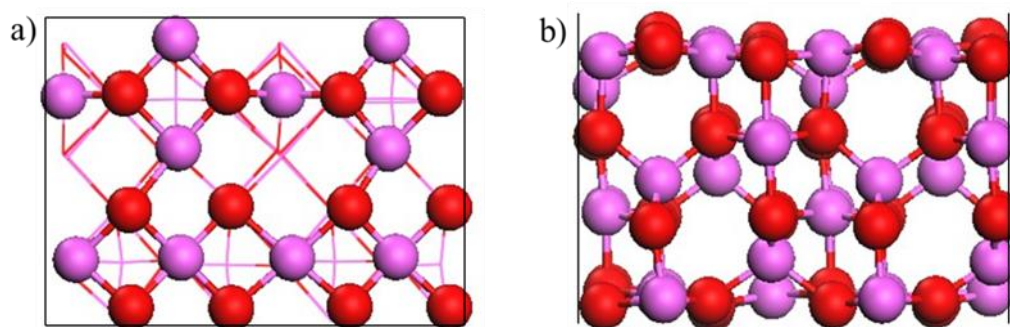


Figure 5.2 The optimized non-spinel type model of  $\gamma$ -Al<sub>2</sub>O<sub>3</sub> (100)-2×1 surface. (a) top view; (b) side view.

## 5.3 Results and discussion

### 5.3.1 Ni<sub>4</sub> Cluster Supported on the $\gamma$ -Al<sub>2</sub>O<sub>3</sub> (100)

*Spinel Type Model.* For Ni<sub>4</sub> cluster adsorption on the spinel type model of  $\gamma$ -Al<sub>2</sub>O<sub>3</sub> (100) surface, S(Ni<sub>4</sub>), different surface sites were investigated and resulted in a number of structures. Figure 5.3 shows the most stable configuration obtained for Ni<sub>4</sub> cluster supported on S(Ni<sub>4</sub>). In this configuration, three Ni atoms are in direct contact with the surface forming two Ni-O bonds and five Ni-Al bonds. The Ni<sub>1</sub> atom is located at the top vertex away from the support surface. The adsorption and interaction energy for this supported Ni<sub>4</sub> cluster obtained for this configuration are -1.84 and -2.27 eV, respectively.

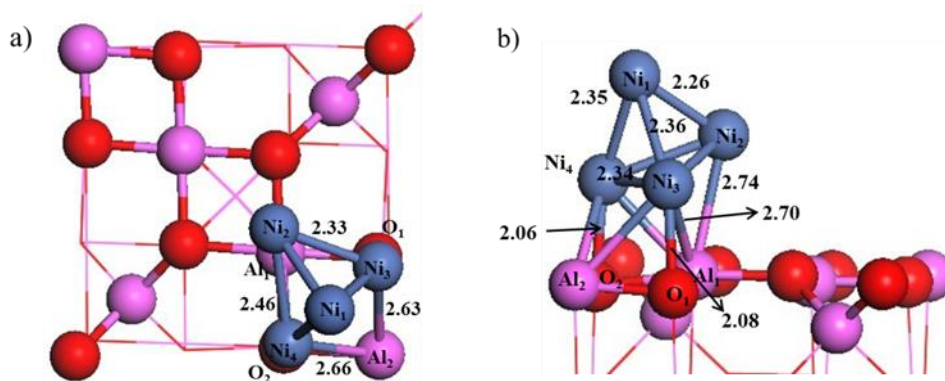


Figure 5.3 The optimized structure of Ni<sub>4</sub> cluster supported on the spinel type  $\gamma$ -Al<sub>2</sub>O<sub>3</sub> (100) surface, S(Ni<sub>4</sub>). (a) top view; (b) side view. Bond lengths are in Å. Dark blue balls stand for Ni atoms, and others are the same as in Figure 5.1.

*Nonspinel Type Model.* Figure 5.4 shows the most stable adsorption configuration for Ni<sub>4</sub> cluster on the nonspinel type model of  $\gamma$ -Al<sub>2</sub>O<sub>3</sub> (100) surface, NS(Ni<sub>4</sub>). The key feature of this structure is that all of the three bottom Ni atoms located at the metal–alumina interface are bonded with the surface O atoms, forming three Ni–O bonds and four Ni–Al bonds. The adsorption energy and the metal-support energy obtained for this configuration are  $-2.28$  and  $-2.79$  eV, respectively.

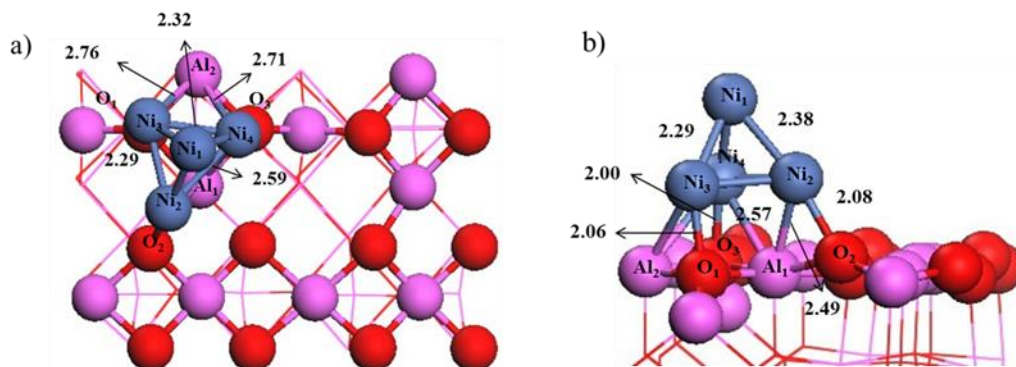


Figure 5.4 The optimized structure of Ni<sub>4</sub> cluster supported on the non-spinel type  $\gamma$ -Al<sub>2</sub>O<sub>3</sub> (100) surface. (a) top view; (b) side view. Bond lengths are in Å.

To gain further insight into the nature of the bonding between the supported Ni<sub>4</sub> cluster and the alumina support, Hirshfeld charges analysis was conducted on the two models. The Hirshfeld charges

distribution of the clean (100) alumina surface and the deposited Ni<sub>4</sub> cluster over the alumina surface are shown in Table 5.1. As shown in this table, the Ni<sub>4</sub> clusters have a total charge of +0.330e and +0.078e on S(Ni<sub>4</sub>) and NS(Ni<sub>4</sub>), respectively. The larger positive charge on the deposited Ni<sub>4</sub> cluster in S(Ni<sub>4</sub>) indicates that more charges were transferred from the Ni cluster to the  $\gamma$ -Al<sub>2</sub>O<sub>3</sub> (100) surface than NS(Ni<sub>4</sub>). The results in Table 5.1 also show that, for both S(Ni<sub>4</sub>) and NS(Ni<sub>4</sub>), the deposition of Ni<sub>4</sub> on the  $\gamma$ -Al<sub>2</sub>O<sub>3</sub> (100) surface resulted in an increase of charge density on the surface Al atoms and a decrease of the charge density on the O atoms, respectively. Therefore, the interaction observed between the Ni atoms and the surface on these configurations is similar to a back-donation interaction [73] where the metal is promoting a charge transfer from the surface oxygen to the aluminum.

Table 5.1 Hirshfeld charges of the supported Ni<sub>4</sub>/  $\gamma$ -Al<sub>2</sub>O<sub>3</sub> (100) complexes.

	Spinel $\gamma$ -Al <sub>2</sub> O <sub>3</sub> : S(Ni <sub>4</sub> )		Non-spinel $\gamma$ -Al <sub>2</sub> O <sub>3</sub> : NS(Ni <sub>4</sub> )	
	$\gamma$ -Al <sub>2</sub> O <sub>3</sub>	Ni <sub>4</sub> / $\gamma$ -Al <sub>2</sub> O <sub>3</sub>	$\gamma$ -Al <sub>2</sub> O <sub>3</sub>	Ni <sub>4</sub> / $\gamma$ -Al <sub>2</sub> O <sub>3</sub>
Ni <sub>4</sub>		0.330		0.078
Al <sub>1</sub>	0.491	0.318	0.589	0.424
Al <sub>2</sub>	0.389	0.360	0.591	0.469
O <sub>1</sub>	-0.366	-0.314	-0.415	-0.312
O <sub>2</sub>	-0.366	-0.313	-0.419	-0.368
O <sub>3</sub>			-0.372	-0.349

### 5.3.2 CH<sub>3</sub> and H adsorption on Ni<sub>4</sub>/ $\gamma$ -Al<sub>2</sub>O<sub>3</sub> (100)

#### 5.3.2.1 CH<sub>3</sub> adsorption

*Spinel Type Model.* The structures for CH<sub>3</sub> fragment adsorbed on different sites of the supported Ni<sub>4</sub> cluster, S(Ni<sub>4</sub>), are presented in Figure 5.5. The corresponding adsorption energies for these configurations are listed in Table 5.2. The results show that CH<sub>3</sub> bonded with Ni<sub>2</sub> atom located at the Ni<sub>4</sub>/ $\gamma$ -Al<sub>2</sub>O<sub>3</sub> interface, which can be referred to as the interface 1 adsorption site (int1), results in the most

stable configuration. It should be noted that CH<sub>3</sub> adsorption on the surface O and Al atoms close to Ni clusters were also studied. In addition, it was found that no stable adsorption configuration was found for CH<sub>3</sub> adsorption at the surface O site; e.g., when CH<sub>3</sub> is placed on top of O, it is pushed away. However, for CH<sub>3</sub> on top of the surface Al atom at the interface region, CH<sub>3</sub> was found moved toward the Ni atoms after geometry optimization forming three bonds with the Al and the two Ni atoms at the interface. The adsorption energy at this site is -2.13 eV. It is a little bit less stable than that at the int1 site where CH<sub>3</sub> is bonded with the Ni<sub>2</sub> atom only. To clarify the support's effects on the CH<sub>3</sub> adsorption properties, Hirshfeld charge analysis was used to determine the charge redistribution upon CH<sub>3</sub> adsorption at the top site (Ni<sub>1</sub>) and at the int1 site (Ni<sub>2</sub>). Comparison with CH<sub>3</sub> top adsorption was chosen, because in this adsorption configuration, CH<sub>3</sub> is bonded with a single Ni atom (Ni<sub>1</sub>) which is similar to the case of int1 adsorption. Note that the charge distribution for CH<sub>3</sub> at the interface 2 site (int2) was also reported (see Table 5.3). The results show that the charge on the CH<sub>3</sub> is -0.191e in the CH<sub>3</sub> top site adsorption. For the CH<sub>3</sub> int1 site adsorption, a charge of -0.291e was transferred to CH<sub>3</sub>. This gives rise to a strong ionic bonding between CH<sub>3</sub> and Ni, which results in a stronger adsorption at this interface site than that at the top site. A detailed analysis of the charges of the surface Al and O atoms shows that the total charges on the substrate surface (especially the Al<sub>1</sub> atom) are more positive when CH<sub>3</sub> is bonded with Ni<sub>2</sub> atom at the int1 site (see Table 5.3). This suggests that the Al<sub>1</sub> atom works primarily as a charge donation partner at the Ni<sub>4</sub>/γ-Al<sub>2</sub>O<sub>3</sub> interface when CH<sub>3</sub> is bonded with the Ni<sub>2</sub> atom. Similarly, the Ni<sub>2</sub> atom acts as a conduit for transferring negative charge to the adsorbate. Thus, the Al (donor)-Ni-CH<sub>3</sub> (acceptor) effect stabilizes the interface adsorption. For the CH<sub>3</sub> at the int2 site where CH<sub>3</sub> also is bonded with the surface Al<sub>3</sub> atom, a charge transfer from CH<sub>3</sub> to Al<sub>3</sub> atom was observed. This can also be explained by the Al (donor)-Ni-CH<sub>3</sub> (acceptor) effect. The only difference is that CH<sub>3</sub> is bonded with the surface Al atom at the other side of the formula, so it is like Al (donor)-Ni-CH<sub>3</sub> (acceptor)-Al (acceptor). Accordingly, the support's effect on the chemisorption properties of the supported metal particle depends on the synergy between the support-particle and the particle-adsorbate electron transfers. This result provides an explanation as to why the CH<sub>3</sub> adsorption energy increases more at the interface adsorption site than at the top adsorption site.

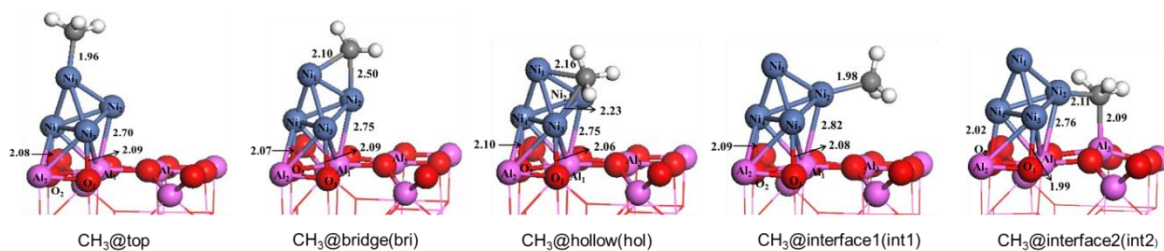


Figure 5.5 Side view of the stable configurations of CH<sub>3</sub> adsorbed on spinel type model of Ni<sub>4</sub>/γ-Al<sub>2</sub>O<sub>3</sub> (100) surface, S(Ni<sub>4</sub>). Bond lengths are in Å. Dark blue: Ni, white: H, Grey: C.

Table 5.2 The adsorption energies for CH<sub>3</sub> and H on the supported Ni<sub>4</sub>/ γ-Al<sub>2</sub>O<sub>3</sub> (100) complexes.

adsorbate	Spinel γ-Al <sub>2</sub> O <sub>3</sub>					Non-spinel γ-Al <sub>2</sub> O <sub>3</sub>				
	top	bri	hol	int1	int2	top	bri	hol	int1	int2
CH <sub>3</sub>	-1.55	-1.58	-1.25	-2.18	-2.13	-1.87	-1.75	-1.17	-2.04	-2.50
H	-1.71	-2.30	-2.21	-2.63	-2.96	-2.00	-2.41	-2.33	-2.34	-2.86

Table 5.3 Hirshfeld charges for CH<sub>3</sub> adsorbed on supported Ni<sub>4</sub>/  $\gamma$ -Al<sub>2</sub>O<sub>3</sub> (100) complexes.

CH <sub>3</sub> adsorption	Spinel $\gamma$ -Al <sub>2</sub> O <sub>3</sub>			Non-spinel $\gamma$ -Al <sub>2</sub> O <sub>3</sub>		
	top	int1	int2	top	int1	int2
CH <sub>3</sub>	-0.191	-0.291	-0.184	-0.211	-0.290	-0.125
Ni <sub>4</sub> (cluster)	0.535	0.581	0.585	0.272	0.225	0.305
Al <sub>1</sub>	0.319	0.358	0.325	0.420	0.420	0.465
Al <sub>2</sub>	0.367	0.355	0.386	0.475	0.513	0.529
Al <sub>3</sub>	0.446	0.474	0.387	0.509	0.513	0.435
O <sub>1</sub>	-0.314	-0.302	-0.307	-0.317	-0.315	-0.319
O <sub>2</sub>	-0.310	-0.318	-0.308	-0.368	-0.356	-0.368
O <sub>3</sub>				-0.354	-0.350	-0.340

The electronic factors that control the chemisorption were also corroborated using projected density of states (PDOS). This method can be used to analyze the electronic factors that stabilize CH<sub>3</sub> adsorption at the interface rather than at the top site. As shown in Figure 5.6, the bonding between CH<sub>3</sub> and the Ni atom is indicated by the overlap of the sp-orbital of C with the sp- and d-orbitals of Ni. This binding energy can be considered to have two components: one from the coupling to the metal sp states and the other due to the extra coupling to the d states [74-77]. The coupling to the d states produces a bonding and an antibonding state. As shown in Figure 5.6, there is an upshift of the orbitals (both Ni-d and C-sp) located around the Fermi energy when CH<sub>3</sub> is bonded with the Ni<sub>2</sub> atom at the int1 site. Note that comparisons were made between CH<sub>3</sub> top and the int1 site adsorption because in both of the adsorption configurations, CH<sub>3</sub> was bonded with a single Ni atom. As the orbitals shift up around the Fermi energy, a distinctive antibonding state appears above the band. Since these antibonding states are above the Fermi level, they are empty; therefore, the bond becomes stronger as the number of empty antibonding states increases. Moreover, it is observed that the bonding sp-levels of carbon shift to lower energies for the int1 site adsorption as compared to that in the top adsorption. This means that more bonding states are

occupied which contributed to the stronger adsorption energy at the interface site. Therefore, this analysis also supports the stronger adsorption energy of CH<sub>3</sub> observed at the interface than at the top site. The d-band analysis was conducted to provide a quantitative explanation of this phenomenon. Details about the d-band analysis method are presented in section 3.3.3, Chapter 3. According to the d-band model, the closer the  $\epsilon_d$  to the Fermi level, the more reactive the catalyst is expected to be. As shown in Table 5.4, the position of  $\epsilon_d$  for the top Ni<sub>1</sub> atom is identical to the Ni<sub>2</sub> atom at the support-Ni interface. Accordingly, it is expected that these two Ni atoms may have similar reactivity toward CH<sub>3</sub> adsorption. However, the adsorption energy results suggest that the bonding strength between CH<sub>3</sub> and Ni<sub>2</sub> at the int1 site is stronger than the one observed between CH<sub>3</sub> and Ni<sub>1</sub> at the top site, which implies that the Ni<sub>2</sub> atom at the metal support interface has a higher reactivity than that of the Ni<sub>1</sub> atom at the atop site. The calculation of the  $\epsilon_d$  for the two Ni atoms upon CH<sub>3</sub> adsorption show that the  $\epsilon_d$  for the Ni<sub>1</sub> atom in the CH<sub>3</sub> top adsorption is shifted from -1.20 to -1.59 eV, whereas the  $\epsilon_d$  for the Ni<sub>2</sub> atom is shifted from -1.20 to -1.33 eV (see Table 5.4). The down shift of the  $\epsilon_d$  for Ni<sub>2</sub> is smaller than that observed for Ni<sub>1</sub>. Note that down shift of  $\epsilon_d$  means the down shift of the average energy of the d-orbital that locates below the Fermi energy. As mentioned above, the charge analysis shows that there exists an electron transfer process from the substrate to the Ni cluster when CH<sub>3</sub> is bonded with the Ni<sub>2</sub> atom at the int1 site. Thus, it is suggested that this small  $\epsilon_d$  down shift is originated from the extra electron provided by the substrate. This result reflects the fact that the reactivity of the surface metal atom depends not only on its initial position of the d-band center, but also on the redistribution of the electrons between the metal cluster and the substrate upon the adsorption of the adsorbates (the substrate effect). Consequently, if the metal atoms are interacting with a particular substrate atom, then the d-band model may fail to predict the reactivity of the catalyst. Instead, the response of the local d-band to the presence of the adsorbate and substrate has to be taken into account.

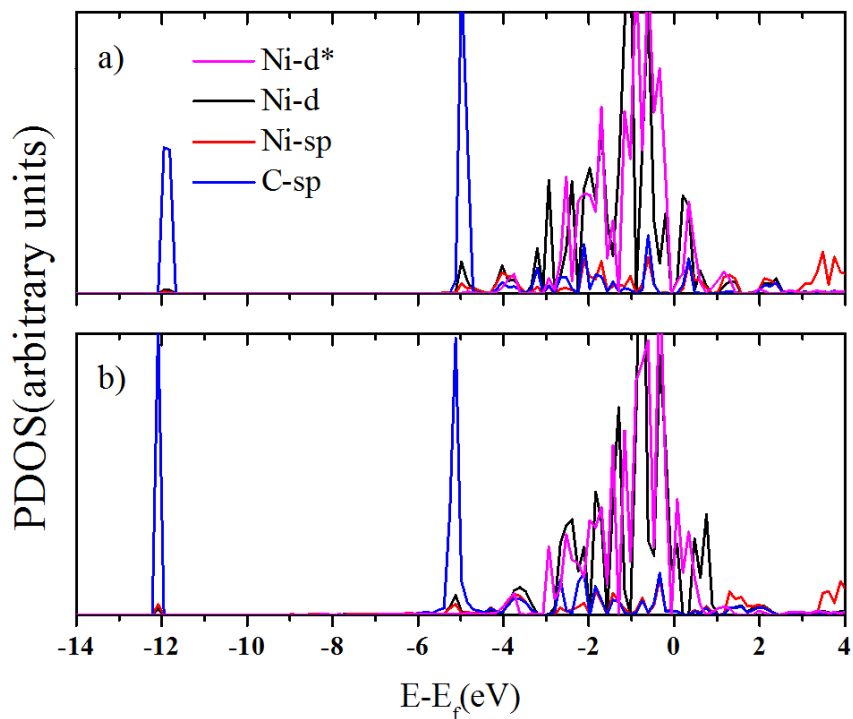


Figure 5.6 Projected density of states (PDOS) for C atom and the individual Ni atom involved in CH<sub>3</sub> adsorption on spinel type model of Ni<sub>4</sub>/γ-Al<sub>2</sub>O<sub>3</sub> (100) surface, S(Ni<sub>4</sub>): (a) top site adsorption (b) interface-1 (int1) adsorption. The pink line represents the d orbital of the individual Ni atom before CH<sub>3</sub> adsorption.

Table 5.4 The d-band energy (eV) of the Ni atoms involved in CH<sub>3</sub> and H adsorption at the top and int1 sites on the supported Ni<sub>4</sub> cluster.

	Spinel γ-Al <sub>2</sub> O <sub>3</sub>			Non-spinel γ-Al <sub>2</sub> O <sub>3</sub>		
	$\epsilon_d(\text{Ni})$	$\epsilon_d(\text{Ni}+\text{CH}_3^*)$	$\epsilon_d(\text{Ni}+\text{H}^*)$	$\epsilon_d(\text{Ni})$	$\epsilon_d(\text{Ni}+\text{CH}_3^*)$	$\epsilon_d(\text{Ni}+\text{H}^*)$
Ni <sub>1</sub> (top)	-1.20	-1.59	-1.51	-0.94	-1.32	-1.23
Ni <sub>2</sub> (int)	-1.20	-1.33	-1.28	-1.29	-1.37	-1.27

*Nonspinel Type Model.* CH<sub>3</sub> adsorption configurations on different sites of the NS(Ni<sub>4</sub>) are shown in Figure 5.7. The corresponding adsorption energies obtained from these configurations are shown in Table 5.2. As in the case of CH<sub>3</sub> adsorption on S(Ni<sub>4</sub>), no stable adsorption configuration was found for CH<sub>3</sub> adsorption at surface O site: it is pushed away after geometry optimization. The two CH<sub>3</sub> interface

adsorptions are found more stable than the top site adsorption. CH<sub>3</sub> int1 adsorption has an adsorption energy of  $-2.04$  eV. For CH<sub>3</sub> adsorption at the int2 site, where CH<sub>3</sub> bonded at the bridge site between Ni atoms with the surface Al at the interface, it has an adsorption energy of  $-2.50$  eV. It is more stable than that at the int1 site. In order to study the charge redistribution of the system upon CH<sub>3</sub> adsorption, Hirshfeld charges analyses were also performed for CH<sub>3</sub> top and two interface adsorptions on NS(Ni<sub>4</sub>). As shown in Table 5.3, the charge on the CH<sub>3</sub> is  $-0.211e$  in the CH<sub>3</sub> top site adsorption, whereas a charge of  $-0.290e$  was obtained when CH<sub>3</sub> is bonded with the Ni<sub>2</sub> atom at the int1 site. The charges on the surface Al and O atoms indicate that they are more positive (especially the Al atoms) for CH<sub>3</sub> int1 site adsorption when compared with that in CH<sub>3</sub> top adsorption. As in the spinel type model, this result indicates that the electrons are transferred from the substrate (mainly from the Al atoms) to the Ni cluster, and the adsorption strength was enhanced for CH<sub>3</sub> int1 adsorption due to the extra substrate-mediated electron transfer from the support to the adsorbates. For the CH<sub>3</sub> at the int2 site where CH<sub>3</sub> also is bonded with the surface Al<sub>3</sub> atom, a charge from CH<sub>3</sub> to Al<sub>3</sub> atom was also observed, as in the case of CH<sub>3</sub> int2 site adsorption on S(Ni<sub>4</sub>) model.

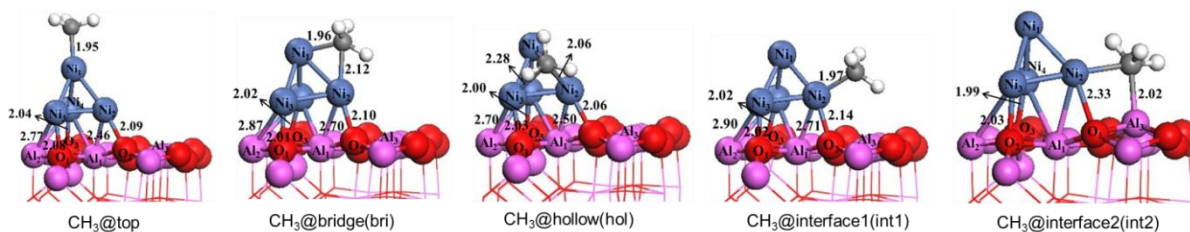


Figure 5.7 Side view for the stable configurations of CH<sub>3</sub> adsorbed on non-spinel type model of Ni<sub>4</sub>/ $\gamma$ -Al<sub>2</sub>O<sub>3</sub> (100) surface, NS(Ni<sub>4</sub>). Bond lengths are in Å. Dark blue: Ni, white: H, Grey: C.

Figure 5.8 shows the PDOS of the C-sp orbital for CH<sub>3</sub> adsorbed on Ni<sub>1</sub> atop site and on Ni<sub>2</sub> site on NS(Ni<sub>4</sub>), respectively. As in the case of CH<sub>3</sub> adsorption on S(Ni<sub>4</sub>), an upshift of the orbitals (both Ni-d and C-sp) located around the Fermi energy was observed when CH<sub>3</sub> is bonded with the Ni<sub>2</sub> atom at the int1 site. The calculated d band center ( $\epsilon_d$ ) of the Ni atoms involved in CH<sub>3</sub> adsorption at the top and int1 site are listed in Table 5.3. Before the adsorption of CH<sub>3</sub>, the  $\epsilon_d$  for the top Ni<sub>1</sub> atom is 0.35 eV higher than that of Ni<sub>2</sub> atom at the support-Ni interface. According to the d-band theory, the top Ni<sub>1</sub> atom may be more reactive toward CH<sub>3</sub> adsorption, which does not agree with the calculated adsorption energy results presented in Table 5.3. Thus, the d-band model may not be suitable to explain the evaluation of the

reactivity of the metal atoms when they are supported on the oxide substrate. Following the idea used in the spinel type model, the  $\varepsilon_d$  for Ni<sub>1</sub> and Ni<sub>2</sub> atom after CH<sub>3</sub> adsorption was calculated and shown in Table 5.4. A larger down shift of the  $\varepsilon_d$  (0.38 eV) for the Ni<sub>1</sub> atom in the CH<sub>3</sub> top adsorption was observed, as compared with that obtained for the Ni<sub>2</sub> atom (0.08 eV), which suggests that there is a stronger bonding strength of CH<sub>3</sub> at the interface which agrees with the DFT results obtained by the present study.

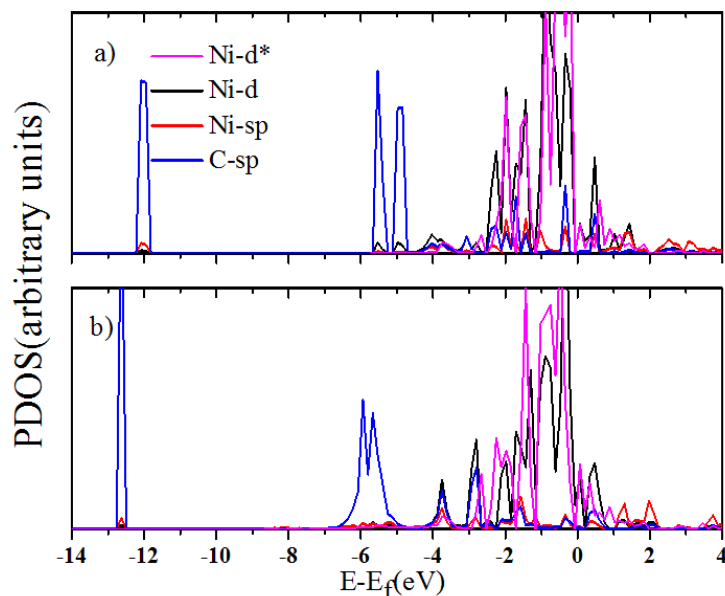


Figure 5.8 Projected density of states (PDOS) for C atom and the individual Ni atom involved in CH<sub>3</sub> adsorption on non-spinel type model of Ni<sub>4</sub>/γ-Al<sub>2</sub>O<sub>3</sub> (100) surface, NS(Ni<sub>4</sub>): (a) top site adsorption (b) interface 1 (int1) adsorption. The pink line represents the d orbital of the individual Ni atom before CH<sub>3</sub> adsorption.

### 5.3.2.2 H adsorption

*Spinel Type Model.* H adsorption on the different sites of the supported Ni<sub>4</sub> cluster was studied on S(Ni<sub>4</sub>). The adsorption configurations and their corresponding adsorption energies are shown in Figure 5.9 and Table 5.2, respectively. The results indicate that the most stable configuration is H bonded with the Ni<sub>2</sub> and Al<sub>3</sub> atoms at the metal support int2 site (−2.96 eV), and then followed by the int1 site adsorption (−2.63 eV). No stable adsorption configuration was found for H on top of O: H moved toward the Ni atoms after geometry optimization. Hirshfeld charge analysis shows that the charge transferred to

H was found to be  $-0.163e$  for the H–Ni<sub>1</sub> top adsorption whereas the charge transfer to H at the int1 site adsorption is  $-0.190e$ , as shown in Table 5.5. The Al1 atom at the H int1 site adsorption has the largest positive charge ( $0.339e$ ). This result shows that the Al1 atom facilitates the H adsorption at the interface by providing extra charges to the adsorbate. For the H at the int2 site, charge transfer from H to Al<sub>3</sub> atom was observed again, resulting a more positive charge on H and negative charge on Al<sub>3</sub>.

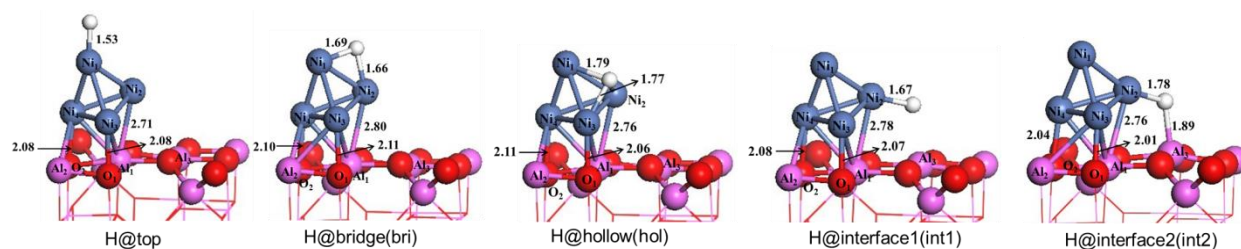


Figure 5.9 Side view for the stable configurations of H adsorbed on spinel type model of Ni<sub>4</sub>/γ-Al<sub>2</sub>O<sub>3</sub> (100) surface, S(Ni<sub>4</sub>). Bond lengths are in Å. Bond lengths are in Å. Dark blue: Ni, White: H.

Table 5.5 Hirshfeld charges for H adsorbed on supported Ni<sub>4</sub>/γ-Al<sub>2</sub>O<sub>3</sub> (100) complexes.

H adsorption	Spinel γ-Al <sub>2</sub> O <sub>3</sub>			Non-spinel γ-Al <sub>2</sub> O <sub>3</sub>		
	top	int1	int2	top	int1	int2
H	-0.163	-0.190	-0.172	-0.198	-0.221	-0.133
Ni <sub>4</sub>	0.492	0.522	0.554	0.234	0.281	0.330
Al <sub>1</sub>	0.320	0.339	0.322	0.424	0.430	0.452
Al <sub>2</sub>	0.369	0.372	0.388	0.475	0.511	0.526
Al <sub>3</sub>	0.447	0.430	0.387	0.511	0.512	0.451
O <sub>1</sub>	-0.314	-0.310	-0.309	-0.314	-0.316	-0.316
O <sub>2</sub>	-0.313	-0.311	-0.310	-0.367	-0.358	-0.369
O <sub>3</sub>				-0.352	-0.348	-0.344

PDOS of the Ni-d and H-s states for H adsorption on S(Ni<sub>4</sub>) are shown in Figure 5.10. This figure shows that there is a strong orbital mixing of s-orbital of H atom with the sp-orbital and the d-orbital of

the Ni atom, which is primarily in the range of  $-5$  to  $-1$  eV below the Fermi level. The upshift of the d-orbital around the Fermi level was also observed at the H interface adsorption. For the H top adsorption, a down shift of the d-orbital around the Fermi level was observed. The d-band center calculation shows that the  $\varepsilon_d$  of Ni<sub>2</sub> is shifted to  $-1.28$  eV after bonding with H, whereas the  $\varepsilon_d$  for the Ni<sub>1</sub> is shifted to  $-1.51$  eV. This result is in agreement with the increased binding energy of the H interface adsorption.

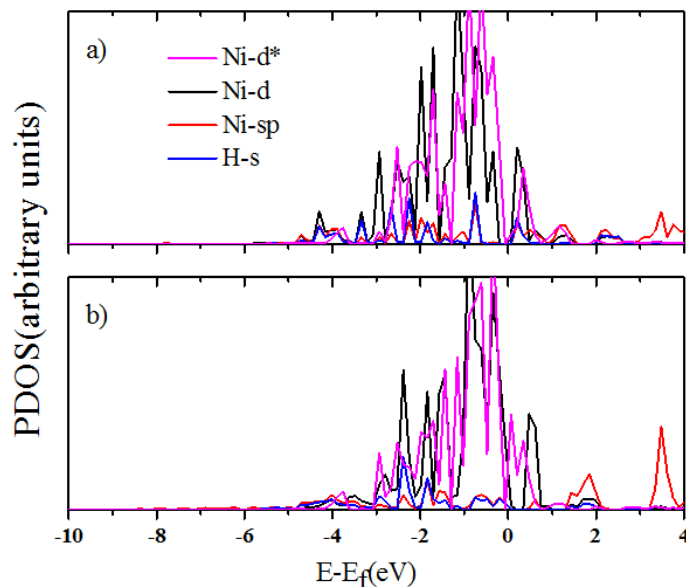


Figure 5.10 Projected density of states (PDOS) for H atom and the individual Ni atom involved in H adsorption on spinel type model of Ni<sub>4</sub>/γ-Al<sub>2</sub>O<sub>3</sub> (100) surface, S(Ni<sub>4</sub>): (a) top site adsorption (b) interface1 (int1) adsorption. Note that the Pink line represents the d orbital of the individual Ni atom before H adsorption.

*Nonspinel Type Model.* The adsorption configurations H on the NS(Ni<sub>4</sub>) are shown in Figure 5.11. The results of the adsorption energies shown in Table 5.2 indicate that H is more stable when bonded with the Ni<sub>2</sub> and Al<sub>3</sub> atoms at the metal support int2 site ( $-2.86$  eV) than the bridge site ( $-2.41$  eV) and the int1 adsorption site ( $-2.34$  eV). For H on top of O, similar results were found as in the case of S(Ni<sub>4</sub>) model: no stable adsorption configuration was found, H moved toward the Ni atoms after geometry optimization. Again, H adsorption at the Ni<sub>1</sub> top site is found less stable than the interface sites with an adsorption energy of  $-2.00$  eV. The Hirshfeld charge analysis results shown in Table 5.5 reveal a charge transfer of  $-0.168e$  to H adsorption when it is adsorbed at the top site. A larger amount of charge transfer ( $-0.208e$ ) was observed when H is adsorbed at the int1 site. Thus, it is expected that this large amount of charge

transfer to the H atom stabilizes the adsorbed complex at the interface. As in the spinel model, more positive charges on the surface Al and O atoms were observed when H is bonded with the Ni<sub>2</sub> atom at the int1 site, as compared with that in H top adsorption. This indicates that electrons are transferred from the substrate (mainly from the Al atom) to the Ni cluster for H interface adsorption, which increases the Ni–H adsorption strength. Figure 5.12 presents the PDOS for H adsorption on NS(Ni<sub>4</sub>). Figure 5.12b clearly shows an upshift of the d-orbital around the Fermi level when H is bonded with the Ni<sub>2</sub> atom at the metal-support interface. The calculated  $\epsilon_d$  shows a large down shift (0.29 eV) of the d band energy upon H top adsorption. However, a small upshift of 0.02 eV was observed for the Ni<sub>2</sub> atom, which explains the higher H adsorption detected at the interface.

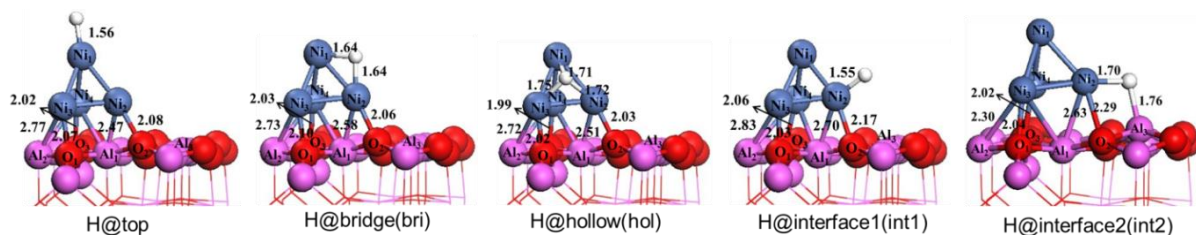


Figure 5.11 Side view for the stable configurations of H adsorbed on non-spinel type model of Ni<sub>4</sub>/γ-Al<sub>2</sub>O<sub>3</sub> (100) surface, NS(Ni<sub>4</sub>). Bond lengths are in Å. Dark blue: Ni, White: H.

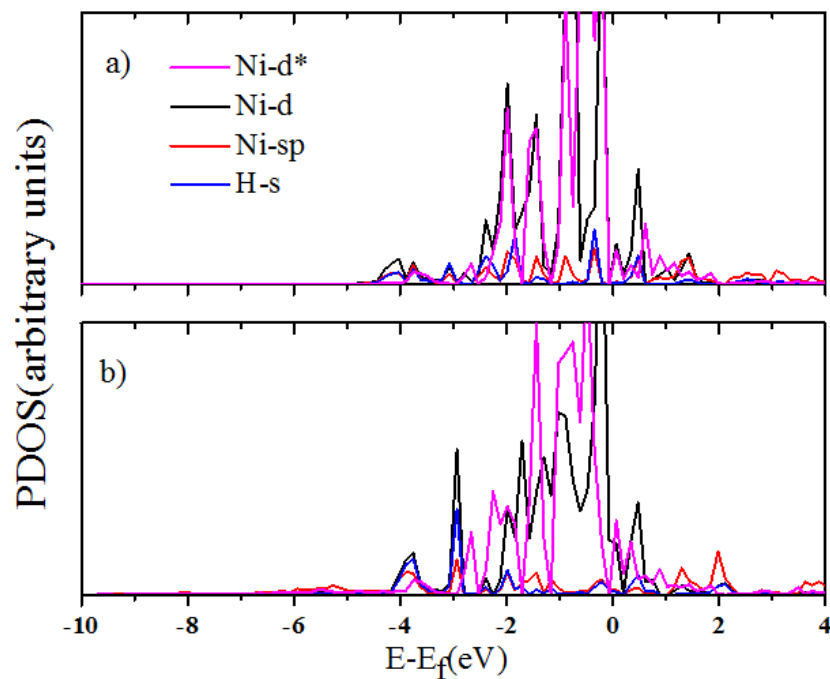


Figure 5.12 Projected density of states (PDOS) for H atom and the individual Ni atom involved in H adsorption on non-spinel type model of  $\text{Ni}_4/\gamma\text{-Al}_2\text{O}_3$  (100) surface, NS( $\text{Ni}_4$ ): (a) top site adsorption (b) interface 1 (int1) adsorption. The pink line represents the d orbital of the individual Ni atom before H adsorption.

To evaluate the size effect of the surface, the adsorption of  $\text{CH}_3$  and H on the top and the interface site on a  $1 \times 1$  unit cell of the nonspinel  $\gamma\text{-Al}_2\text{O}_3$  (100) surface model was also studied. In the  $1 \times 1$  unit cell of the nonspinel  $\gamma\text{-Al}_2\text{O}_3$  (100) surface model, the supported  $\text{Ni}_4$  cluster and the adsorbates are more close to the clusters and adsorbates in neighboring cells, as compared with that in the  $2 \times 1$  unit cell model. The results show that, as compared with the adsorption energies obtained on the  $2 \times 1$  unit cell of the nonspinel model,  $\text{CH}_3$  and H adsorption on the  $1 \times 1$  unit cell generally have smaller adsorption energies:  $\text{CH}_3$  adsorbed at the top site has a adsorption energy of  $-1.60$  eV and that at the interface site is calculated to be  $-1.83$  eV. For H, the adsorption energies at these two sites are  $-1.88$  and  $-2.43$  eV, respectively. The decrease of the adsorption energy may be due to the repulsion between nearest neighbor adsorbates because of the smaller size of the unit cell. This result also indicates that the interface adsorption is more stable than that on the top adsorption regardless of the unit cell size. Noted that the size effect on the spinel  $\gamma\text{-Al}_2\text{O}_3$  (100) surface model are not considered in the present study because of the computational limits while using the “TZP” basis set for larger unit cells.

The results for CH<sub>3</sub> and H adsorption show that, on both S(Ni<sub>4</sub>) and NS(Ni<sub>4</sub>), the CH<sub>3</sub> and H adsorption at the metal support interface is always preferred due to the Al (donor)–Ni–adsorbates (acceptor). The PDOS analysis for both models shows an upshift of the d-orbital around the Fermi energy when CH<sub>3</sub> and H are bonded with the Ni<sub>2</sub> atom at the interface. This upshift of the d-orbital pushes an antibonding state above the Fermi level that results in a strong bonding between Ni<sub>2</sub> and the adsorbates. The d band center ( $\epsilon_d$ ) analysis reveals that the d-band model may not be appropriate in prediction of the reactivity of the supported metal cluster, where the local density of states at the supported metal atoms is strongly perturbed by the presence of the adsorbate and the substrate. Accordingly, the effect of the adsorbate and the substrate, which causes the redistribution of the electrons between the metal cluster and the substrate upon the adsorption of the adsorbates, needs to be considered in the d-band analysis.

### 5.3.3 CH<sub>3</sub> and H adsorption on Ni<sub>5</sub>/ $\gamma$ -Al<sub>2</sub>O<sub>3</sub> (100)

The previous results were obtained on the supported Ni<sub>4</sub> cluster. In order to provide support of the results presented in this study, DFT calculations for CH<sub>3</sub> and H adsorption on a supported Ni<sub>5</sub> cluster were conducted. First, the Ni<sub>5</sub> cluster adsorption on the spinel and non-spinel type model of  $\gamma$ -Al<sub>2</sub>O<sub>3</sub> (100) surface was investigated. Figure 5.13 shows the most stable configuration obtained for Ni<sub>5</sub> cluster supported on the two models. In this configuration, four Ni atoms are in direct contact with the surface atoms. The charge analysis of the two models (see Table 5.6) shows that, as in the case of supported Ni<sub>4</sub> cluster, electrons are transferred from the Ni cluster to the alumina surface when the Ni<sub>5</sub> cluster is deposited on the  $\gamma$ -Al<sub>2</sub>O<sub>3</sub> (100) surface. The adsorption energies for CH<sub>3</sub> and H on the top and interface sites of this supported Ni<sub>5</sub> cluster were calculated. The results were presented in Table 5.7, and their corresponding adsorption configurations were shown in Figure 5.14–5.17. The results of these DFT calculations are as follows: (i) On the spinel type  $\gamma$ -Al<sub>2</sub>O<sub>3</sub> (100) model, S(Ni<sub>5</sub>), CH<sub>3</sub> adsorbed at the two interface sites are generally more stable than that at the top Ni<sub>5</sub> cluster site, the corresponding adsorption energies were –2.89 (int1 site), –2.17 (int2 site) and –2.14 eV respectively. It should be noted that, at the int1 site, CH<sub>3</sub> is bonded with the Ni<sub>2</sub> atom at the metal support interface. For the int2 site adsorption, CH<sub>3</sub> is bonded at the bridge site of Ni<sub>2</sub> and Ni<sub>3</sub> atoms. As shown in Table 5.7, similar results were obtained for H adsorption at these three sites: –2.93 eV at the int1 site, –2.62 eV at int2 site and –1.79 eV at the top site. (ii) On the non-spinel type  $\gamma$ -Al<sub>2</sub>O<sub>3</sub> (100) model, NS(Ni<sub>5</sub>), similar results were obtained for CH<sub>3</sub> and H adsorption as in the case of S(Ni<sub>5</sub>) model: CH<sub>3</sub> and H adsorbed at the interface sites are more stable than that at the top Ni<sub>5</sub> cluster site. Noted that at the int2 site adsorption in the NS(Ni<sub>5</sub>) model, the adsorbates are bonded with the Ni<sub>2</sub> atom and the surface Al atom at the interface. The CH<sub>3</sub> and H

adsorption at this int2 site is found most stable, which is consistent with the previous results obtained with the supported Ni<sub>4</sub> cluster model. Based on the above, it was concluded that the results for the studied even-numbered (Ni<sub>4</sub>) cluster and odd-numbered (Ni<sub>5</sub>) cluster were transferrable.

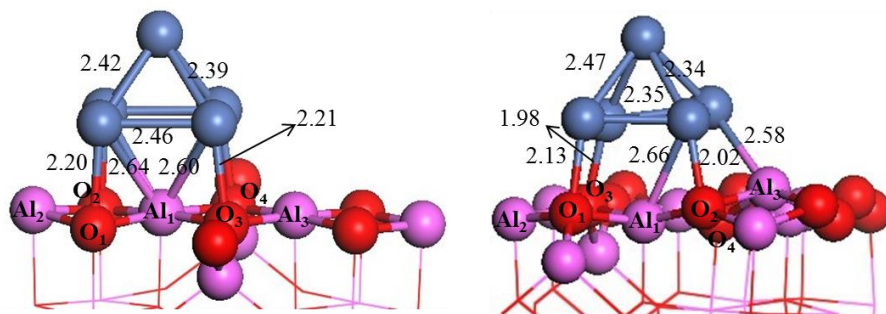


Figure 5.13 The optimized structure of Ni<sub>5</sub> cluster supported on the spinel (left) and non-spinel (right) type  $\gamma$ -Al<sub>2</sub>O<sub>3</sub> (100) surface. Bond lengths are in Å. Oxygen atoms are shown in red and aluminum atoms in magenta. Dark blue balls stand for Ni atoms.

Table 5.6 Hirshfeld charges of the supported Ni<sub>5</sub>/  $\gamma$ -Al<sub>2</sub>O<sub>3</sub> (100) complexes

	Spinel $\gamma$ -Al <sub>2</sub> O <sub>3</sub> : S(Ni <sub>5</sub> )		Non-spinel $\gamma$ -Al <sub>2</sub> O <sub>3</sub> : NS(Ni <sub>5</sub> )	
	$\gamma$ -Al <sub>2</sub> O <sub>3</sub>	Ni <sub>5</sub> / $\gamma$ -Al <sub>2</sub> O <sub>3</sub>	$\gamma$ -Al <sub>2</sub> O <sub>3</sub>	Ni <sub>5</sub> / $\gamma$ -Al <sub>2</sub> O <sub>3</sub>
Ni <sub>5</sub>		0.414		0.355
Al <sub>1</sub>	0.491	0.298	0.589	0.459
Al <sub>2</sub>	0.389	0.351	0.591	0.536
Al <sub>3</sub>	0.491	0.372	0.514	0.329
O <sub>1</sub>	-0.366	-0.319	-0.415	-0.329
O <sub>2</sub>	-0.366	-0.315	-0.419	-0.326
O <sub>3</sub>	-0.341	-0.301	-0.372	-0.327
O <sub>4</sub>	-0.269	-0.300	-0.337	-0.340

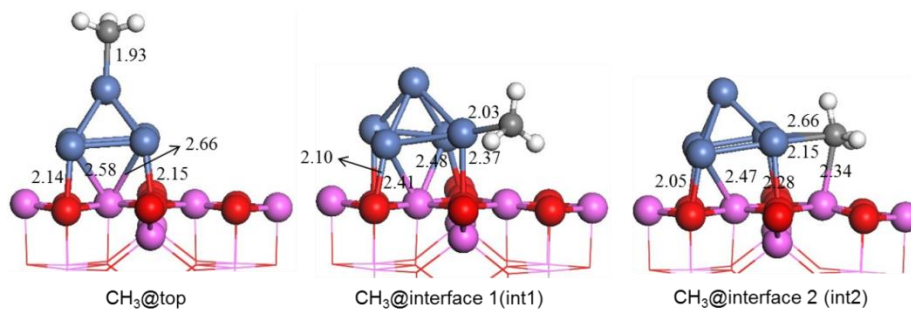


Figure 5.14 Side view for the stable configurations of CH<sub>3</sub> adsorbed on spinel type model of Ni<sub>5</sub>/γ-Al<sub>2</sub>O<sub>3</sub> (100) surface, S(Ni<sub>5</sub>). Bond lengths are in Å. Dark blue: Ni, white: H, Grey: C.

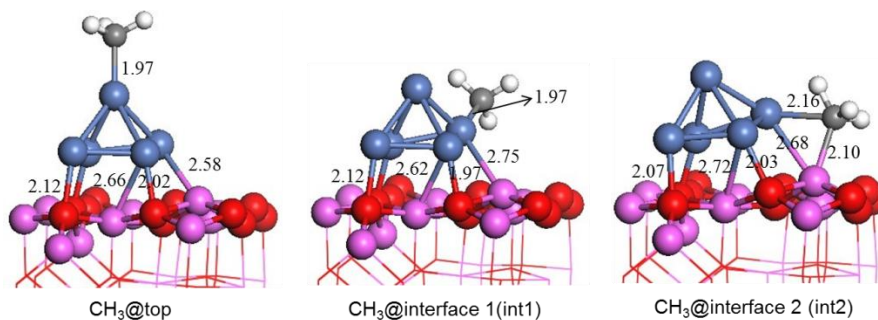


Figure 5.15 Side view for the stable configurations of CH<sub>3</sub> adsorbed on non-spinel type model of Ni<sub>5</sub>/γ-Al<sub>2</sub>O<sub>3</sub> (100) surface, NS(Ni<sub>5</sub>). Bond lengths are in Å. Dark blue: Ni, white: H, Grey: C.

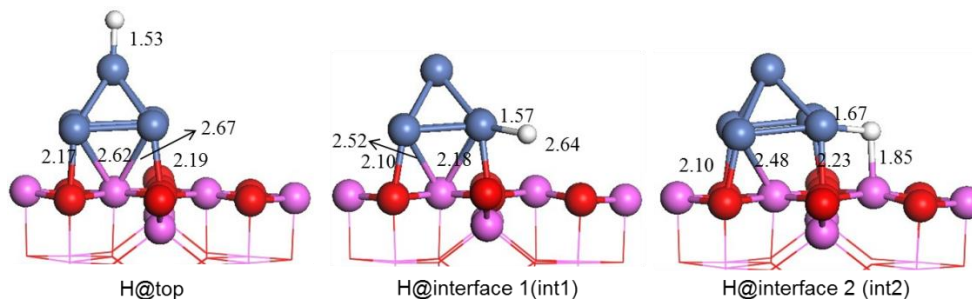


Figure 5.16 Side view for the stable configurations of H adsorbed on spinel type model of Ni<sub>5</sub>/γ-Al<sub>2</sub>O<sub>3</sub> (100) surface, S(Ni<sub>5</sub>). Bond lengths are in Å. Dark blue: Ni, white: H.

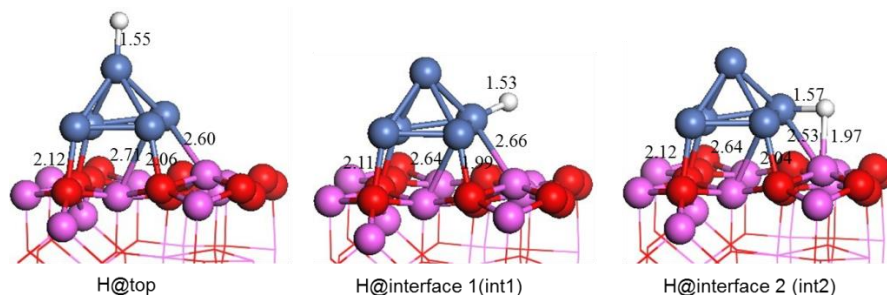


Figure 5.17 Side view for the stable configurations of H adsorbed on non-spinel type model of Ni<sub>5</sub>/γ-Al<sub>2</sub>O<sub>3</sub> (100) surface, NS(Ni<sub>5</sub>). Bond lengths are in Å. Dark blue: Ni, white: H.

Table 5.7 The adsorption energies for CH<sub>3</sub> and H on the supported Ni<sub>5</sub>/ γ-Al<sub>2</sub>O<sub>3</sub> (100) complexes

adsorbate	Spinel γ-Al <sub>2</sub> O <sub>3</sub>			Non-spinel γ-Al <sub>2</sub> O <sub>3</sub>		
	top	int1	int2	top	int1	int2
CH <sub>3</sub>	-2.14	-2.89	-2.17	-1.54	-1.85	-2.31
H	-1.79	-2.93	-2.62	-1.81	-2.29	-2.62

### 5.3.4 Metal-support interaction

In the present work, the metal support interaction ( $E_{MSI}$ ) upon CH<sub>3</sub> and H adsorption on both S(Ni<sub>4</sub>) and NS(Ni<sub>4</sub>) was analyzed. As mentioned in Section 5.2.1, the deposition of the Ni<sub>4</sub> metal cluster on S(Ni<sub>4</sub>) results in an  $E_{MSI}$  of -2.27 eV. Generally, a decrease of the  $E_{MSI}$  after CH<sub>3</sub> adsorption on the Ni<sub>4</sub> cluster was observed. As shown in Table 5.8, the  $E_{MSI}$  decreased to -1.97 eV after CH<sub>3</sub> adsorbed at the top of the Ni cluster whereas the  $E_{MSI}$  decreased to -2.22 eV in the CH<sub>3</sub> interface (int1) adsorption configuration. Similar results were obtained for the  $E_{MSI}$  upon H adsorption. The interaction between the Ni<sub>4</sub> cluster and the alumina support decreases after H adsorbed at the top, bridge, and hollow sites. However, the  $E_{MSI}$  was found to be slightly stronger (0.05 eV) after H adsorbed at the interface site. It is expected that this slight increase of  $E_{MSI}$  is due to the interaction between H and the surface Al atoms, in which a bonding distance of 2.53 Å was observed. For the NS(Ni<sub>4</sub>), the  $E_{MSI}$  results presented in Table 5.8 show that, as in the S(Ni<sub>4</sub>) model, the  $E_{MSI}$  decreases upon CH<sub>3</sub> and H adsorption on NS(Ni<sub>4</sub>). This result

shows that the bonding of adsorbates to the cluster affects the cluster structure and its bonding to the support. This is in agreement with a previous report that showed that, as the concentration of reactive intermediates on Ir<sub>4</sub> increases, the cluster-support interface and the metal-metal bond distance in the cluster were slightly modified during the hydrogenation reactions of ethene, propene, and toluene [78]. Experimental studies have observed that Ni nanoparticle detached from the alumina support and was pushed upward by the carbon nanotubes during its growth [54-56]. Thus, this decrease of metal support interaction found in the present DFT study might provide an explanation of the detachment of the Ni particle in the early stage of CNTs growth process.

Note that it was found that the changes in metal-support interactions are larger for weaker adsorption of CH<sub>3</sub> and H. This condition seems to have originated from the way that the metal-support interaction was calculated. From the definition of the adsorption energy of adsorbate X (eq 5.1) and the metal-support interaction in the present study, it is known that the adsorption energy represents the stability of the adsorption system. In addition, the difference of the metal–support interaction between two adsorption configurations, e.g., A and B, ( $\Delta E_{MSI(A-B)}$ ) can be calculated as follows:

$$\Delta E_{MSI(A-B)} = \Delta E(X-Ni_4/\gamma-Al_2O_3)_{(A-B)} - \Delta E(X-Ni_4)'_{(A-B)} - \Delta E(\gamma-Al_2O_3)'_{(A-B)}, \quad (5.3)$$

where  $\Delta E(X-Ni_4/\gamma-Al_2O_3)_{(A-B)}$  represents the difference between the adsorption energies of X for configurations A ( $E_{ads(A)}$ ) and B ( $E_{ads(B)}$ ), respectively;  $\Delta E(X-Ni_4)'_{(A-B)}$  and  $\Delta E(\gamma-Al_2O_3)'_{(A-B)}$  are the differences in energy for X–Ni<sub>4</sub> and  $\gamma$ -Al<sub>2</sub>O<sub>3</sub> between the two configurations. Our calculations show that  $\Delta E(X-Ni_4/\gamma-Al_2O_3)_{(A-B)}$  is the dominant term in eq. (5.2), which means that stronger adsorption at the metal support interface (a more stable adsorption configuration) results in a stronger metal support interaction.

Table 5.8 The metal support interaction ( $E_{MSI}$ , eV) upon CH<sub>3</sub> and H adsorption on S(Ni<sub>4</sub>) and NS(Ni<sub>4</sub>)

Adsorbate	Spinel $\gamma$ -Al <sub>2</sub> O <sub>3</sub>				Non-spinel $\gamma$ -Al <sub>2</sub> O <sub>3</sub>			
	top	bri	hol	int	top	bri	hol	int
CH <sub>3</sub>	-1.97	-1.98	-2.14	-2.22	-2.65	-2.51	-2.50	-2.55
H	-1.83	-1.93	-2.11	-2.32	-2.46	-2.62	-2.82	-2.38

\*The  $E_{MSI}$  for S(Ni<sub>4</sub>) before CH<sub>3</sub> and H adsorption is -2.27 eV and the  $E_{MSI}$  for NS(Ni<sub>4</sub>) before CH<sub>3</sub> and H adsorption is -2.79 eV

### 5.3.5 CH<sub>4</sub> and H<sub>2</sub> dissociation on Ni<sub>4</sub>/γ-Al<sub>2</sub>O<sub>3</sub> (100)

#### 5.3.5.1 CH<sub>4</sub> dissociation

*Spinel Type Model.* Based the adsorption results presented above, the present study focuses on CH<sub>4</sub> dissociation on the top Ni<sub>1</sub> atom and Ni<sub>2</sub> atom at the interface on S(Ni<sub>4</sub>). The potential energy profile following the dissociation pathway is presented in Figure 5.18. The configurations of the transition states and the product involved in the process are also shown in that figure. The results indicate that CH<sub>4</sub> on top of Ni<sub>1</sub> has adsorption energy of +0.04 eV, which shows the small repulsive nature of the forces between CH<sub>4</sub> and the supported Ni cluster. The study of the transition state (TS) suggests that CH<sub>4</sub> dissociation occurs at the Ni<sub>1</sub> atom and proceeds with a barrier of 0.85 eV. As show in Figure 5.18, the activated C–H bond (denoted as C–H<sub>a</sub> hereafter) is stretched to 1.82 Å at the TS. The C and H<sub>a</sub> atoms are both bonded with the Ni<sub>1</sub> atom with bond distances of 1.97 and 1.46 Å, respectively. The final configuration was CH<sub>3</sub> adsorbed on the top site and the H<sub>a</sub> atom at the neighbor bridge site (see Figure 5.18). The reaction energy obtained for this process was 0.36 eV. For CH<sub>4</sub> dissociation at the cluster oxide interface, it was found that CH<sub>4</sub> was physisorbed at the Ni<sub>2</sub> site with an adsorption energy of –0.13 eV. CH<sub>4</sub> dissociates on Ni<sub>2</sub> with an energy barrier of 0.71 eV. In the TS, the activated C–H<sub>a</sub> bond is stretched to 1.69 Å. The C and H<sub>a</sub> atoms are bonded with the top Ni atom with bond distances of 2.01 and 1.46 Å, respectively. The dissociation at this site is endothermic by 0.47 eV. These results reveal that CH<sub>4</sub> dissociation is preferred kinetically at Ni<sub>2</sub> site located at the nickel-alumina interface as compared with the top Ni<sub>1</sub> site.

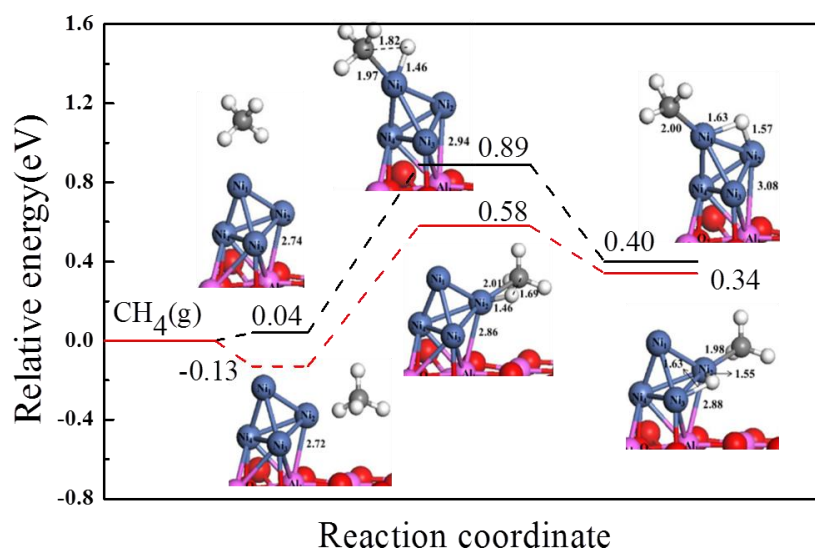


Figure 5.18 The potential energy profile and geometric structures of the initial state (I.S), transition state (T.S), and final state (F.S) for CH<sub>4</sub> dissociation on spinel type model of Ni<sub>4</sub>/γ-Al<sub>2</sub>O<sub>3</sub> (100) surface, S(Ni<sub>4</sub>), at the top site and interface. Dark blue (Ni), gray (C), white (H).

*Nonspinel Type Model.* The configurations for the CH<sub>4</sub> dissociation at the top and at the interface sites on NS(Ni<sub>4</sub>) are shown in Figure 5.19. The energy diagram of the reaction is also sketched in that figure. The results show that the CH<sub>4</sub> adsorption at the top Ni<sub>1</sub> site has an adsorption energy of -0.07 eV. The study of the transition state (TS) indicates that CH<sub>4</sub> dissociation at Ni<sub>1</sub> atom proceeds with a barrier of 1.08 eV. As show in Figure 5.19, the activated C-H<sub>a</sub> bond is stretched to 1.64 Å at the TS. The C and H<sub>a</sub> atoms are both bonded with the top Ni atom with bond distances of 1.99 and 1.55 Å, respectively. The final configuration was methyl adsorbed in the top site and the H<sub>a</sub> atom adsorbed in a neighbored hollow site. The reaction energy obtained for this dissociation process is 0.52 eV. For CH<sub>4</sub> interface dissociation, CH<sub>4</sub> was first adsorbed with an adsorption energy of -0.42 eV followed by its dissociation on the Ni<sub>2</sub> atom with an energy barrier of 0.76 eV. The activated C-H<sub>a</sub> bond is stretched to 1.58 Å in the TS. The C and H<sub>a</sub> atoms are bonded with the Ni<sub>2</sub> atom with bond distances of 2.03 and 1.56 Å, respectively. The dissociation at this site is endothermic by 0.39 eV. As in the spinel type model, the results found by the present study suggest that the dissociation of CH<sub>4</sub> at the metal support interface is much easier than at the Ni<sub>1</sub> top site.

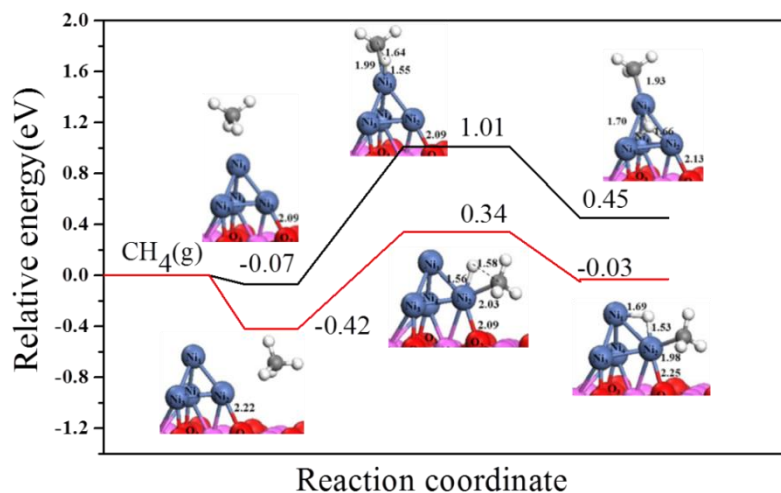


Figure 5.19 The potential energy profile and geometric structures of the initial state (I.S), transition state (T.S), and final state (F.S) for CH<sub>4</sub> dissociation on non-spinel type model of Ni<sub>4</sub>/γ-Al<sub>2</sub>O<sub>3</sub> (100) surface, NS(Ni<sub>4</sub>), at the top site and interface. Dark blue (Ni), gray (C), white (H).

### 5.3.5.2 H<sub>2</sub> dissociation

*Spinel Type Model.* The energy profile and structures for the dissociation of H<sub>2</sub> on S(Ni<sub>4</sub>) is presented in Figure 5.20. As shown in that figure, H<sub>2</sub> was found adsorbed on the Ni<sub>1</sub> top site with an adsorption energy equal to -0.10 eV. Optimization of the isolated H<sub>2</sub> molecule resulted in a value of 0.79 Å for the H–H bond length. The equilibrium geometry of the adsorbed H<sub>2</sub> molecule shows that the H–H bond length is 0.82 Å, which suggests the existence of a precursor state for the H<sub>2</sub> dissociative adsorption [79]. For H<sub>2</sub> adsorption at the Ni<sub>2</sub> atom located at the metal-support interface, it was found that H<sub>2</sub> was physisorbed with a H–H distance of 0.89 Å. The corresponding adsorption energy was -0.25 eV. As shown in Figure 5.20, when the activation of H<sub>2</sub> occurs at the top Ni<sub>1</sub> atom, the activated H<sub>a</sub> atom points toward the adjacent bridge site in the TS. The calculations show that the H–H<sub>a</sub> bond distance stretched from 0.82 Å at the initial state to 1.47 Å at the TS. The H and H<sub>a</sub> atoms are bonded with the Ni<sub>1</sub> atom with bond distances of 1.53 Å. The activation barrier obtained for this top site dissociation is 0.49 eV and is endothermic by 0.18 eV. In the TS for H<sub>2</sub> dissociation at the interface, the H–H<sub>a</sub> bond distance was stretched to 1.56 Å, whereas the two H–Ni distances were found to be 1.50 and 1.52 Å, respectively. The dissociation barrier is 0.31 eV, which indicates that the H<sub>2</sub> dissociation on S(Ni<sub>4</sub>) interface is favored as compared to that on the Ni<sub>1</sub> top site.

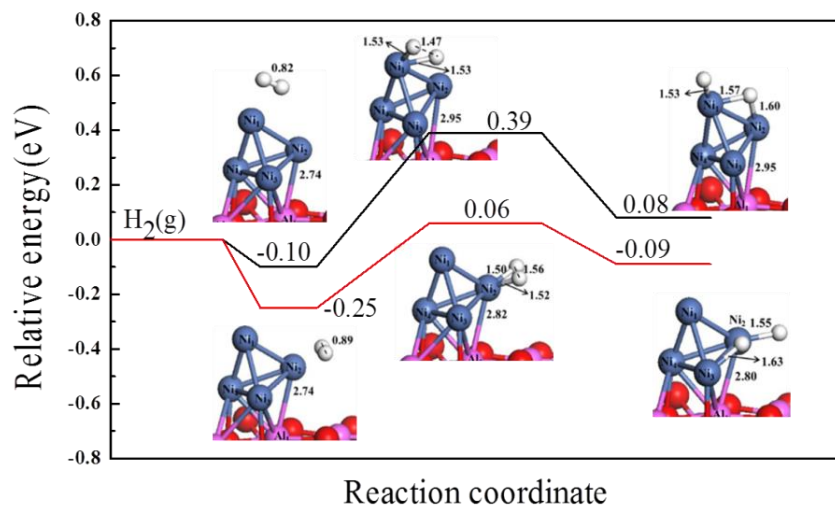


Figure 5.20 The potential energy profile and geometric structures of the initial state (I.S), transition state (T.S), and final state (F.S) for  $H_2$  dissociation on spinel type model of  $Ni_4/\gamma-Al_2O_3$  (100) surface,  $S(Ni_4)$ , at the top site and interface. Dark blue (Ni), white (H).

*Nonspinel Type Model.* The pathway for  $H_2$  dissociation on the top and interface sites on the  $NS(Ni_4)$  surface was also studied in this work. The structures of the transition states and products and the potential energy profile are presented in Figure 5.21. The results indicate that  $H_2$  adsorbed at the top  $Ni_1$  site is a precursor state with a H–H bond length of 0.84 Å and with an adsorption energy of –0.11 eV. As show in Figure 5.21, the activated  $H_a$  atom points toward the adjacent bridge site in the TS; the H– $H_a$  bond is stretched to 1.17 Å. The study of the energy profile indicates that  $H_2$  dissociation at  $Ni_1$  atom has a barrier of 0.31 eV. The final configuration was H adsorbed at the top site and the  $H_a$  atom adsorbed in a neighboring bridge site. The reaction energy obtained for this dissociation process is –0.14 eV. For  $H_2$  dissociation at the metal–support interface, it was found that the precursor state of  $H_2$  is strongly bonded with  $Ni_2$  atom with a H–H bond length of 1.01 Å. In the TS for  $H_2$  dissociation at  $Ni_2$  atom, the H– $H_a$  bond distance was stretched to 1.31 Å whereas the two H–Ni distances were found to be 1.53 and 1.54 Å, respectively. The dissociation barrier is 0.16 eV, which indicates that the  $H_2$  dissociation on  $NS(Ni_4)$  interface is favored as compared to that on the top  $Ni_1$  site (0.31 eV). Note that this dissociation step at the interface is slightly exothermic by 0.13 eV.

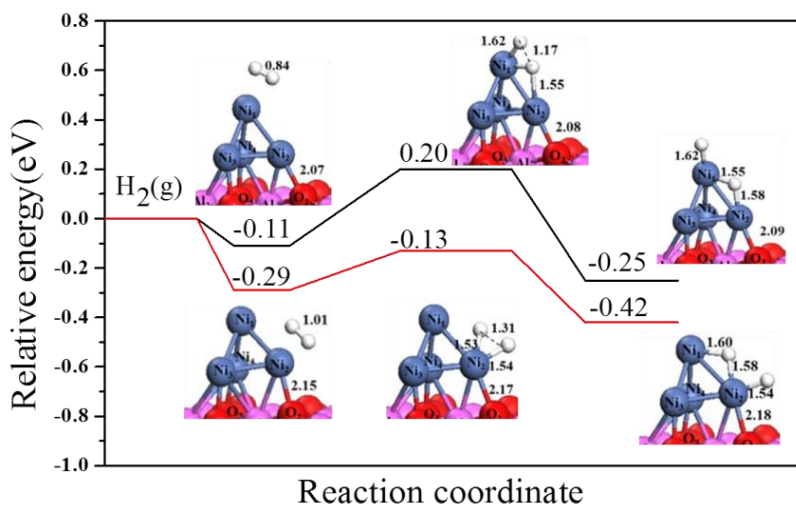


Figure 5.21 Geometric structures of the initial state (I.S), transition state (T.S), and final state (F.S) for  $H_2$  dissociation on the top and interface site of the  $Ni_4/\gamma-Al_2O_3$  (100). Dark blue (Ni), gray (C), white (H).

Our previous DFT study has found that  $CH_4$  dissociation on Ni (111) surface is also an endothermic process (0.91 eV) [16]. However, it has a much higher activation barrier (1.31 eV). It is much higher than that obtained on  $Ni_4/\gamma-Al_2O_3$  (100) top Ni site (1.08 eV) and interface site (0.71 eV). It is believed that this is a result of the increase of metal coordination from 3 neighbors for the tetramer to 9 Ni neighbors on the (111) surface, since transition metals generally exhibit greater reactivity in an environment with low coordination number [80]  $H_2$  dissociation on single crystal Ni (111) surface was found exothermic by  $-0.71$  eV. The energy barrier for  $H_2$  dissociation on single crystal Ni (111) surface is calculated to be 0.29 eV.

## 5.4 Summary

In the present study, the dissociation of  $CH_4$  and  $H_2$  on  $Ni_4$  supported on  $\gamma-Al_2O_3$  (100) catalyst was investigated using density functional theory (DFT) slab calculations. Two systems:  $Ni_4$  cluster supported on the spinel model of  $\gamma-Al_2O_3$  (100) surface,  $S(Ni_4)$ , and on the nonspinel model of  $\gamma-Al_2O_3$  (100) surface,  $NS(Ni_4)$ , have been used to model  $Ni_4/\gamma-Al_2O_3$ . The dissociation barriers and the adsorption properties of the  $CH_3$  and H species using these two models were studied. The insights gained by the present modeling study are as follows:

*i)* On S(Ni<sub>4</sub>), CH<sub>3</sub> and H bonded with the Ni<sub>2</sub> atom at the metal-support interface are the most stable configurations with adsorption energies of -2.18 and -2.96 eV, respectively. On NS(Ni<sub>4</sub>), CH<sub>3</sub> interface adsorption (-2.50 eV) was found to be the most stable structure. For H on NS(Ni<sub>4</sub>), the results show that H bonded with the Ni<sub>2</sub> atom at Ni<sub>4</sub>/γ-Al<sub>2</sub>O<sub>3</sub> interface is still preferred as compared with the Ni<sub>1</sub> top site adsorption on NS(Ni<sub>4</sub>). Hirshfeld charge and PDOS analysis were conducted to provide support of the higher reactivity of the Ni<sub>2</sub> atom located at the nickel-alumina interface, as compared with the top Ni<sub>1</sub> atom. The Hirshfeld analysis of the charges of the surface Al and O atoms showed that the Al atom works primarily as a charge donation partner. Thus, it is expected that the interface adsorption is stabilized by the Al (donor)-Ni-adsorbates (acceptor) effect. The PDOS analysis showed an upshift of the d-orbital around the Fermi energy when CH<sub>3</sub> and H are bonded with the Ni<sub>2</sub> atom at the interface, which pushes the antibonding state above the Fermi level and results in a strong bonding between the Ni<sub>2</sub> atom and the adsorbates.

*ii)* The decrease of the metal support interaction was also observed upon CH<sub>3</sub> and H adsorption on both S(Ni<sub>4</sub>) and NS(Ni<sub>4</sub>). The present study shows that the bonding of adsorbates to the cluster affects the cluster structure and its bonding to the support, resulting in a decrease in the metal-support interaction. This observation might provide insight regarding the interaction between the Ni and the γ-Al<sub>2</sub>O<sub>3</sub> support and the carbon nanotube growth mechanism, in which the weak metal-support interaction is believed to contribute to the tip growth mode of CNTs.

*ii)* The potential energy profile and the transition states following the CH<sub>4</sub> and H<sub>2</sub> dissociation on Ni<sub>4</sub> supported on γ-Al<sub>2</sub>O<sub>3</sub> (100) were identified. On S(Ni<sub>4</sub>), CH<sub>4</sub> dissociates at the interface Ni<sub>2</sub> site with an energy barrier of 0.71 eV, which is lower when compared to that obtained at the Ni<sub>1</sub> top site (0.85 eV). For the H<sub>2</sub> dissociation, the dissociation barrier (0.49 eV) at the Ni<sub>1</sub> top site is higher than that obtained at the Ni<sub>2</sub> site (0.31 eV). Similar results were obtained for the dissociation of CH<sub>4</sub> and H<sub>2</sub> on NS(Ni<sub>4</sub>), i.e., the activation barrier for CH<sub>4</sub> and H<sub>2</sub> dissociation are 1.08 and 0.31 eV, respectively, whereas those at the interface are 0.76 and 0.16 eV, respectively. Although the alumina surface was modeled using two different structures, i.e., spinel and nonspinel models, the results obtained by the present study were consistent and reached the same conclusion: the metal-oxide interface plays an essential role in the dissociation of CH<sub>4</sub> and H<sub>2</sub> on the nickel cluster.

## Chapter 6

### Effects of Metal Elements in Catalytic Growth of Carbon Nanotubes/Graphene

This chapter presents a DFT study on the effect of metal elements in the growth of CNTs/graphene. This effect is analyzed in term of the reactivity of transition metals (Fe, Ni, Co, Cu) towards  $\text{CH}_x$  dissociation, carbon diffusion together with C–C bond coupling reactions. The result obtained from the DFT calculations indicates that Cu may be an appropriate catalyst for the CVD synthesis of high quality graphene. The study also provides support for the fact that Ni-based catalyst is a suitable CVD substrate for growing CNT. The study is organized as follows: the first section presents an introduction of this study. In section 6.2, the models and computational details are described. The calculated activation energies for each elementary step are described in section 6.3. The analysis and discussion of the results are also present in this section. Concluding remarks are presented in section 6.4.

#### 6.1 Introduction

Carbonaceous nanomaterials, e.g. carbon nanotubes (CNTs) and graphene have received an intense research interest due to their extraordinary physical and chemical properties and their potential applications in the industry [1-3]. These materials have been typically synthesized using Chemical Vapor Deposition (CVD), a process on which the carbon atoms are sourced from hydrocarbon gas (methane, ethylene) decomposition over supported transition metal nanoparticles (Fe, Co, Ni or Cu) [4-6]. In fact, the decomposition of the carbon precursors on the metal surface is only the first step in the growth of CNTs/graphene. This is followed by four important processes: (i) carbon diffusion on the nanoparticle surface [7-9] or through the bulk of the catalyst [10-12]; (ii) carbon incorporation into the graphene overlayers on the other side of the catalyst particle producing CNTs; (iii) at the same time, the surface C atoms nucleate together on the metal surface forming graphitic fragments; (iv) as the carbon fragments nucleation continues, it will finally leads to the catalyst deactivation. The reactivity of the catalyst towards the C–H bond breaking reactions dominates the CNTs/graphene growth rate by producing C atoms. Meanwhile, one can expect that the catalyst that provides high nucleation barrier for the surface C atoms will be more resistant to catalyst deactivation. Similarly, if the surface carbon atoms also have good mobility on the catalyst, they are more likely to diffuse to the metal/CNTs edges thus making the catalyst

a suitable substrate for the growth of CNTs. On the other hand, if both C nucleation and surface diffusion are facilitated on the catalyst surface, the surface C atoms will tend to be more uniformly distributed and nucleate easily on the catalyst surface, making this catalyst suitable for graphene production. Therefore, by studying the catalyst reactivity towards C–H bond activation, C diffusion as well as the nucleation kinetics of surface C atoms, a suitable metal alloy can be designed so that it enhances the growth of either CNTs or graphene.

In the past decades,  $\text{CH}_x$  species dissociations on various transition metals (and their corresponding alloys) have been extensively studied [13-21]. Theoretical studies for carbon behavior on transition metals (i.e. Pd, Pt, Ni, Cu) are also available in the literature [22-26]. These theoretical studies have been mostly focused on the adsorption and diffusion characteristics of different carbon species (mainly monomer and dimer) at different surface sites. Thermodynamics of graphene growth on Cu and Ni surfaces have also been reported [27,28]. However, the kinetic properties for carbon atoms nucleation reactions have rarely been studied, i.e., only few studies on the carbon nucleation kinetics on Ni (111) surface are available [29, 30]. Moreover, a comparative study of the C–C bonding kinetics on transition metals is not currently available in the literature. More importantly, the reactivity of the metal catalyst for  $\text{CH}_x$  decomposition or C diffusion by itself cannot be used to explain its activity towards the growth of CNTs/graphene product. Instead, the  $\text{CH}_x$  dissociation, carbon diffusion and C–C bonding kinetics need to be considered together in the analysis to evaluate the reactivity of different catalyst towards CNTs/graphene. As mentioned above, the most suitable catalysts for CNT/graphene growth are those that promote C–H activation with a balanced reactivity towards surface C diffusion and C–C nucleation reactions. The latter raises the question about the effect of metal in the catalytic growth of CNTs/graphene, which has been usually explained by the different solubility (or diffusivity) of C in the metals. A few studies have stated that, due to the strong C–Ni bonding, surface C atoms may easily dissolve in the bulk Ni and precipitate on the other side of the particle promoting the formation of CNTs [31-34]. In the case of Cu, carbon atoms will remain on the surface (due to its small solubility in Cu) leading to the growth of graphitic materials [35]. Nevertheless, the metal reactivity towards C–H activation, C diffusion and C–C nucleation kinetics, which are the critical steps in the catalytic CNTs/graphene growth, were not discussed in those studies. A comparative study of metal reactivity towards these critical processes may provide new insights on the effect of metals in the catalytic CNTs/graphene growth.

In the present study, the role of transition metals (Fe, Ni, Co, Cu) in the growth of CNTs/graphene in CVD is investigated using DFT analysis. To the authors' knowledge, the first comparative DFT study on carbon atoms nucleation kinetics on different transition metals is presented here. Moreover, the C–H bond activation, carbon diffusion together with C–C bonding are investigated together in this study to evaluate the reactivity of different catalyst towards CNTs/graphene growth. Note that since either CH<sub>4</sub> dissociative adsorption or CH dehydrogenation is usually considered as the rate-determining step in methane dissociation [10,36], only the first and the last step (CH dissociation) were considered in this work. The present study provides insights toward the optimal design of catalyst alloys for CNTs/graphene growth in the CVD process.

## **6.2 Computational details**

### **6.2.1 Calculation methods**

The DFT calculation method used in the present study is the same from that in section 3.2.1, Chapter 3.

### **6.2.2 Surface models**

The catalyst surfaces were simulated using the slab super-cell approach with periodic boundary conditions. The lowest energy (111) facets [37], which usually dominate the surfaces of metal nanoparticles [38], are considered in this work. The (111) surfaces were constructed using the calculated equilibrium lattice constants of 2.857 Å (Fe), 3.508 Å (Co), 3.519 Å (Ni), and 3.668 Å (Cu). These estimates agree well with the experimental values of 2.867 Å (Fe), 3.545 Å (Co), 3.524 Å (Ni), and 3.615 Å (Cu) reported in the literature [39]. The Co, Ni and Cu metals with a face centered cubic (fcc) crystal structure were modeled using a three-layer slab with 3×3 unit cell. Note that the three-layer slab was chosen due to the computational limitation while conducting STO-DFT calculations, however, the convergence of using a three-layer slab can be supported by our previous study, where CH<sub>x</sub> adsorption on Ni (111) with 3 and 4-layer 2×2 unit cell was compared [18]. Since the fcc metals structures are very similar to each other, only the Ni (111) surface is presented in Figure 6.1a. Among the 3 layers of metal atoms, the bottom layer was frozen and top 2 metal layers and the adsorbates were allowed to relax during the DFT calculations. The body centered cubic (bcc) Fe (111) surface (Figure 6.1b) was simulated with a six-layer 3×2 slab with the bottom two layers frozen.

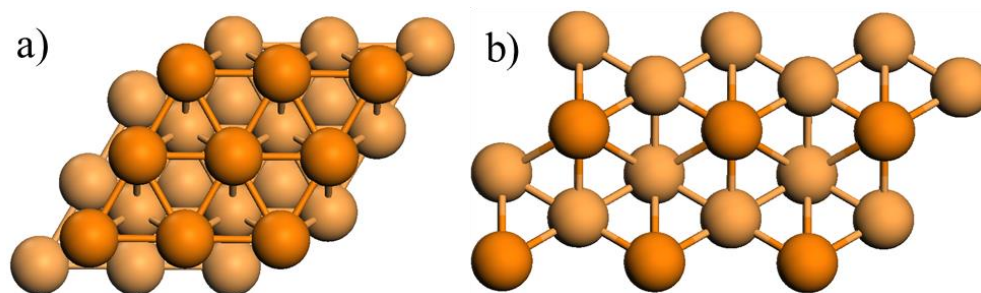


Figure 6.1 Top views of the (111) surfaces of the a) Ni metal; b) Fe metal. Note that the first layer atoms are in darker color.

## 6.3 Results and discussion

### 6.3.1 Dehydrogenation energetics

The dehydrogenation of  $\text{CH}_4$  and  $\text{CH}$  on the (111) surfaces of various transition metals was first studied to understand their catalytic reactivity towards the production of C atoms. Figures 6.2a and 6.3a show the TS for  $\text{CH}_4$  and  $\text{CH}$  dehydrogenation on Fe (111), respectively. The observed TS for both  $\text{CH}_4$  dissociative adsorption and  $\text{CH}$  dehydrogenation on the Co and Ni are quite similar. Therefore, only the TS on Ni (111) is shown here for brevity in Figures 6.2b and 6.3b, respectively. In almost all cases,  $\text{CH}_4$  and  $\text{CH}$  dissociation occurs over the top site, with a single dissociating H atom pointing towards the surface. Note that the TS for  $\text{CH}$  decomposition found on Cu is different from that on Co and Ni surfaces. On Cu (111), the breaking C–H bond is oriented towards the bridge site as shown in Figure 6.3c. The calculated activation energies and some key geometric parameters are listed in Table 6.1.

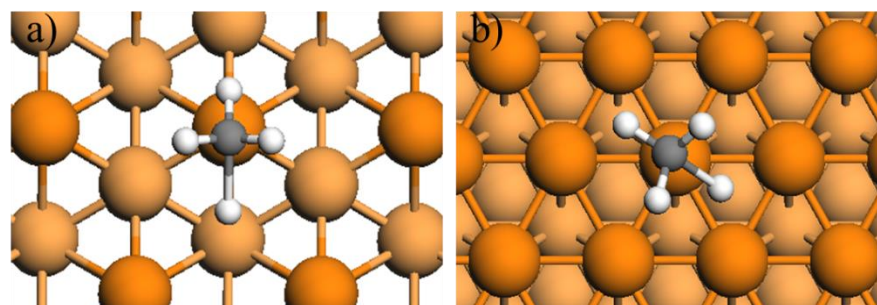


Figure 6.2 Sketches of the TS for  $\text{CH}_4$  dissociation on the (111) surfaces of the a) Fe; b) Ni.

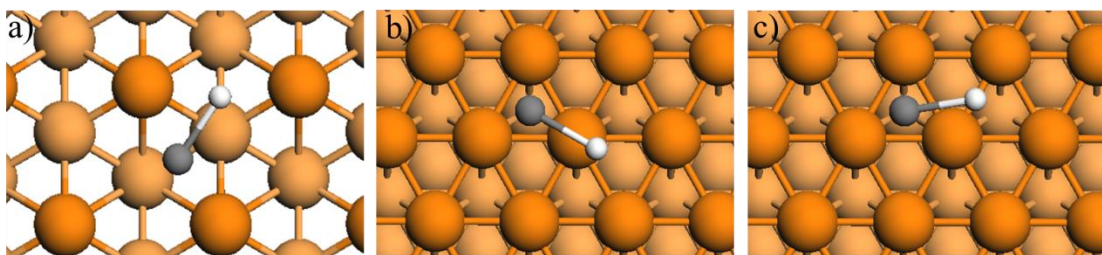


Figure 6.3 Sketches of the TS for CH dissociation on the (111) surfaces of the a) Fe; b) Ni; c) Cu.

Table 6.1 Activation energy,  $E_a$  (eV), for the dissociation of  $\text{CH}_4$  and CH on the (111) surfaces of Fe, Co, Ni and Cu. Distances between detached  $\text{H}_a$  and C ( $d_{\text{C}-\text{H}_a}$ ) and the nearest Metal ( $d_{\text{M}-\text{H}_a}$ ) in the TS of each elementary reaction step are also shown.

Surface	$\text{CH}_4 \rightarrow \text{CH}_3 + \text{H}$			$\text{CH} \rightarrow \text{C} + \text{H}$		
	$E_a$ (eV)	$d_{\text{C}-\text{H}_a}$ (Å)	$d_{\text{M}-\text{H}_a}$ (Å)	$E_a$ (eV)	$d_{\text{C}-\text{H}_a}$ (Å)	$d_{\text{M}-\text{H}_a}$ (Å)
Fe	0.67	1.61	1.63	0.59	1.49	1.69
Co	1.34	1.64	1.58	1.34	1.65	1.53
Ni	1.15	1.62	1.58	1.17	1.74	1.51
Cu	1.95	1.84	1.64	2.06	1.92	1.64

As shown in Table 6.1, the most reactive catalyst for methane dissociative adsorption is Fe, with an activation energy barrier of 0.67eV. Ni is the second more reactive metal of those studied here. The corresponding activation energy on Ni (111) is calculated to be 1.15eV. In the case of Co, the  $\text{CH}_4$  dissociation barrier is 0.20eV higher than that on Ni. The activation energies of  $\text{CH}_4$  on Cu are notably high (about 1.95eV). Thus, dissociation of  $\text{CH}_4$  to surface  $\text{CH}_3$  and H is challenging on Cu. Similar results were obtained for CH dehydrogenation, i.e., the calculated dissociation barriers among these metals vary in the order: Fe (0.59eV) < Ni (1.17eV) < Co (1.34eV) < Cu (2.06eV). This corresponds to the order of the catalytic activities over the metals in C–H bond activation (Fe > Ni > Co > Cu), which is consistent with the metal reactivity

estimated by the d-band center calculation. The d-band center is defined as the average energy of the d-band, and is thus calculated from the projected density of states on the surface atoms [40]. The closer the d-band center to the Fermi level, the more reactive the catalyst metal is expected to be. In the present study, the calculated d-band centers of Fe, Co, Ni and Cu are -1.73, -2.12, -1.80 and -2.54 eV, respectively. This result explains the higher reactivity of Fe, Ni, Co toward C–H activation as compared with Cu.

### 6.3.2 Mobility of C monomers

The first step towards a buildup of carbon on the surface is the diffusion of adsorbed C atoms. A low energy barrier for C atom surface diffusion on the catalyst surface always favors the CNTs/graphene growth process in CVD. The diffusion barriers for monoatomic carbon on metallic nanoparticles are listed in Table 6.2. These results show that diffusion of C on Fe (111) is the most difficult, with a diffusion barrier of 1.05eV. On the other hand, C is found to be highly mobile on the (111) surfaces of Co (0.36eV), Ni (0.29eV) and especially on the Cu (111) surface (0.11eV). However, this barrier alone is not an appropriate measure for the coupling of C atoms to form various C compounds. Hence, it is also necessary to determine the barriers for C–C coupling reactions.

Table 6.2 Carbon monomer (C) diffusion barriers and activation energy,  $E_a$ (eV), for carbon dimer ( $C_2$ ) and trimer ( $C_3$ ) nucleation on the (111) surfaces of Fe, Co, Ni and Cu. Distances between activated C–C bond ( $d_{C-C}$ , Å) in the TS are also shown.

Metal	C diffusion	C+C→C <sub>2</sub>			C <sub>2</sub> +C→C <sub>3</sub>		
	$E_{diff}$	$E_{a,for}$	$E_{a,back}$	$d_{C-C}$	$E_{a,for}$	$E_{a,back}$	$d_{C-C}$
Fe	1.05	1.15	1.88	1.80	1.37	0.52	2.21
Co	0.36	0.86	1.70	1.98	0.86	1.65	2.09
Ni	0.29	0.84	1.48	1.98	0.97	1.29	2.08
Cu	0.11	0.27	4.33	2.34	0.35	2.36	2.19

### 6.3.3 Stability of C species and barriers for carbon dimer and trimer nucleation

C compounds formed on the catalyst surface can block the active sites on the surface thereby deactivating the catalyst. To evaluate this effect, the reaction energetics for the formation of the carbon clusters ( $C_2$  and  $C_3$ ) on the (111) surfaces of Fe, Co, Ni and Cu were calculated to determine the possibility of C–C bond coupling on different transition metals. Before investigating the kinetic properties of C nucleation on these metals, the thermodynamic stability of these carbon species was first studied by calculating the adsorption of atomic C and some small clusters (dimer  $C_2$  and trimer  $C_3$ ) on the (111) surface of Fe, Co, Ni, Cu. Figure 6.4 shows the most stable adsorption configurations for these clusters. On Fe (111) surface, atomic C is found most stable on the bridge (bri) site, while for  $C_2$  and  $C_3$  adsorption it is bri-hcp and bri-hcp-bri, respectively (Figure 6.4a). The calculated adsorption structures on the (111) surfaces of Co, Ni and Cu are somewhat similar. The most stable site for C,  $C_2$  and  $C_3$  adsorption on these metals is the hcp, neighboring hcp-fcc and hcp-fcc-hcp site, respectively (Figure 6.4b). The corresponding adsorption energies of these carbon species on the metal (111) surfaces are listed in Table 6.3. The adsorption energies ( $E_{ads}$ ) of the adsorbates were calculated as follows:

$$E_{ads} = (E_{C_x/slabb} - E_{slabb} - n_C E_C) / n_C, \quad (6.1)$$

where  $E_{C_x/slabb}$  represents the energy between the slab and the adsorbed carbon cluster ( $C_x$ ) on the surface,  $E_{slabb}$  is the energy of a clean relaxed Ni slab,  $E_C$  is the energy of a single carbon atom in its ground state whereas  $n_C$  is the number of carbon atoms per unit cell. A negative  $E_{ads}$  corresponds to a stable adsorbate/slab system.

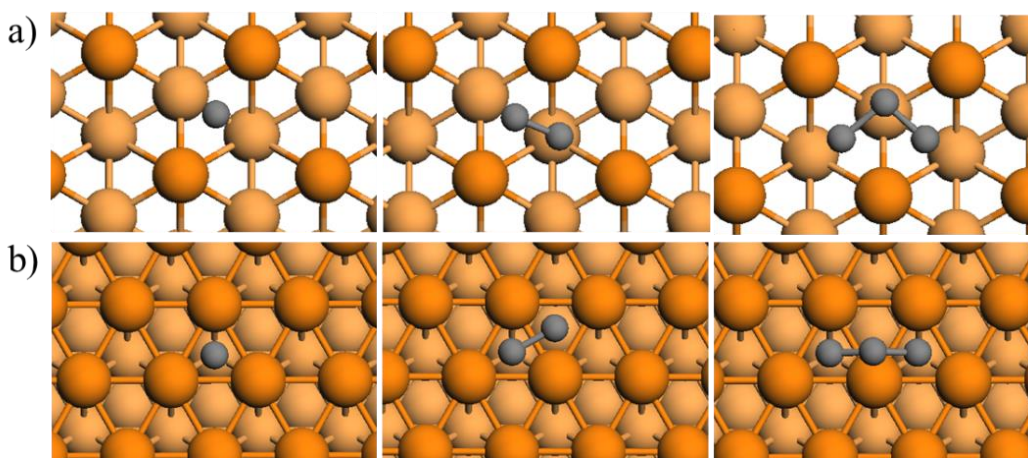


Figure 6.4 Sketches of the most stable adsorption configuration of carbon monomer, dimer and trimer on the (111) surfaces of the a) Fe; b) Ni.

Table 6.3 The adsorption energy,  $E_{\text{ads}}$  (eV), of carbon monomer (C), dimer ( $C_2$ ) and trimer ( $C_3$ ) on the (111) surfaces of Fe, Co, Ni and Cu.

Surface	Adsorption energy (eV)		
	C	$C_2$	$C_3$
Fe	-7.21	-7.36	-6.90
Co	-6.43	-6.70	-6.72
Ni	-6.19	-6.40	-6.44
Cu	-4.19	-6.06	-5.96

The results obtained by the present study show that C atom has a very strong bonding with Fe (-7.21 eV), followed by Co (-6.43 eV) and Ni (-6.19 eV). Atomic carbon on a Cu (111) surface has the lowest adsorption energy (-4.19 eV) among all the metals. This suggests that the bonding between C and the metal surfaces are directly related to the surface diffusion of C: the stronger the bonding, the lower the mobility of the C on the surface. Moreover, the results of this analysis also show that carbon clusters are generally more stable than atomic carbon species, suggesting that the formation of carbon clusters is always thermodynamically favored on the studied metals. It should be mentioned that the  $C_2$  and  $C_3$  are

considerably more stable than the monoatomic C on Cu (111), indicating the large driving force for carbon cluster nucleation on Cu.

Carbon nucleation barriers would be an appropriate measure to understand if C atoms would nucleate into carbon clusters and deactivate the catalyst. Therefore, the nucleation kinetics for the formation of the carbon  $C_2$  and  $C_3$  cluster on the (111) surfaces of Fe, Co, Ni and Cu were studied. The TS along the reaction coordinates for each nucleation reaction were identified and are shown in Figure 6.5; the corresponding nucleation barriers are presented in Table 6.2.

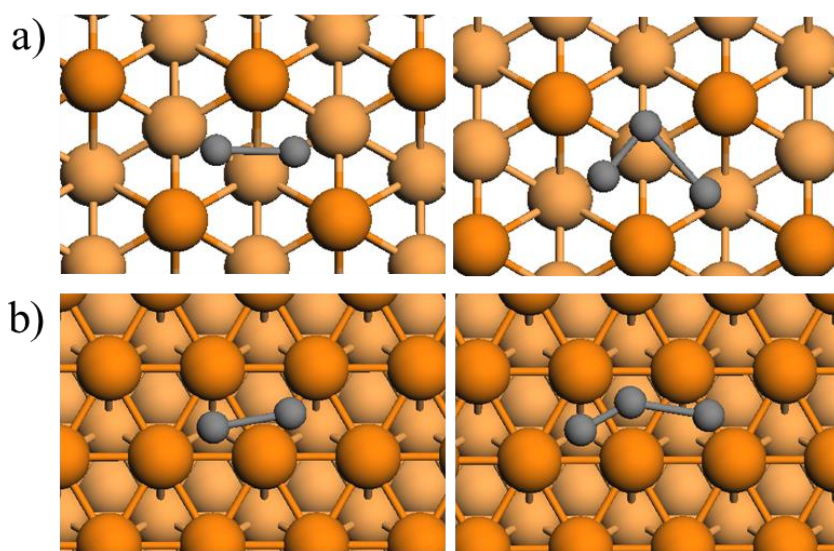


Figure 6.5 Sketches of the TS for  $C_2$  and  $C_3$  nucleation on the (111) surfaces of the a) Fe; b) Ni.

Figure 6.5a) shows the calculated TS structures on Fe (111). The TS structures of  $C + C$  and  $C_2 + C$  coupling reactions on Co, Ni, and Cu surfaces are very similar with each other: at the TS, C is always on the hcp hollow site with the other reactants on the edge-bridge site (Figure 6.5b). The key differences between the metal nanoparticles are the specific bond lengths reported in Table 6.2. The bond distances are longer on Cu than on Co, Ni and Fe. This result agrees with the fact that the lattice constant of these metals follows:  $Cu > Ni \approx Co > Fe$ . As shown in Table 6.2, the energetic results show that  $C_2$  nucleation on the Cu (111) surface has the lowest barrier of about 0.27 eV, while that on the Fe (111) surface requires the largest activation barrier of 1.15 eV. The overall energy barrier increases in the following order:  $Cu < Ni \approx Co < Fe$ . The same behavior was observed for  $C_3$  nucleation. That is, the corresponding energy

barrier for C<sub>3</sub> on Cu is much lower than those on all the other surfaces, and follows the same order, i.e., Cu (0.35 eV) < Co (0.86 eV) < Ni (0.97 eV) < Fe (1.37 eV). The low energy barrier indicates that C atoms on Cu (111) surface will most likely spontaneously form a carbon dimer/trimer. On the other hand, Co, Ni and Fe will be more resistant for C nucleation and therefore to catalyst deactivation.

#### **6.3.4 Effect of transition metals on CNTs/Graphene growth**

As described in Section 6.3.3, C atoms nucleation on Fe (111) surface is relatively difficult as compared with the other metals, making it resistant to C deactivation. However, as reported in Section 6.3.1, Fe has the highest reactivity towards CH<sub>4</sub> and CH dissociation among the studied transition metals. That is, Fe is a very efficient catalyst for a mass production of C atoms. Meanwhile, the diffusion of the surface C atoms is found to be difficult for that metal. This implies that even though Fe is relatively resistant for C deactivation, its high reactivity for C production and the low mobility of C makes Fe not a suitable catalyst for either CNTs or graphene growth. Note that this is concluded by assuming that the CNTs growth is based on the surface diffusion of C atoms. In fact, Fe-based catalyst has been reported for the growth of carbon filaments (CNFs) [41,42]. The growth process has been explained by the C bulk diffusion mechanism, in which the high solubility of C is essential. The study of the solubility of C in Fe is beyond the scope of this work, but the strong Fe–C bonding energy (-7.21eV) observed in the present study may lead surface C atoms to dissolve easily in the bulk Fe providing insights on the high solubility of C in Fe.

Co (111) and Ni (111) surfaces show similar reactivity for C–H bond activation, C diffusion and nucleation. Both Co and Ni have good reactivity towards CH<sub>4</sub> and CH dissociation providing carbon atoms for the CVD process. In addition, the high C mobility and nucleation barrier on Ni and Co allows C to diffuse to the edge site of metal/CNTs before nucleation could take place on the catalyst surface, allowing both Ni and Co surfaces to remain active during long periods of reaction time. Therefore, one can expect that Co and Ni could be a good substrate for CNTs growth. Note that the lower C diffusion barrier on Ni makes this metal a better choice when compared to Co.

In the case of Cu (111) surface, C has a weak C-metal binding on Cu as mentioned above. Meanwhile, it also has the highest mobility and lowest nucleation barrier among these transition metals. This indicates that Cu (111) is more likely to produce graphene because C adatoms diffuse very fast and prefer to nucleate everywhere. The only drawback for using Cu for graphene production will be its limited reactivity towards CH<sub>x</sub> dehydrogenation. Thus, the kinetics of graphene growth on Cu is expected to be strongly dependent on the dissociation of CH<sub>x</sub> species.

### 6.3.5 Cu<sub>8</sub>Ni and Cu<sub>8</sub>Fe alloys for graphene production

As discussed in Section 6.3.1, Fe and Ni based catalysts have high reactivity for CH<sub>x</sub> dissociation. If one can design a Cu based alloy with only trace amounts of Fe or Ni, the surface Fe or Ni atoms will significantly improve the catalyst reactivity towards CH<sub>x</sub> dissociation, acting as the reaction center for CH<sub>x</sub> dehydrogenation to produce C. Since the alloy surface remains Cu dominant, the C–C nucleation kinetics on this alloy catalyst will be similar as that on the pure Cu surface. Based on the above, two bimetallic catalysts, i.e., Cu<sub>8</sub>Ni (111) and Cu<sub>8</sub>Fe (111), were modeled by replacing one of the top surface Cu atom with a Ni and Fe atom, respectively. CH<sub>4</sub> and CH dehydrogenation on the doped Ni and Fe sites of the two bimetallic catalysts surface were studied. For both cases, the TS have similar structure to those obtained with pure Ni, i.e., CH<sub>4</sub> and CH dissociation occurs over the top site of Ni and Fe, with a single dissociating H atom pointing towards the surface. The corresponding reaction barriers for these alloys are shown in Table 6.4.

Table 6.4 Activation energy,  $E_a$ (eV), for the dissociation of CH<sub>4</sub> and CH on the (111) surfaces of Cu<sub>8</sub>Fe and Cu<sub>8</sub>Ni alloy. Distances between detached H and C ( $d_{C-H}$ ) and the nearest Metal ( $d_{M-H}$ ) in the TS of each elementary reaction step are also shown. Note that the carbon monomer (C) diffusion barrier is the energy for C atom to diffuse away from sitting beside the Fe or Ni atom.

Surface	CH <sub>4</sub> →CH <sub>3</sub> +H			CH→C+H			C diffusion
	$E_a$ (eV)	$d_{C-H}$ (Å)	$d_{M-H}$ (Å)	$E_a$ (eV)	$d_{C-H}$ (Å)	$d_{M-H}$ (Å)	$E_{diff}$ (eV)
Cu <sub>8</sub> Fe	1.16	1.61	1.60	1.15	1.58	1.57	1.37
Cu <sub>8</sub> Ni	1.28	1.69	1.54	1.48	1.82	1.52	1.00

As shown in Table 6.4, the reaction barrier on the alloy surfaces represent an intermediate value from those calculated from the pure metals: the CH<sub>4</sub> dissociation barrier on Cu<sub>8</sub>Ni (Cu<sub>8</sub>Fe) decreases to 1.28 eV (1.16 eV), which is about 0.67eV (0.79 eV) lower than that of pure Cu (111) surface. Similar results were obtained for CH decomposition: the dissociation barrier decreased from 2.06 eV on pure Cu to 1.48 eV (1.15 eV) on the Cu<sub>8</sub>Ni (Cu<sub>8</sub>Fe) bimetallic catalyst. This implies that both the Cu<sub>8</sub>Fe and Cu<sub>8</sub>Ni alloys may be suitable catalysts for CH<sub>x</sub> dissociation than pure Cu, with Cu<sub>8</sub>Fe being slightly more reactive. In addition, the ability for the oncoming C, produced from the previous CH dissociation step, to diffuse

away from this doped Fe or Ni site has to be evaluated, i.e., if the C atom is stacked on this site due to the strong bonding between C and doped Fe or Ni, it will block this active site and hinder the oncoming methane dissociation reaction. The calculations show that C atom sitting at doped site (besides the Fe or Ni) needs to overcome a barrier of 1.37 and 1.00 eV to escape on Cu<sub>8</sub>Fe and Cu<sub>8</sub>Ni (111), respectively. This indicates that C atoms on Cu<sub>8</sub>Ni will be more likely move away from this reactive center; otherwise it will block the doped site and deactivate the CH<sub>x</sub> dehydrogenation reactions. Therefore, the Cu<sub>8</sub>Ni (111) alloy seems to be a more suitable catalyst as compared with the pure Cu (111) for graphene production whereas pure Ni seems to be a suitable substrate for CNTs production as discussed in Section 6.3.4. Note that even though the C escape energy barrier (1.00 eV) on Cu<sub>8</sub>Ni (111) is very high, it is still quite lower than the CH<sub>4</sub> dissociation energy barrier (1.95 eV) on the pure Cu (111) surface. This means that the adsorbed C atom sitting beside the Ni atom will diffuse away before CH<sub>4</sub> dehydrogenation occurs on the other sections of the Cu surface.

## 6.4 Summary

Periodic, self-consistent DFT calculations have been used to study the effect of the catalyst in the catalytic Chemical Vapor Deposition (CVD) of different carbonaceous materials, i.e., CNTs and graphene. The growth of these materials in the CVD process was analyzed in terms of the activation of CH<sub>4</sub> and CH dissociation, the binding of C atom and its mobility, the nucleation of diatomic carbon and trimer species on the (111) facets of transition metals (Fe, Co, Ni, Cu).

This study shows that the (111) surfaces of Fe, Co and Ni have a good reactivity towards CH<sub>4</sub> and CH dissociation, as compared with that on Cu (111). The order of catalytic activity of the four transition metals for C–H activation is as follows: Fe > Ni > Co > Cu, which agrees well the d-band model prediction performed in this study. Carbon atoms were found to have good mobility on the Cu, Ni, Co and especially on the Cu surfaces. The calculated energy barrier for carbon surface diffusion on the metals follows the order: Cu (0.11 eV) < Ni (0.29 eV) < Co (0.36 eV) < Fe (1.05 eV). Similar activity trends were observed for C–C and C–C–C coupling reactions; the calculated nucleation barriers follow: Cu << Ni ≈ Co < Fe. These results indicate that Fe, Co and Ni will be more resistant to catalyst deactivation than Cu, because of the surface C nucleation on these metals.

These observations provide insights to design suitable catalysts for CNTs and graphene growth in the CVD process. The good mobility, together with high C–C nucleation barriers on pure Ni, allows the C to diffuse to the CNTs/Ni edge site before they nucleate together and deactivate the Ni surface, making Ni

an appropriate CVD substrate for growing CNTs. On the other hand, the particularly low diffusion and nucleation barriers for C adatoms on Cu suggest that C atoms tend to be more uniformly distributed on the Cu surface and can nucleate everywhere, making Cu suitable for the CVD synthesis of high quality graphene. However, because of its limited reactivity towards C–H bond activation, the kinetics of graphene growth on Cu will strongly depend on the dissociation of  $\text{CH}_x$  species. Therefore, Cu doped by  $\text{CH}_x$  dissociation reactive Fe and Ni atoms, i.e.,  $\text{Cu}_8\text{Fe}$  and  $\text{Cu}_8\text{Ni}$  alloys, were modelled and assessed in the present study. The results show that the alloys designed in this study (especially  $\text{Cu}_8\text{Ni}$ ) increase the reactivity for  $\text{CH}_x$  dehydrogenation, indicating the possibility of realizing mass production of graphene.

## Chapter 7

### Carbon Clusters on the Ni (111) Surface

This chapter presents a DFT study on the adsorption and nucleation of carbon clusters on Ni catalyst. The structure, energetics, and mobility of carbon intermediates up to 6 atoms on the Ni (111) surface were investigated. The DFT calculation results obtained in this study, e.g. nucleation kinetics of carbon atoms and the mobility of the formed carbon clusters will complement the current CNF growth mechanisms on the initial stages of the CNT formation. The study is organized as follows: section 7.1 presents an introduction of this study. In section 7.2, computational details including the DFT methods and the models are described. The analysis and discussion of the results are present in section 7.3. Concluding remarks are presented in section 7.4.

#### 7.1 Introduction

In the past few years, carbonaceous nanomaterials have received considerable attention due to their extraordinary physical and chemical properties [1,2] and their potential applications in the industry [3-6]. CNTs are synthesized mainly by Chemical Vapor Deposition (CVD) [7-9], in which the carbon atoms are sourced from the decomposition of a hydrocarbon gas (methane, ethylene) at the surface of supported catalytic particles (Fe, Co, or Ni). Experimental studies on CNT production have been focusing on the synthesis of these materials in CVD systems at low temperature [10-12] and the reaction conditions that affect the growth of CNTs, e.g. the effect of catalyst composition, the hydrocarbon flow rate, and synthesis temperature [13-15]. In addition to these experimental studies on CNT synthesis, efforts have also been made to identify the mechanism of CNT growth in CVD [16-20]. In general, the following mechanism has often been proposed for the CNT growth in CVD: (1) C atoms and hydrogen molecules are formed with the decomposition of hydrocarbon species such as methane, ethylene, acetylene in the presence of Ni, Fe, or Co nanoparticles; (2) carbon atoms diffuse through the bulk of the catalyst particles [21-25]; (3) the carbons then nucleate and are incorporated into graphene over-layers on the other side of the catalyst particle, which finally lifted up the particle. The key step in this mechanism is believed to be the diffusion of carbon species through the metal from the hotter leading surface to the cooler rear faces [26,27]. This growth process is commonly referred to as the vapor-liquid-solid growth mechanism [28], in which the CNT/CNF growth is generally considered the result of transient evolutions in the carbon bulk diffusion and precipitation driven by temperature [29,30]; or carbon concentration gradients along the

catalyst particle [31,32]. Recently, this mechanism has been challenged by in situ observations made using a transmission electron microscope (TEM): the catalyst remains solid and metallic during the growth process [33-37]. Based on these observations, Hofmann et al. [35] and Lin et al. [36] proposed that the mechanism of CNT growth is not through C precipitation from  $\text{Ni}_3\text{C}$  but rather through the diffusion of C adatoms followed by the dynamic formation and restructuring of monoatomic step-edges at the Ni surface.

Recently, first principles modeling methods such as DFT have also been used to investigate the carbon nanotube growth mechanism at the atomic-scale [37-42]. Cinquini et al. [40] studied carbon adsorption and diffusion on the surface and the subsurface of Ni and  $\text{Ni}_3\text{Pd}$  alloys using DFT analysis. That study concluded that the surface diffusion is the dominant process that contributes to the growth of carbon nanofibers by comparing the diffusion barriers of carbon on the Ni surface (0.45 eV) and in the bulk (1.72 eV). Similar growth mechanisms for catalytic carbon nanofibers based on the surface or subsurface diffusion of carbon atoms are also proposed by other researchers [42]. However, there were reports show that the carbon clusters may have a good mobility at the catalyst surface [43] and graphene is more likely to grow by adding clusters of about five atoms instead of adding the abundant monomers (C adatoms) [44]. This observation suggests that the study of the properties of carbon clusters is necessary for acquiring a thorough understanding of this system. Recently, Chen et al. [45] investigated the formation of a C dimer on a metal surface as the very initial stage in the nucleation of graphene. Cheng et al. [46] and Wang et al. [47] studied the stability and mobility of some small carbon clusters on the Ni (111) surface using plane wave based DFT calculations. Gao et al. [48] studied the nucleation of graphene on the terrace or near a step edge on a Ni (111) surface using DFT calculations. In the latter study, the graphene nucleation barriers were defined as the maximum of the  $G(N)$  curve, where  $G(N)$  is the Gibbs free energies of CNT ground structures on Ni (111) as a function of cluster size. Despite these efforts, a detailed study of the kinetic properties of the carbon cluster on Ni, including the transition state, the activation barrier for a specific nucleation reaction of these carbon clusters, is not currently available. Therefore, very little has been revealed about the diffusion and nucleation kinetics of these carbon clusters at the initial nucleation stages of C adatoms.

In the present study, the properties of the carbon clusters, from linear chains to branched and rings, formed by the nucleation of carbon atoms on the Ni surface were studied in order to understand the very initial stage of catalytic CNT growth. To be specific, the stability and mobility of carbon clusters with different configurations have been analyzed using DFT. The mobility of these clusters is evaluated by

their diffusion barriers. The nucleation of these carbon clusters up to C<sub>6</sub> is also investigated. The corresponding transition states for these nucleation reactions are identified. The nucleation of carbon atoms and the diffusion of the formed carbon clusters will complement the current CNF growth mechanisms so that they can take into account the initial stages of the CNT formation.

## 7.2 Computational details

### 7.2.1 Calculation methods

The same DFT calculation method is used as in section 3.2.1, Chapter 3. The adsorption energies ( $E_{ads}$ ) of the adsorbates on the Ni surface are calculated using equation 6.1, in Chapter 6. Note that the carbon adsorption energy  $E_{ads}$  considers the adsorption strength of carbon on the Ni substrate from isolated atomic states, which includes the carbon-metal and the carbon-carbon interactions. To describe the interactions between the adsorbed carbon clusters and the Ni substrate alone, the carbon-Ni interaction energy,  $E_{int}$ , is defined as follows:

$$E_{int} = (E_{C_x/slabb} - E_{slabb} - E_{C_x})/n_C, \quad (7.1)$$

where  $E_{C_x}$  is the energy of the C cluster calculated at the adsorbed geometry but without substrate.  $E_{C_x}$  results from a single-point calculation with the same parameters as those used for the complete adsorption system. Therefore, the difference between  $E_{int}$  and  $E_{ads}$  provides the interaction energy between the carbon atoms within the clusters adsorbed on the surface, which is referred to from heretofore as  $E_{C-C}$ .

### 7.2.2 Surface models

In the present study, the Ni catalyst was modeled by the most stable Ni surface: Ni (111) [49,50]. The Ni (111) surface was modeled using periodic three-layer slabs. One of the limitations of the periodic cell approach is that extremely large unit cells are required to fit the carbon structures into the unit cell with minimal lateral interactions with neighboring clusters. For this reason, the surface models were set up such that carbon atoms in the structures do not share surface Ni atoms with neighboring clusters. Therefore, to reduce the computational effort, the stability of most of the large structures, i.e. C<sub>5</sub>, C<sub>6</sub> adsorption, calculated in the present study was determined using a periodic 3×3 surface unit cell. Note that the stability of large linear clusters, e.g. C<sub>5</sub>(L) and C<sub>6</sub>(L), was determined using a 2×5 unit cell, since a 3×3 unit cell is not big enough to accommodate these linear clusters. For the relaxation of the Ni

surfaces, the experimental work of Lu et al. [51] found that the relaxation of Ni (111) is less than 2% (with respect to the bulk). A previous DFT study performed by Ledentu et al. [52] has also shown that the top layer of Ni (111) undergoes only very small inward relaxation (0.6%). Therefore, in order to reduce the computational demands, in all calculations performed on the Ni (111) surfaces, the Ni atoms of the uppermost layer and the adsorbed species were allowed to relax whereas the Ni atoms in the remaining layers were constrained to their corresponding bulk positions with the calculated lattice parameter of 3.52 Å.

## 7.3 Results and discussion

### 7.3.1 Adsorption of carbon atoms and clusters (C<sub>2</sub>–C<sub>6</sub>) on Ni (111)

The structures and stabilities of atomic carbon and clusters on the Ni (111) surface with different surface coverage  $\theta_C$  were studied using DFT analysis. Carbon surface coverage  $\theta_C$  is defined as the ratio between the number of deposited C atoms,  $n_C$ , and the number of surface (upper layer) Ni atoms,  $n_{Ni}$ , per unit cell, i.e.,

$$\theta_C = n_C/n_{Ni} \quad (7.2)$$

Thus, one layer that contains more carbon atoms than the surface Ni atoms is characterized by  $\theta_C > 1$  monolayer (ML).

Table 7.1 shows the adsorption energies for a single C on different unit cells equivalent to a surface coverage  $\theta_C$  from 1/9 to 1/4 ML. For the different  $\theta_C$  investigated here, the 3-fold hollow hcp and fcc sites were found to be more energetically stable than the bridge and the top sites. This is because the 3-fold hollow sites have a higher coordination number than the bridge and top site. The results in Table 7.1 also indicate that there is no a clear correlation between  $\theta_C$  and  $E_{ads}$  of the single C adsorption. However, the results show that C on the hcp site is slightly more stable than on the fcc site for every  $\theta_C$  tested.

Table 7.1 Adsorption energies,  $E_{ads}$ , (eV), of a single C atom at different surface sites of Ni (111) as obtained with different surface unit cells and carbon coverages,  $\theta_C$ : on top of a surface Ni atom (top), bridging two surface Ni atoms (bri), at an fcc or hcp three-fold hollow site.

Unit cell	$\theta_C, \text{ML}$	fcc	hcp	bri	top
$(2 \times 2)$	$1/4$	-6.12	-6.22	-5.74	-4.18
$(2 \times 3)$	$1/6$	-6.13	-6.16	-5.80	-4.07
$(3 \times 3)$	$1/9$	-6.13	-6.17	-5.69	-4.34

The adsorption of  $C_2$  dimer and two single C atoms with different separation distances were studied on a  $2 \times 2$  unit cell of Ni (111) surface, which is equivalent to a surface coverage  $\theta_C = 1/2$  ML. As shown in Table 7.2, the most stable adsorption state is the  $C_2$  dimer adsorbed on nearest neighboring hcp and fcc sites (Figure 7.1), with a C–C distance of 133 pm. The adsorption energy per C atom for this system is -6.40 eV, and the calculated interaction energy between the dimer and the Ni surface is -2.96 eV. As shown in Table 7.2, the adsorption of two single C atoms has been found to be much less stable than that obtained for the dimer. This result indicates that, at the carbon coverage  $\theta_C = 1/2$  ML, the formation of  $C_2$  dimers is thermodynamically favored. The  $C_2$  dimer and two single C atoms' adsorption behavior at lower carbon coverage  $\theta_C = 1/3$  and  $2/9$  ML have also been studied and reported on Table 7.3. The results show that the  $C_2$  dimers are still more stable than the adsorbed two single C atoms at  $\theta_C = 1/3$ . That table also shows that, at low coverage ( $2/9$ ), the single C has an adsorption energy of -6.15 eV. As the two single C atoms approach each other at a surface coverage of  $1/2$ , the corresponding adsorption energy becomes -5.55 eV. This indicates that the single carbon atoms become more unstable as the surface coverage increases, due to the strong repulsive interactions between these isolated carbon atoms. Thus, as more carbon is deposited on the Ni (111) surface, the carbon atoms thermodynamically tend to aggregate together. Table 7.3 also shows that the adsorption energy of a carbon dimer on Ni (111) is independent of the surface coverage, indicating that the formation of C–C covalent bonds on Ni surfaces can reduce the repulsion at higher coverages.

Table 7.2 Adsorption energy per atom for the adsorption of two carbon atoms (named C<sup>1</sup> and C<sup>2</sup>) on a 2×2 slab model ( $\theta_C = 1/2$ ) (Site Occupation and the shortest distance between C atoms,  $d_{(C^1-C^2)}$ , are also shown)

adsorbate	Site C <sup>1</sup>	Site C <sup>2</sup>	$d_{(C^1-C^2)}, \text{\AA}$	$E_{ads}, \text{eV}$	$E_{int}, \text{eV}$
single C	fcc	hcp	3.88	-5.27	
single C	hcp	hcp	2.50	-5.55	
single C	fcc	fcc	2.50	-5.51	
dimer C <sub>2</sub>	top	hcp	1.34	-5.87	-2.45
dimer C <sub>2</sub>	top	fcc	1.34	-5.83	-2.41
dimer C <sub>2</sub>	fcc	hcp	1.33	-6.40	-2.96

Table 7.3 Adsorption energies per carbon atom for a C<sub>2</sub> dimer formed at neighboring fcc and hcp sites and two single C Atoms (at the nearby hcp sites) for different  $\theta_C$  [ $d_{(C^1-C^2)}$ , is the C-C distance]

unit cell	$\theta_C, \text{ML}$	dimer C <sub>2</sub>		single C	
		$E_{ads}, \text{eV}$	$d_{(C^1-C^2)}, \text{\AA}$	$E_{ads}, \text{eV}$	$d_{(C^1-C^2)}, \text{\AA}$
(2 × 2)	$1/2$	-6.40	1.33	-5.55	2.50
(2 × 3)	$1/3$	-6.40	1.34	-6.13	3.82
(3 × 3)	$2/9$	-6.36	1.34	-6.15	4.31

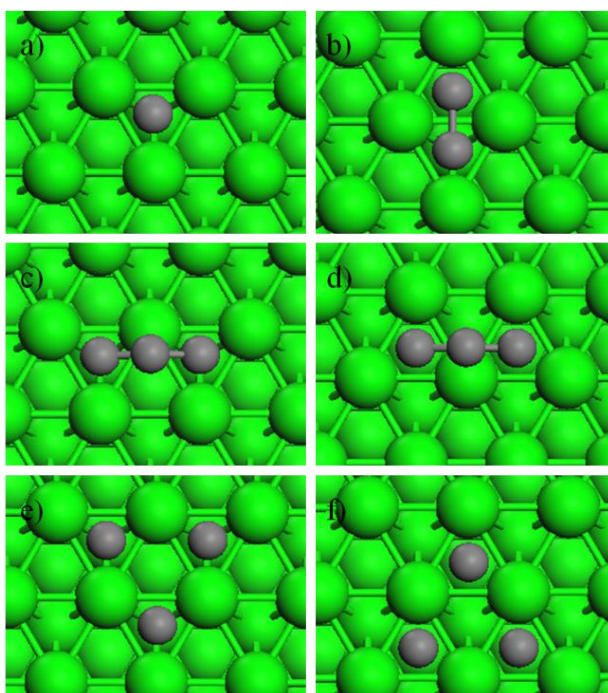


Figure 7.1 Optimized geometries for selected carbon species on Ni (111): a) atomic carbon C@hcp; b) dimer  $C_2$ @hcp-fcc; c) trimer  $C_3$ @fcc-hcp-fcc; d) trimer  $C_3$ @hcp-fcc-hcp; e) three single carbon 3C@hcp-hcp-hcp; f) three single carbon 3C@fcc-fcc-fcc.

Different arrangements of three carbon atoms on a  $3 \times 3$  unit cell of Ni (111) surface were also optimized, i.e.,  $C_3$  trimer in a row (Figure 7.1c and d) or in a triangular shape, three single carbon atoms with different separation distance on different sites (Figure 7.1e and f). The resulting stable adsorption geometries are presented in Figure 7.1. The corresponding adsorption energies for  $C_3$  are shown in Table 7.4. As in the case of  $C_2$  dimer adsorption, the results show that the  $C_3$  trimer is more energetically stable than the three single adsorbed C atoms, indicating that the formation of  $C_3$  trimer is also thermodynamically favored over the single C atoms. The most stable trimer is the one with its three carbon atoms adsorbed on next nearest neighboring hcp-fcc-hcp site with the middle carbon atom slightly lifted.

Table 7.4 Adsorption and cluster-metal interaction energies per carbon atom for C<sub>3</sub> trimers formed around a Ni atom on the (111) surface at a coverage of 1/3 ML, [*d*<sub>(C-C)</sub> is the shortest CvC distance between two C atoms]

Adsorption Geometry	<i>d</i> <sub>(C-C)</sub> , Å	<i>E</i> <sub>ads</sub> , eV	<i>E</i> <sub>int</sub> , eV
trimer C <sub>3</sub> @fcc-hcp-fcc	1.36	-6.42	-1.60
trimer C <sub>3</sub> @hcp-fcc-hcp	1.36	-6.44	-1.58
single carbon 3C@hcp-hcp-hcp	3.28	-6.12	
single carbon 3C@fcc-fcc-fcc	3.20	-5.92	

For carbon aggregates larger than a trimer, the carbon clusters can form linear chains (C<sub>x</sub>,L), branched (C<sub>x</sub>,B) and/or ring (C<sub>x</sub>,R) configurations. The present DFT analysis shows that the carbon tetramer is most stable in a linear chain configuration, C<sub>4</sub>(L) since the two end atoms of the carbon's chain are strongly bonded at the hollow sites of the Ni (111) surface (Figure 7.2), which stabilizes the chain configuration. As shown in Table 7.5, this structure has an adsorption energy of -6.54 eV/atom. The branched structure, C<sub>4</sub>(B), was found to be less stable by 0.27 eV. Note that the calculated metal-cluster interaction energy shows that the most stable C<sub>2</sub> dimer on the Ni (111) surface has an interaction energy of -2.96 eV whereas an interaction energy of -1.60 eV was obtained for the trimer. For the C<sub>4</sub>(L), an even smaller metal-cluster interaction was observed (-1.23 eV). This result shows that, as the size of the carbon chain cluster increases, the interaction between the cluster and the Ni decreases. As it is shown below, this decrease in the metal-cluster interaction energy also holds for the C<sub>5</sub> and C<sub>6</sub> clusters. Note that the C<sub>4</sub>(B) has a metal-cluster interaction of -2.33 eV, indicating that the branched clusters are more strongly bonded with the metal support than the linear clusters.

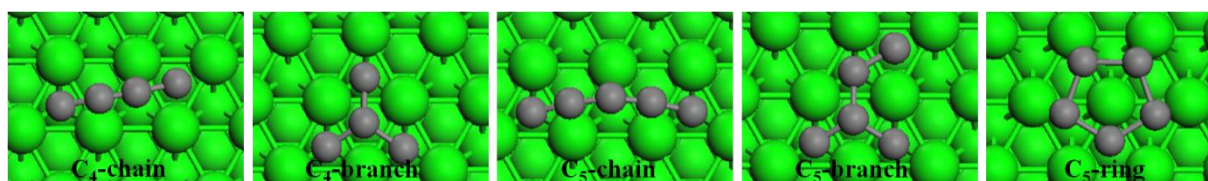


Figure 7.2 Optimized geometries for tetramer (C<sub>4</sub>-chain; C<sub>4</sub>-branch) and pentamer (C<sub>5</sub>-chain; C<sub>5</sub>-branch; C<sub>5</sub>-ring) on Ni (111).

Table 7.5 Adsorption and cluster-metal interaction energies per carbon atom for selected small carbon clusters on the (111) surface.

Adsorption Geometry	$E_{ads}, eV$	$E_{int}, eV$
C <sub>4</sub> (L)	-6.54	-1.23
C <sub>4</sub> (B)	-6.27	-2.33
C <sub>5</sub> (L)	-6.50	-1.01
C <sub>5</sub> (B)	-6.36	-1.94
C <sub>5</sub> (R)	-6.29	-1.94
C <sub>6</sub> (L)	-6.55	-1.08
C <sub>6</sub> (B)	-6.36	-2.06
C <sub>6</sub> (R)	-6.43	-1.18

The results for carbon pentamer, C<sub>5</sub>, are similar to those observed for the tetramer C<sub>4</sub>. That is, the C<sub>5</sub>(L) was found to be the most stable configuration on the Ni (111) surface with an adsorption energy of -6.50 eV whereas C<sub>5</sub>(B) and C<sub>5</sub>(R) are less stable by 0.14 and 0.21 eV, respectively. Similar results were also obtained for C<sub>6</sub> clusters: C<sub>6</sub>(L) is more favored over C<sub>6</sub>(B) and C<sub>6</sub>(R) with an adsorption energy of -6.55 eV. Moreover, a further decrease of the metal-cluster interaction was observed for these C<sub>5</sub> and C<sub>6</sub> clusters, as compared with that obtained for the tetramer. The stable C<sub>6</sub> configurations obtained by the present analysis are presented in Figure 7.3.

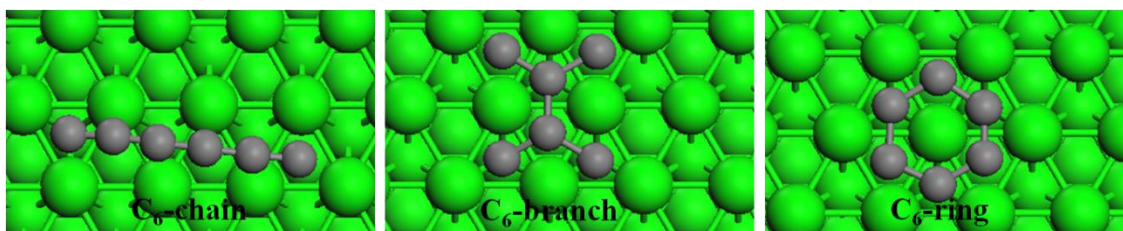


Figure 7.3 Optimized geometry for C<sub>6</sub> (C<sub>6</sub>-chain; C<sub>6</sub>-branch; C<sub>6</sub>-ring) on Ni (111).

In summary, the calculation of  $E_{ads}$  and  $E_{int}$  for the adsorbed carbon cluster systems shows that carbon clusters are more stable than atomic carbon species, indicating that the formation of a carbon cluster is thermodynamically favored. For carbon clusters larger than a trimer, a linear (C<sub>x</sub>,L) configuration is more

avored than the branched ( $C_x,B$ ) and ring ( $C_x,R$ ) configurations, which is in good agreement with the observations reported by Cheng et al.[46]. Moreover, it was found that, as the carbon cluster becomes larger, the interaction between each C adatom and Ni (111) surface decreases while the C–C interaction gradually increases.

To unravel the nature of cluster-metal interaction in terms of electronic structure, the projected density of states (PDOS) analysis was conducted for atomic carbon, carbon dimer and trimer adsorption when they are in their most stable configurations. The PDOS analysis is shown in Figure 7.4. When a single carbon was adsorbed on the Ni surface, there exists a large overlap between C 2p and Ni 3d orbitals. This suggests that the C–Ni interaction was mainly due to the mixing between the C 2p and Ni 3d orbitals. For the case of  $C_2$  dimer adsorption, a perfect overlap between 2s and 2p orbitals of the two C atoms is observed, indicating the strong C–C bonding. However, this comes with a reduction of the overlapping between C 2p–Ni 3d orbitals, which could contribute to a weaker C–Ni interaction as compared with that in atomic C adsorption. Regarding the carbon trimer adsorption, the carbon atom in the middle, denoted as C(b), is strongly bonded with its two neighboring C atoms, referred to as C(a). As shown in Figure 7.4, it was observed that a larger population of the 2p orbital overlap between C(a) and C(b) atoms was shifted to the lower energy levels (around  $-6.0$  eV), indicating a much stronger C–C bonding than that in the  $C_2$  dimer. Meanwhile, a further decrease of the overlap between C 2p and Ni 3d orbitals was also observed. Therefore, it can be expected that as the size of the carbon cluster increases, more electrons in the C 2p orbitals will be shared in between C–C bonding instead of forming bonds with the Ni 3d orbitals, which could result in a decrease of the C–Ni interaction. Note that a stronger C–C bonding also determines the arched shape of the carbon chains since the carbon atoms in the middle can only weakly interact with the metal substrate after forming strong C–C bonds with two carbon neighbors. This strong C–C bonding in the middle of the carbon chains is expected to be a common feature in the growth process of graphene or CNTs on metal substrates [53].

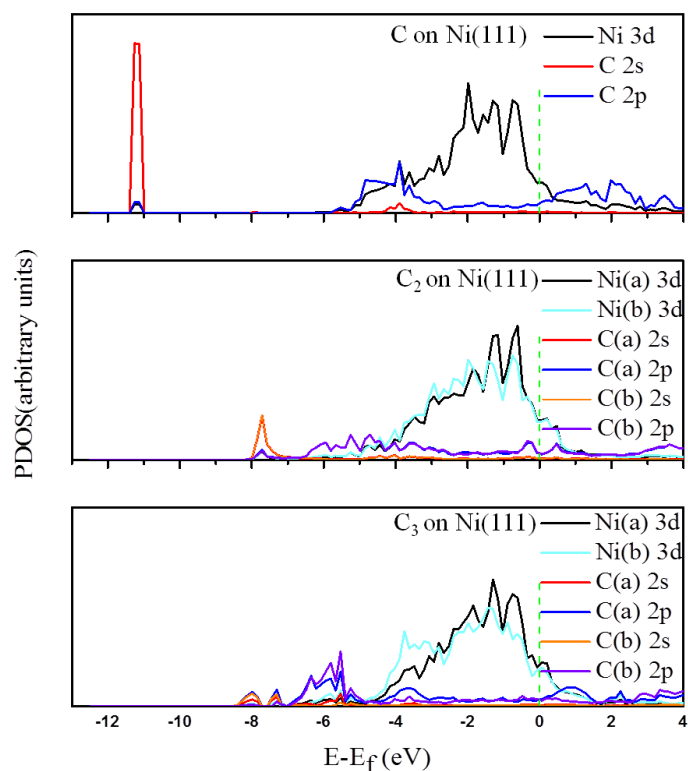


Figure 7.4 Projected density of states (PDOS) in atomic C, C<sub>2</sub> dimer and C<sub>3</sub> trimer adsorption systems. The vertical green-dash line donates the Fermi level. Ni (a) and Ni (b) represent two different Ni atoms on the metal surface. Ni (a) has only one C–Ni bonding, whereas Ni (b) has two C neighbors (two C–Ni bonding). C(a) and C(b) in the C<sub>2</sub>@Ni(111) system are the two carbon atom in the dimer. In C<sub>3</sub>@Ni(111), C(a) is the one of the two siding C atom in the trimer with one C–C bonding, whereas C(b) is the middle C with two C–C bonding.

### 7.3.2 Mobility of the carbon species on the Ni (111) surface

Surface diffusion is known to be crucial to understand epitaxial growth [54]. Thus, the elementary diffusion mechanisms and the corresponding energy barriers governing their mobility for C clusters on the Ni (111) surface were studied. The diffusion pathways were shown in Figure 7.5, and the corresponding energy barriers were reported in Table 7.6. The results show that atomic carbon diffusion via a bridge site has a diffusion barrier of 0.48 eV, which is in good agreement with previous studies reported in the literature (0.45 eV) [40]. For carbon dimers, as shown in Figure 7.5, the dimer is adsorbed at the nearby bridge sites in the transition state. The corresponding diffusion barrier was found to be 0.95

eV. It was observed that the trimer diffuses via an in-channel sliding mechanism with a substantially lower energy barrier (0.21 eV) than the atomic C diffusion. Trimer chains diffusing by sliding are thus much more mobile than either dimers or adatoms.  $C_3$  trimers can also diffuse on the surface by a cross-channel mechanism, which has a higher barrier of 0.48 eV. The results show that the  $C_3$  trimer, as a small cluster, has a very high mobility on the Ni (111) surface. Figure 7.5 also shows the lowest energy diffusion paths for a tetrahedron. The energy barrier for the tetramer chain is 0.62 eV with the in-channel sliding mechanism. The mobility of branched tetramer clusters via diffusion on Ni (111) was found to be less favorable with an energy barrier of 0.73 eV.

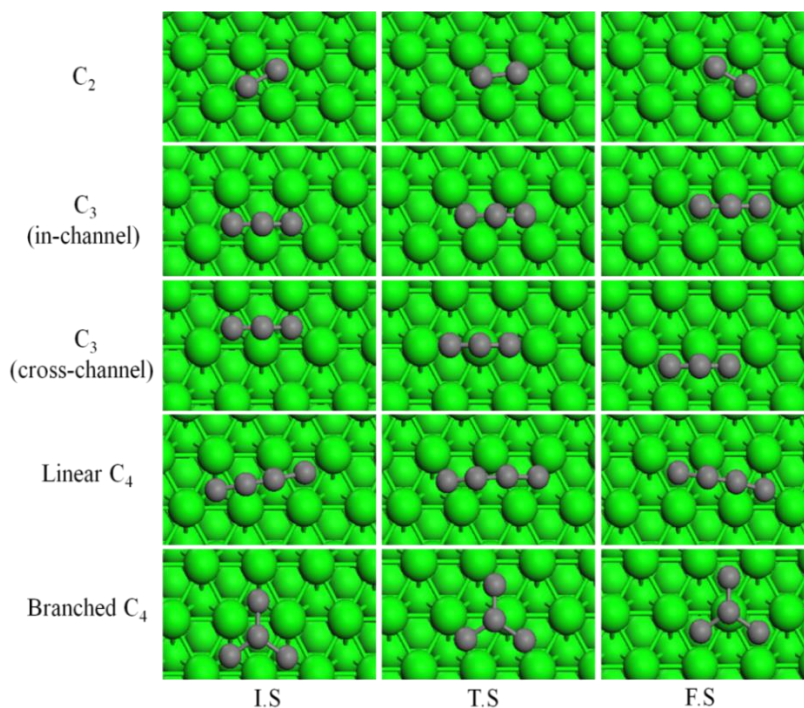


Figure 7.5 Pictorial views of the diffusion mechanisms of selected carbon clusters on Ni (111).

According to the energetics results reported in Section 7.3.1, once the Ni surface is saturated with monomers, mobile monomers will form small clusters of dimers, trimers and tetramers. The results shown in Table 7.6 indicate that the high mobility of the small clusters with respect to monomer hopping may play a significant role in the mass transport during CNT growth, i.e., small clusters may easily diffuse through the Ni surface and bond with monomers or clusters already deposited on the Ni surface thus

contributing to the CNT growth. This mechanism has also been suggested in recent reports [44,55]. This result suggests a very different picture for the growth of CNTs than that usually considered in which only the atomic C is involved and dominates the mass transport of the CNT growth.

Table 7.6 Diffusion barriers of selected carbon species.

Process	$E_a, \text{eV}$
monomer hopping	0.48
dimer diffusion	0.95
linear trimer “in-channel” diffusion	0.21
linear trimer “cross-channel” diffusion	0.48
linear tetramer “in-channel” diffusion	0.62
tetramer diffusion	0.73

### 7.3.3 Carbon cluster nucleation on Ni (111)

The reaction pathways and reaction energetics for the formation of the carbon clusters on the Ni (111) surface are presented in this section. The TS along the reaction coordinates for each elementary reaction was identified. Due to computational limitations, only the formation of small carbon clusters  $C_x(x=2-6)$  was considered in this study.

$C_2$  dimer formation is the first step for the carbon nucleation on the Ni substrate. As discussed above, dimers are much more stable than separated C adatoms by over 0.21 eV at a surface coverage of 2/9 ML on Ni (111). The energy barrier for forming a dimer by two neighboring C adatoms was found to be 0.88 eV. The reverse energy barrier estimated for this reaction was 1.44 eV, indicating that dimer dissociation is not kinetically favored. The geometry of the TS of this nucleation reaction is shown in Figure 7.6 (green dashed-dotted lines), in which one of the C atoms is located over the bridge site. In the TS, the activated C–C bond (denoted as C–C<sub>a</sub> hereafter) has a bond distance of 1.99 Å.

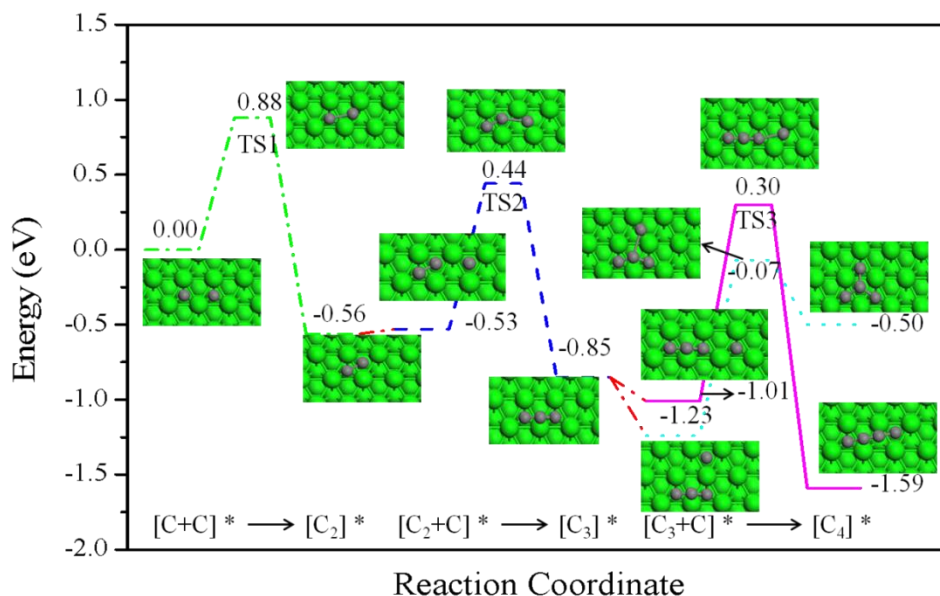


Figure 7.6 Reaction energy diagram of reaction paths for the C cluster ( $C_2\sim C_4$ ) formation on Ni (111) surface. All energies are relative to the energy of the coadsorbed  $[C+C]^*$ .

The transition state that corresponds to the formation of a trimer, by adding a single C to a dimer, is also shown in Figure 7.6 (blue dashed lines). The  $C_a$  atom is located at the bridge site, forming an activated  $C-C_a$  bond with a bond distance of 2.20 Å. This process has an energy barrier of 0.97 eV. The reverse process, the trimer dissociates into a monomer plus a dimer, has an energy barrier of 1.29 eV. As discussed in the previous section, carbon tetramers have two stable configurations:  $C_4(L)$  and  $C_4(B)$ , with  $C_4(L)$  being more stable than  $C_4(B)$  on Ni (111). In order to compare the kinetic properties of each of these clusters, both the linear and branched tetramer configurations were studied here. Both  $C_4(L)$  and  $C_4(B)$  can be either formed by two dimers or by a  $C_3$  trimer and a C monomer. However, it was found that the diffusion of a dimer has an energy barrier that is much higher than that of a trimer and atomic C. This will make the dimer less mobile and “trapped” in the adsorption site in most of the reaction time. Therefore, carbon tetramer formation by the nucleation of two dimers will be a highly activated process and therefore very unlikely to occur. Accordingly, only  $C_4(L)$  and  $C_4(B)$  formation by a  $C_3$  trimer and atomic C nucleation was considered in the present study. The reaction pathway and the energy profile for this process are shown in Figure 7.6. A  $C_4(L)$  forms when an atomic C passes the saddle point configuration toward the terminal C atom in the chain trimer (magenta solid lines). This process presents a barrier of 1.31 eV. On the other hand, the detachment of a terminal C atom from the linear tetramer,

producing thus a trimer, has an energy barrier of 1.89 eV. For the formation of the  $C_4(B)$  cluster, an energy barrier of 1.16 eV has to be overcome (Figure 7.6: cyan dotted lines). This is 0.15 eV lower than that for the  $C_4(L)$  formation. This result shows that the formation of the branched tetramer configuration is kinetically favored over the linear chain configuration. Note that the dissociation of  $C_4(B)$  into  $C_3$  and C is likely to occur since it has a relatively low energy barrier of approximately 0.43 eV. Isomerization between different configurations of the carbon clusters is possible since the reverse process of the nucleation reaction may contribute to these isomerization reactions. For example, the transformation of  $C_4(L)$  into  $C_4(B)$  involves multiple processes: *i*) bond breaking of one of the carbon atoms in  $C_4(L)$  with the neighboring carbon atoms; *ii*) carbon atom diffusion; *iii*) and re-bond with the middle C atom in the trimer. The first step can be achieved by  $C_4(L)$  dissociation into  $C_3$  and C, which is the reverse process of  $C_4(L)$  nucleation. The last step is actually the reaction pathway for the formation of  $C_4(B)$  proposed in the present study.

A  $C_5$  cluster on Ni (111) can also have a linear or a branch configuration. For the formation of linear  $C_5(L)$ , there are two possible pathways: adding a monomer to a  $C_4(L)$  or adding a  $C_3$  trimer to a  $C_2$  dimer. The reaction profile diagrams of these reactions are shown in Figure 7.7. Their corresponding TS are presented in Figure 7.8. As shown in Figure 7.7, the formation of  $C_5(L)$  by  $C_4(L)$  plus C has a barrier height of 1.26 eV, whereas the other reaction pathway has an energy barrier of 1.51 eV. For the  $C_5(B)$  cluster, there are also two pathways: adding a monomer to a  $C_4(B)$  or adding a trimer to a dimer. The reaction profile diagram in Figure 7.7 shows that the addition of an atomic C to  $C_4(B)$  proceeds with a relatively low energy barrier (0.23 eV). The reverse process of this reaction has a barrier of 1.18 eV. On the other hand, the  $C_5(B)$  formation by moving a  $C_3$  trimer to a  $C_2$  dimer has an energy barrier of 0.42 eV, whereas the activation energy for the reverse process is as low as 0.29 eV. These results show that, as in the case of  $C_4$  cluster formation, the formation of a branched  $C_5$  cluster is kinetically favored over the  $C_5$  chains. Moreover, the results show that, in addition to adding C to the existing cluster, the nucleation of these carbon clusters by adding a  $C_3$  trimer is also a feasible process.

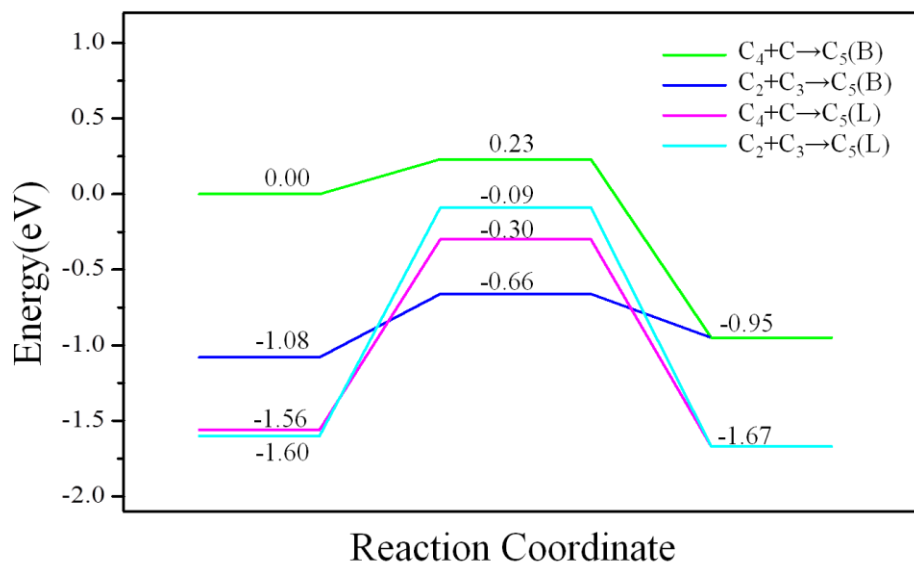


Figure 7.7 Reaction energy diagram of reaction paths for the  $C_5$  cluster formation on Ni (111) surface. All energies are relative to the energy of the coadsorbed  $[C_4(L)+C]^*$ .

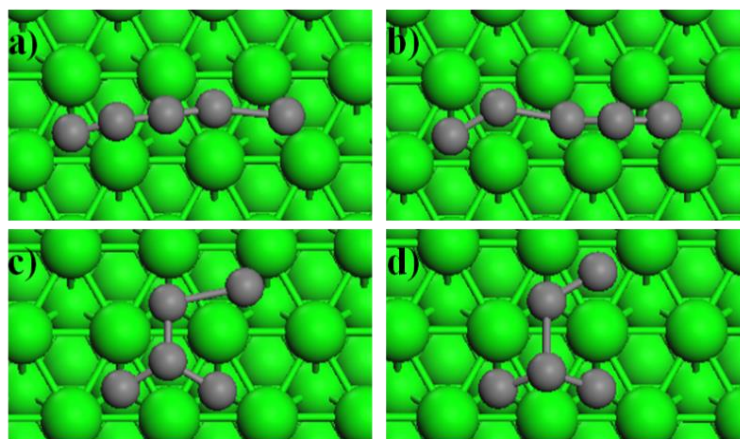


Figure 7.8 Geometric structures of the transition state (T.S.) for the formation of  $C_5(L)$  and  $C_5(B)$  clusters on Ni (111) surface: a)  $C_5(L)$  formation by adding a C atom to a  $C_4$  chain; b)  $C_5(L)$  formation by adding a  $C_3$  trimer to a  $C_2$  dimer; c)  $C_5(B)$  formation by adding a C atom to a branched  $C_4$ ; d)  $C_5(B)$  formation by adding a  $C_3$  trimer to a  $C_2$  dimer.

A reaction energy diagram for the formation of linear, branched, and ring  $C_6$  clusters was calculated and presented in Figure 7.9. A linear  $C_6$  can be nucleated from moving a monomer to the  $C_5$  chain cluster

(Figure 7.10a) by overcoming a barrier height of 1.14 eV. The reverse process, the dissociation of the  $C_6$  chain into a  $C_5$  chain and a  $C$ , has a barrier of 1.26 eV. Two  $C_3$  trimers occupying neighboring sites can also react spontaneously to form a linear  $C_6$  (Figure 7.10b). The reaction energy and the corresponding activation energy were found to be 0.43 eV and 1.22 eV, respectively. Two pathways for the formation of a branched  $C_6$  cluster were considered here: *i*) two  $C_3$  trimers reach and connect each other by the middle  $C$  with a barrier of 0.83 eV, and *ii*) a monomer approaches a branched  $C_5$  cluster with a barrier of 0.25 eV. The formation of a  $C_6$  ring by adding an atomic  $C$  to a bended  $C_5$  chain cluster has a low energy barrier of about 0.17 eV. The other nucleation pathway by two  $C_3$  trimers has an activation energy of 0.97 eV. These results show that the formation of  $C_6(B)$  and  $C_6(R)$  by adding atomic  $C$  to the  $C_5$  cluster has very low energy barriers, and thus are very likely to occur on the Ni surface. These observed low energy barriers can be explained by the stability of these co-adsorbed clusters. As shown in Figure 7.9, the co-adsorbed branched  $[C_5+C]^*$  and bended  $[C_5+C]^*$  are unstable when compared to the other co-adsorbed configurations. This makes these configurations or states to have a very high energy level at the initial state, which finally results in a low energy barrier for their nucleation reaction. Therefore, it can be expected that at low reaction temperatures, where the reaction is more likely to be thermodynamically controlled, the formation of linear carbon chains will dominate the surface reactions. However, at high reaction temperatures, where the existence of the unstable branched or the bended carbon cluster is possible, the formation of  $C_6(B)$  and  $C_6(R)$  will dominate the processes on the Ni (111) surface.

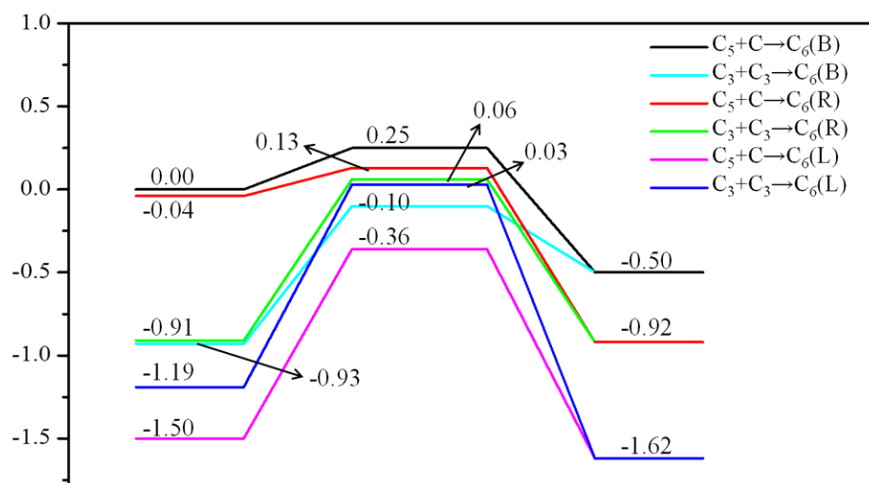


Figure 7.9 Reaction energy diagram of reaction paths for the  $C_6$  cluster formation on Ni (111) surface. All energies are relative to the energy of the coadsorbed  $[C_5(B)+C]^*$ .

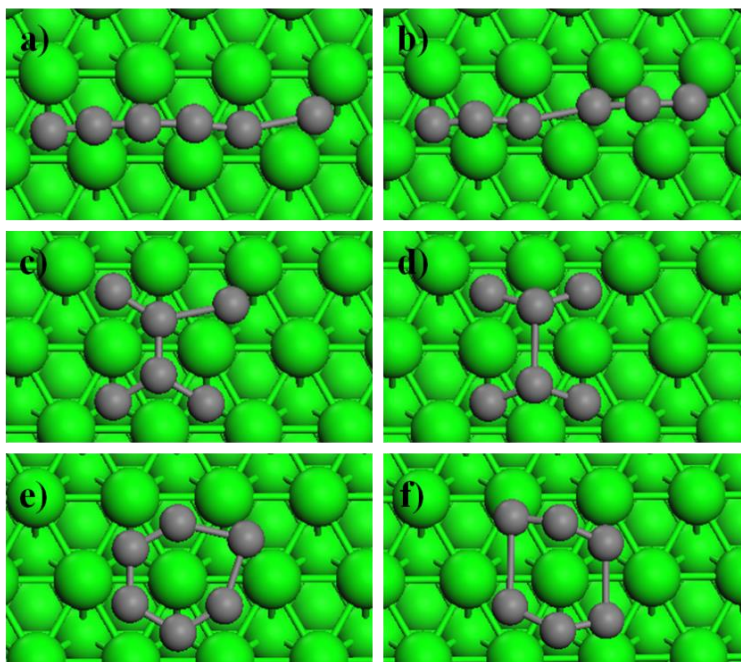


Figure 7.10 Geometric structures of the transition state (T.S.) for the formation of  $C_6(L)$  and  $C_6(B)$  clusters on Ni (111) surface: a)  $C_6(L)$  formation by adding a C atom to a  $C_5$  chain; b)  $C_6(L)$  formation by adding a  $C_3$  trimer to a  $C_3$  trimer; c)  $C_6(B)$  formation by adding a C atom to a branched  $C_5$ ; d)  $C_6(B)$  formation by adding a  $C_3$  trimer to a  $C_3$  trimer. e)  $C_6(R)$  formation by adding a C atom to a bended  $C_5$  chain; f)  $C_6(R)$  formation by adding a  $C_3$  trimer to a  $C_3$  trimer.

## 7.4 Summary

A systematic study of carbon nucleation during the early stages of CNT growth on Ni (111) was performed using Density Functional Theory (DFT) calculations. The structure and relative stability of adsorbed C intermediates up to 6 carbon atoms, and their mobility on the Ni (111) surface were investigated. Moreover, the reaction pathways and energetics for the nucleation of the carbon clusters on the Ni (111) surface were also explored. The outcomes of this study are as follows:

*i)* Atomic carbons tend to nucleate to form carbon clusters on the Ni (111) surface. There is also a thermodynamic preference for different carbon cluster configurations: linear carbon structures are more stable than branched and ring carbon configurations of equal sizes.

*ii)* The monomer is not the only mobile species on the Ni (111) surface. Small clusters, at least up to the tetramer, are also mobile. The dimer is the least mobile cluster with a diffusion barrier of 0.95 eV. The trimer can diffuse with low energy barriers through either a sliding (0.21 eV) or a crossing (0.48 eV) mechanism. The sliding diffusion barrier was even lower than the monomer hopping barrier (0.48 eV). The linear tetramer can diffuse with a barrier of 0.62 eV. The calculation of the interaction between the carbon cluster and the Ni surface shows that branched carbon clusters have stronger interaction with the Ni substrate when compared to the carbon chains. This indicates that carbon chains generally have higher mobility than branched carbons. This cluster mobility is expected to play an important role in the reaction kinetics of C on Ni.

*iii)* The formation of branched C species is kinetically preferred as compared with that of the C chain cluster. The formation of C chain and branched species by the addition of both the single C atom and C<sub>3</sub> trimer is possible. This new insight into the supported C cluster formation is crucial to understand the growth mechanism of CNTs and graphene on transition metal surfaces in CVD experiments. The outcome of this research will present a comprehensive picture of the carbon nucleation reactions at the early stage of the CNT growth.

## Chapter 8

### Carbon Nanotube Growth: Kinetic Monte Carlo Simulations

This Chapter presents kinetic Monte Carlo (KMC) study of the carbon nanotube growth process. A brief introduction and the motivation for this study are given in the first section. A comprehensive CNT growth model is proposed in section 8.2 and the simulation methods used to develop a KMC simulation for CNT growth process are also discussed in this section. Note that since some of the reactions in the proposed CNT growth model have been studied in previous Chapters, their kinetic parameters are directly used in the present study. For example, the  $\text{CH}_x$  dissociation barrier on Ni is taken from Chapter 3, in which the Ni catalyst is modeled by a clean Ni (111) surface with a  $3 \times 3$  unit cell. The carbon surface diffusion and nucleation barriers used in the present study are taken from Chapter 7. In Section 8.3, results obtained from the KMC simulations were presented and implications from the KMC simulations results were also discussed. Concluding remarks are stated in section 8.4.

#### 8.1 Introduction

Since the discovery of carbon nanotubes (CNT), considerable effort has been made to improve the CNT's growth yield and to find out the growth mechanism of these materials [1-3]. Among all the methods used for CNT synthesis, Chemical Vapor Deposition (CVD) is one of the most widely used [4,5]. In CVD growth of CNT, the carbon atoms are sourced from the decomposition of hydrocarbon precursor molecules ( $\text{CH}_4$ ,  $\text{C}_2\text{H}_2$ ,  $\text{C}_2\text{H}_4$ , etc.) at the surface of supported catalytic particles (Fe, Co, or Ni), and their growth mechanism is often described by a vapor-liquid-solid model (VLS) [6]. The model assumes that, *i*) the catalyst particles are in the liquid state. This allows rapid bulk diffusion of carbon atoms throughout the particle, and forms a super-saturation of the C metal solution; *ii*) C segregation and incorporation into graphene over-layers on the other side of the catalyst particle [7-11], leaving the nanoparticles located at the tips or roots of CNT [16-18]; and *iii*) the bulk diffusion of carbon and precipitation are driven by temperature [12, 13] or carbon concentration gradient along the catalyst particle [14, 15].

Recently, this mechanism has been challenged by *in situ* observations made with transmission electron microscope (TEM), which supports the evidence that the catalytic particles stay in solid or metallic state during the CNT growth [19-23]. Based on these observations, Hofmann et al. [21] and Lin et al. [22] have suggested that the mechanism of CNT growth is not through C precipitation from  $\text{Ni}_3\text{C}$

but rather through the surface diffusion of C adatoms. The surface diffusion mechanism was supported by recent DFT studies [23-25]. Surface diffusion of C atoms on a Ni particle surface was found to proceed with low energy barriers (0.4~0.5 eV) making it more favorable than diffusion of carbons through the subsurface (~1.34 eV) and the bulk (1.6~1.8 eV), respectively. This observation is also consistent with the results obtained in recent Molecular Dynamics (MD) simulation studies [26-32], which have found that there is only limited number of C atoms were diffused into the bulk of the catalyst particle.

The aforementioned studies have focused on the behavior of single carbon atoms. Reports have shown that they are generally not strongly bonded with the metal catalyst surface [33, 34]. This suggests that carbon clusters may have a good mobility at the catalyst surface, and therefore play an import role for production of CNT in the CVD process. In fact, the study presented in Chapter 7, have shown that the smaller carbon cluster especially C<sub>3</sub> trimer can diffuse vary fast on the Ni (111) surface. Therefore, a more realistic scenario of the CNT growth will be as follows: in addition of the surface and bulk diffusion of C atoms, they will also nucleate together, forming carbon clusters on the catalyst surface; small carbon clusters may diffuse on the Ni surface, and together with C atoms can contribute to the CNT growth; further nucleation of the small cluster will lead to a graphite monolayer bonded to the surface and eventually cause the deactivation of the catalyst. Therefore, a CNT growth mechanism that consists of the surface and bulk diffusion of C, as well as the possible carbon cluster surface nucleation and diffusion will be more trustworthy.

As already shown by previous studies [35-38], KMC simulations offer an efficient strategy to bridge the gap between the results obtained by DFT at the microscopic scale and the dynamic behavior of the working catalyst surface under given operating conditions. Reliable statistical estimates of macroscopic reaction rates can thus be compared with experimental observations. In this study, the Ni catalytic growth of CNT was investigated KMC simulations. DFT calculations were performed to calculate the reaction barriers and pre-exponential factors of the elementary steps in the proposed CNT growth model. The calculated kinetic parameters were subsequently incorporated into a novel KMC framework that are developed for overcoming large disparities in time scale of the systems, in which conventional KMC is inefficient when fast surface diffusion processes exist. The KMC simulations predict the experimental dynamical formation process of CNT on Ni nanoparticles from first principles, and therefore provide a validation of the proposed Ni catalytic CNT growth mechanism. To the best of the author's knowledge, such a study has not been presented in the open literature.

## 8.2 Simulation details

As mentioned before, KMC simulation of the catalytic reactions involves both the DFT and KMC simulation of the elementary steps in the proposed reaction mechanism. Therefore, in this section, details about the models and simulation methods, e.g. the proposed CNT growth model, models used in DFT calculation and implementation of the KMC simulation, is discussed.

### 8.2.1 CNT growth mechanism

As discussed in the previous section, in addition to the surface and bulk diffusion of carbon atoms, carbon cluster may play a critical role in the CNT growth mechanism. In this study, a CNT growth model that consider nucleation and diffusion carbon cluster is developed. The mechanism proposed for the CNT growth is sketchily presented in Figure 8.1. The growth of CNT is thought to start with the successive  $\text{CH}_4$  dehydrogenation on Ni nanoparticles, producing C and H atoms. H atoms can move on the catalyst surface and  $\text{H}_2$  may be formed when two H atoms “meet” each other. Note that “meet” means that the two atoms are sitting at neighboring sites on the catalyst surface. The C atoms resulted from previous  $\text{CH}_4$  dissociation steps can diffuse on the Ni catalyst surfaces or through the bulk of the Ni particles (Figure 8.1). At the same time, surface C atoms can also nucleate together to form carbon clusters. Some of the small C clusters may also have a good mobility on the catalyst surface. Large C clusters will remain on the Ni surface, and therefore block the active sites; their further nucleation will lead to hemispherical caps that terminate the growth of CNT. The CNT growth proceeds via the addition and attachment of C adatoms and the small movable carbon clusters at the CNT/Ni edge boundary.

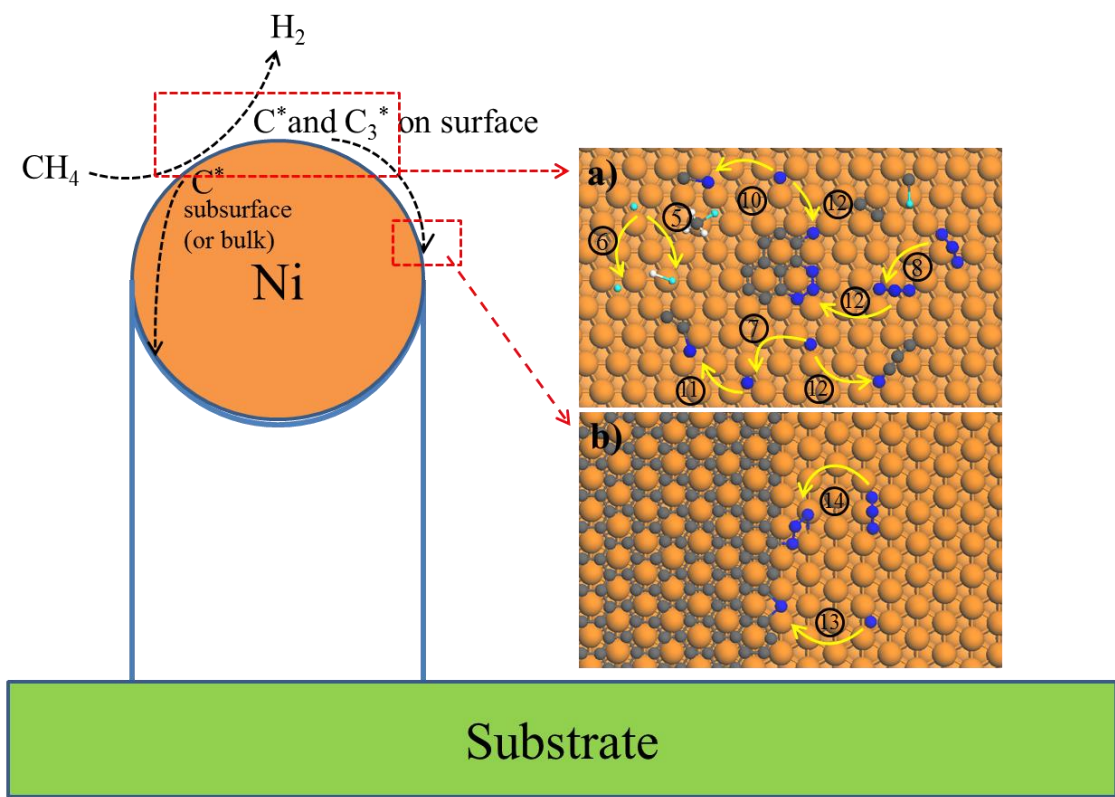


Figure 8.1 The proposed CNT growth mechanism: a) reaction or processes that occur on the Ni catalyst surface; b) reactions that occur on the Ni/CNT growth edge. Some of the important processes were labeled, and they correspond to the elementary steps in Table 1. Orange: Ni, white: H, black: C, light blue: movable H, dark blue: movable C.

### 8.2.2 DFT modeling and intrinsic kinetics calculations

Modeling the Ni catalyst in DFT calculations requires a good understanding of the Ni catalyst surfaces in the growth process of CNTs. High-resolution transmission electron microscopy (HRTEM) observations reported by Ji et al. [39] show that the Ni catalyst at the tips of CNFs with  $\text{CH}_4$  as a carbon source was found to be dominated by low-energy (111) surface facets. Yao et al. [40] showed that most of nickel catalytic particles have a conical shape orientated with a 110 direction along the tube growth axis with the (110) and (111) planes as exposed faces. In fact, the (111) and (110) surfaces have similar properties towards adsorption and diffusion of carbon [41]. Therefore, in the present study, the DFT calculated kinetic parameters that will be used to construct the kinetic data base for KMC simulation are obtained on the most stable Ni (111) surface [41, 42].

The intrinsic kinetics that govern the elementary steps involved in the Ni catalytic CNT growth process were calculated using periodic DFT calculations implemented in the BAND program [43,44]. Further technical details about the DFT calculations, e.g., functional, search for transition state, can be found in section 3.2.1, Chapter 3. The energetics for CH<sub>x</sub> dissociation is obtained on the Ni (111) surface modeled by 3×3 unit cell (see Table 4.6 in Chapter 4). The kinetic properties for C and C cluster diffusion and nucleation are taken from Chapter 7. Table 8.1 gives the details of the surface elementary steps considered in the reaction mechanism presented in Figure 8.1. The CNT growth reactions are modeled by the incorporation reaction of C (or C<sub>3</sub>) with a pre-covered graphene edge on a 5×2 unit cell of Ni (111) surface, in which the bottom layer of the slab was fixed in its bulk positions with a calculated lattice parameter of 3.52 Å; the Ni atoms of the remaining layers and the adsorbed species were set free to relax.

The kinetic rate constant for elementary steps such as surface reaction and diffusion are calculated according to transition state theory as follows [45-47]:

$$k_{TST} = \frac{k_B T}{h} \frac{q_{vib}^{TS}}{q_{vib}^R} \exp\left(-\frac{E_a}{k_B T}\right) \quad (8.1)$$

where  $h$  is Planck's constant;  $k_B$  is Boltzmann's constant;  $T$  is the absolute temperature;  $q_{vib}^{TS}$  and  $q_{vib}^R$  are the vibrational partition functions of the TS and reactants, respectively, and  $E_a$  is the energy barrier.

The dissociative adsorption rate for CH<sub>4</sub> was determined from the following expression [45]:

$$k_{ads} = \frac{h^2 P}{(2\pi m k_B T)^{3/2}} \frac{q_{vib}^{TS}}{q_{rot} q_{vib}} \exp\left(-\frac{E_a}{k_B T}\right) \quad (8.2)$$

where  $P$  is the gas pressure;  $m$  is the mass of the molecule.

Table 8.1 contains activation barriers and vibrational frequencies for the transition states computed from DFT calculations, which are used to calculate the kinetic rate constants. Note that the frequency values of the TS in step 12 are for C<sub>3</sub>+C reaction. Vibrational frequencies (>200 cm<sup>-1</sup>) of gas phase and surface species are presented in Table 8.2. Detail discussion about the DFT calculation results and the elementary reactions implemented in KMC simulation is described next.

Table 8.1 Vibrational frequencies ( $>200 \text{ cm}^{-1}$ ) of the transition states, forward ( $E_{a,f}$ ) and backward ( $E_{b,f}$ ) activation energy barriers of elementary steps for CNT growth on Ni (111).

Elementary step	Transition state frequencies ( $\text{cm}^{-1}$ )	$E_{a,f}/E_{a,b}$ (eV)
<i>Methane decomposition reactions</i>		
1) $\text{CH}_4(\text{gas}) \rightarrow \text{CH}_3^* + \text{H}^*$	309, 543, 581, 960, 995, 1134, 1172, 1359, 1392, 2897, 2977, 3034	1.14/0.65
2) $\text{CH}_3^* \rightarrow \text{CH}_2^* + \text{H}^*$	265, 441, 502, 711, 865, 1241, 1846, 2859, 3061	0.73/0.95
3) $\text{CH}_2^* \rightarrow \text{CH}^* + \text{H}^*$	235, 331, 396, 516, 691, 851, 1943, 3136	0.34/1.05
4) $\text{CH}^* \rightarrow \text{C}^* + \text{H}^*$	450, 503, 593, 1847	1.17/1.21
5) $\text{H}^* + \text{H}^* \rightarrow \text{H}_2(\text{gas})$	244, 379, 1662, 1853	1.31/0.43
<i>Surface diffusion of H and C species</i>		
6) $\text{H}^*(\text{S1}) \rightarrow \text{H}^*(\text{S2})$	1005, 1279	0.28
7) $\text{C}^*(\text{S1}) \rightarrow \text{C}^*(\text{S2})$	635, 663	0.48
8) $\text{C}_3^*(\text{S1}) \rightarrow \text{C}_3^*(\text{S2})$	—————	0.48
<i>C bulk (or subsurface) diffusion</i>		
9) $\text{C}^*(\text{S}) \rightarrow \text{C}^*(\text{B})$	—————	1.80 (1.34) <sup>125</sup>
<i>C nucleation reactions</i>		
10) $\text{C}^* + \text{C}^* \rightarrow \text{C}_2^*$	332, 456, 537, 560, 609	0.88/1.44
11) $\text{C}_2^* + \text{C}^* \rightarrow \text{C}_3^*$	223, 276, 334, 406, 454, 548, 622, 1435	0.97/1.29
12) $\text{C}_{x(x \geq 3)}^* + \text{C}^*(\text{or } \text{C}_3^*) \rightarrow \text{C}_x^*$	249, 261, 295, 324, 371, 403, 455, 462, 481, 507, 1083, 1166, 1394, 1596	1.31/1.55
<i>CNT growth reactions</i>		
13) $\text{C}^*(\text{E}) + \text{CNT}(\text{n})_{\text{C}} \rightarrow \text{CNT}(\text{n}+1)_{\text{C}}$	—————	0.89
14) $\text{C}_3^*(\text{E}) + \text{CNT}(\text{n})_{\text{C}} \rightarrow \text{CNT}(\text{n}+3)_{\text{C}}$	—————	0.89

‘—’ signifies lack of a vibrational frequencies at the transition state. The pre-exponential factor “ $A$ ” in process 8, 9 are set up the same as in 7; the pre-exponential factors used in reactions 13 and 14 are taken the same as in 12.

Table 8.2 Vibrational frequencies ( $>200\text{ cm}^{-1}$ ) of gas phase and surface species on Ni (111) used in the kinetic model of CNT growth.

Species	Frequencies ( $\text{cm}^{-1}$ )
CH <sub>4</sub> (gas)	1296, 1296, 1296, 1519, 1519, 2956, 3067, 3067, 3067
CH <sub>3</sub>	262, 317, 437, 515, 1165, 1196, 1282, 2740, 2884, 2893
CH <sub>2</sub>	245, 356, 491, 539, 687, 1364, 2579, 3074
CH	414, 425, 617, 685, 719, 3016
C	504, 518, 599
H	795, 822, 1205
C <sub>2</sub>	306, 307, 309, 425, 438, 1476
C <sub>3</sub>	243, 274, 333, 396, 434, 439, 461, 1137, 1442

### 8.2.3 Elementary steps in KMC simulation

The elementary steps that are implemented in the KMC simulation are as follows:

#### *i)* Methane decomposition and hydrogen production

Methane in the gas phase dissociates on to the surface of Ni catalyst, produces CH<sub>3</sub> and H atom. CH<sub>3</sub> adsorbed on the Ni surface then undergo a series of hydrogen abstraction reactions, and ultimately results in the adsorbed C and H atoms. The energy barriers for these dissociation reactions are listed in Table 8.1. Note that the barriers for the reverse process of CH<sub>3</sub> and CH<sub>2</sub> dissociation are much higher than its forward process. Moreover, due to the low diffusion barrier of H atoms on the Ni surface (0.28 eV), the H surface diffusion is orders of magnitude faster than CH<sub>3</sub> and CH<sub>2</sub> production reaction, and therefore it will more likely diffuse away instead of remaining at the neighboring site of CH<sub>3</sub> and CH<sub>2</sub> after the dissociation. These conditions would make the CH<sub>3</sub> and CH<sub>2</sub> production process very unlikely to occur. Accordingly, the reverse reaction of CH<sub>3</sub> and CH<sub>2</sub> dissociation were not considered in the present analysis.

## ii) Surface and bulk diffusion

As shown in Table 8.1, the adsorbed H and C atoms have small diffusion barriers, i.e., 0.28 and 0.48 eV, respectively, and therefore they are assumed to diffuse over Ni surface. Hydrocarbon radicals, e.g. CH<sub>3</sub>, CH<sub>2</sub> and CH, produced during CH<sub>4</sub> dehydrogenation are assumed to be immobile. This is because that, during the evolution of the system, the surface diffusion of these hydrocarbon radicals only contributes to the CH<sub>x</sub> production reaction when they “meet” H atoms on the catalyst surface. However, this contribution can be compensated by the fast diffusion of H atoms. For the carbon cluster, the study presented in Chapter 7 has shown that, among the small clusters (C<sub>2</sub>, C<sub>3</sub> and C<sub>4</sub>) studied, C<sub>3</sub> trimer diffusion proceeds with a relatively small diffusion barrier (0.48 eV), showing its high mobility on the Ni surface. Therefore, in the KMC simulations, the carbon cluster diffusion will be represented by the C<sub>3</sub> trimer diffusion. This cluster was treated as one entity (C<sub>3</sub>) that diffuses as a whole on the lattice. Note that the bulk diffusion of C atoms was also implemented in the model of KMC simulations. Previous DFT studies by Abild-Pedersen et al. [25] reported that C subsurface and bulk diffusion to the CNT/Ni interface has a barrier of 1.34 and 1.80 eV, respectively. To simplify the KMC simulation model, the subsurface and bulk diffusion are treated as one single pathway that lead surface C atoms to the inner layers of the CNT. The corresponding diffusion barrier is in the range of 1.34–1.80 eV, which is in between the C subsurface and bulk diffusion barriers.

## iii) Carbon nucleation

In addition to the surface and bulk diffusion, C atoms will also nucleate together on the Ni surface and form carbon clusters of various size and configurations. As reported in Chapter 7, the nucleation of large carbon clusters is very complex: even carbon clusters with the same number of C atoms will have different configurations, e.g. chain, branch or ring, with different stabilities. To simplify the KMC simulation model, the nucleation of C<sub>2</sub> dimer and C<sub>3</sub> trimer are explicitly considered, whereas carbon clusters larger than the C<sub>3</sub> trimer are represented as single unit species (C<sub>x</sub>). The kinetics properties of the large carbon cluster (C<sub>x</sub>) were represented by that of the chain clusters. This is due to the fact that carbon chain clusters are more thermodynamically stable than the other configurations, e.g. branch and ring. Due to its relatively large size, C<sub>x</sub> cluster are assumed to remain on the same lattice site (not movable) on the Ni catalyst surface. Since C and C<sub>3</sub> are assumed as the only carbon species that can diffuse on the Ni surface, the nucleation reactions that can form C<sub>x</sub> cluster will be as follows: C<sub>3</sub>+C→C<sub>x</sub>, C<sub>2</sub>+C<sub>3</sub>→C<sub>x</sub>, C<sub>3</sub>+C<sub>3</sub>→C<sub>x</sub>, C<sub>x</sub>+C→C<sub>x</sub>, C<sub>x</sub>+C<sub>3</sub>→C<sub>x</sub>. These reactions are represented as C<sub>x</sub>(x≥3)\*+C\*(or C<sub>3</sub>\*) → C<sub>x</sub>\* (see

reaction 12 in Table 8.1). To reduce the complexity of KMC simulation model, an energy barrier of 1.31 eV was used to model these  $C_x$  cluster nucleation reactions, as shown in Table 8.1. This energy barrier was taken as the average of the nucleation barrier for the formation of  $C_4$ ,  $C_5$  and  $C_6$  chains, which is reported in Chapter 7 (section 7.3.3). Therefore, one can expect that, as more  $C_x$  clusters are formed on the Ni surface, this will deactivate the Ni catalyst reactivity by blocking the active site towards  $CH_4$  dissociation. When the Ni surface is fully covered by  $C_x$ , it stops the CNT growth. Note that the reverse C–C bond breaking reaction of  $C_x$  cluster has an averaged energy barrier of 1.55 eV; also, the  $C_x$  nucleation reaction is assumed to be irreversible in the KMC simulations.

#### *iv*) CNT growth reactions

When the adsorbed C and  $C_3$  cluster are diffused to the CNT/Ni edge sites (a nearby site of the CNT open end), they can be incorporated (or attached) into the CNT wall, and therefore contribute to the CNT growth. To model this process, a graphene edge attached on Ni (111) surface is used here to model a fraction of the CNT-catalyst interface (see Figure 8.1b). The C and  $C_3$  incorporation reactions are then studied by DFT calculations. The barriers of incorporating C and  $C_3$  into a CNT wall were calculated to be 0.76 and 1.02 eV, respectively. To simplify the KMC simulation model, the C and  $C_3$  incorporation reactions were treated as one single event with an average energy barrier of 0.89 eV. These carbon incorporation reactions are assumed to be irreversible.

### **8.2.4 Accelerated kinetic Monte Carlo (AKMC)**

As discussed above, in KMC algorithm s, the probability to choose or execute a specific event in the KMC simulations is calculated from the event's rate. Therefore, for systems that involve large differences in the rates, most of the computational time will be consumed by the event with the fastest reaction rate, and low rate events will rarely occur during the simulation although they might dominate the actual kinetics of real catalytic system. This is usually referred as stiff problems, and it represents a major challenge in KMC modeling.

In the past decades, lots of efforts have been done for developing efficient methods to overcome the stiff problem in KMC, which have met only partial success. The Poisson and binomial  $\tau$ -leap methods [46–48] can partly solve the underlying challenges by selecting multiple processes in a single KMC iteration. However, they are approximate and in some cases  $\tau$ -leap leads to unphysical results [49]. Snyder et al. [50] proposed a net-event kinetic Monte Carlo for overcoming stiffness problem for systems

involves fast reversible processes. In that study, the fast reversible processes into single was consolidated into “net events” and the associated rate of this net-event is calculated as the difference of the rates of the forward process and the reverse process. Chatterjee et al. [51] developed a so-called accelerated superbasin kinetic Monte Carlo (AS-KMC) algorithm, in which the rate constants for processes that are observed many times are lowered during the course of a simulation. As a result, rare processes are observed more frequently than in KMC and the time progresses faster. An error estimates strategy is derived for AS-KMC when the rate constants are modified. Guerrero et al.[52,53] introduced a approach for solving the stiff problems by using a logarithmic transformation of rates for calculating the distributions of event probabilities (abbreviated as Log-KMC).

For the current CNT growth systems, H and C surface diffusion event proceeds with small energy barriers and their rates are orders of magnitude faster than other processes, e.g. CH<sub>4</sub> dissociative adsorption. Thus, in conventional KMC (referred from heretofore as ConKMC), most of the computational effort will be spent on simulating the repetitive motion of H or C on the catalyst surface. That is, the simulation is “trapped” in this low barrier surface diffusion process for a large number of KMC iterations. This limits the ability to render the long-time evolution of the system.

In the present study, a rational statistical based approach, named Accelerated Kinetic Monte Carlo (AKMC), has been developed to overcome this typical problem in ConKMC. The difference between AKMC and ConKMC is the method used to treat the fast surface diffusion events and the evaluation of the slow reaction rates in the system. In AKMC, when the system is “trapped” in fast surface diffusion process, instead of running the repetitive motion of the surface diffusion event, low rate events are executed directly based on their statistical probability. Take the simplest case as an example: when there is only one H atom on the lattice, the possible events that could occur on the surface are: CH<sub>4</sub> dissociative adsorption, H surface diffusion. Based on the kinetic parameters presented in Table 8.1, H diffusion rate is estimated about  $k$  ( $\approx 10^6$ ) times faster than that of CH<sub>4</sub> dissociative adsorption. This means that, from the statistical point of view, it will take an average of  $k$  H diffusion iterations to pick up one CH<sub>4</sub> dissociative adsorption event in ConKMC simulations. However, in AKMC, instead of running H diffusion  $k$  times, CH<sub>4</sub> dissociative adsorption is directly executed, and the time step will be updated as  $\Delta t = k\Delta t'$ , where  $\Delta t'$  is the time spend for one H diffusion event and that was calculated as *a priori*. The implementation becomes more complicated when there is more than one H atom on the lattice. The possible events that could occur are H diffusion, CH<sub>4</sub> dissociation and H<sub>2</sub> production. Their corresponding rates are  $r_1$ ,  $r_2$  and  $r_3$  ( $r_3 \approx r_2 \ll r_1$ ), respectively. However, for H<sub>2</sub> production, it will be only possibly to occur when the

two H atoms are close to each other during their diffusion on the lattice. this means that the  $r_1$  and  $r_2$  exist at every H diffusion step, while the  $H_2$  production rate  $r_3$  only occurs at specific situations that H atoms are sitting at neighboring sites of the lattice. If one know the probability ( $P$ ) that having two neighboring H atoms on the lattice during H diffusion, the average rate for  $H_2$  production for each H diffusion step can be scaled to  $r_3' = Pr_3$ . The probability  $P$  can be estimated by Monte Carlo simulations: perform  $n$  steps of H diffusion step on an  $N \times N$  square lattice, and the number of times that the two H atoms sitting beside each other is counted as  $m$ . Therefore, for each H diffusion step,  $m/n$  will be the estimated probability ( $P$ ) for two H atoms sitting at neighboring sites of the lattice. Data regression returns the following relation between the probability  $P$  and the lattice size  $N$ :

$$P = \frac{1}{1667} \left(\frac{70}{N}\right)^2 \quad (8.6)$$

Now, there are three events in the system: H diffusion and  $CH_4$  dissociation and  $H_2$  production with rates of  $r_1$ ,  $r_2$  and  $r_3'$ , respectively. This means that it will take an average of  $S = r_1/(r_2 + r_3')$  H diffusion steps to execute either  $CH_4$  dissociative or  $H_2$  production event in ConKMC simulations. In AKMC, the H diffusion event is skipped, and the slow event  $CH_4$  dissociation or  $H_2$  production will be executed directly base on the probability of  $r_2/(r_2 + r_3')$  and  $r_3/(r_2 + r_3')$ , respectively. Meanwhile, the  $\Delta t$  will be updated as  $\Delta t = S\Delta t'$ . By doing this, the AKMC allows the simulation get out of the “trap” caused by the surface diffusion of H. The same is true when C diffusion event are present in the event list. Therefore, the methodology discussed above can be applied to deal with the  $H+H \rightarrow H_2$ ,  $C+C \rightarrow C_2$ ,  $C+H \rightarrow CH$  and C (or  $C_3$ )-CNT attachment events since the occurrence of these events also involve the fast surface diffusion of surface species like H, C and  $C_3$ . A detailed discussion on the scaled rates for these events is presented in Appendix B. Note that for cases that there exist one or more events whose reaction rate is close to H or C diffusion rate, the AKMC will be similar to the ConKMC algorithm. Note that, in the development of AKMC, the probability ( $P$ ) parameter used in the scaled reaction rate is developed by assuming all the surface species can move freely on the lattice. If the lattice sites are blocked by non-movable intermediates, e.g. large  $C_x$  cluster, this will change the probability ( $P$ ) that two diffusive atoms will “meet” each other, and therefore affects the accuracy of the AKMC prediction. This is rise significant problem especially at a high  $C_x$  surface coverage. In such cases, a more accurate fitting of the  $P$  parameter is required. This is the main limitation of the present AKMC algorithm. On the other hand, on a non- or relatively low  $C_x$  blocked surface, the AKMC allows the simulation of the present catalytic system  $10^5 \sim 10^6$  time faster than the ConKMC, thus making this the key benefit of the present approach. A comparison between the two approaches is presented in section 8.3. Note that the selected event can be

executed according to the reaction patterns presented in the Appendix A. For example, if the CH<sub>4</sub> dissociative adsorption event is chosen, CH<sub>3</sub> and H atom are added to two neighboring unoccupied sites in the simulation grid.

#### 8.2.4.1 Size of the lattice

The KMC simulations will be executed over Ni (111) surface represented by an N×N lattice. The edges of the simulation lattice are assumed to be the CNT/Ni intersections. Therefore, no periodic boundary conditions were applied at the edge of the simulation lattice. The Ni catalyst is assumed to be a sphere particle with a diameter of  $d$  nm. During the CNT growth, this sphere particle is lifted up with the top half surface exposed to the gas phase CH<sub>4</sub>. The surface area of this half sphere particle is  $\pi d^2/2$ , which is assumed to be equal to the surface area of the lattice  $(0.249N)^2 \text{ nm}^2$ . Note that the bonding distance between two Ni atoms on the Ni (111) surface is about 0.249 nm. This result in a relation between the diameter of the particle  $d$  and size of the lattice N as follows:

$$d = 0.249N \sqrt{\frac{2}{\pi}} \text{ nm} \quad (8.7)$$

The above equation allows us to predict the CNT growth rate as a function of the size of the Ni catalyst particle.

### 8.3 Results and discussion

A series of KMC simulations for the Ni catalytic CNT growth was performed at different temperatures ranging from 500 to 650 °C over the Ni (111) surface to predict the CNT growth kinetics. The gas phase is pure CH<sub>4</sub>, and the pressure was set constant at 1 atm. The simulation conditions were chosen to mimic those of the experiments of Amin et al. [54], in which porous alumina supported Ni were used as the catalysts with 100% methane at a flow rate of 240 ml/min.

In order to validate the proposed AKMC algorithm, the CNT growth rate at different temperatures predicted via ConKMC and AKMC have been compared (Figure 8.3). The results show a reasonable quantitative agreement in the solution of the two methods. That is, the CNT growth rate predicted by AKMC agrees with that obtained by ConKMC. However, the CPU time consumed by each method differs substantially. At T=500°C and simulation time  $t \approx 8.2 \times 10^{-4}$  s, the mean CPU time spend with ConKMC is

about 70h. However, the CPU time required by the AKMC is around 0.6s, which is approximately  $4 \times 10^5$  times faster than the traditional KMC method (ConKMC). Note that the mean CPU time is obtained by performing multiple runs and that the markers in the figures represent the min/max obtained from these multiple simulations.

Figure 8.3 also shows that the computational speed-up obtained with AKMC depends on the temperature of the system. As the temperature increases, the rates of slow events increased more rapidly than that of the fast events. This reduces the rate scale separations (ratio of rate constant between the fast and slow event) of the systems. For instance, the rate scale separations between C diffusion and  $\text{CH}_4$  dissociation is  $4.2 \times 10^8$  at  $T=650^\circ\text{C}$ ,  $8.1 \times 10^8$  at  $T=600^\circ\text{C}$ , and  $3.6 \times 10^9$  at  $T=500^\circ\text{C}$ . This shows that the CPU time for the AKMC method depend strongly on the rate scale separation.

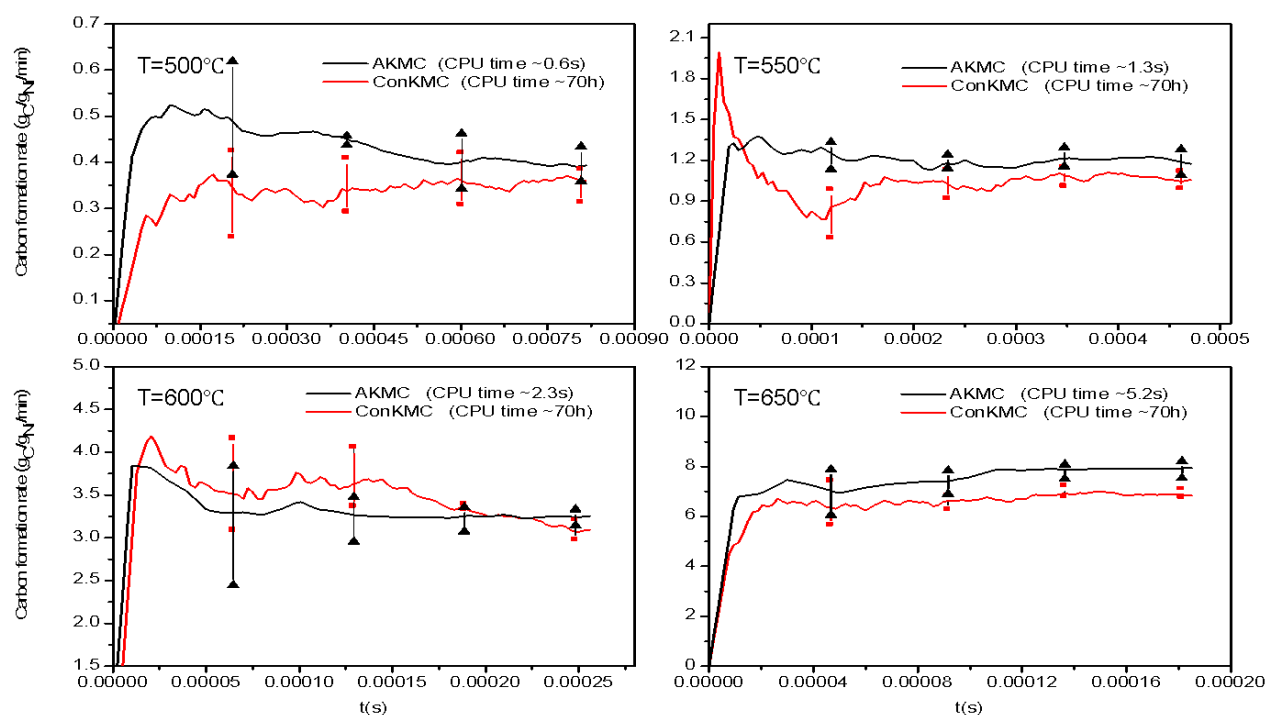


Figure 8.2 CNT growth rate predicted by a ConKMC and AKMC simulation by using the same kinetic parameters under different temperature on a  $150 \times 150$  lattice ( $d=30\text{nm}$ ).

### 8.3.1 Validation of the CNT growth model

The experimental study of Amin et al. [54] was used as a reference in the present AKMC simulations to validate the present microkinetic model. In that study, the CNT growth rate at 500, 550, 600 and  $650^\circ\text{C}$

was reported (Figure 8.4), and they observed that the diameters of the Ni particles are in the range of 20–40 nm at 550°C. Therefore, the AKMC simulations were first performed at 550 °C on a 100×100 and 200×200 lattice, which correspond to Ni particles with diameters around 20 and 40nm, respectively. The corresponding CNT growth rate predicted at T=550°C by AKMC simulations are 1.78 and 0.91g<sup>C</sup>/g<sup>Ni</sup>/min for the 100×100 and 200×200 lattices, respectively,. These estimates are in the same order with the reported experimental growth rate 0.70g<sup>C</sup>/g<sup>Ni</sup>/min. Although the CNT growth rate predicted with the microkinetic model was overestimated, this deviation is related to the size of the Ni particle (the lattice) and the kinetic parameters (energy barriers) calculated from DFT, which are the key inputs to the model. Therefore, the effect of particle size on the CNT growth rate and its sensitivity on some of the important kinetic parameters, e.g. the energy barrier for CH<sub>4</sub> dissociation, C surface diffusion and C–CNT incorporation, were studied and described next

### 8.3.2 Ni particle size effect

As reported in many experimental studies [55–61], as the growth temperature increases, more agglomeration occurs resulting in larger-sized catalyst particles and therefore larger diameter nanotubes. Fu et al. [56] reported that CNTs synthesized at 500°C, 550°C, and 700°C had outer diameter distribution of 15 ~ 30, 20 ~ 40, and 20 ~ 90 nm, respectively. Michalkiewicz et al., [57] reported that the average diameters of carbon nanomaterial produced over Ni/ZSM–5 (300) increased from 23 to 57 nm as the temperature increased from 450 to 650°C. Note that this is only the average diameter of the CNT, i.e., there will be a wider range of the size distribution at different temperatures. Based on these experimental observations, a size distribution of 20–80nm at reaction temperatures from 500–650°C was considered in the present study. Figure 8.4 shows the CNT growth rates predicted by the AKMC simulations at different temperatures and size of Ni particles. As shown in this Figure, the AKMC simulation follows the behaviour exhibited by the experimental data. Moreover, a qualitative agreement between the experimental data and AKMC predictions was observed at the following the particle size distribution: d=40nm at T=500°C, 40~60nm at 550°C, 60~80nm at T=600°C and ~80nm at T=650°C. These results suggests that the CNT scheme shown in Table 8.1 captures the essential surface chemistry involved in the growth of CNTs on Ni. Moreover, it also validates the proposed CNT growth mechanism by the surface diffusion of C atoms and small carbon clusters.

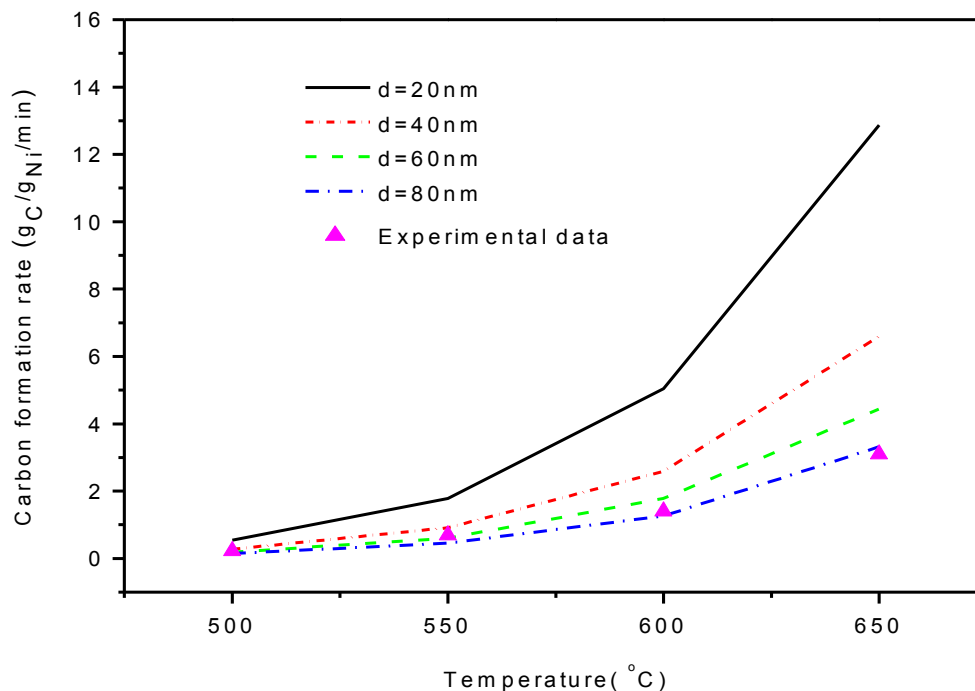


Figure 8.3 CNT growth rates obtained at different temperatures predicted by AKMC simulations. The experimental data is taken from reference [54].

### 8.3.3 Sensitivity on the kinetic parameters

Thus far, the CNT growth rate predicted by AKMC simulations are obtained by using the kinetic parameters directly obtained from DFT calculations. Previous experimental and theoretical studies have reported that the activation energies associated with Ni catalytic methane cracking are in the range of 0.91–1.01 eV [62-64] and 1.06–1.32 eV [65-67], respectively. These discrepancies in the results illustrate the uncertainties in the DFT estimation of activation energies, which translates into uncertainties in the predicted CNT growth rate. To examine the sensitivity of the predicted CNT growth rates on the energetics used in the AKMC simulations, the uncertainty associated with the energetics in the critical elementary steps were studied.

The important elementary steps for Ni catalytic CNT growth are *i*) CH<sub>4</sub> dissociative adsorption, which is the rate-determining step for CH<sub>4</sub> dissociation on Ni, producing the feeding source of C atoms; *ii*) C surface diffusion, which determines the rate that the C atom can reach the CNT/Ni; *iii*) C

incorporation reaction at the CNT/Ni edges, which determines the rate that C atoms contribute to the CNT growth; *iv*)  $C_x$  cluster nucleation, i.e., the formation rate of non-movable large  $C_x$  cluster that is directly related with the deactivation of Ni catalyst. To evaluate the sensitivity of the predicted CNT growth rates on the energetics of these reactions, their energy barriers were adjusted with reasonable ranges ( $\pm 10\%$ ). Note that the energetic parameters for all the other elementary steps were kept fixed in the analysis. Figure 8.5 compares the simulation results obtained at different deviations in  $CH_4$  dissociation barriers. The results show that CNT growth rate is very sensitive to the  $CH_4$  dissociation barrier, i.e., uncertainty in the  $CH_4$  dissociation barrier of 0.05 eV yields an uncertainty in the CNT growth rate of a factor of 2 at the investigated temperatures. This indicates that  $CH_4$  dissociative adsorption is the rate-determining step for CNT growth. The analysis also show that the deviation ( $\pm 10\%$ ) of the barriers of the C surface diffusion, C incorporation reaction and  $C_x$  cluster nucleation has only minor effects on the steady state CNT growth rate. Since variability is very small, this effect is not show in Figure 8.5. However, they are expected to affect the deactivation of the catalyst. The relative barriers for the C–CNT incorporation and  $C_x$  cluster formation determined the competition between CNT growth and catalyst deactivation. Low  $C_x$  cluster nucleation barrier means high probability for  $C_x$  cluster formation, which will results in a fast deactivation of the catalyst. On the other hand, low barrier for C–CNT incorporation will make the addition of surface C atoms in to CNT wall much easier. This reduces the chances for C atoms to remain on the catalyst surface and therefore hinders the formation of  $C_x$  clusters. However, the study on the uncertainty of these barriers on catalyst deactivation is limited by the computational resources, i.e., no deactivation was observable while simulating the model for a reasonable CPU time (7days).

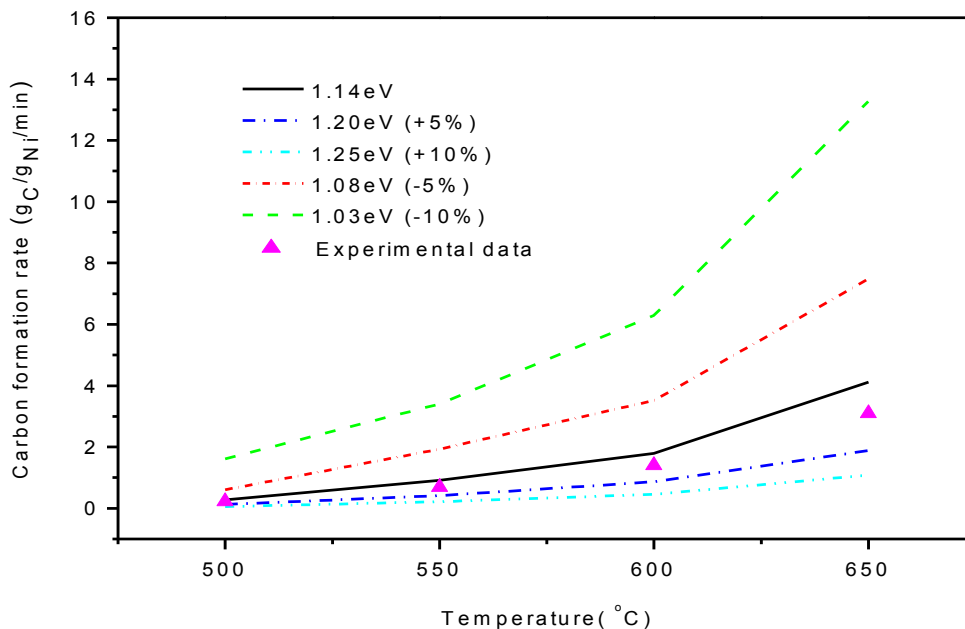


Figure 8.4 Sensitivity of the CNT growth rates on the CH<sub>4</sub> dissociation energetics. The simulations were performed on different particle size at different temperatures: d=40nm at T=500°C and 550°C, d=60nm at T=600°C and d=60nm at T=650°C.

### 8.3.4 Role of C cluster surface diffusion

As discussed in section 8.2.1, the C<sub>3</sub> trimer surface diffusion and incorporation to the CNT wall were explicitly considered in the proposed CNT growth mechanism. To determine the role of cluster surface diffusion on the CNT growth kinetics, simulations were carried out in both the presence and absence of C<sub>3</sub> surface diffusion in the model. Note that in the absence of C<sub>3</sub> surface diffusion means that only C atoms were allowed to move on the catalyst surface. The results show that the simulations carried out in the absence of C<sub>3</sub> cluster surface diffusion resulted in an initial CNT growth rate of 0.41 g<sup>C</sup>/g<sup>Ni</sup>/min at T=500°C and d=30nm. The CNT growth rate starts to decrease after t=3s, showing the fast deactivation of the Ni catalyst due to the formation of C<sub>x</sub> clusters. This is because the relatively small energy barrier for C<sub>2</sub> dimer and C<sub>3</sub> trimer nucleation lead to a relatively easy formation of small C<sub>2</sub> and C<sub>3</sub> clusters, when there is enough C atoms on the catalyst surface. Since C<sub>3</sub> trimer are assumed to remain on the same lattice site on the catalyst surface, it will be fast nucleated with oncoming C atoms and be able to form larger

carbonaceous clusters ( $C_x$ ), which will eventually deactivate the catalyst. Simulations carried out in the presence of  $C_3$  surface diffusion resulted in a same CNT steady growth rate with that obtained in the absence of  $C_3$  surface diffusion. However, by allowing the  $C_3$  cluster to diffuse on the surface and nucleate to CNTs, no deactivation is observed during the first 8 mins of the reaction process. Note that the CPU times required to reach  $t=8$ mins at  $T=500^\circ\text{C}$  and  $d=30\text{nm}$  is about 130h. The KMC simulation indicates that sufficiently rapid C and  $C_3$  cluster diffusion is required to avoid the catalyst encapsulation. During CNT growth, the deposited C atoms together with the small clusters must incorporate into the CNT wall through the CNT-catalyst contact edge.

### 8.3.5 Carbon bulk diffusion and bamboo-like CNT

As reported in many studies, CNT can be produced with the bamboo structure [59,60,68,69]. It is believed that the surface and bulk diffusions of carbons play an important role in determining their structure [68-70]: C atoms surface diffusion forms the walls of the carbon nanotubes from the side surface of the catalyst, whereas the inner separation layers were formed by carbon bulk diffusion. Due to difference between the rate of carbon surface and bulk diffusion in the catalyst, then a bamboo-like CNT will be produced [68].

As discussed in section 8.2, both surface and bulk diffusion of C atoms is considered in the proposed CNT growth mechanism. Therefore, the C atoms surface and bulk diffusion can explicitly tracked during the KMC simulation model, and therefore evaluate the effect of particle size and temperature on the structure of the bamboo-like CNTs by counting the number of C atoms ( $N_b$ ) that diffuse through the Ni particle and the number of C atoms ( $N_s$ ) that contributed to CNT walls by surface diffusion. A high  $N_b/N_s$  ratio represents more C atoms was diffused into the bulk of Ni. Figure 8.5 shows the calculated  $N_b/N_s$  ratio at various sizes of particle and temperature. The results show that CNT growth by C surface diffusion is favoured with small particle size and low temperature. On other hand, an increase number of C atoms will go through bulk diffusion on a large sized particle and high temperature. This is due to the fact that, on a small catalytic particle, the surface diffusion of C atoms will be restricted to a limited area. This increases the probability that the surface C atoms diffuse to the CNT/Ni edges and then promote the C incorporation into CNT wall. For the temperature effect, as discussed in section 8.3 the time scale separation decreases as the temperature increases. That is, as the temperature increases, the slow bulk diffusion rate increases more rapidly than that of the fast surface diffusion. Consequently, there will be more surface C atoms contribute to the CNT growth by the surface diffusion at a low temperature. Since

the separation layers are grown mainly by the bulk diffusion of carbons, its rate decreases as the particle size or temperature decreases. Consequently, at low temperatures or with a small particle size at which bulk diffusion is hampered, one may expect higher spacing between two adjacent bamboo structures; whereas at high temperatures or with a large particle, the spacing is relatively short due to the rapidly increase of bulk diffusion rate. These results are in good agreements with the experimental observations [69-71].

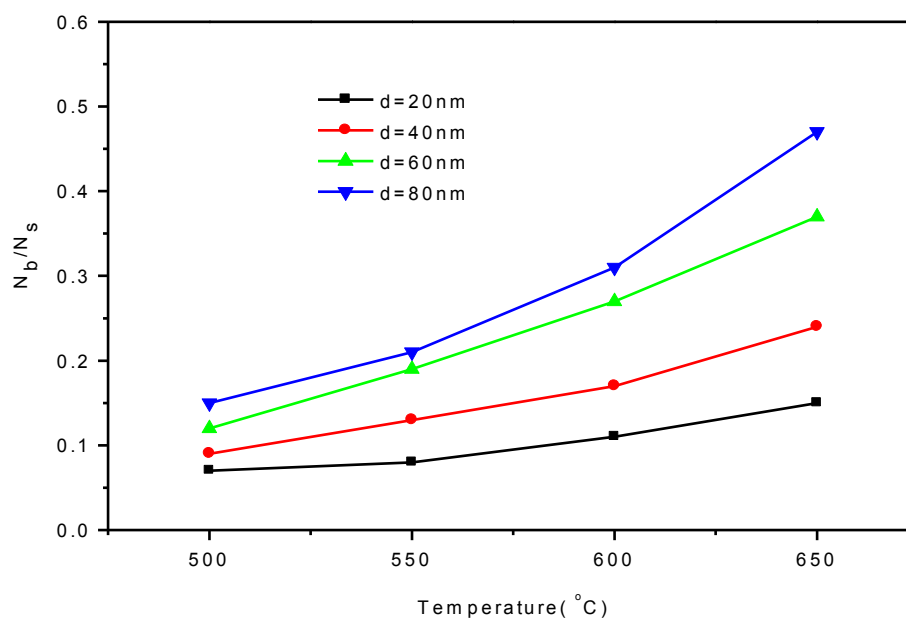


Figure 8.5 The ratio  $S$  between number of C atoms that go through bulk diffusion and surface diffusion at different temperatures and size of Ni particles.

## 8.4 Summary

A KMC model was constructed and used to follow the molecular transformations and the kinetics for the CNT growth from  $\text{CH}_4$  feedstock over the Ni catalyst. The CNT growth kinetics was established from first-principles-based DFT calculations over Ni (111) surface. The *ab initio* results were used to construct a kinetic database for a novel variable time step KMC framework that was developed to overcome the large disparities in time scale in the present system. The simulations explicitly follow the elementary steps involved in the CNT growth that include  $\text{CH}_4$  dissociation, C surface and bulk diffusion, C atoms

nucleation, C<sub>3</sub> trimer diffusion and C and C<sub>3</sub> incorporation into CNT wall. The KMC simulation matches experiment measurements and provide new insights regarding the mechanism of CNT growth.

The KMC simulations leads to some general conclusions regarding the CNT growth process over Ni catalyst: *i*) the growth of CNT is due to the addition and attachment of C adatoms and small carbon clusters, e.g. C<sub>3</sub>, through surface diffusion at the multistep graphite-Ni edges; *ii*) the surface diffusion of small carbon clusters, e.g. C<sub>3</sub> trimer, is crucial for a realistic description of the CNT growth kinetics since it prevents further nucleation of the C atoms on the catalyst surface, and therefore inhibits fast deactivation of the catalyst; *iii*) sensitivity analyses reveal that the overall CNT growth rate is dominated by the dissociative adsorption of CH<sub>4</sub> onto the Ni surface; *iv*) the activity of the Ni catalyst is controlled by the balance of C atoms nucleation on the surface, C and C<sub>3</sub> trimer surface diffusion and their addition in to the CNT wall at the boundary of the Ni–CNT growth interface. If the mobility and addition of these carbon species is not sufficient, the slowly moving C atoms may nucleate into graphitic islands on the catalyst surface and eventually encapsulate the catalyst; *v*) the differences between the rates of C surface and bulk diffusion in the catalyst result in the formation of the bamboo-like CNT; its structure depends on the size of the Ni particle and temperature of the system.

## Chapter 9

### Conclusions and Recommendations

#### 9.1 Conclusions

The focus of this research was to provide a comprehensive understanding of Ni catalytic methane cracking and carbon nanotube/nanofiber growth mechanism by using DFT calculations. The influence of the Ni catalyst surface topologies and the carbon depositions on the methane dissociation properties were studied first. It was found that the less packed Ni surfaces, e.g. Ni (100) and Ni (553) are generally more reactive towards  $\text{CH}_x$  (1-4) adsorption and dissociation than the close packed Ni (111) surface. This is explained by the investigation of the d-band center of the Ni atoms on the three surfaces. The results show that the Ni atoms with low co-ordination number shifted the d-band center towards the Fermi level and changed the width of the d-band, which makes the Ni (553) and Ni (100) surfaces more reactive. The results also suggest that the C formation is highly likely to occur at the step and at the open surfaces. For the effect of carbon deposition, the results show that  $\text{CH}_x$  species adsorption on C deposited Ni surface is less stable as compared with that on Ni (111) clean surface. Moreover, the study of the  $\text{CH}_x$  dehydrogenation shows that the presence of carbon increases the barrier for  $\text{CH}_x$  activation, especially for  $\text{CH}_x$  dehydrogenation on Ni (111)- $\text{C}_{\text{on}}$  where the Ni surface was pre-covered with surface C atom:  $\text{CH}_x$  species encounter a highest energy barrier for dissociation due to the electronic deactivation induced by C-Ni bonding and the strong repulsive carbon-adsorbates interaction. This study provided a more realistic estimation of the kinetic parameters for this system, where the effect of carbon deposition on the  $\text{CH}_x$  dissociation barriers should be considered in the analysis.

The study of Ni catalytic methane cracking is then further extended by considering the effect of  $\gamma$ - $\text{Al}_2\text{O}_3$  support on the energetics of  $\text{CH}_4$  and  $\text{H}_2$  dissociation. This study found that  $\text{CH}_4$  and  $\text{H}_2$  dissociations are kinetically preferred at the particular Ni atoms located at the nickel-alumina interface when compared with the top of the Ni cluster. The same is true for  $\text{CH}_3$  and H adsorption. The Hirshfeld analysis of the charges of the surface Al and O atoms showed that the Al atom works primarily as a charge donation partner. Thus, it is expected that the interface adsorption is stabilized by the Al (donor)-Ni-adsorbates (acceptor) effect. The results obtained from the DFT calculations have indicated that the metal-oxide interface plays an essential role in the dissociation of  $\text{CH}_4$  and  $\text{H}_2$ . Moreover, in this study, the decrease of the metal support interaction was observed upon  $\text{CH}_3$  and H adsorption on both  $\text{S}(\text{Ni}_4)$  and  $\text{NS}(\text{Ni}_4)$ . The present study shows that the bonding of adsorbates to the cluster affects the

cluster structure and its bonding to the support, resulting in a decrease in the metal-support interaction. This observation might provide insight regarding the interaction between the Ni and the  $\gamma$ -Al<sub>2</sub>O<sub>3</sub> support and the carbon nanotube (CNT) growth mechanism, in which the weak metal-support interaction is believed to contribute to the tip growth mode of CNT.

The carbon atoms, as a result of the methane cracking reaction, can form various carbonaceous materials, i.e., CNTs and graphene, depending on the catalyst and reaction conditions. To have a better understanding of the role of metal elements in the catalytic growth of these carbonaceous materials, the energetics of the crucial steps involved in the growth of CNTs/graphene, e.g., C–H bond activation, C atoms diffusion and the nucleation of diatomic carbon and trimer species on the (111) facets of transition metals (Fe, Co, Ni, Cu), was investigated using DFT. It was found that Fe is the most active metal for CH<sub>x</sub> dissociation followed by Ni, Co and Cu. Also, the mobility of the surface C atoms follows the order: Cu < Ni < Co < Fe. A somewhat similar trend was observed for the carbon nucleation barriers: Cu < Ni  $\approx$  Co < Fe. These observations explain why Ni-based catalyst is a suitable CVD substrate for growing CNT: the relatively low energy barrier for C–H bond activation on Ni provides an easy source for the C atoms; the good mobility of the surface C atoms, together with high C–C nucleation barriers, allows the C atoms easily diffuse to the CNTs/Ni edge and contribute to the CNT growth, before they nucleate together and deactivate the Ni surface. Meanwhile, this study also showed that Cu may be an appropriate catalyst for the CVD synthesis of graphene due to the particularly low diffusion and nucleation barriers of C adatoms on Cu, which suggest that C atoms tend to be more uniformly distributed on the Cu surface and can easily nucleate the Cu surface. The low reactivity of Cu towards C–H bond activation, however, will limit the graphene growth rate. Therefore, Cu-based catalyst doped by CH<sub>x</sub> dissociation reactive Fe and Ni atoms, i.e., Cu<sub>8</sub>Fe and Cu<sub>8</sub>Ni alloy, were proposed. The DFT results study show that the designed alloys (especially Cu<sub>8</sub>Ni) increase the reactivity for CH<sub>x</sub> dehydrogenation, indicating that it can be a suitable catalyst for the mass production of graphene.

Ni-based catalyst has been supported by previous DFT calculations as a suitable substrate for CNT growth. To provide more insights regarding the Ni catalytic CNT/CNF growth mechanism, a systematic study of the behavior of the carbon atom and cluster during the early stages of CNT growth on Ni (111) was performed using DFT calculations. The structure and relative stability of adsorbed C intermediates, and their mobility on the Ni (111) surface were investigated in this work. Moreover, the reaction pathways and energetics for the nucleation of the carbon clusters on the Ni (111) surface were also explored. The calculations show that carbon clusters are more stable than the separated carbon atoms.

This indicates that, thermodynamically, atomic carbons tend to nucleate to form carbon clusters on the Ni (111) surface. There is also a thermodynamic preference for different carbon cluster configurations: linear carbon structures are more stable than branched and ring carbon configurations of equal sizes. This study also found that the monomer is not the only mobile species on the Ni (111) surface; small clusters, at least up to the tetramer, are also mobile. The calculation of the interactions between the carbon cluster and the Ni surface shows that branched carbon clusters have stronger interaction with the Ni substrate when compared to the carbon chains. This indicates that carbon chains generally have higher mobility than branched carbons. This cluster mobility is expected to play an important role in the reaction kinetics of C on Ni. Moreover, it was found that the formation of C chain and branched species by the addition of both the single C atom and C<sub>3</sub> trimer is possible. These new insights about the properties of C cluster are crucial to understand the growth mechanism of CNT.

Finally, a first principle-based KMC model for CNT growth from CH<sub>4</sub> feedstock over the Ni catalyst was developed, in which the energetic results obtained from DFT calculations were used to construct the kinetic database for a novel KMC framework (AKMC) that are developed for overcoming large disparities in time scale of the system. The proposed KMC simulation explicitly follows the elementary steps involved in the CNT growth that include CH<sub>4</sub> dissociation, C surface and bulk diffusion, C cluster nucleation and diffusion, CNT growth contributed by C and C<sub>3</sub> incorporation into CNT wall. The first-principles-based KMC simulation matches experiment measurements verifying the proposed CNT growth mechanism. This study provides new insights regarding the mechanism of CNT growth. That is, CNT growth is dominated by the surface diffusion of carbon species. Moreover, the surface diffusion of the small carbon cluster, e.g. trimer, is also a critical step in the growth mechanism of the CNT. It prevents further nucleation of the C atoms on the catalyst surface, and therefore inhibits the deactivation of the catalyst.

## 9.2 Recommendations

This research represents a promising step towards a clear understanding of methane catalytic cracking and CNT growth mechanism. However, there are still many challenges ahead for the development of novel catalysts methane catalytic cracking and CNT growth. The following are recommendations for future research:

### i) Catalyst deactivation due to C surface nucleation

Even though good agreement between the KMC simulated CNT growth rate results and the experimental data were obtained, the current KMC simulation is not fully applicable to model the catalyst deactivation resulted by the formation of large non-movable  $C_x$  clusters. This is due to the limitations of the present AKMC algorithm in calculating the scaled reaction rate, which has been discussed in section 8.2.4, Chapter 8. Therefore, an advanced KMC algorithm and modeling method that can accurately describe the catalyst deactivation due to large C cluster formation is needed. This study may provide insight for the catalyst deactivation during the CNT growth.

### ii) The effects of alloys

The present study has shown that methane dissociation and CNT growth properties varies with different transition metals (e.g. Ni, Cu, Co and Fe). It has also shown that Ni- catalyst can be good candidate for CNT growth. However, knowledge of the alloying effect on the Ni catalytic CNT growth is still limited. Theoretical study on this topic is rarely reported in the open literature. Such studies will help for a better design of catalyst for CNT growth.

### iii) The role of the oxide supports in the CNT growth

Regarding the CNT growth mechanism, the current studies have only focused on the carbon diffusion and nucleation on the metal catalyst surface. These reactions, however, may also occur on the oxide supports. The study on the role of the oxide supports in the CNT growth will further extends the understanding of the CNT growth mechanism.

## Publications

1. Li J, Croiset E, Ricardez-Sandoval L. Methane dissociation on Ni (100), Ni (111), and Ni (553): A comparative density functional theory study. *Journal of Molecular Catalysis A: Chemical*, 2012; 365:103–114
2. Li J, Croiset E, Ricardez-Sandoval L. Effect of metal–support interface during CH<sub>4</sub> and H<sub>2</sub> dissociation on Ni/ $\gamma$ -Al<sub>2</sub>O<sub>3</sub>: a density functional theory study. *The Journal of Physical Chemistry C*, 2013; 117: 16907–16920
3. Li J, Croiset E, Ricardez-Sandoval L. Carbon clusters on the Ni (111) surface: a density functional theory study. *Physical Chemistry Chemical Physics*, 2014; 16: 2954–2961
4. Li J, Croiset E, Ricardez-Sandoval L. Effect of carbon on the Ni catalyzed methane cracking reaction: A DFT study. *Applied Surface Science*, 2014; 311: 435–442
5. Li J, Croiset E, Ricardez-Sandoval L. Effects of metal elements in catalytic growth of carbon nanotubes/graphene. *Applied Surface Science*, 2014, Submitted.
6. Li J, Croiset E, Ricardez-Sandoval L. Carbon nanotube growth: first-principles-based Kinetic Monte Carlo simulations. In preparation.
7. Hassan FM, Chabot V, Li J, Kim BK, Ricardez-Sandoval L, Yu A. Pyrrolic-structure enriched nitrogen doped graphene for highly efficient next generation supercapacitors. *Journal of Materials Chemistry A*, 2013; 1: 2904–2912

## Copyright Permissions



RightsLink®

Home

Account  
Info

Help



**Title:** Methane dissociation on Ni (100), Ni (111), and Ni (553): A comparative density functional theory study  
**Author:** Jingde Li, Eric Croiset, Luis Ricardez-Sandoval  
**Publication:** Journal of Molecular Catalysis A: Chemical  
**Publisher:** Elsevier  
**Date:** December 2012  
Copyright © 2012, Elsevier

Logged in as:  
Jingde Li  
Account #:  
3000782230

LOGOUT

### Order Completed

Thank you very much for your order.

This is a License Agreement between Jingde Li ("You") and Elsevier ("Elsevier"). The license consists of your order details, the terms and conditions provided by Elsevier, and the [payment terms and conditions](#).

[Get the printable license.](#)

License Number	3397811502950
License date	May 28, 2014
Licensed content publisher	Elsevier
Licensed content publication	Journal of Molecular Catalysis A: Chemical
Licensed content title	Methane dissociation on Ni (100), Ni (111), and Ni (553): A comparative density functional theory study
Licensed content author	Jingde Li, Eric Croiset, Luis Ricardez-Sandoval
Licensed content date	December 2012
Licensed content volume number	365
Number of pages	12
Type of Use	reuse in a thesis/dissertation
Portion	full article
Format	both print and electronic
Are you the author of this Elsevier article?	Yes
Will you be translating?	No
Title of your thesis/dissertation	Theoretical Investigation of Catalytic Methane Cracking and Carbon Nanotube Growth
Expected completion date	Aug 2014
Estimated size (number of pages)	170
Elsevier VAT number	GB 494 6272 12
Permissions price	0.00 USD
VAT/Local Sales Tax	0.00 USD / 0.00 GBP
Total	0.00 USD

ORDER MORE...

CLOSE WINDOW

Copyright © 2014 Copyright Clearance Center, Inc. All Rights Reserved. [Privacy statement](#).  
Comments? We would like to hear from you. E-mail us at [customer@copyright.com](mailto:customer@copyright.com)



**Title:** Effect of Metal–Support Interface During CH<sub>4</sub> and H<sub>2</sub> Dissociation on Ni/γ-Al<sub>2</sub>O<sub>3</sub>: A Density Functional Theory Study

**Author:** Jingde Li, Eric Croiset, and Luis Ricardez-Sandoval

**Publication:** The Journal of Physical Chemistry C

**Publisher:** American Chemical Society

**Date:** Aug 1, 2013

Copyright © 2013, American Chemical Society

Logged in as:  
Jingde Li  
Account #:  
3000782230

[LOGOUT](#)

## PERMISSION/LICENSE IS GRANTED FOR YOUR ORDER AT NO CHARGE

This type of permission/license, instead of the standard Terms & Conditions, is sent to you because no fee is being charged for your order. Please note the following:

- Permission is granted for your request in both print and electronic formats, and translations.
- If figures and/or tables were requested, they may be adapted or used in part.
- Please print this page for your records and send a copy of it to your publisher/graduate school.
- Appropriate credit for the requested material should be given as follows: "Reprinted (adapted) with permission from (COMPLETE REFERENCE CITATION). Copyright (YEAR) American Chemical Society." Insert appropriate information in place of the capitalized words.
- One-time permission is granted only for the use specified in your request. No additional uses are granted (such as derivative works or other editions). For any other uses, please submit a new request.

[BACK](#)

[CLOSE WINDOW](#)

## Acknowledgements to be used by RSC authors

Authors of RSC books and journal articles can reproduce material (for example a figure) from the RSC publication in a non-RSC publication, including theses, without formally requesting permission providing that the correct acknowledgement is given to the RSC publication. This permission extends to reproduction of large portions of text or the whole article or book chapter when being reproduced in a thesis.

The acknowledgement to be used depends on the RSC publication in which the material was published and the form of the acknowledgements is as follows:

- For material being reproduced from an article in *New Journal of Chemistry* the acknowledgement should be in the form:
  - [Original citation] - Reproduced by permission of The Royal Society of Chemistry (RSC) on behalf of the Centre National de la Recherche Scientifique (CNRS) and the RSC
- For material being reproduced from an article *Photochemical & Photobiological Sciences* the acknowledgement should be in the form:
  - [Original citation] - Reproduced by permission of The Royal Society of Chemistry (RSC) on behalf of the European Society for Photobiology, the European Photochemistry Association, and RSC
- For material being reproduced from an article in *Physical Chemistry Chemical Physics* the acknowledgement should be in the form:
  - [Original citation] - Reproduced by permission of the PCCP Owner Societies
- For material reproduced from books and any other journal the acknowledgement should be in the form:
  - [Original citation] - Reproduced by permission of The Royal Society of Chemistry

The acknowledgement should also include a hyperlink to the article on the RSC website.

The form of the acknowledgement is also specified in the RSC agreement/licence signed by the corresponding author.

Except in cases of republication in a thesis, this express permission does not cover the reproduction of large portions of text from the RSC publication or reproduction of the whole article or book chapter.

A publisher of a non-RSC publication can use this document as proof that permission is granted to use the material in the non-RSC publication.



**Title:** Effect of carbon on the Ni catalyzed methane cracking reaction: A DFT study  
**Author:** Jingde Li, Eric Croiset, Luis Ricardez-Sandoval  
**Publication:** Applied Surface Science  
**Publisher:** Elsevier  
**Date:** 21 May 2014  
Copyright © 2014, Elsevier

Logged in as:  
Jingde Li  
Account #:  
3000782230  
[LOGOUT](#)

## Order Completed

Thank you very much for your order.

This is a License Agreement between Jingde Li ("You") and Elsevier ("Elsevier"). The license consists of your order details, the terms and conditions provided by Elsevier, and the [payment terms and conditions](#).

[Get the printable license.](#)

License Number	3411400548135
License date	Jun 17, 2014
Licensed content publisher	Elsevier
Licensed content publication	Applied Surface Science
Licensed content title	Effect of carbon on the Ni catalyzed methane cracking reaction: A DFT study
Licensed content author	Jingde Li, Eric Croiset, Luis Ricardez-Sandoval
Licensed content date	21 May 2014
Number of pages	1
Type of Use	reuse in a thesis/dissertation
Portion	full article
Format	both print and electronic
Are you the author of this Elsevier article?	Yes
Will you be translating?	No
Title of your thesis/dissertation	Theoretical Investigation of Catalytic Methane Cracking and Carbon Nanotube Growth
Expected completion date	Aug 2014
Estimated size (number of pages)	170
Elsevier VAT number	GB 494 6272 12
Permissions price	0.00 USD
VAT/Local Sales Tax	0.00 USD / 0.00 GBP
Total	0.00 USD

## References

### Chapter 1

- [1] Wee J, Lee K.Y. Overview of the development of CO-tolerant anode electrocatalysts for proton-exchange membrane fuel cells. *J. Power Sources* 2006; 157: 128–135.
- [2] Bhatia KK, Wang CY. Transient carbon monoxide poisoning of a polymer electrolyte fuel cell operating on diluted hydrogen feed. *Electrochimica Acta*. 2004; 49: 2333–2341.
- [3] Amina AM, Croiset E, Epling W. Review of methane catalytic cracking for hydrogen production. *Int. J. Hydrogen Energy* 2011; 36: 2904–2935
- [4] Rahman M, Croiset E, et al. Catalytic decomposition of methane for hydrogen production. *Topics in Catalysis* 2006; 37: 137–145.
- [5] Dussault, L, Dupin J. C, et al. Development of Ni–Cu–Mg–Al catalysts for the synthesis of carbon nanofibres by catalytic decomposition of methane. *J. Catal.* 2007; 251: 223–232.
- [6] Ermakova, MA, Ermakov DY, et al. Effective catalysts for direct cracking of methane to produce hydrogen and filamentous carbon: Part I. Nickel catalysts. *Appl. Catal. A: General*. 2000; 201: 61–70.
- [7] Aiello, R, Fiscus JE, et al. Hydrogen production via the direct cracking of methane over Ni/SiO<sub>2</sub>: catalyst deactivation and regeneration. *Appl. Catal. A: General*. 2000; 192: 227–234.
- [8] Takenaka, S, Kobayashi S, et al. Ni/SiO<sub>2</sub> catalyst effective for methane decomposition into hydrogen and carbon nanofibre. *J. Catal.* 2003; 217: 79–87.
- [9] Niu C, Sichel EK, Hoch R, Moy D, Tennent H. High power electrochemical capacitors based on carbon nanotube electrodes. *Appl. Phys. Lett.* 1997; 70: 1480–1482.
- [10] Xie H, Lee H, Youn W. Nanofluids containing multiwalled carbon nanotubes and their enhanced thermal conductivities. *J. Appl. Phys.* 2003; 94: 4967–4971.
- [11] Gadd GE, Blackford M, Moricca S, Webb N, et al. The world's smallest gas cylinders? *Science*. 1997; 277: 933–936
- [12] Dillon AC, Jones KM, Bekkedahl TA, Klang CH, Bethune DS, Heben MJ. Storage of hydrogen in single-walled carbon nanotubes. *Nature*, 1997; 386: 377–379.
- [13] Yang QY, Maynard KJ, Johnson AD, Ceyer ST. The structure and chemistry of CH<sub>3</sub> and CH radicals adsorbed on Ni (111). *J. Chem. Phys.* 1995; 102: 7734–7749.
- [14] Michaelides A, Hu P. A density functional theory study of CH<sub>2</sub> and H adsorption on Ni (111). *J. Chem. Phys.* 2000; 112: 6006–6014.
- [15] Haroun MF, Moussounda PS, Légaré P. Dissociative adsorption of methane on Ni (111) surface with and without adatom: A theoretical study. *J. Mol. Struct. THEOCHEM*. 2009; 903: 83–88.
- [16] Lai W, Xie D, Zhang DH. First-principles study of adsorption of methyl, coadsorption of methyl and hydrogen, and methane dissociation on Ni (100). *Surf. Sci.* 2005; 594: 83–92.
- [17] Nave S, Tiwari AK, Jackson B. Methane dissociation and adsorption on Ni (111), Pt (111), Ni (100), Pt (100), and Pt (110)–(1×2) : Energetic study *J. Chem. Phys.* 2010;132: 054705 1–12.
- [18] Wang SG, Cao DB, Li YW, Wang J, Jiao H. CH<sub>4</sub> dissociation on Ni surfaces: density functional theory study. *Surf. Sci.* 2006; 600: 3226–3234.
- [19] Bunnik BS, Kramer GJ. Energetics of methane dissociative adsorption on Rh {111} from DFT calculations. *J. Catal.* 2006; 242: 309–318.
- [20] Tiwari AK, Nave S, Jackson B. Methane dissociation on Ni (111): A new understanding of the lattice effect. *Phys. Rev. Lett.* 2009; 103: 253201 1–4.
- [21] Zuo Z, Huang W, Han P, Li Z. A density functional theory study of CH<sub>4</sub> dehydrogenation on Co(111). *Appl. Surf. Sci.* 2010; 256: 5929–5934.
- [22] Jiang B, Liu R, Li J, Xie D, Yang M, Guo H. Mode selectivity in methane dissociative chemisorption on Ni (111). *Chem. Sci.* 2013; 4: 3249–3254.

- [23] Sinnott, SB, Andrews R, et al. Model of carbon nanotube growth through chemical vapour deposition. *Chem. Phys. Lett.* 1999; 315: 25–30.
- [24] Helveg, S, Lopez-Cartes C, et al. Atomic-scale imaging of carbon nanofibre growth. *Nature* 2004; 427: 426–429.
- [25] Hofmann, S, Csányi G, Ferrari AC, Payne MC, Robertson J. Surface diffusion: the low activation energy path for nanotube growth. *Phys. Rev. Lett.* 2005; 95: 036101 1–4.
- [26] Cinquini, F, Delbecq F, et al. A DFT comparative study of carbon adsorption and diffusion on the surface and subsurface of Ni and Ni<sub>3</sub>Pd alloy. *Phys. Chem. Chem. Phys.* 2009; 11: 11546–11556.
- [27] Abild-Pedersen F, Nørskov JK, Rostrup-Nielsen JR, Sehested J, Helveg S. Mechanisms for catalytic carbon nanofiber growth studied by ab initio density functional theory calculations. *Phys. Rev. B.* 2006; 73: 115419 1–13.

## Chapter 2

- [1] Kong J, Cassell AM, Dai H. Chemical vapor deposition of methane for single-walled carbon nanotubes. *Chem Phys Lett* 1998; 292: 567–574.
- [2] Cassell AM, Raymakers JA, Kong J, Dai H. Large scale CVD synthesis of single-walled carbon nanotubes. *J Phys Chem B* 1999; 103: 6484–6492.
- [3] Talapatra S, Migone AD. Adsorption of methane on bundles of closed-ended single-wall carbon nanotubes. *Phys Rev B* 2002; 65:045416 1–6.
- [4] Park S, Srivastava D, Cho K. Generalized chemical reactivity of curved surfaces: carbon nanotubes. *Nano Lett* 2003; 3:1273–1277.
- [5] Jariwala D, Sangwan VK, Lauhon LJ, Marks TJ, Hersam MC. Carbon nanomaterials for electronics, optoelectronics, photovoltaics, and sensing. *Chem. Soc. Rev.* 2013; 42: 2824–2860.
- [6] Arnold MS, Blackburn JL, Crochet JJ, et al. Recent developments in the photophysics of single-walled carbon nanotubes for their use as active and passive material elements in thin film photovoltaics. *Phys. Chem. Chem. Phys.* 2013;15:14896–14918.
- [7] Byrne MT, Gun'ko YK. Recent advances in research on carbon nanotube–polymer composites. *Adv. Mater.* 2010; 22: 1672–1688.
- [8] Louchev OA, Laude T, Sato Y, Kanda H. Diffusion-controlled kinetics of carbon nanotube forest growth by chemical vapor deposition. *J. Chem. Phys.* 2003; 118:7622–7634.
- [9] Snoeck JW, Froment GF, Fowles M. Filamentous carbon formation and gasification: Thermodynamics, driving force, nucleation, and steady-state growth. *J. Catal.* 1997; 169: 240–249.
- [10] Yang RT, Chen JP. Mechanism of carbon filament growth on metal catalysts. *J. Catal.* 1989; 115: 52–64.
- [11] Hofmann S, Sharma R, Ducati C, et al. In situ observations of catalyst dynamics during surface-bound carbon nanotube nucleation. *Nano Lett.* 2007; 7: 602–608.
- [12] Lin M, Tan JPY, Boothroyd C, Loh KP, Tok ES, Foo Y–L. Dynamical observation of bamboo-like carbon nanotube growth. *Nano Lett.* 2007; 7: 2234–2238.
- [13] Hofmann S, Csányi G, Ferrari AC, Payne MC, Robertson J. Surface diffusion: the low activation energy path for nanotube growth. *Phys. Rev. Lett.* 2005; 95: 036101 1–4.
- [14] Cinquini F, Delbecq F, Sautet P. A DFT comparative study of carbon adsorption and diffusion on the surface and subsurface of Ni and Ni<sub>3</sub>Pd alloy. *Phys. Chem. Chem. Phys.* 2009; 11:11546–11556.
- [15] Abild-Pedersen F, Nørskov JK, Rostrup-Nielsen JR, Sehested J, Helveg S. Mechanisms for catalytic carbon nanofiber growth studied by ab initio density functional theory calculations. *Phys. Rev. B.* 2006; 73: 115419 1–13.
- [16] David S. S, Janice A. S. *Density functional theory: a practical introduction.* John Wiley & Sons, Inc. Hoboken, New Jersey 2009
- [17] Pierre H, Kohn W. Inhomogeneous electron gas. *Physical Review* 1964; 136: 864–871.
- [18] Kohn W, Sham L. J. Self-Consistent equations including exchange and correlation effects. *Phys. Rev.* 1965; 140: 1133–1138.
- [19] Von Barth U; Hedin L. A local exchange-correlation potential for the spin polarized case. *J. Phys. C: Solid State Phys.* 1972; 5: 1629–1642.
- [20] Perdew JP, Burke K. Study of the density-gradient expansion for the exchange energy. *Phys. Rev. B* 1982; 26: 4371–4377.
- [21] Ermakova MA, Ermakov DY, Kuvshinov GG. Effective catalysts for direct cracking of methane to produce hydrogen and filamentous carbon. Part I. Nickel catalysts. *Appl. Catal. A Gen.* 2000; 201: 61–70.
- [22] Muradov NZ. How to produce hydrogen from fossil fuels without CO<sub>2</sub> emission. *Int. J. Hydrogen Energy.* 1993; 18:211–215.

- [23] Zhang T, Amiridis MD. Hydrogen production via the direct cracking of methane over silica-supported nickel catalysts. *Appl. Catal. A Gen.* 1998; 167:161–172.
- [24] Takenaka, S, Kobayashi S, et al. Ni/SiO<sub>2</sub> catalyst effective for methane decomposition into hydrogen and carbon nanofibre. *J. Catal.* 2003; 217: 79–87.
- [25] Rahman M, Croiset E, et al. Catalytic Decomposition of methane for hydrogen production. *Topics in Catalysis* 2006; 37: 137–145.
- [26] Echegoyen Y, Suelves I, La'zaro MJ, Moliner R, Palacios JM. Hydrogen production by thermocatalytic decomposition of methane over NieAl and NieCueAl catalysts: effect of calcination temperature. *J. Power. Sources.* 2007; 169:150–157
- [27] Figueiredo JL, O' rfa' o JJM, Cunha AF. Hydrogen production via methane decomposition on Raney-type catalysts. *Int. J. Hydrogen. Energy.* 2010; 35: 9795–9800.
- [28] Chesnokov VV, Chichkan AS. Production of hydrogen by methane catalytic decomposition over NieCueFe/Al<sub>2</sub>O<sub>3</sub> catalyst. *Int J Hydrogen Energy* 2009; 34: 2979–2985.
- [29] Gac W, Denis A, Borowiecki T, Kepinski L. Methane decomposition over Ni-MgO-Al<sub>2</sub>O<sub>3</sub> catalysts. *Appl. Catal. A.* 2009; 357: 236–243.
- [30] Venugopal A, Naveen Kumar S, Ashok J, Hari Prasad D, Durga Kumari V, Prasad KBS, et al. Hydrogen production by catalytic decomposition of methane over Ni/SiO<sub>2</sub>. *Int. J. Hydrogen. Energy.* 2007; 32:1782–1788.
- [31] Takenaka S, Ogihara H, Yamanaka I, Otsuka K. Decomposition of methane over supported-Ni catalysts: effects of the supports on the catalytic lifetime. *Appl. Catal.* 2001; 217:101–110.
- [32] Kaminsky MP, Winograd N, Geoffroy GL, Albert Vannice M. Direct SIMS observation of methylidyne, methylene, and methyl intermediates on a Ni (111) methanation catalyst. *J. Am. Chem. Soc.* 1986; 108: 1315–1316.
- [33] Beebe Jr. TP, Goodman DW, Kay BD, Yates Jr. JT. Kinetics of the activated dissociative adsorption of methane on the low index planes of nickel single crystal surfaces. *J. Chem. Phys.* 1987; 87: 2305–2315.
- [34] Schouten FC, Gijzeman OLJ, Bootsma GA. Reaction of methane with nickel single crystal surfaces and the stability of surface nickel carbides. *Bull. Soc. Chim. Belg.* 1979; 88: 541–547.
- [35] Abbott HL, Bukoski A, Kavulak DF, Harrison I. Dissociative chemisorption of methane on Ni (100): Threshold energy from CH<sub>4</sub>(2v<sub>3</sub>) eigenstate-resolved sticking measurements. *J. Chem. Phys.* 2003;119:6407–6410.
- [36] Guo H, Zaera F. Thermal chemistry of iodomethane on Ni (110). 1. Clean and hydrogen-predosed surfaces. *J. Phys. Chem. B.* 2004;108:16220–16225.
- [37] Watwe RM, Bengaard HS, Rostrup-Nielsen JR, Dumesic JA, Nørskov JK. Theoretical studies of stability and reactivity of CH<sub>x</sub> species on Ni (111). *J. Catal.* 2000; 189:16–30.
- [38] Ledentu V, Dong W, Sautet P. Heterogeneous catalysis through subsurface sites. *J. Am. Chem. Soc.* 2000;122:1796–1801.
- [39] Yang H, Whitten JL. Ab initio chemisorption studies of CH<sub>3</sub> on Ni (111). *J. Am. Chem. Soc.* 1991; 113: 6442–6449.
- [40] Kratzer P, Hammer B, Nørskov JK. A theoretical study of CH<sub>4</sub> dissociation on pure and gold-alloyed Ni(111) surfaces. *J. Chem. Phys.* 1996; 105: 5595–5604.
- [41] Wang SG, Cao DB, Li YW, Wang J, Jiao H. CO<sub>2</sub> reforming of CH<sub>4</sub> on Ni (111): A density functional theory calculation. *J. Phys. Chem. B.* 2006; 110: 9976–9983.
- [42] Lee MB, Yang QY, Ceyer ST. Dynamics of the activated dissociative chemisorption of CH<sub>4</sub> and implication for the pressure gap in catalysis: A molecular beam-high resolution electron energy loss study. *J. Chem. Phys.* 1987; 87: 2724–2741.

- [43] Lee MB, Yang QY, Tang SL, Ceyer ST. Activated dissociative chemisorption of CH<sub>4</sub> on Ni (111): Observation of a methyl radical and implication for the pressure gap in catalysis. *J. Chem. Phys.* 1986; 85:1693–1694.
- [44] Kaminsky M.P., Winograd N., Geoffroy G.L., Vannice M. Albert, Direct SIMS observation of methylidyne, methylene, and methyl intermediates on a nickel (III) methanation catalyst. *J. Am. Chem. Soc.* 1986; 108: 1315–1316.
- [45] Yang QY, Maynard KJ, Johnson AD, Ceyer ST. The structure and chemistry of CH<sub>3</sub> and CH radicals adsorbed on Ni (111). *J. Chem. Phys.* 1995; 102: 7734–7749.
- [46] Au CT, Ng CF, Liao MS. Methane Dissociation and Syngas Formation on Ru, Os, Rh, Ir, Pd, Pt, Cu, Ag, and Au: A Theoretical Study. *J. Catal.* 1999; 185: 12–22.
- [47] Kua J, Faglioni F, Goddard WA. Thermochemistry for Hydrocarbon Intermediates Chemisorbed on Metal Surfaces: CH<sub>n</sub> (CH<sub>3</sub>)<sub>m</sub> with n= 1, 2, 3 and m ≤ n on Pt, Ir, Os, Pd, Rh, and Ru. *J. Am. Chem. Soc.* 2000; 122: 2309–2321.
- [48] Henkelman G, Jónsson H. Theoretical calculations of dissociative adsorption of CH<sub>4</sub> on an Ir (111) surface. *Phys. Rev. Lett.* 2001; 86: 664–667.
- [49] Michaelides A, Hu P. Insight into microscopic reaction pathways in heterogeneous catalysis. *J. Am. Chem. Soc.* 2000; 122: 9866–9867.
- [50] Michaelides A, Hua P. A first principles study of CH<sub>3</sub> dehydrogenation on Ni (111). *Chem. Phys.* 2000; 112: 8120–8125.
- [51] Zuo, Z. A density functional theory study of CH<sub>4</sub> dehydrogenation on Co (111). *Appl. Surf. Sci.* 2010; 256: 5929–5934.
- [52] Lai W, Xie D, Zhang DH. First-principles study of adsorption of methyl, coadsorption of methyl and hydrogen, and methane dissociation on Ni (100). *Surf. Sci.* 2005; 594: 83–92.
- [53] Nave S, Tiwari AK, Jackson B. Methane dissociation and adsorption on Ni (111), Pt (111), Ni (100), Pt (100), and Pt (110)-(1×2) : Energetic study *J. Chem. Phys.* 2010; 132: 054705 1–12.
- [54] Wang SG, Cao DB, Li YW, Wang J, Jiao H. CH<sub>4</sub> dissociation on Ni surfaces: Density functional theory study. *Surf. Sci.* 2006; 600: 3226–3234.
- [55] Delbecq F, Sautet P. Adsorption of aldehydes and ketones on platinum and palladium: influence of steps, open faces and metal nature. A theoretical study. *Surf. Sci.* 1993; 295:353–373.
- [56] Delbecq F, Moraweck B, Vérité L. Adsorption of CO and NO on (111) and (100) surfaces of Pd<sub>3</sub>Mn compared with Pd: A theoretical approach. *Surf. Sci.* 1998; 396: 156–175.
- [57] Chizallet C, Costentin G, Che M, Delbecq F, Sautet P. Revisiting acido-basicity of the MgO surface by periodic density functional theory calculations: Role of surface topology and ion coordination on water dissociation. *J. Phys. Chem. B.* 2006; 110: 15878–15886.
- [58] Loffreda D, Simon D, Sautet P. Structure sensitivity for NO dissociation on palladium and rhodium surfaces. *J. Catal.* 2003; 213: 211–225.
- [59] Stroppa A, Mittendorfer F, Andersen JN, et al. Adsorption and dissociation of CO on bare and Ni-decorated stepped Rh(553) surfaces. *J. Phys. Chem. C.* 2009; 113: 942–949.
- [60] Xu Y, Mavrikakis M. Adsorption and dissociation of O<sub>2</sub> on gold surfaces: Effect of steps and strain. *J. Phys. Chem. B.* 2003; 107: 9298–9307.
- [61] Bengaard HS, Nørskov JK, Sehested J, et al. Steam reforming and graphite formation on Ni catalysts. *J. Catal.* 2002; 209: 365–384.
- [62] Abild-Pedersen F, Lytken O, Engbæk J, Nielsen G, Chorkendorff I, Nørskov JK. Methane activation on Ni (111): Effects of poisons and step defects. *Surf. Sci.* 2005; 590: 127–137.
- [63] Niu C, Sichel EK, Hoch R, Moy D, Tennent H. High power electrochemical capacitors based on carbon nanotube electrodes. *Appl. Phys. Lett.* 1997; 70: 1480–1482.
- [64] Xie H, Lee H, Youn W. Nanofluids containing multiwalled carbon nanotubes and their enhanced thermal conductivities. *J. Appl. Phys.* 2003; 94: 4967–4971.

- [65] Gadd GE, Blackford M, Moricca S, Webb N, J. Evans P, Smith AM, Jacobson G, Leung S, Day A, Hua Q. The world's smallest gas cylinders? *Science*, 1997; 277: 933–936.
- [66] Dillon AC, Jones KM, Bekkedahl TA, Klang CH, Bethune DS, Heben MJ. Storage of hydrogen in single-walled carbon nanotubes. *Nature*, 1997; 386: 377–379.
- [67] Cassell AM, Raymakers JA, Kong J. Large scale CVD synthesis of single-walled carbon nanotubes. *J. Phys. Chem. B*, 1999; 103: 6484–6492.
- [68] Gavillet, J, Thibault J., et al. Nucleation and growth of single-walled nanotubes: the role of metallic catalysts. *J. Nanosci. Nanotech.* 2004; 4: 346–359.
- [69] Kong J, Cassell AM, Dai H. Chemical vapour deposition of methane for single-walled carbon nanotubes. *Chem. Phys. Lett.* 1998; 292: 567-574.
- [70] Mo YH, Kibria AKMF, Nahm KS. The growth mechanism of carbon nanotubes from thermal cracking of acetylene over nickel catalyst supported on alumina. *Synth. Met.* 2001; 122 : 443–447.
- [71] Mora E, Harutyunyan AR. Study of single-walled carbon nanotubes growth via the catalyst lifetime. *J. Phys. Chem. C* 2008; 112: 4805–4812.
- [72] Lu C, Liu J. Controlling the diameter of carbon nanotubes in chemical vapour deposition method by carbon feeding. *J. Phys. Chem. B*. 2006; 110: 20254–20257.
- [73] Anna M, et al. The role of metal nanoparticles in the catalytic production of single-walled carbon nanotubes—a review. *J. Phys.: Condensed Matter* 2003; 15: 3011–3035.
- [74] Li YM, Kim W, Zhang YG, Rolandi M, Wang DW, Dai HJ, Growth of single-walled carbon nanotubes from discrete catalytic nanoparticles of various sizes. *J. Phys. Chem. B* 2001; 105: 11424–11431.
- [75] Huang, SM, Woodson, M, Smalley R, Liu J. Growth mechanism of oriented long single walled carbon nanotubes using “fast-heating” chemical vapour deposition process. *Nano Lett.* 2004; 4: 1025–1028.
- [76] Franklin NR, Dai HJ. An enhanced CVD approach to extensive nanotube networks with directionality. *Adv. Mater.* 2000; 12: 890–894.
- [77] Hornyak, GL, Grigorian L, Dillon AC, Parilla PA, Jones KM, Heben MJ. A temperature window for chemical vapour decomposition growth of single-wall carbon nanotubes. *J. Phys. Chem. B*, 2002; 106: 2821–2825.
- [78] Wagg, LM, Hornyak G L, Grigorian L, Dillon AC, Jones KM, Blackburn J, Parilla P A, Heben MJ. Experimental Gibbs free energy considerations in the nucleation and growth of single-walled carbon nanotubes. *J. Phys. Chem. B* 2005; 109: 10435–10440.
- [79] Zhang Y, Smith KJ. Carbon formation thresholds and catalyst deactivation during CH<sub>4</sub> decomposition on supported Co and Ni catalysts. *Catal Lett.* 2004; 95: 7–12.
- [80] Yang, RT, Chen JP. Mechanism of carbon filament growth on metal catalysts. *J. Catal.* 1989; 115: 52–64.
- [81] Baker RTK, Barber MA, Harris PS, Feates FS, Waite RJ. Nucleation and growth of carbon deposits from the nickel catalyzed decomposition of acetylene. *J Catal* 1972; 26: 51–62.
- [82] Kock AJHM, de Bokx PK, Boellaard E, Klop W, Geus JW. The formation of filamentous carbon on iron and nickel catalysts: II. Mechanism. *J Catal* 1985; 96: 468–480.
- [83] Toebes ML, Bitter JH, van Dillen AJ, de Jong KP. Impact of the structure and reactivity of nickel particles on the catalytic growth of carbon nanofibers. *Catal Today* 2002; 76: 33–42.
- [84] McCarty JG, Hou PY, Sheridan D, Wise H. Reactivity of surface carbon on nickel catalysts: temperature programmed surface reaction with hydrogen and water. In: Albright LF, Baker RTK, editors. *Coke formation on metal surfaces*, Washington: American Chemical Society; 1982; 202: 253–282.
- [85] Ohta Y, Okamoto Y, et al. Rapid growth of a single-walled carbon nanotube on an iron cluster: density-functional tight-binding molecular dynamics simulations. *ACS Nano* 2008; 2: 1437–1444.

- [86] Page, AJ, Ohta Y, et al. Mechanisms of single-walled carbon nanotube nucleation, growth, and healing determined using QM/MD methods. *Acc. Chem. Res.* 2010; 43: 1375–1385.
- [87] Gokhale AA, Kandoi S, Greeley, JP, Mavrikakis M D, James A. Molecular-level descriptions of surface chemistry in kinetic models using density functional theory. *Chem. Eng.Sci.* 2004; 59: 4679–4691.
- [88] Snoeck JW, Froment GF, Fowles M. Kinetic study of the carbon filament formation by methane cracking on a nickel catalyst, *J. Catal.* 1997; 169: 250–262.
- [89] Demicheli MC, Ponzi EN, Ferretti OA, Yeramian AA. Kinetics of carbon formation from CH<sub>4</sub>-H<sub>2</sub> mixtures on nickel–alumina catalyst, *Chem. Eng. J.* 1991; 46: 129–136.
- [90] Zein SHS, Mohamed AR, Sai PST. Kinetic studies on catalytic decomposition of methane to hydrogen and carbon over Ni/TiO<sub>2</sub> catalyst, *Ind. Eng. Chem. Res.* 2004; 43: 4864–4870.
- [91] Alstrup I, Tavares MT. The kinetics of carbon formation from CH<sub>4</sub> + H<sub>2</sub> on a silica-supported nickel catalyst, *J. Catal.* 1992; 135: 147–155.
- [92] Alstrup I, Tavares MT. Kinetics of carbon formation from CH<sub>4</sub>+H<sub>2</sub> on silica-supported nickel and Ni–Cu catalysts. *J. Catal.* 1993; 139: 513–524.
- [93] K. Reuter, M. Scheffler, First-principles kinetic Monte Carlo simulations for heterogeneous catalysis: Application to the CO oxidation at RuO<sub>2</sub> (110), *Phys. Rev. B* 2006; 73: 045433 1–17.
- [94] Sendner C, Sakong S, Grob A. Kinetic Monte Carlo simulations of the partial oxidation of methanol on oxygen-covered Cu (110), *Surf. Sci.* 2006; 600: 3258–3265.
- [95] Mei DH, Du JC, Neurock M. First-Principles-Based Kinetic Monte Carlo simulation of nitric oxide reduction over platinum nanoparticles under Lean-Burn conditions, *Ind. Eng. Chem. Res.* 2010; 49: 10364–10373.
- [96] Mei DH, Neurock M, Smith CM. Hydrogenation of acetylene–ethylene mixtures over Pd and Pd–Ag alloys: First-principles-based kinetic Monte Carlo simulations, *J. Catal.* 2009; 268: 181–195.
- [97] K. Reuter, Deutschmann O. *Modeling heterogeneous catalytic reactions: from the molecular process to the technical system*, Wiley VCH, Weinberg, 2009. [98] Hess F, Over H. Kinetic monte carlo simulations of heterogeneously catalyzed oxidation reactions, *Catal. Sci. Technol.*, 2014, 4, 583–598.
- [99] Hong S, KarimA, Rahman TS, Jacobi K, Ertl G. Selective oxidation of ammonia on RuO<sub>2</sub> (110): A combined DFT and KMC study, *J. Catal.* 2010; 276: 371–381.
- [100] Hansen EW, Neurock M. First-principles based kinetic simulations of acetic acid temperature programmed reaction on Pd (111), *J. Phys. Chem. B* 2001; 105: 9218–9229.
- [101] Aleksandrov HA, Moskaleva LV, Zhao Z, Basaran D, Chen Z, Mei D, Rösch N. Ethylene conversion to ethylidyne on Pd (111) and Pt (111): a first-principles-based kinetic monte carlo study, *J.Catal.* 2012; 285: 187–195.
- [102] Stamatakis M, Chen Y, Vlachos DG. First-principles-based kinetic monte carlo simulation of the structure sensitivity of the water gas shift reaction on platinum surfaces, *J. Phys. Chem. C.* 2011; 115: 24750–24762.

### Chapter 3

- [1] Haryanto A, Fernando S, Murali N, Adhikari S. Current status of hydrogen production techniques by steam reforming of ethanol: A review. *Energy Fuels*. 2005; 19: 2098–2106.
- [2] Matsumura Y, Nakamori T. Steam reforming of methane over nickel catalysts at low reaction temperature. *Appl. Catal. A Gen.* 2004; 258:107–114.
- [3] Wei J, Iglesia E. Isotopic and kinetic assessment of the mechanism of methane reforming and decomposition reactions on supported iridium catalysts. *Phys. Chem. Chem. Phys.* 2004; 6: 3754–3759.
- [4] Laosiripojana N, Assabumrungrat S. Methane steam reforming over Ni/Ce–ZrO<sub>2</sub> catalyst: Influences of Ce–ZrO<sub>2</sub> support on reactivity, resistance toward carbon formation, and intrinsic reaction kinetics. *Appl. Catal. A Gen.* 2005; 290:200–211.
- [5] Jones G, Jakobsen JG, Shim SS, et al. First principles calculations and experimental insight into methane steam reforming over transition metal catalysts. *J. Catal.* 2008; 259:147–160.
- [6] Blaylock DW, Ogura T, Green WH, Beran GJO. Computational investigation of thermochemistry and kinetics of steam methane reforming on Ni (111) under realistic conditions. *J. Phys. Chem. C*. 2009; 113: 4898–4908.
- [7] Hou K, Hughes R. The kinetics of methane steam reforming over a Ni/ $\alpha$ -Al<sub>2</sub>O<sub>3</sub> catalyst. *Chem. Eng. J.* 2001; 82: 311–328.
- [8] Fonseca A, Assaf EM. Production of the hydrogen by methane steam reforming over nickel catalysts prepared from hydrotalcite precursors. *J. Power Sources*. 2005; 142:154–159.
- [9] Das SK, Reis A, Berry KJ. Experimental evaluation of CO poisoning on the performance of a high temperature proton exchange membrane fuel cell. *J. Power Sources*. 2009; 193: 691–698.
- [10] Amin AM, Croiset E, Epling W. Review of methane catalytic cracking for hydrogen production. *Int. J. Hydrogen Energy*. 2011; 36: 2904–2935.
- [11] Rahman MS, Croiset E, Hudgins RR. Catalytic decomposition of methane for hydrogen production. *Top. Catal.* 2006; 37:137–145.
- [12] Muradov NZ. How to produce hydrogen from fossil fuels without CO<sub>2</sub> emission. *Int. J. Hydrogen Energy*. 1993; 18:211–215.
- [13] Muradov NZ. CO<sub>2</sub>-free production of hydrogen by catalytic pyrolysis of hydrocarbon fuel. *Energy Fuels*. 1998; 12:41–48.
- [14] Zhang T, Amiridis MD. Hydrogen production via the direct cracking of methane over silica-supported nickel catalysts. *Appl. Catal. A Gen.* 1998; 167:161–172.
- [15] Zhang R, Tsui RK, Tresek J, et al. Formation of single-walled carbon nanotubes via reduced-pressure thermal chemical vapor deposition. *J. Phys. Chem. B*. 2003; 107: 3137–3140.
- [16] Jodin L, Dupuis AC, Rouvière E, Reiss P. Influence of the catalyst type on the growth of carbon nanotubes via methane chemical vapor deposition. *J. Phys. Chem. B*. 2006; 110: 7328–7333.
- [17] Takagi D, Homma Y, Hibino H, Suzuki S, Kobayashi Y. Single-walled carbon nanotube growth from highly activated metal nanoparticles. *Nano Lett.* 2006; 6: 2642–2645.
- [18] Ermakova MA, Ermakov DY, Kuvshinov GG. Effective catalysts for direct cracking of methane to produce hydrogen and filamentous carbon. Part I. Nickel catalysts. *Appl. Catal. A Gen.* 2000; 201:61–70.
- [19] Aiello R, Fiscus JE, Loye HC, Amiridis MD. Hydrogen production via the direct cracking of methane over Ni/SiO<sub>2</sub>: catalyst deactivation and regeneration. *Appl. Catal. A*. 2000; 192: 227–234.
- [20] Takenaka S, Kobayashi S, Ogihara H, Otsuka K. Ni/SiO<sub>2</sub> catalyst effective for methane decomposition into hydrogen and carbon nanofiber. *J. Catal.* 2003; 217: 79–87.
- [21] Villacampa JI, Royo C, Romeo E, Montoya JA, Del Angel P, Monzón A. Catalytic decomposition of methane over Ni–Al<sub>2</sub>O<sub>3</sub> coprecipitated catalysts Reaction and regeneration studies. *Appl. Catal. A Gen.* 2003; 252: 363–383.

- [22] Venugopal A, Naveen Kumar S, Ashok J, et al. Hydrogen production by catalytic decomposition of methane over Ni / SiO<sub>2</sub>. *Int. J. Hydrogen Energy*. 2007; 32: 1782–1788.
- [23] Kaminsky MP, Winograd N, Geoffroy GL, Albert Vannice M. Direct SIMS observation of methylidyne, methylene, and methyl intermediates on a Ni (111) methanation catalyst. *J. Am. Chem. Soc.* 1986; 108:1315–1316.
- [24] Beebe Jr. TP, Goodman DW, Kay BD, Yates Jr. JT. Kinetics of the activated dissociative adsorption of methane on the low index planes of nickel single crystal surfaces. *J. Chem. Phys.* 1987; 87:2305–2315.
- [25] Schouten FC, Gijzeman OLJ, Bootsma GA. Reaction of methane with nickel single crystal surfaces and the stability of surface nickel carbides. *Bull. Soc. Chim. Belg.* 1979; 88: 541–547.
- [26] Abbott HL, Bukoski A, Kavulak DF, Harrison I. Dissociative chemisorption of methane on Ni (100): Threshold energy from CH<sub>4</sub>(2v<sub>3</sub>) eigenstate-resolved sticking measurements. *J. Chem. Phys.* 2003;119:6407–6410.
- [27] Guo H, Zaera F. Thermal chemistry of iodomethane on Ni (110). 1. Clean and hydrogen-predosed surfaces. *J. Phys. Chem. B*. 2004; 108:16220–16225.
- [28] Watwe RM, Bengaard HS, Rostrup-Nielsen JR, Dumesic JA, Nørskov JK. Theoretical studies of stability and reactivity of CH<sub>x</sub> species on Ni (111). *J. Catal.* 2000; 189:16–30.
- [29] Ledentu V, Dong W, Sautet P. Heterogeneous catalysis through subsurface sites. *J. Am. Chem. Soc.* 2000; 122:1796–1801.
- [30] Yang H, Whitten JL. Ab initio chemisorption studies of CH<sub>3</sub> on Ni (111). *J. Am. Chem. Soc.* 1991;113:6442–6449.
- [31] Kratzer P, Hammer B, Nørskov JK. A theoretical study of CH<sub>4</sub> dissociation on pure and gold-alloyed Ni(111) surfaces. *J. Chem. Phys.* 1996; 105: 5595–5604.
- [32] Wang SG, Cao DB, Li YW, Wang J, Jiao H. CO<sub>2</sub> reforming of CH<sub>4</sub> on Ni (111): A density functional theory calculation. *J. Phys. Chem. B*. 2006; 110: 9976–9983.
- [33] Lee MB, Yang QY, Ceyer ST. Dynamics of the activated dissociative chemisorption of CH<sub>4</sub> and implication for the pressure gap in catalysis: a molecular beam-high resolution electron energy loss study. *J. Chem. Phys.* 1987; 87: 2724–2741.
- [34] Lee MB, Yang QY, Tang SL, Ceyer ST. Activated dissociative chemisorption of CH<sub>4</sub> on Ni (111): Observation of a methyl radical and implication for the pressure gap in catalysis. *J. Chem. Phys.* 1986; 85: 1693–1694.
- [35] Kaminsky MP, Winograd N, Geoffroy GL, Vannice M A. Direct SIMS observation of methylidyne, methylene, and methyl intermediates on a nickel (III) methanation catalyst. *J. Am. Chem. Soc.* 1986; 108: 1315–1316.
- [36] Yang QY, Maynard KJ, Johnson AD, Ceyer ST. The structure and chemistry of CH<sub>3</sub> and CH radicals adsorbed on Ni(111). *J. Chem. Phys.* 1995; 102: 7734–7749.
- [37] Michaelides A, Hu P. A density functional theory study of CH<sub>2</sub> and H adsorption on Ni (111). *J. Chem. Phys.* 2000; 112: 6006–6014.
- [38] Haroun MF, Mousounda PS, Légaré P. Dissociative adsorption of methane on Ni (111) surface with and without adatom: A theoretical study. *J. Mol. Struct. THEOCHEM*. 2009; 903: 83–88.
- [39] Lai W, Xie D, Zhang DH. First-principles study of adsorption of methyl, coadsorption of methyl and hydrogen, and methane dissociation on Ni (100). *Surf. Sci.* 2005; 594: 83–92.
- [40] Nave S, Tiwari AK, Jackson B. Methane dissociation and adsorption on Ni (111), Pt (111), Ni (100), Pt (100), and Pt (110)–(1×2) : Energetic study *J. Chem. Phys.* 2010;132: 054705 1–12.
- [41] Wang SG, Cao DB, Li YW, Wang J, Jiao H. CH<sub>4</sub> dissociation on Ni surfaces: Density functional theory study. *Surf. Sci.* 2006; 600: 3226–3234.
- [42] Delbecq F, Sautet P. Adsorption of aldehydes and ketones on platinum and palladium: influence of steps, open faces and metal nature. A theoretical study. *Surf. Sci.* 1993; 295: 353–373.

- [43] Delbecq F, Moraweck B, Vérité L. Adsorption of CO and NO on (111) and (100) surfaces of Pd<sub>3</sub>Mn compared with Pd: A theoretical approach. *Surf. Sci.* 1998; 396: 156–175.
- [44] Chizallet C, Costentin G, Che M, Delbecq F, Sautet P. Revisiting acido-basicity of the MgO surface by periodic density functional theory calculations: Role of surface topology and ion coordination on water dissociation. *J. Phys. Chem. B.* 2006; 110: 15878–15886.
- [45] Loffreda D, Simon D, Sautet P. Structure sensitivity for NO dissociation on palladium and rhodium surfaces. *J. Catal.* 2003; 213: 211–225.
- [46] Stroppa A, Mittendorfer F, Andersen JN, et al. Adsorption and dissociation of CO on bare and Ni-decorated stepped Rh (553) surfaces. *J. Phys. Chem. C.* 2009; 113: 942–949.
- [47] Xu Y, Mavrikakis M. Adsorption and dissociation of O<sub>2</sub> on gold surfaces: Effect of steps and strain. *J. Phys. Chem. B.* 2003; 107: 9298–9307.
- [48] Bengaard HS, Nørskov JK, Sehested J, et al. Steam reforming and graphite formation on Ni catalysts. *J. Catal.* 2002; 209: 365–384.
- [49] Abild-Pedersen F, Lytken O, Engbæk J, Nielsen G, Chorkendorff I, Nørskov JK. Methane activation on Ni (111): effects of poisons and step defects. *Surf. Sci.* 2005; 590: 127–137.
- [50] Te Velde G, Baerends EJ. Precise density-functional method for periodic structures. *Phys. Rev. B.* 1991; 44: 7888–7903.
- [51] Wiesenekker G, Baerends EJ. Quadratic integration over the three-dimensional Brillouin zone. *J. Phys. Condens. Matter.* 1991; 3: 6721–6742.
- [52] Hammer B, Hansen LB, Nørskov JK. Improved adsorption energetics within density-functional theory using revised Perdew-Burke-Ernzerhof functionals. *Phys. Rev. B – Condens. Matter Mater. Phys.* 1999; 59: 7413–7421.
- [53] Perdew JP, Burke K, Ernzerhof M. Generalized gradient approximation made simple. *Phys. Rev. Lett.* 1996; 77: 3865–3868.
- [54] Yang K, Zheng J, Zhao Y, Truhlar DG. Tests of the RPBE, revPBE,  $\tau$ -HCTHhyb,  $\omega$ B97X-D, and MOHLYP density functional approximations and 29 others against representative databases for diverse bond energies and barrier heights in catalysis. *J. Chem. Phys.* 2010; 132: 164117 1–10.
- [55] Cramer CJ, Truhlar DG. Density functional theory for transition metals and transition metal chemistry. *Phys. Chem. Chem. Phys.* 2009; 11:10757–10816.
- [56] Fouqueau A, Mer S, Casida ME, et al. Comparison of density functionals for energy and structural differences between the high-[5T2g:(t2g)4(eg)2] and low-[1A1g:(t2g)6(eg)0] spin states of the hexaquoferrous cation [Fe(H<sub>2</sub>O)<sub>6</sub>]<sup>2+</sup>. *J. Chem. Phys.* 2004; 120: 9473–9486.
- [57] Bengaard HS, Nørskov JK, Sehested J, et al. Steam reforming and graphite formation on Ni catalysts. *J. Catal.* 2002; 209:365–384.
- [58] te Velde G, Baerends EJ. Numerical integration for polyatomic systems. *J. Comput. Phys.* 1992; 99:84–98.
- [59] Paul JF, Sautet P. Chemisorption and Transformation of CH<sub>x</sub> Fragments (x = 0-3) on a Pd (111) Surface: A Periodic Density Functional Study. *J. Phys. Chem. B.* 1998; 102: 1578–1585.
- [60] Y. Aray, Je Rodriguez, J. Rivero, D. Vega. Theoretical study of the CO adsorption on the (100) surface of the face-centered cubic d-block transition metals, *Surf. Sci.* 1999; 441: 344–350.
- [61] [http://www.scm.com/Doc/Doc2012/BAND/BandUsersGuide/page39.html#keyterm ACCURACY](http://www.scm.com/Doc/Doc2012/BAND/BandUsersGuide/page39.html#keyterm%20ACCURACY).
- [62] Wiesenekker G, te Velde G, Baerends EJ. Analytic quadratic integration over the two-dimensional Brillouin zone *J. Phys. C: Solid State Phys.* 1988; 21:4263–4283.
- [63] Wolff SK, Ziegler T, van Lenthe E, Baerends EJ. Density functional calculations of nucleus magnetic shieldings using the zeroth-order regular approximation (ZORA) for relativistic effects: ZORA nucleus magnetic resonance, *J. Chem. Phys.* 1999; 110: 7689–7698.
- [64] Van Santen RA. Theory, spectroscopy and kinetics of zeolite catalysed reactions. *Catal. Today.* 1999; 50: 511–515.

- [65] Medlin JW, Barteau MA. The formation of epoxides from reactions of oxametallacycles on Ag (110): A density functional theory study. *J. Phys. Chem. B.* 2001; 105: 10054–10061.
- [66] Linic S, Barteau MA. Construction of a reaction coordinate and a microkinetic model for ethylene epoxidation on silver from DFT calculations and surface science experiments. *J. Catal.* 2003; 214: 200–212.
- [67] Lu HC, Gusev EP, Garfunkel E, Gustafsson T. A MEIS study of thermal effects on the Ni (111) surface. *Surf. Sci.* 1996; 21: 352–354.
- [68] Demuth JE, Marcus PM, Jepsen DW. Analysis of low-energy-electron-diffraction intensity spectra for (001), (110), and (111) nickel. *Phys. Rev. B.* 1975; 11: 1460–1474.
- [69] te Velde G, Visser O. BAND 1.0. Scientific computing modelling, Chemistry Department, Vrije Universiteit, The Netherlands, 1998.
- [70] Aray Y, Rodriguez J, Rivero J, Vega D. Theoretical study of the CO adsorption on the (100) surface of the face-centered cubic d-block transition metals. *Surf. Sci.* 1999; 441: 344–350.
- [71] Hjortstam O, Baberschke K, Wills JM, Johansson B, Eriksson O. Magnetic anisotropy and magnetostriction in tetragonal and cubic Ni. *Phys. Rev. B–Condens. Matter Mater. Phys.* 1997; 55: 15026–15032.
- [72] Cinquini F, Delbecq F, Sautet P. A DFT comparative study of carbon adsorption and diffusion on the surface and subsurface of Ni and Ni<sub>3</sub>Pd alloy. *Phys. Chem. Chem. Phys.* 2009; 11: 11546–11556.
- [73] Fan C, Zhou XG, Chen D, Cheng HY, Zhu YA. Toward CH<sub>4</sub> dissociation and C diffusion during Ni/Fe–catalytic carbon nanofiber growth: A density functional theory study. *J. Chem. Phys.* 2011;134:1347041–1347042.
- [74] Zhu YA, Dai YC, Chen D, Yuan WK. First-principles calculations of CH<sub>4</sub> dissociation on Ni (100) surface along different reaction pathways. *J. Mol. Catal. A–Chem.* 2007; 264: 299–308.
- [75] Michaelides A, Hu P. Methyl chemisorption on Ni (111) and C–H–M multicentre bonding: A density functional theory study. *Surf. Sci.* 1999; 437: 362–376.
- [76] Bengaard HS, Alstrup I, Chorkendorff I, Ullmann S, Rostrup-Nielsen JR, Nørskov JK. Chemisorption of methane on Ni (100) and Ni (111) surfaces with preadsorbed potassium. *J. Catal.* 1999; 187: 238–244.
- [77] Wang SG, Liao XY, Hu J, et al. Kinetic aspect of CO<sub>2</sub> reforming of CH<sub>4</sub> on Ni(111): A density functional theory calculation. *Surf. Sci.* 2007; 601:1271–1284.
- [78] Mueller JE, Van Duin ACT, Goddard III WA. Structures, energetics, and reaction barriers for CH<sub>x</sub> bound to the nickel (111) surface. *J. Phys. Chem. C.* 2009; 113: 20290–20306.
- [79] Rostrup-Nielsen J, Nørskov JK. Step sites in syngas catalysis. *Top. Catal.* 2006; 40:45–48.
- [80] Logadóttir Á, Nørskov JK. Ammonia synthesis over a Ru (0001) surface studied by density functional calculations. *J. Catal.* 2003; 220:273–279.
- [81] Offermans WK, Jansen APJ, Van Santen RA, Novell–Leruth G, Ricart JM, Pérez-Ramírez J. Ammonia dissociation on Pt{100}, Pt{111}, and Pt{211}: a comparative density functional theory study. *J. Phys. Chem. C.* 2007; 111:17551–17557.
- [82] Van Grootel PW, Van Santen RA, Hensen EJM. Methane dissociation on high and low indices Rh surfaces. *J. Phys. Chem. C.* 2011;115:13027–13034.
- [83] Miller SD, Kitchin JR. Relating the coverage dependence of oxygen adsorption on Au and Pt fcc (1 1 1) surfaces through adsorbate-induced surface electronic structure effects. *Surf. Sci.* 2009; 603:794–801.
- [84] Mavrikakis M, Hammer B, Nørskov JK. Effect of strain on the reactivity of metal surfaces. *Phys. Rev. Lett.* 1998; 81: 2819–2822.
- [85] Kitchin JR, Nørskov JK, Barteau MA, Chen JG. Modification of the surface electronic and chemical properties of Pt (111) by subsurface 3d transition metals. *J. Chem. Phys.* 2004; 120:10240–10246.
- [86] Hammer B, Nørskov JK. Electronic factors determining the reactivity of metal surfaces. *Surf. Sci.* 1995; 343: 211–220.

- [87] Kitchin JR, Nørskov JK, Barteau MA, Chen JG. Role of strain and ligand effects in the modification of the electronic and chemical Properties of bimetallic surfaces. *Phys. Rev. Lett.* 2004; 93:156801–156804.
- [88] Dong C, An L, Yang Y, Zhang J. Asia-Pacific Power and Energy Engineering Conference (APPEEC), 2010.
- [89] Michaelides A, Liu ZP, Zhang CJ, Alavi A, King DA, Hu P. Identification of general linear relationships between activation energies and enthalpy changes for dissociation reactions at surfaces. *J. Am. Chem. Soc.* 2003; 125: 3704–3705.
- [90] Liu ZP, Hu P. General rules for predicting where a catalytic reaction should occur on metal surfaces: A density functional theory study of C–H and C–O bond breaking/making on flat, stepped, and kinked metal surfaces. *J. Am. Chem. Soc.* 2003; 125:1958–1967.

## Chapter 4

- [1] Rahman M, Croiset E, et al. Catalytic decomposition of methane for hydrogen production. *Topics in Catalysis* 2006; 37: 137–145.
- [2] Li Y, Li D, Wang G. Methane decomposition to CO<sub>x</sub>-free hydrogen and nano-carbon material on group 8–10 base metal catalysts: A review, *Catal. Today*. 2011; 162: 1–48.
- [3] Takagi D, Homma Y, Hibino H, Suzuki S, Kobayashi Y. Single-walled carbon nanotube growth from highly activated metal nanoparticles. *Nano Lett.* 2006; 6: 2642–2645.
- [4] Nikolla E, Schwank J, Linic S, Comparative study of the kinetics of methane steam reforming on supported Ni and Sn/Ni alloy catalysts: the impact of the formation of Ni alloy on chemistry, *J. Catal.* 2009; 263: 220–227.
- [5] Shen W, Huggins F E, Shah N, Jacobs G, Wang Y, Novel Fe–Ni nanoparticle catalyst for the production of CO- and CO<sub>2</sub>-free H<sub>2</sub> and carbon nanotubes by dehydrogenation of methane, *Appl. Catal. A: Gen.* 2008; 351: 102–110.
- [6] Nuernberg GD, Fajardo HV, Foletto EL, Hickel-Probst SM, Carreño NLV, Probst LFD, Barrault J. Methane conversion to hydrogen and nanotubes on Pt/Ni catalysts supported over spinel MgAl<sub>2</sub>O<sub>4</sub>, *Catal. Today*. 2011; 176: 465–469.
- [7] Xiong J, Dong X, Dong Y, Hao X, Hampshire S, Dual-production of nickel foam supported carbon nanotubes and hydrogen by methane catalytic decomposition, *Int. J. Hydrogen Energy*. 2012; 37: 12307–12316.
- [8] Abbott HL, Bukoski A, Kavulak DF, Harrison I. Dissociative chemisorption of methane on Ni (100): Threshold energy from CH<sub>4</sub>(2v<sub>3</sub>) eigenstate-resolved sticking measurements. *J. Chem. Phys.* 2003; 119: 6407–6410.
- [9] Ermakova, MA, Ermakov DY, et al. Effective catalysts for direct cracking of methane to produce hydrogen and filamentous carbon: Part I. Nickel catalysts. *Appl. Catal. A: General*. 2000; 201: 61–70.
- [10] Michaelides A, Hu P. A density functional theory study of CH<sub>2</sub> and H adsorption on Ni (111). *J. Chem. Phys.* 2000; 112: 6006–6014.
- [11] Nave S, Tiwari AK, Jackson B. Methane dissociation and adsorption on Ni (111), Pt (111), Ni (100), Pt (100), and Pt (110)–(1×2) : Energetic study *J. Chem. Phys.* 2010;132: 054705 1–12.
- [12] Abild-Pedersen F, Lytken O, Engbæk J, Nielsen G, Chorkendorff I, Nørskov JK. Methane activation on Ni (111): Effects of poisons and step defects, *Surf. Sci.* 2005; 590: 127–137.
- [13] Li J, Croiset E, Ricardez-Sandoval L, Methane dissociation on Ni (100), Ni (111), and Ni (553): A comparative density functional theory study, *J. Mol. Catal. A: Chem.* 2012; 365: 103–114.
- [14] Xu Y, Fan C, Zhu Y, Li P, Zhou X, Chen D, Yuan W, Effect of Ag on the control of Ni-catalyzed carbon formation: A density functional theory study, *Catal. Today*, 2012; 186: 54–62.
- [15] Wang SG, Cao DB, Li YW, Wang J, Jiao H. CH<sub>4</sub> dissociation on Ni surfaces: density functional theory study. *Surf. Sci.* 2006; 600: 3226–3234.
- [16] Bengaard HS, Nørskov JK, Sehested J, et al. Steam reforming and graphite formation on Ni catalysts. *J. Catal.* 2002; 209: 365–384.
- [17] Liu H, Wang B, Fan M, Henson N, Zhang Y, Towler BF, Harris HG. Study on carbon deposition associated with catalytic CH<sub>4</sub> reforming by using density functional theory, *Fuel*. 2013; 113: 712–718.
- [18] Wiltner A, Linsmeier C, Jacob T. Carbon reaction and diffusion on Ni (111), Ni (100), and Fe (110): kinetic parameters from x-ray photoelectron spectroscopy and density functional theory analysis, *J. Chem. Phys.* 2008; 129: 084704 1–10.
- [19] Rinaldi A, Tessonier JP, Schuster ME, Blume R, Girgsdies F, Zhang Q, Jacob T, Hamid SBA, Su D, Schlogl R. Dissolved carbon controls the initial stages of nanocarbon growth, *Angew. Chem. Int. Ed.* 2011; 50: 3313–3317.
- [20] Bartholomew CH, Mechanisms of catalyst deactivation, *Appl. Catal. A: Gen.* 2001; 212: 17–60.

- [21] Chen D, Lodeng R, Anundskas A, Olsvik O, Holmen A. Deactivation during carbon dioxide reforming of methane over Ni catalyst: microkinetic analysis, *Chem. Eng. Sci.* 2001; 56: 1371–1379.
- [22] Vitos L, Ruban AV, Skriver HL, Kollár J. The surface energy of metals. *Surf. Sci.* 1998; 411: 186–202.
- [23] Baletto F, Ferrando R, Structural properties of nanoclusters: energetic, thermodynamic, and kinetic effects. *Rev. Mod. Phys.* 2005; 77: 371–423.
- [24] Hofmann S, Sharma R, Ducati C, et al. In situ observations of catalyst dynamics during surface-bound carbon nanotube nucleation. *Nano Lett.* 2007; 7: 602–608.
- [25] Liu C, Ye J, Jiang J, Pan Y. Progresses in the preparation of coke resistant Ni-based catalyst for steam and CO<sub>2</sub> reforming of methane, *ChemCatChem.* 2011; 3: 529–541.
- [26] Weatherup RS, Bayer BC, Blume R, Ducati C, Baehtz C, Schlögl R, Hofmann S. In situ characterization of alloy catalysts for low-temperature graphene growth, *Nano Lett.* 2011; 11: 4154–4160.
- [27] Amin A M, Croiset E, Constantinou C, Epling W, Methane cracking using Ni supported on porous and non-porous alumina catalysts, *Int. J. Hydrogen Energy* 2012; 37: 9038–9048.
- [28] Mortensen JJ, Hammer B, Nørskov JK, A theoretical study of adsorbate-adsorbate interactions on Ru (0001), *Surf. Sci.* 1998; 414: 315–329.
- [29] Zhu Y, Chen D, Zhou X, Yuan W. DFT studies of dry reforming of methane on Ni catalyst. *Catal Today.* 2009; 148: 260–70.
- [30] Andersson MP, Abild-Pedersen F, et al. Structure sensitivity of the methanation reaction: H<sub>2</sub>-induced CO dissociation on nickel surfaces. *J Catal.* 2008; 255: 6–19.
- [31] Abild-Pedersen F, Nørskov JK, Rostrup-Nielsen JR, Sehested J, Helveg S. Mechanisms for catalytic carbon nanofiber growth studied by ab initio density functional theory calculations. *Phys. Rev. B.* 2006; 73: 115419 1–13.
- [32] Blaylock DW, Ogura T, Green WH, Beran GJO. Computational investigation of thermochemistry and kinetics of steam methane reforming on Ni (111) under realistic conditions. *J. Phys. Chem. C.* 2009; 113: 4898–4908.
- [33] Andersson MP, Density functional theory with modified dispersion correction for metals applied to self-assembled monolayers of thiols on Au (111), *J. Theor. Chem.*, 2013; 2013: 327839 1–9
- [34] Mason SE, Grinberg I, Rappe AM. First-principles extrapolation method for accurate CO adsorption energies on metal surfaces, *Physical Review B*, 2004; 69: 161401 1–4.
- [35] Grimme S, Anthony J, Ehrlich S, Krieg H, A consistent and accurate ab initio parametrization of density functional dispersion correction (DFT-D) for the 94 elements, *J. Chem. Phys.* 2010; 132: 154104 1–19.
- [36] Wang S, Liao X, Hu J, Cao D, Li Y, Wang J, Jiao H, Kinetic aspect of CO<sub>2</sub> reforming of CH<sub>4</sub> on Ni (111): A density functional theory calculation, *Surf. Sci.* 2007; 601: 1271–1284.
- [37] Liu H, Zhang R, Yan R, Li J, Wang B, Xie K. Insight into CH<sub>4</sub> dissociation on NiCu catalyst: a first-Principles study. *Appl Surf Sci.* 2012; 258: 8177–8184.
- [38] Snoeck JW, Froment GF, Fowles M. Kinetic study of the carbon filament formation by methane cracking on a nickel catalyst. *J. Catal.* 1997; 169: 250–262.

## Chapter 5

- [1] Ancilotto F, Chiarotti GL, Scandolo S, Tosatti E. Dissociation of methane into hydrocarbons at extreme (planetary) pressure and temperature. *Science*. 1997; 275: 1288–1290.
- [2] Fujitani T, Nakamura I, Akita T, Okumura M, Haruta M. No Title. *Angew. Chem*. 2009; 121: 9679–9682.
- [3] Pozzo M, Alfè D. Hydrogen dissociation and diffusion on transition metal (= Ti, Zr, V, Fe, Ru, Co, Rh, Ni, Pd, Cu, Ag)-doped Mg (0001) surfaces. *Int. J. Hydrogen Energy*. 2009; 34: 1922–1930.
- [4] Jones G, Jakobsen JG, Shim SS, et al. First principles calculations and experimental insight into methane steam reforming over transition metal catalysts. *J. Catal*. 2008; 259: 147–160.
- [5] Abanades S, Flamant G. Experimental study and modeling of a high-temperature solar chemical reactor for hydrogen production from methane cracking. *Int. J. Hydrogen Energy*. 2007; 32: 1508–1515.
- [6] Rostrup-Nielsen JR, Sehested J, Nørskov JK. Hydrogen and synthesis gas by steam and CO<sub>2</sub> reforming. *Adv. Catal*. 2002; 47: 65–139.
- [7] Aiello R, Fiscus JE, Zur LHC, Amiridis MD. Hydrogen production via the direct cracking of methane over Ni/SiO<sub>2</sub>: Catalyst deactivation and regeneration. *Appl. Catal. A Gen*. 2000; 192:227–234.
- [8] Amin A, Epling W, Croiset E. Reaction and deactivation rates of methane catalytic cracking over nickel. *Ind. Eng. Chem. Res*. 2011; 50: 12460–12470.
- [9] Li Y, Zhang B, Xie X, Liu J, Xu Y, Shen W. Novel Ni catalysts for methane decomposition to hydrogen and carbon nanofibers. *J. Catal*. 2006; 238: 412–424.
- [10] Dong WS, Roh HS, Jun KW, Park SE, Oh YS. Methane reforming over Ni/Ce–ZrO catalysts: Effect of nickel content. *Appl. Catal. A Gen*. 2002; 226: 63–72.
- [11] Kuijpers EGM, Jansen JW, van Dillen AJ, Geus JW. The reversible decomposition of methane on a Ni SiO<sub>2</sub> catalyst. *J. Catal*. 1981; 72: 75–82.
- [12] Watwe RM, Bengaard HS, Rostrup-Nielsen JR, Dumesic JA, Nørskov JK. Theoretical Studies of Stability and Reactivity of CH<sub>x</sub> Species on Ni (111). *J. Catal*. 2000; 189:16–30.
- [13] Xiao L, Wang L. Methane activation on Pt and Pt<sub>4</sub>: a density functional theory study. *J. Phys. Chem. B*. 2007; 111:1657–1663.
- [14] Ledentu V, Dong W, Sautet P. Heterogeneous catalysis through subsurface sites. *J. Am. Chem. Soc*. 2000; 122: 1796–1801.
- [15] Wang SG, Cao DB, Li YW, Wang J, Jiao H. CO<sub>2</sub> reforming of CH<sub>4</sub> on Ni (111): a density functional theory calculation. *J. Phys. Chem. B*. 2006; 110: 9976–9983.
- [16] Li J, Croiset E, Ricardez-Sandoval L. Methane dissociation on Ni (100), Ni (111), and Ni (553): a comparative density functional theory study. *J. Mol. Catal. A Chem*. 2012; 365:103–114.
- [17] Haroun MF, Moussounda PS, Légaré P. Dissociative adsorption of methane on Ni(111) surface with and without adatom: a theoretical study. *J. Mol. Struct. THEOCHEM*. 2009; 903: 83–88.
- [18] Abild-Pedersen F, Lytken O, Engbæk J, Nielsen G, Chorkendorff I, Nørskov JK. Methane activation on Ni (111): effects of poisons and step defects. *Surf. Sci*. 2005; 590: 127–137.
- [19] Alikhani ME, Minot C. A DFT study of the mechanism of the spontaneous activation of H<sub>2</sub> by Ni, Pd, Pt, and Pd<sub>2</sub>. *J. Phys. Chem. A*. 2003; 107: 5352–5355.
- [20] Burghgraef H, Jansen APJ, van Santen RA. Electronic structure calculations and dynamics of the chemisorption of methane on a Ni (111) surface. *Chem. Phys*. 1993; 177: 407–420.
- [21] Charlot MF, Kahn O. Activation de l'hydrogène moléculaire par une petite particule de nickel. *Surf. Sci*. 1979; 81: 90–108.
- [22] Álvarez YL, López GE, Cruz AJ. Quantum dissociation dynamics of H<sub>2</sub> and D<sub>2</sub> on a Ni<sub>13</sub> cluster. *J. Chem. Phys*. 1997; 107: 1420–1427.
- [23] Liu B, Lusk MT, Ely JF. Influence of nickel catalyst geometry on the dissociation barriers of H<sub>2</sub> and CH<sub>4</sub>: Ni<sub>13</sub> versus Ni (111). *J. Phys. Chem. C*. 2009; 113: 13715–13722.

- [24] Nave S, Tiwari AK, Jackson B. Methane dissociation and adsorption on Ni (111), Pt (111), Ni (100), Pt(100), and Pt(110)-(1×2): Energetic study. *J. Chem. Phys.* 2010; 132: 054705 1–12.
- [25] Bengaard HS, Nørskov JK, Sehested J, et al. Steam reforming and graphite formation on Ni catalysts. *J. Catal.* 2002; 209: 365–384.
- [26] Blaylock DW, Ogura T, Green WH, Beran GJO. Computational investigation of thermochemistry and kinetics of steam methane reforming on Ni (111) under realistic conditions. *J. Phys. Chem. C.* 2009; 113: 4898–4908.
- [27] Zhu YA, Chen D, Zhou XG, Yuan WK. DFT studies of dry reforming of methane on Ni catalyst. *Catal. Today.* 2009; 148: 260–267.
- [28] Yan Q, Toghiani H, White MG. Combined temperature-programmed processes, pulse reactions, and on-line mass spectroscopy study of CH<sub>4</sub>, CO, and H<sub>2</sub> interaction with Ni/Al<sub>2</sub>O<sub>3</sub> catalysts. *J. Phys. Chem. C.* 2007; 111:18646–18662.
- [29] Wang S, Lu GQ. A comprehensive study on carbon dioxide reforming of methane over Ni/γ-Al<sub>2</sub>O<sub>3</sub> catalysts. *Ind. Eng. Chem. Res.* 1999; 38: 2615–2625.
- [30] Dropsch H, Baerns M. CO adsorption on supported Pd catalysts studied by adsorption microcalorimetry and temperature programmed desorption. *Appl. Catal. A Gen.* 1997; 158: 163–183.
- [31] Cao DB, Li YW, Wang J, Jiao H. Mechanism of γ-Al<sub>2</sub>O<sub>3</sub> support in CO<sub>2</sub> reforming of CH<sub>4</sub>—A density functional theory study. *J. Phys. Chem. C.* 2011; 115: 225–233.
- [32] Briquet LG V, Catlow CRA, French SA. Platinum group metal adsorption on clean and hydroxylated corundum surfaces. *J. Phys. Chem. C.* 2009; 113: 16747–16756.
- [33] Mei D, Kwak JH, Szanyi J, Ge Q, Peden CHF. Catalyst size and morphological effects on the interaction of NO<sub>2</sub> with BaO/γ-Al<sub>2</sub>O<sub>3</sub> materials. *Catal. Today.* 2010; 151:304–313.
- [34] Liu Z, Ma L, Junaid ASM. NO and NO<sub>2</sub> adsorption on Al<sub>2</sub>O<sub>3</sub> and Ga modified Al<sub>2</sub>O<sub>3</sub> surfaces: A density functional theory study. *J. Phys. Chem. C.* 2010; 114: 4445–4450.
- [35] Briquet LG V, Catlow CRA, French SA. Structure and reactivity of aluminum oxide supported nickel clusters. *J. Phys. Chem. C.* 2010; 114: 22155–22158.
- [36] Valero MC, Raybaud P, Sautet P. Interplay between molecular adsorption and metal–support interaction for small supported metal clusters: CO and C<sub>2</sub>H<sub>4</sub> adsorption on Pd<sub>4</sub>/γ-Al<sub>2</sub>O<sub>3</sub>. *J. Catal.* 2007; 247: 339–355.
- [37] Cheng L, Ge Q. Effect of γ-Al<sub>2</sub>O<sub>3</sub> substrate on NO<sub>2</sub> interaction with supported BaO clusters. *Surf. Sci.* 2007; 601: 65–68.
- [38] Kacprzak KA, Czekaj I, Mantzaras J. DFT studies of oxidation routes for Pd<sub>9</sub> clusters supported on γ-alumina. *Phys. Chem. Chem. Phys.* 2012; 14: 10243–10247.
- [39] Wang S, Lu GQ. A comprehensive study on carbon dioxide reforming of methane over Ni/γ-Al<sub>2</sub>O<sub>3</sub> catalysts. *Ind. Eng. Chem. Res.* 1999; 38: 2615–2625.
- [40] Seok SH, Sun HC, Park ED, Sung HH, Jae SL. Mn-promoted Ni/Al<sub>2</sub>O<sub>3</sub> catalysts for stable carbon dioxide reforming of methane. *J. Catal.* 2002; 209: 6–15.
- [41] Ji Y, Li W, Xu H, Chen Y. Catalytic partial oxidation of methane to synthesis gas over Ni/γ-Al<sub>2</sub>O<sub>3</sub> catalyst in a fluidized-bed. *Appl. Catal. A Gen.* 2001; 213: 25–31.
- [42] Rahman MS, Croiset E, Hudgins RR. Catalytic decomposition of methane for hydrogen production. *Top. Catal.* 2006; 37:137–145.
- [43] Amin AM, Croiset E, Epling W. Review of methane catalytic cracking for hydrogen production. *Int. J. Hydrogen Energy.* 2011; 36: 2904–2935.
- [44] Pinto H, Nieminen R, Elliott S. Ab Initio Study of γ-Al<sub>2</sub>O<sub>3</sub> Surfaces. *Phys. Rev. B.* 2004; 70:1–11.
- [45] Ionescu A, Allouche A, Aycard JP, Rajzmann M, Hutschka F. Study of γ-alumina surface reactivity: Adsorption of water and hydrogen sulfide on octahedral aluminum sites. *J. Phys. Chem. B.* 2002; 106: 9359–9366.

- [46] Krokidis X, Raybaud P, Gobichon AE, Rebours B, Euzen P, Toulhoat H. Theoretical study of the dehydration process of boehmite to  $\gamma$ -alumina. *J. Phys. Chem. B.* 2001; 105: 5121–5130.
- [47] Digne M, Sautet P, Raybaud P, Euzen P, Toulhoat H. Use of DFT to achieve a rational understanding of acid–basic properties of  $\gamma$ -alumina surfaces. *J. Catal.* 2004; 226: 54–68.
- [48] Paglia G, Buckley CE, Rohl AL, et al. Tetragonal structure model for boehmite–derived  $\gamma$ -alumina. *Phys. Rev. B–Condens. Matter Mater. Phys.* 2003; 68:1441101–14411011.
- [49] Proupin EM, Gutiérrez G. Electronic Properties of Bulk  $\gamma$ -Al<sub>2</sub>O<sub>3</sub>. *Phys. Rev. B.* 2005; 72: 1–9.
- [50] Sun M, Nelson AE, Adjaye J. Examination of spinel and nonspinel structural models for  $\gamma$ -Al<sub>2</sub>O<sub>3</sub> by DFT and rietveld refinement simulations. *J. Phys. Chem. B.* 2006; 110: 2310–2317.
- [51] Digne M, Raybaud P, Sautet P, Rebours B, Toulhoat H. Comment on “examination of spinel and nonspinel structural models for  $\gamma$ -Al<sub>2</sub>O<sub>3</sub> by DFT and Rietveld refinement simulations.” *J. Phys. Chem. B.* 2006; 110: 20719–20720.
- [52] Paglia G, Buckley CE, Rohl AL. Comment on “examination of spinel and nonspinel structural models for  $\gamma$ -Al<sub>2</sub>O<sub>3</sub> by DFT and Rietveld–refinement simulations.” *J. Phys. Chem. B.* 2006; 110: 20721–20723.
- [53] Nelson AE, Sun M, Adjaye J. Reply to “comments on ‘examination of spinel and nonspinel structural models for  $\gamma$ -Al<sub>2</sub>O<sub>3</sub> by DFT and Rietveld refinement simulations’.” *J. Phys. Chem. B.* 2006; 110: 20724–20726.
- [54] Vander Wal RL, Ticich TM, Curtis VE. Substrate-support interactions in metal-catalytic carbon nanofiber growth. *Carbon.* 2001; 39: 2277–2289.
- [55] Ago H, Nakamura K, Uehara N, Tsuji M. Roles of metal-support interaction in growth of single- and double-walled carbon nanotubes studied with diameter-controlled iron particles supported on MgO. *J. Phys. Chem. B.* 2004; 108: 18908–18915.
- [56] Mattevi C, Wirth CT, Hofmann S, et al. In-situ X-ray photoelectron spectroscopy study of catalyst-support interactions and growth of carbon nanotube forests. *J. Phys. Chem. C.* 2008; 112: 12207–12213.
- [57] Hirshfeld FL. Bonded-atom fragments for describing molecular charge densities. *Theor. Chim. Acta.* 1977; 44:129–138.
- [58] <http://www.scm.com/Doc/Doc2012/BAND/BandUsersGuide/page121.html>.
- [67] Van Santen RA. Theory, spectroscopy and kinetics of zeolite catalysed reactions. *Catal. Today.* 1999; 50: 511–515.
- [68] Medlin JW, Barteau MA. The formation of epoxides from reactions of oxametallacycles on Ag (110): A density functional theory study. *J. Phys. Chem. B.* 2001; 105: 10054–10061.
- [69] Linic S, Barteau MA. Construction of a reaction coordinate and a microkinetic model for ethylene epoxidation on silver from DFT calculations and surface science experiments. *J. Catal.* 2003; 214: 200–212.
- [59] Gutiérrez G, Taga A, Johansson B. Theoretical structure determination of  $\gamma$ -Al<sub>2</sub>O<sub>3</sub>. *Phys. Rev. B.* 2001; 65:1–4.
- [60] Paglia G, Rohl AL, Buckley CE, Gale JD. Determination of the structure of  $\gamma$ -alumina from interatomic potential and first–principles calculations: The requirement of significant numbers of nonspinel positions to achieve an accurate structural model. *Phys. Rev. B – Condens. Matter Mater. Phys.* 2005; 71: 224115 1–16.
- [61] Loviat F, Czekaj I, Wambach J, Wokaun A. Nickel deposition on  $\gamma$ -Al<sub>2</sub>O<sub>3</sub> model catalysts: An experimental and theoretical investigation. *Surf. Sci.* 2009; 603: 2210–2217.
- [62] Márquez AM, Sanz JF. Adsorption of Pd atoms on  $\gamma$ -Al<sub>2</sub>O<sub>3</sub>: a density functional study of metal–support interactions. *Appl. Surf. Sci.* 2004; 238: 82–85.
- [63] Streit FH, Mintmire JW. Energetics of aluminum vacancies in gamma alumina. *Phys. Rev. B – Condens. Matter Mater. Phys.* 1999; 60: 773–777.

- [64] Digne M, Sautet P, Raybaud P, Euzen P, Toulhoat H. Hydroxyl groups on  $\gamma$ -alumina surfaces: a DFT study. *J. Catal.* 2002; 211:1–5.
- [65] Kwak JH, Hu JZ, Kim DH, Szanyi J, Peden CHF. Penta-coordinated  $\text{Al}^{3+}$  ions as preferential nucleation sites for BaO on  $\gamma$ - $\text{Al}_2\text{O}_3$ : An ultra-high-magnetic field  $^{27}\text{Al}$  MAS NMR study. *J. Catal.* 2007; 251: 189–194.
- [66] Knoezinger H, Ratnasamy P. Catalytic aluminas: surface models and characterization of surface sites. *Catal Rev.* 1978; 17: 31–70.
- [67] Zhang R, Wang B, Liu H, Ling L. Effect of surface hydroxyls on  $\text{CO}_2$  hydrogenation over  $\text{Cu}/\gamma$ - $\text{Al}_2\text{O}_3$  catalyst: A theoretical study. *J. Phys. Chem. C.* 2011; 115: 19811–19818.
- [68] Pan YX, Liu CJ, Ge Q. Effect of surface hydroxyls on selective  $\text{CO}_2$  hydrogenation over  $\text{Ni}_4/\gamma$ - $\text{Al}_2\text{O}_3$ : A density functional theory study. *J. Catal.* 2010; 272: 227–234.
- [69] Pan Y, Liu CJ, Ge Q. Adsorption and protonation of  $\text{CO}_2$  on partially hydroxylated  $\gamma$ - $\text{Al}_2\text{O}_3$  surfaces: A density functional theory study. *Langmuir.* 2008; 24: 12410–12419.
- [70] Ryota I, Changho J, Hideyuki T, et al. Periodic density functional and tight-binding quantum chemical molecular dynamics study of catalytic properties on  $\gamma$ - $\text{Al}_2\text{O}_3$  supported Pt catalysts. *Appl. Catal. A.* 2006; 305: 64–69.
- [71] Petkov PS, Petrova GP, Vayssilov GN, Rösch N. Saturation of small supported metal clusters by adsorbed hydrogen. a computational study on tetrahedral models of  $\text{Rh}_4$ ,  $\text{Ir}_4$ , and  $\text{Pt}_4$ . *J. Phys. Chem. C.* 2010; 114:8500–8506.
- [72] Shi XR, Sholl DS. Nucleation of  $\text{Rh}_n$  ( $n=1$ -5) clusters on  $\gamma$ - $\text{Al}_2\text{O}_3$  surfaces: A density functional theory study. *J. Phys. Chem. C.* 2012; 116: 10623–10631.
- [73] Briquet LG V, Catlow CRA, French SA. Comparison of the adsorption of Ni, Pd, and Pt on the (0001) surface of  $\alpha$ -alumina. *J. Phys. Chem. C.* 2008; 112:18948–18954.
- [74] Lundqvist BI, Gunnarsson O, Hjelmberg H, Nørskov JK. Theoretical description of molecule-metal interaction and surface reactions. *Surf. Sci.* 1979; 89:196–225.
- [75] Lambert RM, Pacchioni G. Chemisorption and reactivity on supported clusters and thin films: towards an understanding of microscopic processes in catalysis; Kluwer Academic: Dordrecht, 1997.
- [76] Norskov JK. Chemisorption on metal surfaces. *Reports Prog. Phys.* 1990; 53: 1253–1295.
- [77] Hammer B, Nørskov JK. Electronic factors determining the reactivity of metal surfaces. *Surf. Sci.* 1995; 343: 211–220.
- [78] Argo AM, Odzak JF, Goellner JF, Lai FS, Xiao FS, Gates BC. Catalysis by oxide-supported clusters of iridium and rhodium: hydrogenation of ethene, propene, and toluene. *J. Phys. Chem. B.* 2006; 110: 1775–1786.
- [79] Busnengo HF, Dong W, Salin A. Trapping, molecular adsorption, and precursors for nonactivated chemisorption. *Phys. Rev. Lett.* 2004; 236103 1–4.
- [80] Van Santen RA, Neurock M. Molecular heterogeneous catalysis: a conceptual and computational approach. John Wiley & Sons: New York, 2006.

## Chapter 6

- [1] Dresselhaus MS, Dresselhaus G, Avouris P. Carbon nanotubes: synthesis, structure, properties, and applications. Springer: Berlin, 2001.
- [2] Reina A, Jia XT, Ho J, Nezich D, Son HB, Bulovic V, Dresselhaus MS, Kong J. Large area, few-layer graphene films on arbitrary substrates by chemical vapor deposition. *Nano Lett.* 2009; 9: 30–35.
- [3] Kim KS, Zhao Y, Jang H, Lee SY, Kim JM, Kim KS, Ahn JH, Kim P, Choi JY, Hong BH. Large-scale pattern growth graphene films for stretchable transparent electrodes. *Nature*, 2009; 457: 706–710.
- [4] Atthipalli G, Epur R, Kumta PN, Yang M, Lee JK, Gray JL. Nickel catalyst-assisted vertical growth of dense carbon nanotube forests on bulk copper. *J. Phys. Chem. C* 2011; 115: 3534–3538.
- [5] Kidambi PR, Ducati C, Dlubak B, Gardiner D, Weatherup RS, Martin MB, Seneor P, Coles H, Hofmann S. The parameter space of graphene chemical vapor deposition on polycrystalline Cu. *J. Phys. Chem. C* 2012; 116: 22492–22501.
- [6] Li XS, Cai WW, An JH, Kim S, Nah J, Yang DX, Piner R, Velamakanni A, Jung I, Tutuc E, et al. Large-area synthesis of high-quality and uniform graphene films on copper foils. *Science* 2009; 324: 1312–1314.
- [7] Abild-Pedersen F, Nørskov JK, Rostrup-Nielsen JR, Sehested J, Helveg S. Mechanisms for catalytic carbon nanofiber growth studied by ab initio density functional theory calculations. *Phys. Rev. B.* 2006; 73: 115419 1–13.
- [8] Hofmann S, Sharma R, Ducati C, et al. In situ observations of catalyst dynamics during surface-bound carbon nanotube nucleation. *Nano Lett.* 2007; 7: 602–608.
- [9] Lin M, Tan JPY, Boothroyd C, Loh KP, Tok ES, Foo YL. Dynamical observation of bamboo-like carbon nanotube growth. *Nano Lett.* 2007; 7: 2234–2238.
- [10] Snoeck JW, Froment GF, Fowles M. Filamentous carbon formation and gasification: Thermodynamics, driving force, nucleation, and steady-state growth. *J. Catal.* 1997; 169: 240–249.
- [11] Wirth CT, Zhang C, Zhong G, Hofmann S, Robertson J. Diffusion and reaction limited growth of carbon nanotube forests, *ACS Nano*, 2009; 3: 3560–3566.
- [12] Rodríguez-Manzo JA, Terrones M, Terrones H, Kroto HW, Sun L, Banhart F. In situ nucleation of carbon nanotubes by the injection of carbon atoms into metal particles. *Nat. Nanotechnol.* 2007; 2: 307–311.
- [13] Blaylock DW, Ogura T, Green WH, Beran GJO. Computational investigation of thermochemistry and kinetics of steam methane reforming on Ni (111) under realistic conditions. *J. Phys. Chem. C.* 2009; 113: 4898–4908.
- [14] Xiao L, Wang L. Methane activation on Pt and Pt<sub>4</sub>: a density functional theory study. *J. Phys. Chem. B.* 2007; 111:1657–1663.
- [15] Yuan S, Meng L, Wang J. Greatly improved methane dehydrogenation via Ni adsorbed Cu (100) surface. *J. Phys. Chem. C* 2013; 117: 14796–14803.
- [16] Bunnik BS, Kramer GJ. Energetics of methane dissociative adsorption on Rh {111} from DFT calculations. *J. Catal.* 2006; 242: 309–318.
- [17] Liu H, Wang B, Fan M, Henson N, Zhang Y, Towler BF, Harris HG. Study on carbon deposition associated with catalytic CH<sub>4</sub> reforming by using density functional theory. *Fuel* 2013; 113: 712–718.
- [18] Li J, Croiset E, Ricardez-Sandoval L, Methane dissociation on Ni (100), Ni (111), and Ni (553): A comparative density functional theory study, *J. Mol. Catal. A: Chem.* 2012; 365: 103–114.
- [19] Nave S, Jackson B. Methane dissociation on Ni (111) and Pt (111): energetic and dynamical studies *J. Chem. Phys.* 2009; 130: 054701 1–14.
- [20] Gajewski G, Pao C. *Ab initio* Calculations of the reaction pathways for methane decomposition over the Cu (111) surface. *J. Chem. Phys.* 2011; 135: 064707 1–10.

- [21] An W, Zeng XC, Turner CH. J. Chem. Phys. First-principles Study of Methane Dehydrogenation on a Bimetallic Cu/Ni (111) Surface. *J. Chem. Phys.* 2009; 131: 174702 1–12.
- [22] Yazyev OV, Pasquarello A. Effect of metal elements in catalytic growth of carbon nanotubes. *Phys. Rev. Lett.* 2008; 100: 156102 1–4.
- [23] Chen H, Zhu W, Zhang Z. Contrasting behavior of carbon nucleation in the initial stages of graphene epitaxial growth on stepped metal surfaces. *Phys. Rev. Lett.* 2010; 104: 186101 1–4.
- [24] Cinquini F, Delbecq F, Sautet P. A DFT comparative study of carbon adsorption and diffusion on the surface and subsurface of Ni and Ni<sub>3</sub>Pd alloy. *Phys. Chem. Chem. Phys.* 2009; 11: 11546–11556.
- [25] Ding F, Rose´na A, Bolton K. Dependence of SWNT growth mechanism on temperature and catalyst particle size: bulk versus surface diffusion. *Carbon* 2005; 43: 2215–2217.
- [26] Wang S, Liao X, Cao D, Li Y, Wang J, Jiao H. Formation of carbon species on Ni (111): structure and stability. *J. Phys. Chem. C* 2007; 111: 10894–10903.
- [27] Zhang W, Wu P, Li Z, Yang J. First-principles thermodynamics of graphene growth on Cu surfaces. *J. Phys. Chem. C* 2011; 115: 17782–17787.
- [28] Cheng D, Barcaro G, Charlier JC, Hou M, Fortunelli A. Homogeneous nucleation of graphitic nanostructures from carbon chains on Ni (111). *J. Phys. Chem. C*, 2011; 115: 10537–10543.
- [29] Gao J, Yip J, Zhao J, Yakobson B I, Ding F. Graphene nucleation on transition metal surface: Structure transformation and role of the metal step edge. *J. Am. Chem. Soc.* 2011; 133: 5009–5015.
- [30] Li J, Croiset E, Ricardez-Sandoval L. Carbon clusters on the Ni (111) surface: a density functional theory study. *Phys. Chem. Chem. Phys.* 2014; 16: 2954–296.
- [31] Terrado E, Tacchini I, Benito AM, Maser WK, Mart´inez MT. Optimizing catalyst nanoparticle distribution to produce densely-packed carbon nanotube growth. *Carbon* 2009; 47: 1989–2001.
- [32] Rinaldi A, Tessonier JP, Schuster ME, Blume R, Girgsdies F, Zhang Q, Jacob T, Hamid SBA, Su D, Schlogl R. Dissolved carbon controls the initial stages of nanocarbon growth, *Angew. Chem. Int. Ed.* 2011; 50: 3313–3317.
- [33] Li X, Magnuson CW, Venugopal A, Tromp RM, Hannon JB, Vogel EM, Colombo L, Ruoff RS, Large-area graphene single crystals grown by low-pressure chemical vapor deposition of methane on copper. *J. Am. Chem. Soc.* 2011; 133: 2816–2819.
- [34] Hu B, Ago H, Ito Y, Kawahara K, Tsujia M, Magome E, Sumitani K, Mizuta N, Ikeda K, Mizuno S. Epitaxial growth of large-area dingle-layer graphene over Cu (111)/sapphire by stmospheric pressure CVD. *Carbon* 2012; 50: 57–65.
- [35] Li X, Cai W, Colombo L, Ruoff RS. Evolution of graphene growth on Ni and Cu by carbon isotope labeling. *Nano Lett.* 2009; 9: 4268–4272.
- [36] Liu H, Zhang R, Yan R, Li J, Wang B, Xie K. Insight into CH<sub>4</sub> dissociation on NiCu catalyst: a first-principles study. *Appl. Surf. Sci.* 2012; 258: 8177–8184.
- [37] Vitos L, Ruban AV, Skriver HL, Koll´ar J. The surface energy of metals. *Surf. Sci.* 1998; 411: 186–202.
- [38] Baletto F, Ferrando R, Structural properties of nanoclusters: energetic, thermodynamic, and kinetic effects. *Rev. Mod. Phys.* 2005; 77: 371–423.
- [39] <http://periodictable.com/Properties/A/LatticeConstants.html>
- [32] Wang S, Liao X, Hu J, Cao D, Li Y, Wang J, Jiao H, Kinetic aspect of CO<sub>2</sub> reforming of CH<sub>4</sub> on Ni (111): A density functional theory calculation, *Surf. Sci.* 2007; 601: 1271–1284.

- [33] Liao MS, Au CT, Ng CF. Methane dissociation on Ni, Pd, Pt and Cu metal (111) surfaces-a theoretical comparative study. *Chem. Phys. Lett.* 1997; 272: 445–452.
- [40] Nilsson A, Pettersson LGM, Hammer B, Bligaard T, Christensen CH, Nørskov JK. The electronic structure effect in heterogeneous catalysis. *Catal. Letters.* 2005; 100: 111–114.
- [41] Ermakova MA, Yu D, Chuvilin AL, Kuvshinov GG. Decomposition of methane over iron catalysts at the range of moderate temperatures: the influence of structure of the catalytic systems and the reaction conditions on the yield of carbon and morphology of carbon filaments. *J. Catal.* 2001; 201:183–197.
- [42] Takenaka S, Serizawa M, Otsuka K. Formation of filamentous carbons over supported Fe catalysts through methane decomposition. *J. Catal.* 2004; 222: 520–531.

## Chapter 7

- [1] Saito R, Dresselhaus G, Dresselhaus MS. Physical properties of carbon nanotubes, Imperial College Press, London, 1998.
- [2] Dresselhaus MS, Dresselhaus G, Avouris P. Carbon nanotubes: synthesis, structure, properties and applications, Springer, Berlin, 2001.
- [3] Arnold MS, Blackburn JL, Crochet JJ, et al. Recent developments in the photophysics of single-walled carbon nanotubes for their use as active and passive material elements in thin film photovoltaics. *Phys. Chem. Chem. Phys.* 2013; 15: 14896–14918.
- [4] Long D, Lin H, Scheblykin IG. Carbon nanotubes as photoprotectors of organic dyes: reversible photoreaction instead of permanent photo-oxidation. *Phys. Chem. Chem. Phys.* 2011; 13: 5771–5777.
- [5] Jariwala D, Sangwan VK, Lauhon LJ, Marks TJ, Hersam MC. Carbon nanomaterials for electronics, optoelectronics, photovoltaics, and sensing. *Chem. Soc. Rev.* 2013; 42: 2824–2860.
- [6] Lu W, Goering A, Qu L, Dai L. Lithium-ion batteries based on vertically-aligned carbon nanotube electrodes and ionic liquid electrolytes. *Phys. Chem. Chem. Phys.* 2012; 14: 12099–12104.
- [7] Rodriguez NM, Chambers A, Baker RTK. Catalytic engineering of carbon nanostructures. *Langmuir.* 1995; 11:3862–3866.
- [8] Fenelonov VB, Derevyankin AY, Okkel LG, et al. Structure and texture of filamentous carbons produced by methane decomposition on Ni and Ni–Cu catalysts. *Carbon* 1997; 35: 1129–1140.
- [9] Shaikhutdinov SK, Zaikovskii VI, Avdeeva LB. Coprecipitated Ni-alumina and Ni–Cu–alumina catalysts of methane decomposition and carbon deposition III. morphology and surface structure of the carbon filaments. *Appl. Catal. A Gen.* 1996; 148: 123–133.
- [10] Gavillet J, Thibault J, Stéphan O, et al. Nucleation and growth of single-walled nanotubes: The role of metallic catalysts. *J. Nanosci. Nanotechnol.* 2004; 4: 346–359.
- [11] Kong J, Cassell AM, Dai H. Chemical vapor deposition of methane for single-walled carbon nanotubes. *Chem. Phys. Lett.* 1998; 292: 567–574.
- [12] Mo YH, Kibria AKMF, Nahm KS. The growth mechanism of carbon nanotubes from thermal cracking of acetylene over nickel catalyst supported on alumina. *Synth. Met.* 2001; 122: 443–447.
- [13] Mora E, Harutyunyan AR. Study of single-walled carbon nanotubes growth via the catalyst lifetime. *J. Phys. Chem. C.* 2008; 112: 4805–4812.
- [14] Lu C, Liu J. Controlling the diameter of carbon nanotubes in chemical vapor deposition method by carbon feeding. *J. Phys. Chem. B.* 2006; 110: 20254–20257.
- [15] Moisala A, Nasibulin AG, Kauppinen EI. The role of metal nanoparticles in the catalytic production of single-walled carbon nanotubes-a review. *J. Phys. Condens. Matter.* 2003;15: 3011–3035.
- [16] Li Y, Kim W, Zhang Y, Rolandi M, Wang D, Dai H. Growth of single-walled carbon nanotubes from discrete catalytic nanoparticles of various sizes. *J. Phys. Chem. B.* 2001; 105: 11424–11431.
- [17] Huang S, Woodson M, Smalley R, Liu J. Growth mechanism of oriented long single walled carbon nanotubes using “fast-heating” chemical vapor deposition process. *Nano Lett.* 2004; 4: 1025–1028.
- [18] Franklin NR, Dai H. Enhanced CVD approach to extensive nanotube networks with directionality. *Adv. Mater.* 2000;12: 890–894.
- [19] Hornyak GL, Grigorian L, Dillon AC, Parilla PA, Jones KM, Heben MJ. A temperature window for chemical vapor decomposition growth of single-wall carbon nanotubes. *J. Phys. Chem. B.* 2002;106: 2821–2825.
- [20] Wagg LM, Hornyak GL, Grigorian L, et al. Experimental gibbs free energy considerations in the nucleation and growth of single-walled carbon nanotubes. *J. Phys. Chem. B.* 2005; 109: 10435–10440.
- [21] Alstrup I, Tavares MT. Kinetics of carbon formation from  $\text{CH}_4 + \text{H}_2$  on silica-supported nickel and Ni–Cu catalysts. *J. Catal.* 1993; 139: 513–524.

- [22] Snoeck JW, Froment GF, Fowles M. Filamentous carbon formation and gasification: Thermodynamics, driving force, nucleation, and steady-state growth. *J. Catal.* 1997; 169: 240–249.
- [23] Snoeck JW, Froment GF, Fowles M. Kinetic study of the carbon filament formation by methane cracking on a nickel catalyst. *J. Catal.* 1997; 169: 250–262.
- [24] De Jong KP, Geus JW. Carbon nanofibers: catalytic synthesis and applications. *Catal. Rev.–Sci. Eng.* 2000; 42: 481–510.
- [25] Rodríguez-Manzo JA, Terrones M, Terrones H, Kroto HW, Sun L, Banhart F. In situ nucleation of carbon nanotubes by the injection of carbon atoms into metal particles. *Nat. Nanotechnol.* 2007; 2:307–311.
- [26] Louchev OA, Laude T, Sato Y, Kanda H. Diffusion-controlled kinetics of carbon nanotube forest growth by chemical vapor deposition. *J. Chem. Phys.* 2003;118:7622–7634.
- [27] Shi XH, Li HJ, Fu QG, Zhang SY, Guo LJ, Lu JH. Carbon infiltration of carbon-fiber preforms by catalytic CVD. *Carbon* 2006; 44:1198–1202.
- [28] Baker RTK, Barber MA, Harris PS, Feates FS, Waite RJ. Nucleation and growth of carbon deposits from the nickel catalytic decomposition of acetylene. *J. Catal.* 1972; 26: 51–62.
- [29] Audier M, Coulon M. Kinetic and microscopic aspects of catalytic carbon growth. *Carbon* 1985; 23: 317–323.
- [30] Yang RT, Chen JP. Mechanism of carbon filament growth on metal catalysts. *J. Catal.* 1989; 115: 52–64.
- [31] Alstrup I. A new model explaining carbon filament growth on nickel, iron, and NiCu alloy catalysts. *J. Catal.* 1988;109: 241–251.
- [32] Rostrup-Nielsen J, Trimm DL. Mechanisms of carbon formation on nickel-containing catalysts. *J. Catal.* 1977; 48: 155–165.
- [33] Lin M, Tan JPY, Boothroyd C, Loh KP, Tok ES, Foo Y-L. Direct observation of single-walled carbon nanotube growth at the atomistic scale. *Nano Lett.* 2006; 6: 449–452.
- [34] Yoshida H, Takeda S, Uchiyama T, Kohno H, Homma Y. Atomic-scale in-situ observation of carbon nanotube growth from solid state iron carbide nanoparticles. *Nano Lett.* 2008; 8: 2082–2086.
- [35] Hofmann S, Sharma R, Ducati C, et al. In situ observations of catalyst dynamics during surface-bound carbon nanotube nucleation. *Nano Lett.* 2007; 7: 602–608.
- [36] Lin M, Tan JPY, Boothroyd C, Loh KP, Tok ES, Foo YL. Dynamical observation of bamboo-like carbon nanotube growth. *Nano Lett.* 2007; 7: 2234–2238.
- [37] Hofmann S, Csányi G, Ferrari AC, Payne MC, Robertson J. Surface diffusion: the low activation energy path for nanotube growth. *Phys. Rev. Lett.* 2005; 95: 036101 1–4.
- [38] Louchev OA, Sato Y, Kanda H. Morphological stabilization, destabilization, and open-end closure during carbon nanotube growth mediated by surface diffusion. *Phys. Rev. E.* 2002; 66:11601 1–17.
- [39] Louchev OA, Hester JR. Kinetic pathways of carbon nanotube nucleation from graphitic nanofragments. *J. Appl. Phys.* 2003; 94: 2002–2010.
- [40] Cinquini F, Delbecq F, Sautet P. A DFT comparative study of carbon adsorption and diffusion on the surface and subsurface of Ni and Ni<sub>3</sub>Pd alloy. *Phys. Chem. Chem. Phys.* 2009;11:11546–11556.
- [41] Ding F, Rosén A, Bolton K. Dependence of SWNT growth mechanism on temperature and catalyst particle size: Bulk versus surface diffusion. *Carbon* 2005; 43: 2215–2217.
- [42] Abild-Pedersen F, Nørskov JK, Rostrup-Nielsen JR, Sehested J, Helveg S. Mechanisms for catalytic carbon nanofiber growth studied by ab initio density functional theory calculations. *Phys. Rev. B.* 2006; 73: 115419 1–13.
- [43] Viñes F, Neyman KM, Görling A. Carbon on platinum substrates: From carbidic to graphitic phases on the (111) surface and on nanoparticles. *J. Phys. Chem. A.* 2009; 113:11963–11973.
- [44] Loginova E, Bartelt NC, Feibelman PJ, McCarty KF. Evidence for graphene growth by C cluster attachment. *New J. Phys.* 2008; 10: 093026 1–16.

- [45] Chen H, Zhu W, Zhang Z. Contrasting behavior of carbon nucleation in the initial stages of graphene epitaxial growth on stepped metal surfaces. *Phys. Rev. Lett.* 2010; 104 186101 1–4.
- [46] Cheng D, Barcaro G, Charlier JC, Hou M, Fortunelli A. Homogeneous nucleation of graphitic nanostructures from carbon chains on Ni (111). *J. Phys. Chem. C.* 2011; 115: 10537–10543.
- [47] Wang SG, Liao XY, Cao DB, Li YW, Wang J, Jiao H. Formation of carbon species on Ni (111): Structure and stability. *J. Phys. Chem. C.* 2007; 111: 10894–10903.
- [48] Gao J, Yip J, Zhao J, Yakobson BI, Ding F. Graphene nucleation on transition metal surface: Structure transformation and role of the metal step edge. *J. Am. Chem. Soc.* 2011; 133: 5009–5015.
- [49] Leidheiser Jr. H, Gwathmey AT. The selective deposition of carbon on the (111) face of a nickel crystal in the catalytic decomposition of carbon monoxide. *J. Am. Chem. Soc.* 1948; 70: 1206.
- [50] Hong S, Shin YH, Ihm J. Crystal shape of a nickel particle related to carbon nanotube growth. *Japanese J. Appl. Physics, Part 1 Regul. Pap. Short Notes Rev. Pap.* 2002; 41: 6142–6144.
- [51] Lu HC, Gusev EP, Garfunkel E, Gustafsson T. A MEIS study of thermal effects on the Ni (111) surface. *Surf. Sci.* 1996; 352–354: 21–24.
- [52] Ledentu V, Dong W, Sautet P. Heterogeneous catalysis through subsurface sites. *J. Am. Chem. Soc.* 2000; 122: 1796–1801.
- [53] He P, Mao Y, Sun L, Zhong J. First-principles study of the initial growth stages of carbon chain on Ni (111) surface. *J. Comput. Theor. Nanosci.* 2010; 7: 2063–2067.
- [54] Kessler DA, Levine H, Sander LM. Molecular-beam epitaxial growth and surface diffusion. *Phys. Rev. Lett.* 1992; 69: 100–103.
- [55] Neyts EC, Shibuta Y, Van Duin ACT, Bogaerts A. Catalytic growth of carbon nanotube with definable chirality by hybrid molecular dynamics-force biased monte carlo simulations. *ACS Nano.* 2010; 4: 6665–6672.

## Chapter 8

- [1] Saito R, Dresselhaus G, Dresselhaus MS. Physical properties of carbon nanotubes, Imperial College Press, London, 1998.
- [2] Dresselhaus MS, Dresselhaus G, Avouris P. Carbon nanotubes: synthesis, structure, properties, and applications. Springer: Berlin, 2001.
- [3] Xie H, Lee H, Youn W. Nanofluids containing multiwalled carbon nanotubes and their enhanced thermal conductivities. *J. Appl. Phys.* 2003; 94: 4967–4971.
- [4] Rodriguez NM, Chambers A, Baker RTK. Catalytic engineering of carbon nanostructures. *Langmuir.* 1995; 11:3862–3866.
- [5] Fenelonov VB, Derevyankin AY, Okkel LG, et al. Structure and texture of filamentous carbons produced by methane decomposition on Ni and Ni–Cu catalysts. *Carbon.* 1997; 35: 1129–1140.
- [6] Wagner RS, Ellis WC, Vapor-Liquid-Solid mechanism of single crystal growth. *Appl. Phys. Lett.* 1964; 4: 89–90.
- [7] Alstrup I, Tavares MT. Kinetics of carbon formation from  $\text{CH}_4 + \text{H}_2$  on silica-supported nickel and Ni–Cu catalysts. *J. Catal.* 1993; 139: 513–524.
- [8] Snoeck JW, Froment GF, Fowles M. Filamentous carbon formation and gasification: thermodynamics, driving force, nucleation, and steady-state growth. *J. Catal.* 1997; 169: 240–249.
- [9] Rodríguez-Manzo JA, Terrones M, et al. In situ nucleation of carbon nanotubes by the injection of carbon atoms into metal particles. *Nat. Nanotechnol.* 2007; 2: 307–311.
- [10] Shi XH, Li HJ, Fu QG, Zhang SY, Guo LJ, Lu JH. Carbon infiltration of carbon-fiber preforms by catalytic CVI. *Carbon.* 2006; 44:1198–1202.
- [11] Gorbunov A, Jost O, Pompe W, Graff A. Solid-liquid-solid growth mechanism of single-wall carbon nanotubes, *Carbon.* 2002; 40: 113–118.
- [12] Audier M, Coulon M. Kinetic and microscopic aspects of catalytic carbon growth. *Carbon.* 1985; 23: 317–323.
- [13] Yang RT, Chen JP. Mechanism of carbon filament growth on metal catalysts. *J. Catal.* 1989; 115: 52–64.
- [14] Alstrup I. A new model explaining carbon filament growth on nickel, iron, and NiCu alloy catalysts. *J. Catal.* 1988;109: 241–251.
- [15] Rostrup-Nielsen JR, Trimm DL. Mechanisms of carbon formation on nickel-containing catalysts. *J. Catal.* 1977; 48: 155–165.
- [16] Melechko AV, Merkulov VI, Lowndes DH, Guillorn MA, Simpson ML. Transition between ‘Base’ and ‘Tip’ carbon nanofiber growth modes. *Chem. Phys. Lett.* 2002; 356: 527–533.
- [17] Kiselev NA, Hutchison JL, Moravsky AP, Rakova EV, Dreval EV, Hetherington CJD, Zakharov DN, Sloan J, Loutfy RO, Carbon micro- and nanotubes synthesized by PE–CVD technique: tube structure and catalytic particles crystallography. *Carbon.* 2004; 42: 149–161.
- [18] He ZB, Lee CS, Maurice JL, Pribat D, Haghi-Ashtiani P, Cojocaru CS, Vertically oriented nickel nanorod/carbon nanofiber core/shell structures synthesized by plasma-enhanced chemical vapor deposition. *Carbon.* 2011; 49: 4710–4718.
- [19] Lin M, Tan JPY, Boothroyd C, Loh KP, Tok ES, Foo YL, Direct observation of single-walled carbon nanotube growth at the atomistic scale, *Nano Lett.* 2006; 6: 449–452.
- [20] Yoshida H, Takeda S, Uchiyama T, Kohno H, Homma Y. Atomic-scale in-situ observation of carbon nanotube growth from solid state iron carbide nanoparticles. *Nano Lett.* 2008; 8: 2082–2086.
- [21] Hofmann S, Sharma R, Ducati C, et al. In situ observations of catalyst dynamics during surface-bound carbon nanotube nucleation. *Nano Lett.* 2007; 7: 602–608.
- [22] Lin M, Tan JPY, Boothroyd C, Loh KP, Tok ES, Foo YL. Dynamical observation of bamboo-like carbon nanotube growth. *Nano Lett.* 2007; 7: 2234–2238.

- [23] Hofmann S, Csányi G, Ferrari AC, Payne MC, Robertson J. Surface diffusion: the low activation energy path for nanotube growth. *Phys. Rev. Lett.* 2005; 95: 036101 1–4.
- [24] Cinquini, F, Delbecq F, et al. A DFT comparative study of carbon adsorption and diffusion on the surface and subsurface of Ni and Ni<sub>3</sub>Pd alloy. *Phys. Chem. Chem. Phys.* 2009; 11: 11546–11556.
- [25] Abild-Pedersen F, Nørskov JK, Rostrup-Nielsen JR, Sehested J, Helveg S. Mechanisms for catalytic carbon nanofiber growth studied by ab initio density functional theory calculations. *Phys. Rev. B.* 2006; 73: 115419 1–13.
- [26] Ding F, Rosén A, Bolton K. Dependence of SWNT growth mechanism on temperature and catalyst particle size: Bulk versus surface diffusion. *Carbon.* 2005; 43: 2215–2217.
- [27] Ding F, Rosen A, Campbell EEB, Falk LKL, Bolton K. Graphitic Encapsulation of Catalyst Particles in Carbon Nanotube Production, *J. Phys. Chem. B* 2006; 110: 7666–7670.
- [28] Ribas MA, Ding F, Balbuena PB, Yakobson BI, Nanotube nucleation versus carbon–catalyst adhesion- probed by molecular dynamics simulations. *J. Chem. Phys.* 2009; 131: 224501 1–7.
- [29] Raty JY, Gygi F, Galli G. Growth of carbon nanotubes on metal nanoparticles: a microscopic mechanism from ab initio molecular dynamics simulations. *Phys. Rev. Lett.* 2005, 95, 096103 1–4.
- [30] Neyts EC, Shibuta Y, Van Duin ACT, Bogaerts A. Catalytic growth of carbon nanotube with definable chirality by hybrid molecular dynamics-force biased monte carlo simulations. *ACS Nano.* 2010; 4: 6665–6672.
- [31] Shibuta Y, Maruyama S. Molecular dynamics simulation of generation process of SWNTs. *Phys. B* 2002; 323: 187–189.
- [32] Ohta Y, Okamoto Y, Irle S, Morokuma K. Density-functional tight-binding molecular dynamics simulations of SWCNT growth by surface carbon diffusion on an iron cluster, *Carbon.* 2009; 47: 1270–1275.
- [33] Viñes F, Neyman KM, Görling A. Carbon on platinum substrates: From carbidic to graphitic phases on the (111) surface and on nanoparticles. *J. Phys. Chem. A.* 2009; 113:11963–11973.
- [34] Loginova E, Bartelt NC, Feibelman PJ, McCarty KF. Evidence for graphene growth by C cluster attachment. *New J. Phys.* 2008; 10: 093026 1–16.
- [35] Hansen EW, Neurock M, Modeling surface kinetics with first-principles-based molecular simulation, *Chem. Eng. Sci.* 1999; 54: 3411–3421.
- [36] Rogal J, Reuter K, Scheffler M. First-principles statistical mechanics study of the stability of a subnanometer thin surface oxide in reactive environments: CO oxidation at Pd (100), *Phys. Rev. Lett.* 2007; 98: 046101 1–4.
- [37] Rogal J, Reuter K, Scheffler M. CO oxidation on Pd (100) at technologically relevant pressure conditions: first-principles kinetic Monte Carlo study, *Phys. Rev. B* 2008; 77: 155410 1–12.
- [38] Neurock M, Mei D. Effects of alloying Pd and Au on the hydrogenation of ethylene: An ab initio-based dynamic Monte Carlo study, *Topics Catal.* 2002; 20: 5–23.
- [39] Ji J, Duan X, Qian G, Zhou X, Chen D, Yuan W. In Situ production of Ni catalysts at the tips of carbon nanofibers and application in catalytic ammonia decomposition, *Ind. Eng. Chem. Res.* 2013; 52: 1854–1858
- [40] Yao Y, Falk LKL, Morjan RE, Nerushev OA, Campbell EEB. Cross-sectional TEM investigation of nickel-catalysed carbon nanotube films grown by plasma enhanced CVD, *J. Microscopy*, 2005; 219: 69–75.
- [41] Hong S, Shin Y, Ihm J, Crystal shape of a nickel particle related to carbon nanotube growth, *Jpn. J. Appl. Phys.* 2002; 41: 6142–6144.
- [42] H. Leidheiser and A.T. Gwathmey, The selective deposition of carbon on the (111) face of a nickel crystal in the catalytic decomposition of carbon monoxide, *J. Am. Chem. Soc.* 1948; 70: 1206–1206.
- [43] Te Velde G, Baerends EJ. Precise density-functional method for periodic structures. *Phys. Rev. B.* 1991; 44: 7888–7903.

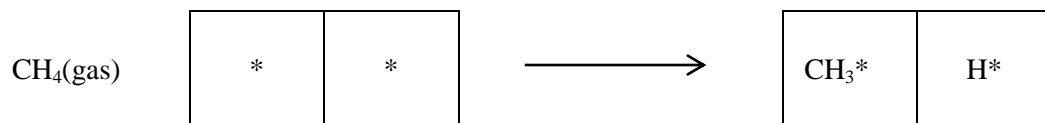
- [44] Wiesenekker G, Baerends EJ. Quadratic integration over the three-dimensional Brillouin zone. *J. Phys. Condens. Matter.* 1991; 3: 6721–6742.
- [45] Jansen APJ. An introduction to kinetic monte carlo simulations of surface reactions, Heidelberg; New York: Springer, 2012
- [46] D. T. Gillespie, Approximate accelerated stochastic simulation of chemically reacting systems. *J. Chem. Phys.* 2001;115: 1716–1733.
- [47] Chatterjee A, Vlachos DG, Katsoulakis MA, Binomial distribution based  $\tau$ -leap accelerated stochastic simulation, *J. Chem. Phys.* 2005;122: 0241121–0241127.
- [48] Tian T, Burrage K, Binomial leap methods for simulating stochastic chemical kinetics, *J. Chem. Phys.* 2004; 121: 10356–10364.
- [49] Cao Y, Gillespie DT, Petzold LR, The slow-scale stochastic simulation algorithm, *J. Chem. Phys.* 2005;122: 0141161–01411618.
- [50] Snyder MA, Chatterjee A, Vlachos DG, Net-event kinetic Monte Carlo for overcoming stiffness in spatially homogeneous and distributed systems, *Comp. Chem. Eng.* 2005;29:701–712.
- [51] Chatterjee A, Voter AF, Accurate acceleration of kinetic Monte Carlo simulations through the modification of rate constants, *J. Chem. Phys.* 2010;132:1941011–19410112
- [52] Guerrero S, Wolf EE, Kinetic Monte Carlo simulation of the preferential oxidation of CO using normally distributed rate probabilities, *Chem. Eng. Sci.* 2011; 66: 4477–4487.
- [53] Guerrero S, Wolf EE, Monte Carlo Simulation of stiff systems of catalytic reactions by sampling normally distributed rate probabilities. *AICHE J.* 2009; 55:3022–3025.
- [54] Amin A M, Croiset E, Constantinou C, Epling W, Methane cracking using Ni supported on porous and non-porous alumina catalysts, *Int. J. Hydrogen Energy* 2012; 37: 9038–9048.
- [55] Ermakova, MA, Ermakov DY, et al. Effective catalysts for direct cracking of methane to produce hydrogen and filamentous carbon: Part I. Nickel catalysts. *Appl. Catal. A: General.* 2000; 201: 61–70.
- [56] Fu X, Cui X, Wei X, Ma J. Investigation of low and mild temperature for synthesis of high quality carbon nanotubes by chemical vapor deposition, *Appl. Surf. Sci.* 2014; 292: 645–649.
- [57] Michalkiewicz B, Majewska J, Diameter-controlled carbon nanotubes and hydrogen production, *Int. J. Hydrogen Energy* 2014; 39: 4691–4697.
- [58] Singh C, Shaffer MS, Windle AH. Production of controlled architectures of aligned carbon nanotubes by an injection chemical vapour deposition method, *Carbon.* 2003; 41: 359–368.
- [59] Lee CJ, Lyu SC, Kim HW, Lee JH, Cho KI. Synthesis of bamboo-shaped carbon-nitrogen nanotubes using  $C_2H_2-NH_3-Fe(CO)_5$  system, *Chem. Phys. Lett.* 2002; 359: 115–120.
- [60] Yadav RM, Dobal PS, Shripathi T, Katiyar RS, Srivastava ON. Effect of growth temperature on bamboo-shaped carbon-nitrogen (C–N) nanotubes synthesized using ferrocene acetonitrile precursor, *Nanoscale. Res. Lett.* 2009; 4: 197–203
- [61] Cantoro M, Hofmann S, Pisana S, Scardaci V, Parvez A, Ducati C, Ferrari AC, Blackburn AM, Wang KY, Robertson J. Catalytic chemical vapor deposition of single-wall carbon nanotubes at low temperatures, *Nano Lett.* 2006; 6: 1107–1112.
- [62] Demicheli MC, Ponzi EN, Ferretti OA, Yeramian AA. Kinetics of carbon formation from  $CH_4-H_2$  mixtures on nickel-alumina catalyst, *Chem. Eng. J.* 1991; 46: 129–136.
- [63] Kuvshinov GG, Mogilnykh YI, Kuvshinov DG. Kinetics of carbon formation from  $CH_4-H_2$  mixtures over a nickel containing catalyst. *Catalysis Today*, 1998; 42: 357–360.
- [64] Gilliland ER, Harriott P. Reactivity of deposited carbon. *Ind. Eng. Chem.* 1954; 46: 2195–2202.
- [65] Nave S, Tiwari AK, Jackson B. Methane dissociation and adsorption on Ni (111), Pt (111), Ni (100), Pt (100), and Pt (110)-(1 $\times$ 2) : Energetic study *J. Chem. Phys.* 2010;132: 054705 1–12.
- [66] Wang SG, Liao XY, Hu J, Cao DB, Li YW, Wang JG, Jiao HJ. Kinetic aspect of  $CO_2$  reforming of  $CH_4$  on Ni (111): a density functional theory calculation, *Surf. Sci.* 2007; 601, 1271–1284.

- [67] Bengaard HS, Alstrup I, Chorkendorff I, Ullmann S, Rostrup-Nielsen JR, Nørskov JK. Chemisorption of methane on Ni (100) and Ni (111) surfaces with preadsorbed potassium. *J. Catal.* 1999; 187: 238–244.
- [68] Zhao NQ, He CN, Ding J, Zou TC, Qiao ZJ, Shi CS, Du XW, Li JJ, Li YD. Bamboo-shaped carbon nanotubes produced by catalytic decomposition of methane over nickel nanoparticles supported on aluminum. *J. Alloy. Compd.* 2007; 428: 79–83.
- [69] Lee CJ, Park JH, Park J. Synthesis of bamboo-shaped multiwalled carbon nanotubes using thermal chemical vapor deposition, *Chem. Phys. Lett.* 2000; 323: 560–565.
- [70] Lee CJ, Park J. Growth and structure of carbon nanotubes produced by thermal chemical vapor deposition, *Carbon* 2001; 39: 1891–1896.
- [71] Juang ZY, Lai JF, Weng CH, Lee JH, Lai HJ, Lai TS, Tsai CH. On the kinetics of carbon nanotube growth by thermal CVD method, *Diam. Relat. Mater.* 2004; 13: 2140–2146.

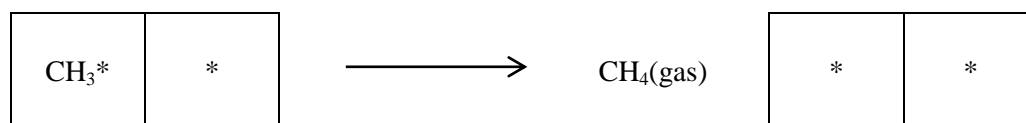
## Appendix

### Appendix A: Elementary Reaction Patterns

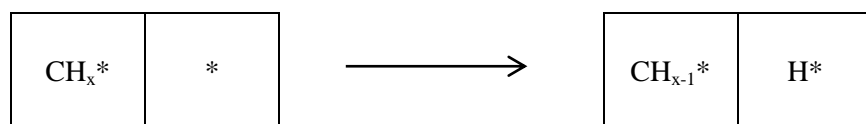
1) CH<sub>4</sub> dissociative adsorption:



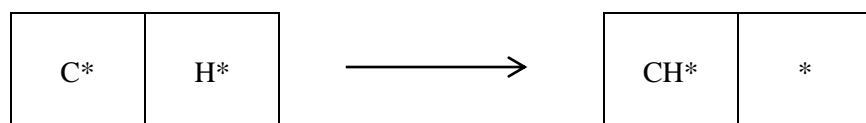
2) CH<sub>4</sub> production:



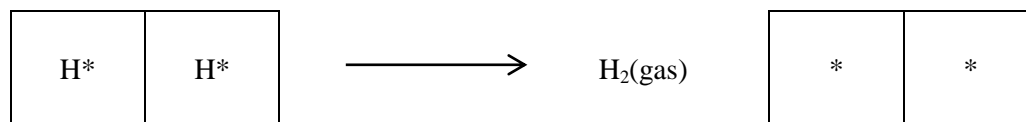
3) CH<sub>x</sub> (x=1-3) dissociation:



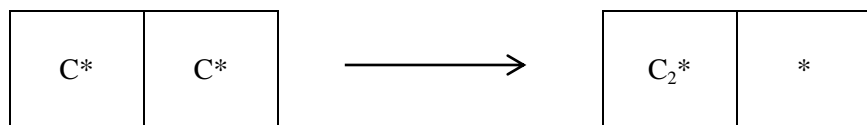
4) CH production:



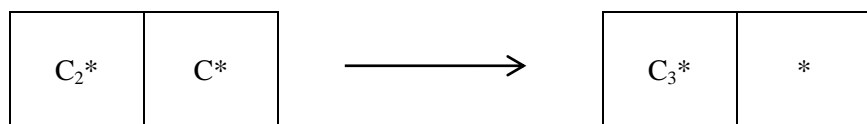
5) H<sub>2</sub> production:



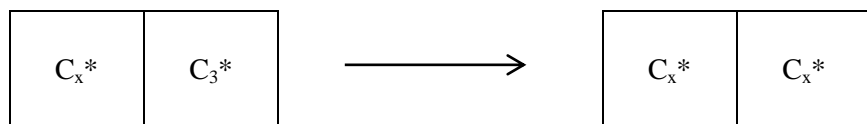
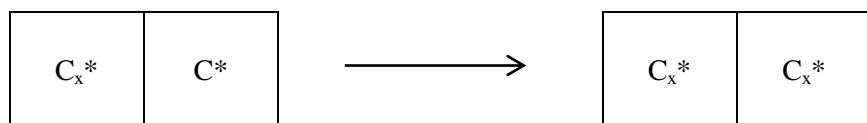
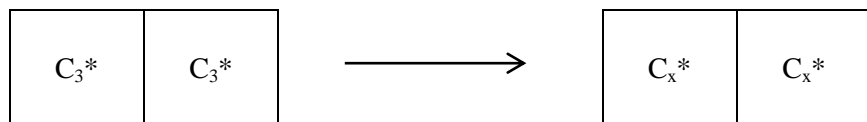
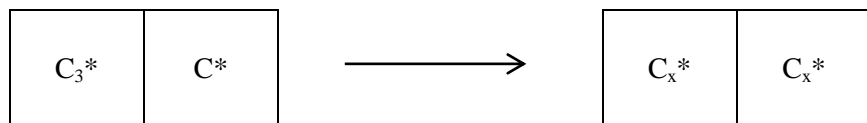
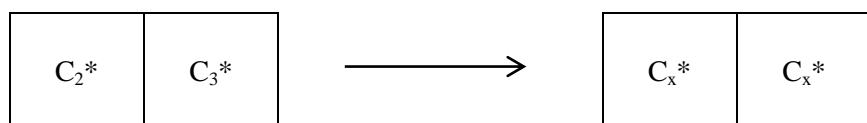
6) C<sub>2</sub> nucleation reaction:



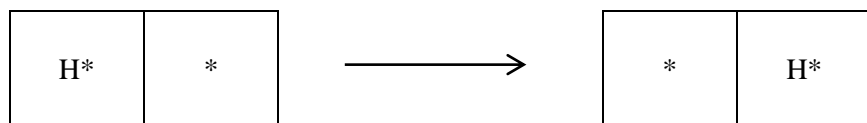
7)  $C_3$  nucleation reaction:



8)  $C_x$  nucleation reactions:



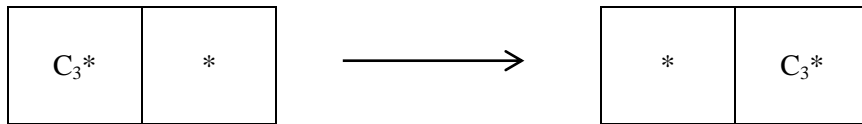
9) H surface diffusion:



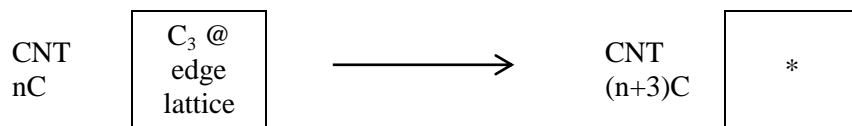
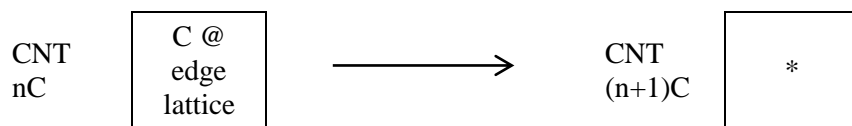
10) C surface diffusion:



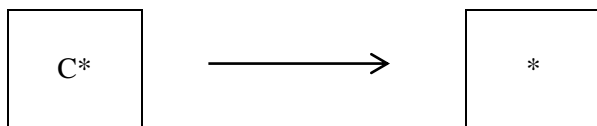
11) C<sub>3</sub> surface diffusion:



12) CNT growth:



13) C bulk diffusion:



(C disappear on the lattice, and is counted as go into the bulk)

## Appendix B: Reaction rate in AKMC:

1) Frequencies ( $N_{AA}$ ) that two molecular A sitting as neighboring sites on the lattice.  $N_A$  is the total number of A on the lattice;  $N \times N$  is the size of the lattice.

$$N_{AA} = \frac{N_A^2 - 2}{2} \frac{1}{1667} \left(\frac{70}{W}\right)^2$$

Modified reaction rate:

$$r_{i,AA} = k_i N_{AA}$$

Reactions that applied:  $H+H \rightarrow H_2$ ;  $C+C \rightarrow C_2$

2) Frequencies ( $N_{AB}$ ) that molecular A and B sitting as neighboring sites on the lattice.  $N_A$  and  $N_B$  are the total number of A and B on the lattice, respectively.

$$N_{AB} = \frac{N_A * N_B}{1667} \left(\frac{70}{N}\right)^2$$

Modified reaction rate:

$$r_{i,AB} = k_i N_{AB}$$

Reactions that applied:  $C+H \rightarrow CH$ ;  $C_2+C \rightarrow C_3$

3) Frequencies ( $N_{AE}$ ) that molecular A reaches the edge sites on the lattice.

$$N_{AE} = \frac{N_A}{23} \left(\frac{70}{N}\right)$$

Modified reaction rate:

$$r_{i,AE} = k_i N_{AE}$$

Reactions that applied:  $C^*(E)+CNT(n)_C \rightarrow CNT(n+1)_C$ ;  $C_3^*(E)+CNT(n)_C \rightarrow CNT(n+3)_C$